MICROSCALE MODELING OF GAS EXCHANGE DURING C_4 PHOTOSYNTHESIS

Moges RETTA

Supervisors:
Prof. Bart Nicolai
Prof. Paul Struik
Dr. Pieter Verboven

Members of the Examination Committee:
Prof. André Maes (chairman)
Prof. Maurice De Proft
Prof. Leo Marcelis
Prof. Wouter Saeys
Prof. Olaf Van Kooten

Dissertation presented in partial fulfilment of the requirements for the joint degree of Doctor of Bioscience Engineering (PhD) at KU Leuven by the authority of the Rector of KU Leuven Prof. Rik Torfs and Doctor at Wageningen University by the authority of the Rector Magnificus Prof. A.P.J Mol

January 2017

Doctoraatsproefschrift nr. 1397 aan de faculteit Bio-ingenieurswetenschappen van de KULeuven

This research was conducted under supervision of the Arenberg Doctoral School, KU Leuven, Belgium and the C.T. de Wit Graduate school for Production Ecology and Resource Conservation, Wageningen University and Research, The Netherlands.

Acknowledgements

Firstly, I would like to express my sincere gratitude to my promotor Prof. Bart Nicolai for his patience, motivation, and continuous support of my PhD study. My sincere thanks also goes to my co-promotor Prof. Paul Struik for his guidance throughout the research and the writing of this thesis.

My profound gratitude goes to Dr. Quang Tri Ho who has supervised me daily and closely during my PhD research. I would also like to thank Dr. Xinyou Yin for his dedicated, professional evaluation and contribution to the success of my research. My thanks also goes to Dr. Pieter Verboven for all the insightful discussions.

Besides my advisors, I would like to thank the rest of my thesis committee: Prof. Olaf Van Kooten, Prof. Leo Marcelis, Prof. Wouter Saeys and Prof. Maurice De Proft, for their insightful comments which incented me to widen my research from various perspectives.

My sincere thanks also goes to Prof. Johan Billen, Peter Van Der Putten, and Tiny Fransson, who gave access to the laboratory and research facilities and support during the experiments.

I thank my colleagues at MeBios and VCBT in for the stimulating discussions and for all the fun we have had in the last five years. Also I thank my friends in Wageningen University and Research.

This research was funded by KU Leuven (OT 12/055), the Research Fund Flanders (project G.0645.13) and BioSolar Cells project of Wageningen University and Research. Their contribution is gratefully acknowledged.

Last but not the least; I would like to thank my dear wife Hana Aragie and my kids Leul, Adonia and Elana for the love, support and understanding. I love you all! I would like to thank my mother, my brothers and sister for supporting me spiritually.

Moges Ashagrie Retta

Leuven, January 2017

Abstract

Improving the efficiency of photosynthesis could contribute to better food security under an unprecedented rise in global population and climate-change. The photosynthesis pathway in C_4 plants, such as maize (*Zea mays* L.), Miscanthus (*Miscanthus* x *giganteus*), and sugarcane (*Saccharum officinarum* L.), results in higher productivity and photosynthetic nitrogen and water-use efficiencies than in C_3 plants. The mechanism of photosynthesis in C_4 crops depends on the archetypal Kranz anatomy, which determines the leaf internal environment, for it influences gas diffusion and light distribution. The low permeability of bundle sheath cell walls to CO_2 (g_{bs}) and the high CO_2 conductance of mesophyll cells (g_m) are crucial for a high C_4 photosynthetic efficiency. So far, the relationship between leaf anatomical properties and CO_2 conductances such as g_{bs} and g_m in C_4 plants received less attention than in C_3 plants. In addition, these conductances lump a number of anatomical features; mechanistic understanding of the role of each microstructure element in the efficiency of photosynthesis is, therefore, limited. Furthermore, there are only few studies addressing the potential limitations of C_4 leaf anatomy on light propagation and efficiency of photosynthesis.

To investigate the role of leaf anatomy, as altered by leaf nitrogen content and age on the efficiency of C_4 photosynthesis, maize (*Zea mays* L.) plants were grown under three contrasting nitrogen levels. Combined gas exchange and chlorophyll fluorescence measurements were carried out on fully grown leaves at two leaf ages: young and old. The measured data were combined with a biochemical model of C_4 photosynthesis to estimate g_{bs}. The leaf microstructure and ultrastructure were quantified using images obtained from micro-computed tomography and microscopy. Increased nitrogen supply resulted in higher leaf nitrogen content and rate of photosynthesis, whereas leaf aging decreased them. There was a strong positive correlation between g_{bs} and leaf nitrogen content (LNC) while old leaves had lower g_{bs} than young leaves. g_m also increased with LNC and decreased with leaf aging. The increase of g_{bs} with LNC was little explained by a change in leaf anatomy. By contrast, the combined effects of LNC and leaf age on anatomical features were responsible for differences in g_{bs} between young leaves and old leaves. It is recommended that changes in the leaf ultrastructure at levels of membranes and plasmodesmata should be investigated to unravel the relationship between anatomy and CO_2 conductances further. Furthermore, since g_{bs} thus estimated, lumps a number of microstructural features, the contribution of each individual leaf

microstructural feature could not be determined. Therefore, a microscale modeling approach that accounts for each leaf microstructural and ultrastructural features is recommended.

A two-dimensional microscale model of gas diffusion and photosynthesis in C_4 leaves that incorporates the physical obstructions of leaf anatomy and ultrastructure on gas transport was developed. The leaf anatomical geometry was developed from light microscopy images of the same leaf that was also used in gas exchange measurements. Features such as cell walls, biological membranes, plasmodesmata and suberin layers around bundle sheath cell walls were modeled as resistances. Reaction-diffusion equations for CO_2 and bicarbonate in liquid phase media were developed and discretized over the two-dimensional leaf geometry. The model predicted the responses of photosynthesis to irradiance and intercellular CO_2 in agreement with that obtained from measurement. The impact of components of the CO_2 diffusion pathway on photosynthesis was evaluated quantitatively. The CO_2 permeability of the mesophyll-bundle sheath and air space-mesophyll interfaces strongly affected the rate of photosynthesis and g_{bs}. Carbonic anhydrase influenced the rate of photosynthesis, especially at low intercellular CO_2 levels. In addition, the suberin layer at the exposed surface of the bundle sheath cells was found beneficial in reducing the retro-diffusion of CO_2.

One or two-dimensional gas transport models, when applied to analyze the gas diffusion in leaves understate the three-dimensional nature of gas exchange. Therefore, a 3-D microscale model incorporating the actual leaf microstructure was developed. The distribution of light through the leaf tissue was modeled using an adapted Monte Carlo photon transport method. Diffusion of CO_2 and O_2 was coupled with C_4 photosynthesis kinetics and a model of light penetration inside the leaf tissue. The temperature dependency of biochemical and biophysical parameters was incorporated. The typical Kranz-anatomy of the leaf tissue caused large gradients of light intensity and concentration of gases. Maximum photosynthesis at low leakiness was obtained when chlorophyll contents of mesophyll and bundle sheath cells were equal. At elevated CO_2, photosynthesis in bundle sheath cells of juvenile leaves could potentially be supported by direct diffusion. Simulations also suggest that the effect of temperature on biophysical processes, in contrast to that on biochemical processes, has little influence on the temperature response of C_4 photosynthesis and leakiness. In addition, a systematic analysis showed that cytosolic CO_2 release due to decarboxylation of C_4 acids would reduce the efficiency of photosynthesis only moderately. The model may serve as a tool to further investigate improving C_4 photosynthesis in relation to gas exchange and light propagation.

Beknopte samenvatting

Het verbeteren van de efficiëntie van de fotosynthese kan bijdragen tot een betere voedselzekerheid in het kader van een stijging van de wereldbevolking zonder weerga en klimaatsverandering. De fotosyntheseroute in C_4-planten zoals maïs (*Zea mays* L.), Miscanthus (*Miscanthus x giganteus)* en suikerriet (*Saccharum officinarum* L.), resulteert in een hogere productiviteit en efficiëntie van fotosynthetisch stikstof- en waterverbruik vergeleken met deze in C_3-planten. Het mechanisme van de fotosynthese in C_4-planten hangt af van de archetypische Kranz-anatomie, die de interne omgeving van het blad bepaalt en zo de diffusie van gas en de lichtdistributie beïnvloedt. Een lage permeabiliteit van de vaatbundelschedecellen voor CO_2 (g_{bs}) en een hoge geleidbaarheid van CO_2 in de mesofylcellen (g_m) zijn van cruciaal belang voor de efficiëntie van de C_4-fotosynthese. De relatie tussen bladanatomische eigenschappen en CO_2-geleidbaarheid, zoals g_{bs} en g_m, in C_4-planten was tot nu toe minder het onderwerp van onderzoek, in tegenstelling tot de situatie bij C_3-planten. Bovendien voegen deze geleidbaarheden verschillende anatomische kenmerken samen, waardoor het mechanistisch begrip van de rol van elk afzonderlijk microstructuurelement met betrekking tot de efficiëntie van fotosynthese beperkt blijft. Tenslotte zijn er maar weinig studies over de mogelijke beperkingen door de C_4-bladanatomie van lichtdoorlating en efficiëntie van fotosynthese.

Om het effect van bladanatomie, zoals beïnvloed door de hoeveelheid stikstof per bladoppervlakte en bladleeftijd, op de efficiëntie van C_4-fotosynthese te onderzoeken, werden maïs (*Zea mays* L.) planten bij drie contrasterende stikstofniveaus geteeld. Gecombineerde gasuitwisselings- en chlorofylfluorescentiemetingen werden uitgevoerd op volledig volgroeide bladeren tijdens twee bladleeftijden: jong en oud. De data van de metingen werden gecombineerd met een biochemisch model van de fotosynthese in C_4-planten om de g_{bs} te schatten. De micro –en ultrastructuur van het blad werden gekwantificeerd op basis van afbeeldingen verkregen met X-stralenmicrotomografie en microscopie. Een hogere stikstofgift resulteerde in een grotere hoeveelheid stikstof per bladoppervlakte en een hogere fotosynthesesnelheid, terwijl de snelheid van bladveroudering afnam. Er was een sterke positieve correlatie tussen g_{bs} en de stikstofinhoud van het blad (LNC), terwijl oude bladeren een lagere g_{bs} hadden dan jonge bladeren. g_m nam ook toe met een toename van de LNC, maar nam af tijdens bladveroudering. De toename van g_{bs} met LNC werd weinig verklaard door

verandering in bladanatomie. Daarentegen waren de gecombineerde effecten van LNC en bladleeftijd op de anatomische eigenschappen verantwoordelijk voor verschillen in g_{bs} tussen jonge en oude bladeren. Het wordt aanbevolen de veranderingen in de ultrastructuur van het blad op het niveau van de membranen en plasmodesmata te onderzoeken om de relatie tussen anatomie en CO_2 geleidbaarheid verder te achterhalen. Aangezien g_{bs}, aldus geschat, een aantal microstructurele eigenschappen samenvoegt, kon de bijdrage van elke individuele microstructurele bladeigenschap niet worden vastgesteld. Daarom wordt een microschaal modelleeraanpak aanbevolen die rekening houdt met elke microstructurele en ultrastructurele bladeigenschap.

Een tweedimensionaal microschaal model van gasuitwisseling en fotosynthese in C_4-bladeren werd ontwikkeld, dat rekening houdt met de fysieke obstakels van de bladanatomie en ultrastructuur voor gastransport. De bladanatomische geometrie werd ontwikkeld op basis van lichtmicroscopiebeelden van hetzelfde blad dat was gebruikt voor de metingen van de gasuitwisseling. De ultrastructurele kenmerken, zoals celwanden, biologische membranen, plasmodesmata en suberinelagen rond de bundelschede-celwanden werden gemodelleerd als weerstanden. Reactie-diffusievergelijkingen voor CO_2 en bicarbonaat in de vloeibare fase-media werden ontwikkeld en gediscretiseerd over de tweedimensionale bladgeometrie. Het model voorspelde de reacties van fotosynthese op instraling en intercellulaire CO_2 overeenkomstig die verkregen via de meting. De effecten van de componenten van de CO_2-diffusieroute op de fotosynthese werden kwantitatief geëvalueerd. De CO_2-permeabiliteit van de mesofylbundelschede en luchtruimte-mesofyl contactoppervlakken beïnvloedden in sterke mate de snelheid van fotosynthese en g_{bs}. Koolzuuranhydrase beïnvloedde de snelheid van de fotosynthese, in het bijzonder bij lage intercellulaire CO_2-niveaus. Daarnaast werd de suberine-laag op het blootgestelde oppervlak van de vaatbundelschedecellen voordelig bevonden voor het reduceren van retro-diffusie van CO_2.

Wanneer één of tweedimensionale gastransport modellen worden toegepast om de gasdiffusie in bladeren te analyseren, onderschatten zij duidelijk de driedimensionale natuur van gastransport. Daarom werd een 3-D-microschaal model gebaseerd op de actuele bladmicrostructuur ontwikkeld. De lichtdoordringing in het bladweefsel werd gemodelleerd gebruikmakend van een aangepaste Monte Carlo fotontransportmethode. Diffusie van CO_2 en O_2 werd gekoppeld aan de C_4-fotosynthesekinetiek en een model van lichtpenetratie in het

bladweefsel. De temperatuurafhankelijkheid van biochemische en biofysische parameters werd in beschouwing genomen. De typische Kranz-anatomie van het bladweefsel veroorzaakte grote gradiënten in lichtintensiteit in het blad. Maximum fotosynthese bij lage lekkages werd verkregen wanneer de chlorofylgehalten in het mesofyl en in de vaatbundelschedecellencellen gelijk waren. Bij verhoogde CO_2 kon de fotosynthese in de vaatbundelschedecellen van jonge bladeren potentieel worden ondersteund door directe diffusie. Simulaties suggereren ook dat het effect van temperatuur op biochemische processen sterker is dan het effect op biofysische processen in het bepalen van de temperatuurrespons van de fotosynthese en van vaatbundellekkage. Daarnaast toonde een systematische analyse aan dat de cytosolische CO_2 afgifte ten gevolge van toenemende PSII-abundantie in de vaatbundelschedecellen of decarboxylatie van C_4-zuren de efficiëntie van de fotosynthese reduceert. De ontwikkelde modellen kunnen dus dienen als een middel om de gasuitwisseling en C_4-fotosynthese verder te onderzoeken.

Table of Contents

Nomenclature

Variables	Definitions	Units
A	Net photosynthesis rate	μmol m^{-2} s^{-1}
B	Net hydration of CO_2 to bicarbonate	μmol m^{-2} s^{-1}
C	Concentration of chemical species	μmol mol^{-1}
C_a	Concentration of ambient CO_2	μmol mol^{-1}
$\bar{C}_c$	Mean CO_2 concentration in bundle sheath chloroplast	μmol mol^{-1}
$\bar{C}_m$	Mean CO_2 concentration in mesophyll cytosol	μmol mol^{-1}
D	Diffusivity of chemical species	m^2 s^{-1}
D_{CO_2}	Diffusivity of CO_2	m^2 s^{-1}
$D_{HCO_3^-}$	Diffusivity of HCO_3^-	m^2 s^{-1}
D_{O_2}	Diffusivity of O_2	m^2 s^{-1}
d	Average thickness of leaf tissue	μm
E	Activation energy	kJ mol^{-1}
E_o	Rate of oxygen evolution in chloroplasts	μmol m^{-2} s^{-1}
f	Volume fraction of leaf microstructure components	m^3 m^{-3}
f_{chl}	Ratio of concentration of chlorophyll in bundle sheath to that of mesophyll cells	Dimensionless
f_{ASP}	Fraction of CO_2 release in bundle sheath cytosol	Dimensionless
$F_m^{'}$	Maximum fluorescence yield in light	Dimensionless
F_s	Steady state relative fluorescence yield	Dimensionless
f_{tot}	Total number of organelles per unit volume	Number μm^{-3}

g_{bs}	Bundle sheath conductance	mmol m^{-2} s^{-1}
g_m	Mesophyll conductance	mol m^{-2} s^{-1}
g_s	Stomatal conductance	mol m^{-2} s^{-1}
H	Henry's constant	Dimensionless
H	Energy of deactivation	kJ mol^{-1}
$[H^+]$	H^+ concentration	mol L^{-1}
I_{inc}	Incident photon flux density	μmol m^{-2} s^{-1}
J	Flux of gases or bicarbonate through interfaces	μmol m^{-2} s^{-1}
j	Potential electron transport rate	μmol m^{-2} s^{-1}
j_{ATP}	Potential total rate of ATP production	μmol m^{-2} s^{-1}
$j_{\max}$	Light-saturated rate of potential electron transport	μmol m^{-2} s^{-1}
k_a	Turnover rate of carbonic anhydrase enzyme	s^{-1}
k_1	CO_2 hydration velocity constant	s^{-1}
k_2	CO_2 dehydration velocity constant	s^{-1}
K_{bs}	Light absorbed per unit photosystem in bundle sheath cells	Dimensionless
K_{CO_2}	Michaelis-Menten constant for carbonic anhydrase hydration	μmol m^{-3}
K_{eq}	Equilibrium constant of carbonic anhydrase	μmol m^{-3}
K	Acid dissociation constant for H_2CO_3	mol L^{-1}
K_m	Light absorbed per unit photosystem in mesophyll cells	Dimensionless
$K_{m,C}$	Michaelis-Menten constant of Rubisco for CO_2	μbar
K_h	Michaelis-Menten constant of PEPc for HCO_3^-	μM
$K_{HCO_3^-}$	Michaelis-Menten constant for carbonic anhydrase	μM

	dehydration	
$K_{m,O}$	Michaelis-Menten constant of Rubisco for O_2	mbar
K_p	Michaelis-Menten constant of PEPc for CO_2	μbar
L	Rate of CO_2 leakage from bundle sheath cells	μmol m^{-2} s^{-1}
L_{pd}	Length of mesophyll-bundle sheath interface	μm
n_b	Base leaf nitrogen content	g m^{-2}
P	Permeability of biological membranes	m s^{-1}
P	Atmospheric pressure	Atm
R_{bs}	Rate of CO_2 release from bundle sheath cells due day respiration	μmol m^{-2} s^{-1}
R_{epi}	Rate of CO_2 release from bundle sheath cells due day respiration	μmol m^{-2} s^{-1}
R_m	Rate of CO_2 release from mesophyll cells due day respiration	μmol m^{-2} s^{-1}
R_v	Rate of CO_2 release from vasculature due day respiration	μmol m^{-2} s^{-1}
R	Universal gas constant	L atm K^{-1} mol^{-1}
R_d	Rate of day respiration	μmol m^{-2} s^{-1}
$\overline{r}$	Mean equivalent radius of organelles	μm
r_p	Photorespiratory CO_2 release from mitochondria	μmol m^{-2} s^{-1}
r_{p,O_2}	Photorespiratory O_2 consumption	μmol m^{-2} s^{-1}
S	Entropy term	kJ mol^{-1}
s'	Lumped calibration factor	Dimensionless
S_{bs}	Surface area of bundle sheath cell per unit leaf area	Dimensionless
$S_{C/O}$	Relative CO_2/O_2 specificity factor for Rubisco	Dimensionless

S_m	Surface area of mesophyll cell per unit leaf area	Dimensionless
V_c	Gross rate of CO_2 fixation	μmol m^{-2} s^{-1}
$V_{c,max}$	Maximum rate of Rubisco activity-limited carboxylation	μmol m^{-2} s^{-1}
V_p	Rate of PEP carboxylation based on bicarbonate ions	μmol m^{-2} s^{-1}
$V_{p,c}$	Rate of PEP carboxylation limited by CO_2	μmol m^{-2} s^{-1}
$V_{p,j}$	Rate of PEP carboxylation limited by electron transport	μmol m^{-2} s^{-1}
$V_{p,max}$	Maximum rate of enzyme activity-limited PEP carboxylation	μmol m^{-2} s^{-1}
w_c	Rubisco-limited rate of carboxylation	μmol m^{-2} s^{-1}
w_j	Electron-transport-limited rate of carboxylation	μmol m^{-2} s^{-1}
x	Partitioning factor of J_{ATP} to the C_4 cycle	Dimensionless
X	Slope of linearity between a parameter and leaf nitrogen content	mol g^{-1} s^{-1}
X_a	Concentration of carbonic anhydrase	mol m^{-3}
α	Fraction of PSII in bundle sheath cells	Dimensionless
ϕ	Leakiness	Dimensionless
Φ_{CO_2}	Quantum efficiency of CO_2 fixation	Dimensionless
Φ_{PSII}	Quantum efficiency of PSII electron transport	Dimensionless
Φ_{1LL}	Quantum efficiency of PSI electron transport at limiting light	Dimensionless
Φ_{2LL}	Quantum efficiency of PSII electron transport at limiting light	Dimensionless
θ	Ratio of the total area of plasmodesmata to that of the mesophyll-bundle sheath interface.	Dimensionless

Θ	Convexity coefficient	Dimensionless
γ^*	Half the inverse of $S_{C/O}$	Dimensionless
ζ	Effective porosity	Dimensionless
η	Viscosity of cell medium relative to water	Dimensionless
μ_a	Absorption coefficient	cm^{-1}
μ_s	Scattering coefficient	cm^{-1}
γ	Anisotropy factor	Dimensionless

Notations

Overscore	Mean value

Subscripts

a	Ambient
abs	Absorbed
ASP	Aspartate
bs	Bundle sheath
bs,ch	Bundle sheath chloroplast
bs,cy	Bundle sheath cytosol
c	Chloroplast; Carboxylation
C	CO_2
CA	Carbonic anhydrase
CF	Chlorophyll fluorescence
CET	Cyclic electron transport
d	Day
epi	Epidermis
i	Intercellular air space
inc	Incident
j	Electron transport
k	In Kelvin scale

LET	Linear electron transport
LL	Light limited
MAL	Malate
m	Mesophyll
m,cy	Mesophyll cytosol
max	Maximum
N	Nitrogen
NCA	No carbonic anhydrase
O	O_2
resp.	Respiratory tissue
vs	Vascular bundles

Superscripts

$*$	Volumetric

Abbreviations

ATP	Adenosine triphosphate
2-D	Two dimensional
3-D	Three dimensional
ca.	Circa
CCM	CO_2 concentration mechanism
LMA	Leaf dry mass per unit area
LNC	Leaf nitrogen content
Vol.	Volume
PEPC	Phosphoenolpyruvate carboxylase
PPDK	Pyruvate, phosphate dikinase
NADP-ME	$NADP^+$-dependent malic enzyme
PEPCK	Phosphoenolpyruvate carboxykinase
PEP	Phosphoenolpyruvate
NADP	Nicotinamide adenine dinucleotide phosphate

1 General introduction

1.1 C_4 photosynthesis

C_4 plants are called so because during photosynthesis of CO_2 they form four-carbon intermediate products. Maize (*Zea mays* L.), pearl millet (*Pennisetum glaucum*), sorghum (*Sorghum bicolor*), Miscanthus (*Miscanthus x giganteus*), sugarcane (*Saccharum officinarum* L.) and switchgrass (*Panicum virgatum*) are some examples of C_4 plants. C_4 plants cover less than one-fourth of the vegetated land surface globally and account for about 23 % of total gross primary production (Still *et al.*, 2003; Meiyappan and Jain, 2012). They are common in tropical and subtropical grasslands and savanna regions primarily due to warm conditions and availability of high light intensity (Sage *et al.*, 1999; Still *et al.*, 2003). In Europe, the central and southern part has a high abundance of C_4 plants dominated by monocotyledons (Pyankov *et al.*, 2010).

C_4 plants such as maize, sugarcane, millet and sorghum are important food and bioenergy sources. Global maize production was about 1 billion tons by the year 2013 which is about 40 % increase in a decade (FAO, 2013). The leading producers of maize, based on total production over the last four years, were USA, Brazil, China and Argentina (Table 1.1). The annual production of maize in Belgium has doubled over the last decade to ca. 0.6 million tonnes in 2013 (FAO, 2013). In The Netherlands, annual production remained at ca. 0.25 million tonnes for the past 10 years. C_4 plants are potential biofuel sources due to their higher biomass production than C_3 plants (van der Weijde *et al.*, 2013). This has been exploited in Brazil and the USA, which already use bioethanol, made from refining sugar in sugar cane or maize, as a transportation fuel (Pohit *et al.*, 2009). C_4 grasses such as Miscanthus and switchgrass are increasingly becoming biofuel sources in the USA and Europe (Heaton *et al.*, 2008; van der Weijde *et al.*, 2013). In addition, C_4 plants would remain important under extreme environmental conditions due to climate change (Byrt *et al.*, 2011). These benefits originate from and depend on the mechanism of photosynthesis in these plants which results in higher productivity and resource-use efficiency than in C_3 plants (Ghannoum *et al.*, 2010; van der Weijde *et al.*, 2013).

Table 1.1. Maize production (MT) from the year 2004 to 2014 (FAO, 2016). The quantities represent total cereal production. Rank is based on based on the total production.

Rank	Countries	Year							
		2014	2013	2012	2011	2009/10	2007/08	2004/07	Total
1	USA	361.1	353.7	273.8	313.9	648.7	638.3	849.6	3439.2
2	Mexico	23.3	22.7	22.1	17.6	648.7	638.3	706.7	2079.4
3	China	215.6	218.5	205.6	192.8	341.4	318.2	421.3	1913.4
4	Brazil	79.9	80.3	71.1	55.7	106.1	111.0	119.6	623.6
5	Italy	9.2	7.9	7.9	9.8	22.4	38.1	317.0	412.3
6	Indonesia	19.0	18.5	19.4	17.6	73.4	34.1	43.3	225.3
7	Argentina	33.0	32.1	23.8	23.8	23.5	38.7	46.7	221.6
8	India	23.7	23.3	22.3	21.8	40.3	38.7	21.4	191.4
9	Ukraine	28.5	30.9	21.0	22.8	15.4	11.4	8.0	138.1
10	Canada	11.5	14.2	13.1	10.7	22.4	34.8	28.9	135.6
11	Romania	12.0	11.3	6.0	11.7	16.4	6.2	45.8	109.3
12	South Africa	15.0	12.5	11.8	10.4	27.1	19.8	11.2	107.8
13	Hungary	9.3	6.8	4.8	8.0	14.5	12.9	29.8	86.1
14	Philippines	7.8	7.4	7.4	7.0	14.3	20.5	17.9	82.3
15	Nigeria	10.8	8.4	8.7	8.9	15.0	14.6	15.5	81.9
16	Serbia	8.0	5.9	3.5	6.5	14.7	10.1	24.6	73.2
17	Russian	11.3	11.6	8.2	7.0	7.0	10.5	10.2	65.9
18	Ethiopia	7.2	6.5	6.2	6.1	10.3	7.1	4.0	47.4
19	Tanzania	6.7	5.4	5.1	4.3	8.1	6.2	5.4	41.2

1.2 Problem statement

Photosynthesis is an important physiological process in plant growth and productivity. It is closely linked to global bioenergy and food supply. Due to the rapid growth in global population, thus increased demand for food and energy under increasingly scare arable land, compared with slower improvement in crop yield, an agricultural crisis is believed to be looming (Long *et al.*, 2006). In this regard, improving crop productivity by boosting photosynthesis is believed to contribute to tackle such a crisis (Long *et al.*, 2006; Ort *et al.*, 2015). This is exemplified by the efforts to increase the productivity of the C_3 crop rice, a

major food item in most populated regions of Asia, by engineering the more efficient photosynthesis mechanism of C_4 plants such as maize, sorghum, millet and sugar cane (Ort *et al.*, 2015). The high efficiency is due to the CO_2 concentration mechanism in these plants which allows them to accumulate CO_2 near fixation sites to concentrations higher than the ambient. In the CO_2 fixation process of C_4 plant leaves, unlike in the leaves of C_3 plants, the CO_2 is first fixed to C_4 acids in mesophyll cells. These acids are transported to bundle sheath cells where CO_2 is produced back, accumulated and fixed in CO_2-leakage-resistant bundle sheath cells (Hatch, 1987). This results in improved carbon conversion by minimizing photorespiration, a side-reaction which results in loss of fixed carbon; higher photosynthesis rate per leaf nitrogen; and, conservation of water since the CO_2 accumulation creates a weak coupling between transpiration and photosynthesis (Ghannoum *et al.*, 2010). In addition, a unique leaf structure that rapidly absorbs CO_2 and minimizes loss of the accumulated CO_2 is essential to the mechanism of C_4 photosynthesis (Hatch, 1987). In this case, mesophyll cells should be less resistant to CO_2 entry (have a high mesophyll conductance), and bundle sheath cells should resist CO_2 leakage (have a low bundle sheath conductance). These conductances were not extensively quantified due to the shortcomings of experimental methods like carbon isotope discrimination for C_4 plants (Farquhar, 1983). This quantitative information is essential to understand anatomical and biochemical limitations of photosynthesis as demonstrated by numerous studies on mesophyll conductance in C_3 plants (reviewed by Flexas *et al.* 2008). Instead, mathematical models were used to assess their responses to environmental changes and developmental stages (He and Edwards, 1996; Yin *et al.*, 2011*b*). For instance, bundle sheath conductance was shown to vary in response to factors such as nitrogen supply and leaf age (He and Edwards, 1996; Yin *et al.*, 2011*b*). However, the role of changes in leaf anatomy in such responses was not exhaustively analyzed. Further detailed insight could be gained by quantification of leaf structural changes simultaneously.

Physiology and anatomy are interwoven *in vivo*; thus it is difficult to experimentally assess the importance of one independently of the other. A model of leaf gas exchange that covers the entire leaf is today also computationally infeasible. These problems can be circumvented by the multiscale modeling paradigm. In an interconnected hierarchy of sub models, multiscale models can describe a physiological phenomenon at different spatial or temporal scales. This allows the simplicity of continuum-type models defined at the macroscale level to be combined at the level of detail of models incorporating microscale features, resulting in a

computationally feasible model. The approach facilitates investigations of the mechanisms of gas exchange phenomena in relation to the actual leaf microstructure as shown clearly for the gas exchange mechanism of C_3 plant leaves in recent studies (Ho *et al.*, 2012, 2016). However, application of such models to study photosynthesis of C_4 plants has received much less attention compared to C_3 photosynthesis. Previously, gas exchange in C_4 leaves has been described by simple (lumped) CO_2 transport models (Jenkins *et al.*, 1989*b*; Chen *et al.*, 1994; von Caemmerer and Furbank, 2003) resulting in apparent conductances that also incorporate the effect of leaf microstructure. Due to lack of explicit description of leaf anatomy, therefore, mechanistic understanding of the C_4 leaf gas exchange has been limited. This may not be desirable to efforts to improve photosynthesis since these would benefit from increased quantitative insights into the mechanism of photosynthesis generated from mechanistically-rich models.

1.3 Objectives and outline

The main objective of this dissertation is to contribute to the mechanistic understanding of the photosynthesis of C_4 plants through increased quantitative insight into gas transport. Thereto, the impact of resistances to gas transport provided by leaf microstructure on the efficiency of C_4 photosynthesis will be investigated experimentally and by using a mathematical modeling approach. Microscale models of gas exchange developed for C_3 plant leaves (Ho *et al.*, 2012, 2016) will then be extended to C_4 plant leaves with the aim of deriving mechanistic understanding on the role of each leaf microstructural component and leaf biochemistry to the efficiency of photosynthesis. Maize (*Zea mays* L.) will be used as a model system. The following sub-objectives were set out to achieve the main objective.

1. To introduce the fundamentals, the practices and challenges of modeling gas transport during photosynthesis of C_4 plants.
2. To investigate the impact of leaf anatomy as altered by increased nitrogen supply and leaf ageing on the efficiency of the CO_2 concentration using experiment and mathematical modeling.
3. To develop a two-dimensional microscale model of CO_2 exchange at tissue level and assess the roles of leaf microstructure, ultrastructural and biochemistry to the efficiency of CO_2 concentration mechanism and the rate of C_4 photosynthesis.

4. To develop a full three-dimensional model of gas transport and light propagation, investigate how the rate of C_4 photosynthesis can be improved, and examine its responses to environmental factors.

The thesis is outlined in the following way to achieve the sub-objectives sequentially. In Chapter 2, fundamentals of photosynthesis and CO_2 concentration mechanism will be introduced. Specific attention will also be given for the photosynthesis mechanism of maize. Factors causing loss of efficiency in C_4 photosynthesis will be described. After an introduction about the multiscale modeling approach and its application to gas transport modeling, the discussion will be focused on models of gas transport in a leaf of C_4 plants. The state of the art and challenges of modeling gas transport in C_4 leaves will be discussed.

In Chapter 3, experimental investigation of leaf anatomy of maize, differing in age and leaf nitrogen content will be explained. Plant growth conditions, measurements of gas exchange and chlorophyll fluorescence and leaf anatomical properties will be discussed. The estimation of the resistance of bundle sheath cells to CO_2 leakage through mathematical modeling will be explained, and results will be provided. Then, alterations of leaf anatomy by leaf nitrogen content and age will be related to resistances to CO_2 leak using statistical methods.

In Chapter 4, a two-dimensional (2-D) geometry of maize leaf will be developed from maize plant used in the imaging experiments in Chapter 3. The model will be validated using gas exchange and chlorophyll fluorescence data obtained in Chapter 3. Simulations will be carried out to investigate the role of leaf ultrastructural features and biochemistry to the efficiency of photosynthesis.

In Chapter 5, a three-dimensional (3-D) geometry of maize leaf will be developed using microscopy images obtained from the experiments in Chapter 3. The gas exchange model developed in Chapter 4 will be extended to a 3-D reaction-diffusion model that includes diffusion of CO_2, O_2, temperature responses of parameters and propagation of light to investigate improving photosynthesis and its response to perturbation in environmental changes. Simulations of the responses of photosynthesis to CO_2 and irradiance will be compared with those measured in Chapter 3. To improve the rate of photosynthesis, chlorophyll distribution between mesophyll and bundle sheath cells will be varied. A new light propagation profile will be computed for each distribution of chlorophyll and the

irradiance responses of photosynthesis and leakiness will be simulated. To examine the role of leaf microstructure in the response of C_4 photosynthesis to environmental variables such as elevated CO_2 and temperature; (i) the extent of contribution of direct CO_2 diffusion to bundle sheath cells of juvenile leaves will be simulated; and, (ii) temperature response of photosynthesis will be simulated to discern the relative contributions of biochemical and biophysical factors. In addition, the effect of CO_2 release in bundle sheath cytosol in relation to centrifugal position of bundle sheath chloroplasts on the efficiency of photosynthesis will be systematically evaluated by (i) considering various degrees of CO_2 release in the cytosol and (ii) by promoting photorespiration through enhanced oxygen evolution due to PSII abundance.

In Chapter 6, general conclusions and future perspectives will be given.

2 Essentials of C_4 photosynthesis and gas exchange modeling

2.1 Photosynthesis and photorespiration

Photosynthesis is a process by which energy from a light source, mainly the sun, is converted into chemical energy that is used for the functioning of organisms. Generally, carbon dioxide and water react in organelles called chloroplasts consuming the energy to produce carbohydrate and oxygen. The process steps of photosynthesis are divided broadly into two categories: light reactions and carbon reactions (Taiz and Zeiger, 2003).

Light reactions of photosynthesis occur in thylakoid membranes, which are present in chloroplasts. The membranes contain light-harvesting protein complexes among which major ones such as photosystem II (PSII), cytochrome b6f, photosystem I (PSI) and ATP synthase work in tandem to produce high-energy molecules, adenosine trisphosphate (ATP) and nicotinamide adenine dinucleotide phosphate (NADPH). The carbon fixation reactions of photosynthesis that convert CO_2 into carbohydrates, also known as the Calvin cycle, take place in the inner compartment of chloroplasts called the stroma. The cycle begins with the enzyme ribulose-1,5-bisphosphate (RuBP) carboxylase/oxygenase (Rubisco) catalyzing the reaction between CO_2 and RuBP. Some of the resulting three-carbon intermediate products are eventually reduced to glyceraldehyde-3-phosphate (GAP) using the ATP and NADPH produced during the light reactions. Some of the GAP molecules are further converted into carbohydrates such as glucose, fructose, starch, sucrose and cellulose. The electron acceptor RuBP is regenerated from the rest of the GAP molecules, thereby completing the cycle. Other than CO_2, Rubisco also reacts with oxygen in the first step of a process called photorespiration. This side reaction produces intermediates that are removed by the cooperation of peroxisomes and mitochondria, ultimately releasing CO_2 into the cytosol (Somerville, 2001). The removal processes waste the energy obtained from the light reactions, but some of the carbon lost from the Calvin cycle is recovered.

2.2 C_4 photosynthesis and carbon concentration mechanism

C_4 plants and algae responded to the decline of CO_2 and rise of O_2 levels in the atmosphere, which elevated photorespiration, by adding a carbon concentration mechanism (CCM) to the existing C_3 carbon fixation cycle (Sage, 2004; Christin *et al.*, 2008). The CCM elevates the concentration of inorganic carbon near Rubisco so that photorespiration is minimized. Due to the CCM, C_4 plants generally have higher water-use efficiency (ratio of photosynthesis to transpiration) and photosynthetic nitrogen-use efficiency (ratio of photosynthesis to leaf nitrogen content) than C_3 plants of similar rate of photosynthesis (Sage *et al.*, 1987). This is because CCM results in high rates of photosynthesis for a given leaf nitrogen content and, at low atmospheric CO_2, allows C_4 plants to close their stomata and reduce transpiration without a large drop in rate of photosynthesis (Sage and Pearcy, 2000).

There are three types of CCMs: C_4 photosynthesis, crassulacean acid metabolism (CAM) and CO_2 pumps. During C_4 photosynthesis, CO_2 is initially fixed into 4-carbon compounds, which are then moved to a separate compartment where decarboxylation of them produces CO_2 for fixation (Hatch and Slack, 1970). In a similar way, CAM plants assimilate CO_2 in mesophyll cytosol into a 4-carbon compound, malate, which accumulates in the vacuole of the same cell, but only during the night time. At day time, malate is transported to the chloroplasts of the cell and subsequently decarboxylated to release CO_2, which it is then reduced to sugars. Algae and cyanobacteria actively accumulate bicarbonate ions from the surrounding aquatic environment and convert them into CO_2 using carbonic anhydrase – a CO_2 pump embedded in the plasma membrane. Each of these CCMs is an ecophysiological adaptation to environmental conditions. For instance, C_4 plants are abundant in sites that are hot and dry; CAM is commonly found in plants in arid environments; and aquatic plants use CO_2 pumps.

C_4 plants evolved several times, resulting in three subtypes that are traditionally classified using the main decarboxylation enzyme as NADP-malic enzyme (NADP-ME), NAD-malic enzyme (NAD-ME) and PEP-carboxykinase (PEP-CK) types (Kanai and Edwards, 1999). Examples include maize, sorghum and millet for NADP-ME subtypes; vegetable amaranth (*Amaranthus tricolor*), grain amaranth (*Amaranthus edulis*) and tef (*Eragrostis tef*) for NAD-ME; and Guinea grass (*Panicum maximus*) and Rhodes grass (*Chloris gayana*) for PEP-CK subtypes. These subtypes have one common feature in carbon assimilation in mesophyll cells:

CO_2 in the form of bicarbonate which is produced by carbonic anhydrase (CA) is fixed by phosphoenolpyruvate (PEP) carboxylase (PEPC) in the mesophyll cytosol to produce oxaloacetate. Oxaloacetate (OAA) is converted predominantly into C_4 acids such as malate in NADP-ME plants, or into aspartate in NAD-ME and PEP-CK types (Kanai and Edwards, 1999). PEP-CK types also produce malate from OAA. The C_4 acids are transported to bundle sheath cells through plasmodesmata in all the subtypes. CO_2 is then produced in the bundle sheath cells through decarboxylation of the C_4 acids inside chloroplasts (NADP-ME), mitochondria (NAD-ME) or cytosol and chloroplasts (PEP-CK) (Kanai and Edwards, 1999; von Caemmerer and Furbank, 2003). Decarboxylation also produces pyruvate (all subtypes) and PEP (PEP-CK). To complete the cycle, pyruvate and PEP are directly returned to mesophyll cells (PEP-CK and NADP-ME) or pyruvate is converted to alanine (NAD-ME) and returned to mesophyll cells to regenerate PEP (Hatch, 1987). Recent researches provided evidence that the classification may not be rigid (Furbank, 2011) as some NADP-ME subtype plants such as *Zea mays* (Pick *et al.*, 2011) and *Flaveria bidentis* have substantial activity of PEP-CK that is also involved in the decarboxylation. In addition, the NAD-ME type *Cleome gynandra* has been shown to engage PEP-CK (Sommer *et al.*, 2012).

Some features of the Kranz-anatomy differ among these subtypes of C_4 plants (Kanai and Edwards, 1999; Edwards and Voznesenskaya, 2010). In NADP-ME types, bundle sheath chloroplasts are located close to the outer surface of bundle sheath cells adjoining mesophyll cells, commonly called centrifugal position; bundle sheath chloroplasts have less-developed grana than mesophyll chloroplasts; and the bundle sheath cell wall is suberized. In NAD-ME types, the bundle sheath chloroplasts are located near the vascular bundles, also called centripetal position; they have better developed grana than mesophyll chloroplasts; and the outer surface of the bundle sheath cells lacks a suberin layer. Bundle sheath chloroplasts in PEP-CK are either centrifugally or centripetally located, and the development of grana is similar in mesophyll and bundle sheath chloroplasts. In addition, bundle sheath cells of PEP-CK are suberized. These differences have implications for the photosynthesis efficiency. For instance, the centripetal positioning of chloroplast was related to the efficiency of photosynthesis through minimization of CO_2 leak from bundle sheath cells (von Caemmerer and Furbank, 2003). In addition, the suberine lamella was suggested to be beneficial in restricting leakage (Dengler *et al.*, 1994), although the absence of it in NAD-ME subtypes did not make the latter have a higher conductance to CO_2 leakage (Leegood, 2004). Furthermore,

the consequences of the difference in the nature of chloroplasts on the theoretical energy demand for fixation and the PSII to PSI activity in relation to the contribution of cyclic versus non cyclic electron transport were shown (Edwards and Walker, 1983; Hatch, 1987). Mesophyll chloroplasts capture more light energy while bundle sheath chloroplasts mainly fix CO_2 in cooperation with mesophyll cells because of the insufficient production of ATP and NADPH in the bundle sheath cells (due to less access to light and cyclic electron transport). In addition, a reduced PSII content in the bundle sheath minimizes oxygen evolution and the potential for photorespiration (Hatch, 1987). However, the significance of the chloroplast positioning and of the suberin layer for photosynthesis efficiency is not well established yet (Zhu *et al.*, 2010). In comparison to the anatomy of C_3 plants, there is a lower ratio of mesophyll to bundle sheath cells, a closer vein spacing, minimal exposure of bundle sheath cells to the intercellular air space and less volume of the intercellular air space in leaf anatomy of C_4 plants (Dengler *et al.*, 1994; Muhaidat *et al.*, 2007). Despite variations in the Kranz-anatomy among C_4 plants, positioning of chloroplasts in bundle sheath cells, having distinct chloroplast between mesophyll and bundle sheath cells, and the deposition of the suberin lamellae around the cell are believed to be important features (von Caemmerer *et al.*, 2007).

The physiology of C_4 plants explains their global distribution (Sage and Pearcy, 2000). C_4 plants are successful in warm climates due to their superior quantum yield, but not in cool climates due to chilling sensitivity of fixation enzymes. Ample access to sunlight in low latitudes favors C_4 plants due their high requirement of energy for photosynthesis. The better performance of C_4 plants compared to ecologically similar C_3 plants in low altitude (low photorespiration), saline soil (higher water-use efficiency), arid lands (higher water-use efficiency) and nitrogen deficient soil (higher nitrogen-use efficiency) are mainly due to the superior mechanism of photosynthesis (Sage and Pearcy, 2000) (see section 2.5 for more discussion). Among subtypes of the C_4 pathway, NADP-ME and PEP-CK exceed NAD-ME type grasses in photosynthetic nitrogen-use efficiency partly due to the differences in subtype (Pinto *et al.*, 2015) besides a faster Rubisco in NADP-ME grasses (Ghannoum *et al.*, 2005). By contrast, these differences were argued to be minimal under large interspecific differences (Taub and Lerdau, 2000). NADP-ME plants have higher quantum yield than NAD-ME plants due to differences in leakiness and efficiency of light absorption (Sage and Pearcy, 2000). The leaf water-use efficiency was shown to be comparable between NADP-ME and NAD-ME (Ghannoum *et al.*, 2001).

2.3 C_4 photosynthesis in maize

NADP-ME subtypes such as maize and sugar cane are the most economically significant C_4 plants, with maize being the most produced crop (FAO, 2013). The mechanism of C_4 photosynthesis in maize requires a spatial separation of the sites of CO_2 capture and CO_2 fixation. This is achieved by a specialized leaf anatomy called the Kranz-anatomy (Kranz is a German word meaning wreath).

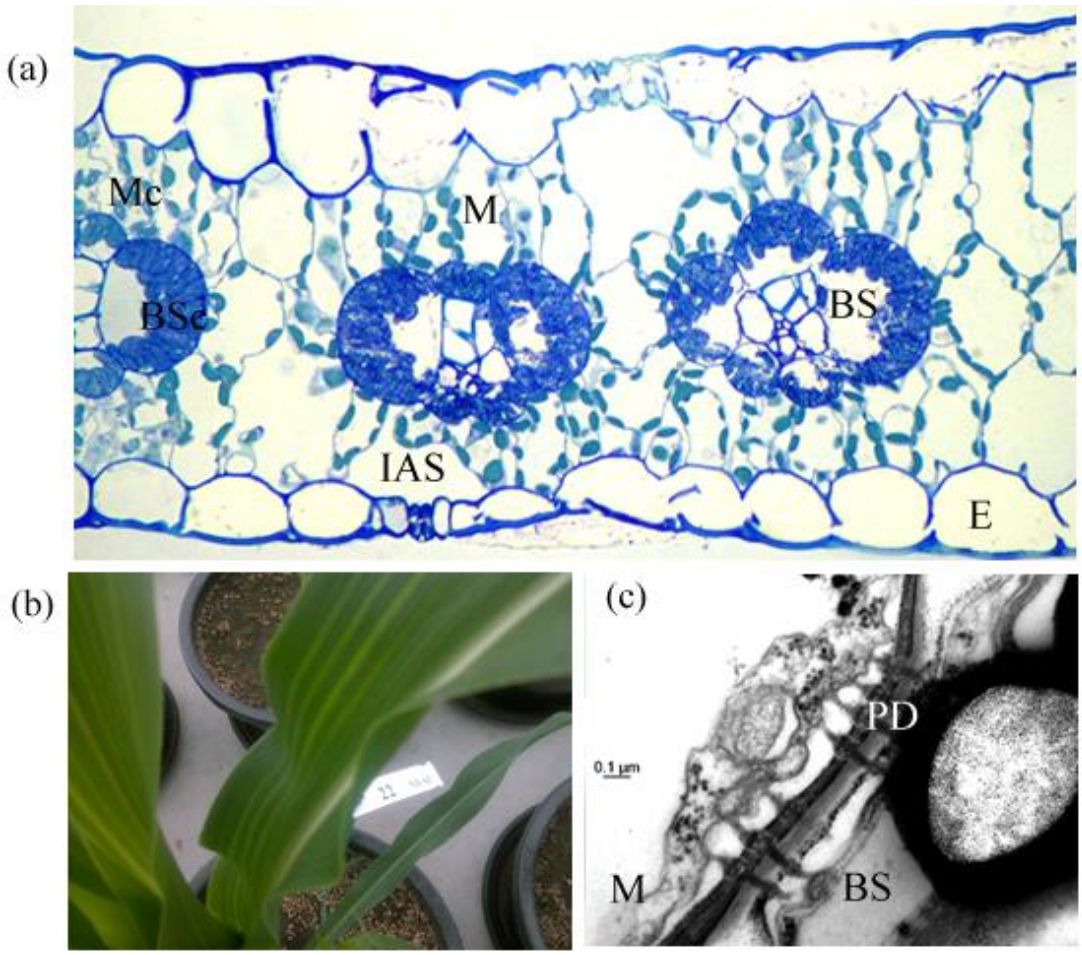

Figure 2.1. Maize leaf and internal structure. Shown in (a) are mesophyll cells (M), chloroplasts of mesophyll cells (Mc), bundle sheath cells (BS), chloroplasts of bundle sheath cells (BSc), intercellular air spaces (IAS) and epidermis (E). A picture of a maize leaf is shown in (b). M and BS cells are shown connected by plasmodesmata (PD) in (c).

The appearance, internal anatomy and ultrastructure of a maize leaf are shown in Fig. 2.1. Typical of the Kranz-anatomy, mesophyll cells surround bundle sheath cells, which

themselves are distributed around the vascular bundles (Fig. 2.1A). Such arrangements allow them to assimilate CO_2 using O_2-insensitive enzymes in mesophyll cells and to restrict direct access of bundle sheath cells to O_2 thereby reducing the potential for photorespiration. The inner layer, bundle sheath cells, accumulates and fixes CO_2 (Fig. 2.1A). These specializations are a common feature of several variants of the Kranz-anatomy which arose due to multiple evolutions from the leaf anatomy of C_3 plants (Sage, 2004). Common to most C_4 plants, one to two layers of mesophyll cells surround bundle sheath cells except in the husk of some plants where the number of layers is three (Pengelly *et al.*, 2011). Fig. 2.1A shows that chloroplasts are more numerous in bundle sheath cells than in mesophyll cells, which is a typical feature of the leaf anatomy of NADP-ME plants (Dengler and Nelson, 1999). Fig. 2.1 (C) also shows that mesophyll and bundle sheath cells are connected by plasmodesmata through which exchange of photosynthetic metabolites occurs. The importance of leaf anatomy to photosynthesis in maize is discussed in Section 2.4.

The mechanism of photosynthesis in maize is schematically depicted in Fig. 2.2. CO_2 is hydrated by carbonic anhydrase in the mesophyll cytosol to produce bicarbonate ions (Kanai and Edwards, 1999). PEPC then catalyzes the reaction of PEP and bicarbonate ions in a process known as PEP carboxylation producing an intermediate C_4 acid, oxaloacetate. In mesophyll chloroplasts, OAA is converted into malate by NADP-malate dehydrogenase (NADP-MDH). Malate subsequently diffuses into bundle sheath cells through plasmodesmata and is decarboxylated by NADP-ME to produce CO_2 in bundle sheath chloroplasts. Recent studies suggest that some flexibility exist in maize as OAA is also converted into aspartate by aspartate transaminase (Furbank, 2011; Pick *et al.*, 2011); however, the pathway of CO_2 donation from aspartate through combination of aspartate transaminase and PEP-CK is not yet clear (Wang *et al.*, 2014*a*). The decarboxylation produces pyruvate, NADPH and CO_2 around the vicinity of Rubisco, which is exclusively located in bundle sheath cells. The process steps so far collectively constitute the "C_4 cycle" while subsequent reactions of fixation of CO_2 are referred to as the "C_3 cycle" (Fig. 2.2). NADPH is donated to the Calvin cycle in bundle sheath cells while pyruvate is returned to mesophyll cells. PEP is regenerated from pyruvate by pyruvate, phosphate dikinase (PPDK). This regeneration of PEP in mesophyll chloroplasts requires energy in the form of ATP, which is supplied from the absorbed light. PEP is exported to the mesophyll cytosol and used in PEP carboxylation, thereby completing the cycle. The carboxylation and oxygenation of Rubisco as described in Section 2.1

(Photosynthesis and photorespiration) also take place. Oxygenation of Rubisco produces glycollate from which CO_2 is recovered by cooperation of mitochondria and peroxisomes. Furthermore, the intermediates of the Calvin cycle such as phosphoglyceric acid (PGA) and glycerate 3-phosphate (GAP) are partly transported to mesophyll for reduction since the low PSII activity and cyclic electron transport lead to less reducing power available in bundle sheath chloroplasts. The transport of metabolites across envelopes and membranes is facilitated by translocator proteins embedded in them (Leegood, 2004).

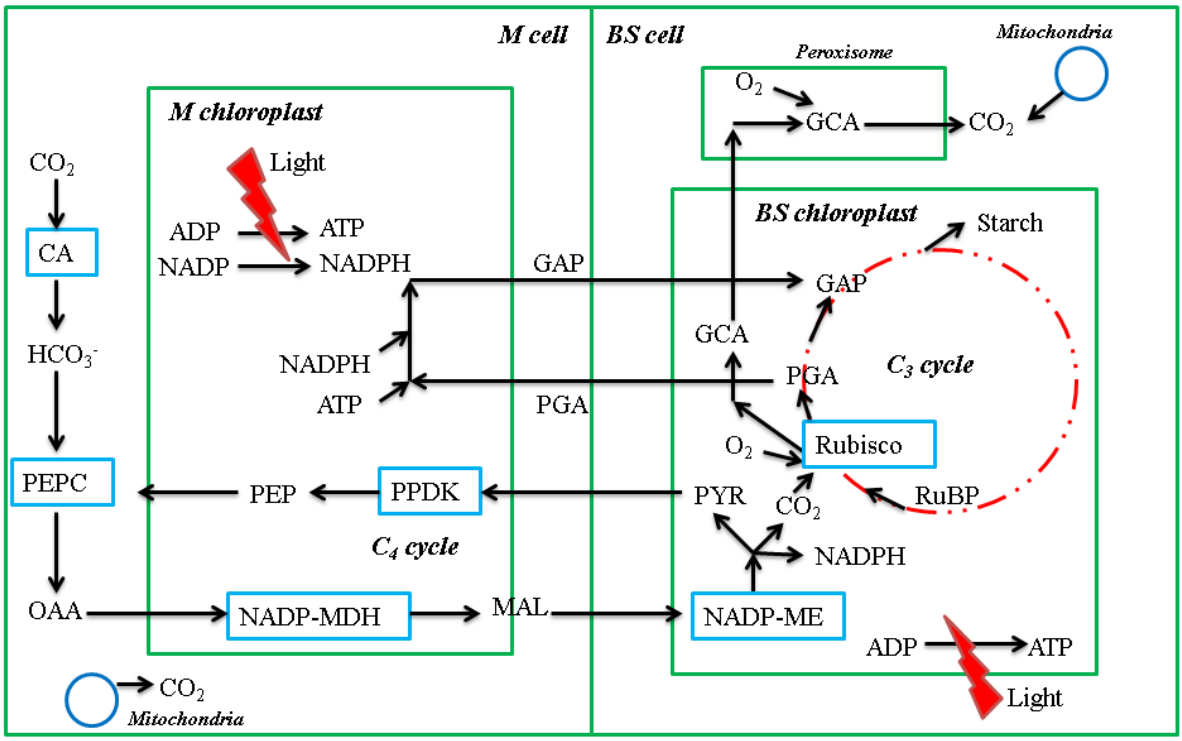

Figure 2.2. Schematic representation of simplified mechanism of C_4 photosynthesis in NADP-ME subtype. Abbreviations are: mesophyll (M), bundle sheath (BS), carbonic anhydrase (CA), phosphoenolpyruvate (PEP) carboxylase (PEPC), bicarbonate (HCO_3^-), oxaloacetate (OAA), malate (MAL), NADP-malate dehydrogenase (NADP-MDH), NADP-malic enzyme (NADP-ME), pyruvate (PYR), pyruvate Pi dikinase (PPDK), phosphoglyceric acid (PGA), glyceraldehyde 3-phosphate (GAP), ribulose-1,5-bisphosphate (RuBP) carboxylase/oxygenase (Rubisco) and glycollate (GCA); Figure adapted from various sources (von Caemmerer and Furbank, 1999; Wang *et al.*, 2014*b*).

2.4 Functional leaf anatomy of maize

Leaf anatomy plays a critical role in growth and metabolism through its influence in light absorption, CO_2 acquisition, assimilate transport and temperature regulation. In this section, key anatomical traits that control CO_2 concentration and light propagation are discussed. The influence of growth conditions and development stages are briefly described.

The flux of gases diffusing into leaves is related to the driving force, concentration gradient, using a proportionality constant termed conductance (Nobel, 2005). The inverse of conductance is called resistance. Conductance is usually a more preferable term than resistance in photosynthesis research (Nobel, 2005). Fig. 2.3 shows various conductances in a maize leaf.

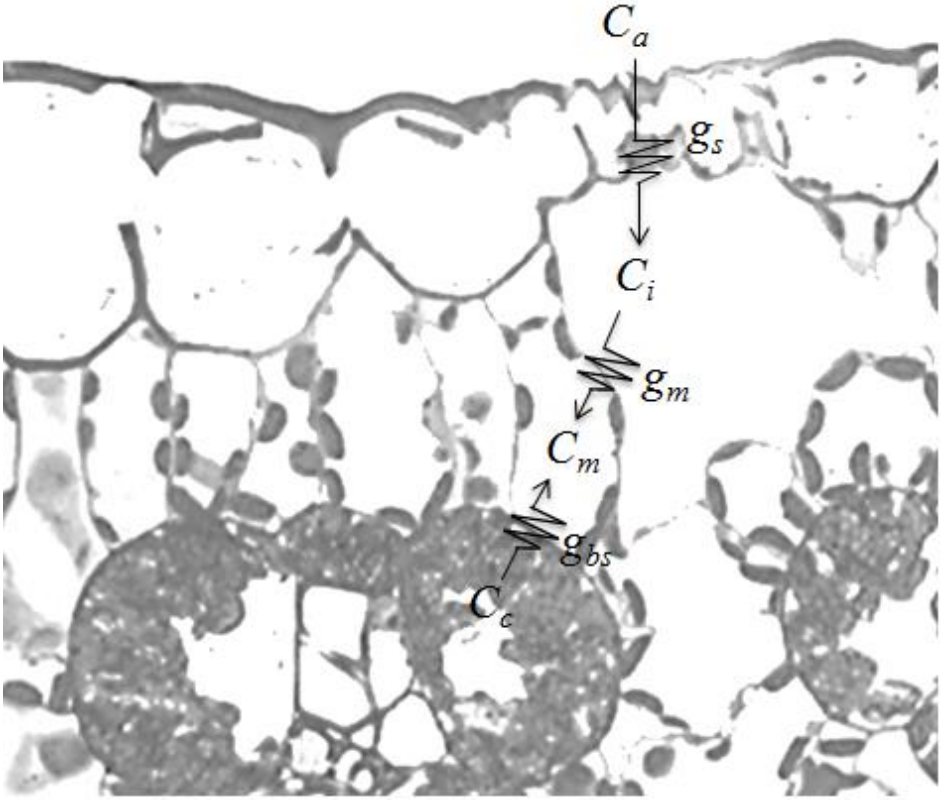

Figure 2.3. Pathway of CO_2 diffusion in maize leaf and various conductances. Stomatal conductance (g_s) is responsible for the drawdown of CO_2 concentration from ambient (C_a) to intercellular air spaces (C_i). Mesophyll conductance (g_m) determines the gradient in CO_2 from C_i to the concentration in mesophyll cytosol (C_m). Bundle sheath conductance (g_{bs}) affects CO_2 diffusion to mesophyll cells due to high concentration of CO_2 in bundle sheath cells (C_c).

During photosynthesis, CO_2 diffuses from the atmosphere to sites of fixation facing various resistances along the way. Gases must diffuse through the stagnant layer of air near the leaf surfaces, the resistance of which is called boundary-layer resistance. This resistance is usually smaller than the resistance of stomata. In a well-mixed cuvette during gas exchange measurement, boundary-layer resistance is usually neglected (Evans *et al.*, 2004; Nobel, 2005). The main pathway of gas diffusion is through stomata since the cuticle layer prevents water loss and CO_2 diffusion. Stomatal conductance (g_s) determines the gradient in CO_2 concentration from the atmosphere to sub stomatal cavities when the conductance of the cuticle is assumed low. g_s is estimated from transpiration measurement based on an assumption that water and CO_2 share the same diffusion pathway (von Caemmerer and Farquhar, 1981). It responds to changes in environmental variables such as leaf water potential, leaf-to-air vapor pressure difference, temperature and CO_2 concentration (Zeppel *et al.*, 2012).

In a maize leaf, the diffusion of CO_2 from the substomatal cavities to the mesophyll cytosol is constrained by the mesophyll conductance (g_m). g_m is a composite of the conductance of the intercellular air space, the cellular conductance and leaf anatomy (Longstreth *et al.*, 1980). The conductance of the intercellular air space depends on mesophyll porosity, leaf thickness, stomatal distribution and bundle sheath extensions. This conductance in a maize leaf is high since it is an amphistomatous leaf (Driscoll *et al.*, 2006); has a thin leaf (El-Sharkawy, 2009); and high porosity (El-Sharkawy, 2009). The cellular conductance is limiting the overall transport since diffusion in the liquid phase is several magnitudes slower than in the gaseous phase. The cellular conductance lumps the conductances of the cell wall, plasma membrane and mesophyll cytosol. The porosity, tortuosity and thickness of the cell wall are some of the anatomical factors influencing the conductance (Evans *et al.*, 2009). The permeability may be enhanced by membrane embedded components such as aquaporins and carbonic anhydrase (Utsunomiya and Muto, 1993; Maurel *et al.*, 2015). The conductance of the cytosol is determined by its thickness and composition, which may be different from pure water due to fibrous proteins (Nobel, 2005). In addition, g_m depends on the exposed surface area of mesophyll cells per unit leaf area (S_m). On a leaf area basis, g_m is thus the product of the cellular conductance and S_m.

C_4 plants are believed to have a higher g_m than C_3 plants despite the former having a lower exposed surface of mesophyll cells (von Caemmerer and Furbank, 2003). This conductance was not extensively quantified for C_4 plants due to lack of substantial sensitivity of the biochemical fractionation of the carbon isotope discrimination method (von Caemmerer *et al.*, 2014). g_m is reported to vary from 0.5 to 3.5 mol m^{-2} s^{-1} for various C_4 plants (Gillon and Yakir, 2000; Pengelly *et al.*, 2010; Kromdijk *et al.*, 2010; Yin *et al.*, 2011*b*; Barbour *et al.*, 2016). In response to treatments, a few reports show that g_m increased with the leaf nitrogen content (Yin *et al.*, 2011*b*), decreased with age (Yin *et al.*, 2011*b*; Barbour *et al.*, 2016) and responded to growth light intensity through changes in S_m (Pengelly *et al.*, 2010). However, the mechanisms contributing to the high g_m are not understood well (von Caemmerer and Furbank, 2003; Weber and von Caemmerer, 2010).

CO_2 accumulated in bundle sheath cells also diffuses back (referred to as retro-diffusion) to surrounding mesophyll cells inevitably due to connection of these cells by plasmodesmata (Hatch, 1987). The rate of this retro-diffusion depends on the balance of CO_2 supply by PEPC and CO_2 assimilation by Rubisco (mainly) and the resistance of bundle sheath cells (Kromdijk *et al.*, 2014). The bundle sheath resistance (inverse of bundle sheath conductance, g_{bs}) is composed of the resistances of the gas transport pathway from the bundle sheath to mesophyll cells. On a leaf area basis, g_{bs} is the product of cellular conductances and surface area of bundle sheath cells per unit leaf area (S_b). The cellular conductance is composed of the conductances of chloroplast envelope, cytosol, cell wall, plasmodesmata, plasma membrane and suberin lamella. In a maize leaf, CO_2 is released by decarboxylation of C_4 acids, photorespiration and respiration inside chloroplasts and the bundle sheath cytosol (Section 2.3). Thus, the resistance imposed by the chloroplast envelope is an important constraint. In addition, CO_2 leakage is constrained by plasmodesmata which account for 3 to 6 % of the bundle sheath cell wall surface (Tyree, 1970; Sowiński *et al.*, 2008; Danila *et al.*, 2016). Since the bundle sheath is suberized, direct leakage through the cell wall occurs through plasmodesmata (Dengler and Nelson, 1999).

g_{bs} determines the concentration of CO_2 in bundle sheath cells and constraints the rate of retro-diffusion (Hatch, 1987; Leegood, 2002), thereby greatly controlling the efficiency of CCM. However, due to lack of experimental methods to determine it, g_{bs} is also a poorly constrained parameter as there are only few estimates of its magnitude (He and Edwards,

1996; Kiirats *et al.*, 2002; Yin *et al.*, 2011*b*; Bellasio and Griffiths, 2014*c*). g_{bs} is usually estimated from biochemical models (Yin *et al.*, 2011*b*). Estimates of the resistance vary from 400 – 1600 m^2 s mol^{-1} (von Caemmerer and Furbank, 2003; Yin *et al.*, 2011*b*). g_{bs} also responds to growth conditions and leaf age (Kiirats *et al.*, 2002; Yin *et al.*, 2011*b*, 2016).

Overall, g_m and g_{bs} are important determinants of C_4 photosynthesis and the efficiency of the CCM. However, estimates of them are not widely available for C_4 plants. Since these conductances are constrained by leaf anatomy, their response to growth conditions could be properly examined by considering leaf anatomy simultaneously. In addition, mechanistic understanding of them could be obtained by considering individual components of the resistance explicitly using appropriate modeling approaches.

Leaf anatomy of maize impacts the distribution of light and thus photosynthesis (Bellasio and Lundgren, 2016). The concentric arrangement of mesophyll and bundle sheath cells implies that light reaches mesophyll cells before penetrating into the bundle sheath cells. Consequently, more light is absorbed by mesophyll cells than by bundle sheath cells (Evans *et al.*, 2007; Bellasio and Lundgren, 2016). Red, green and blue light differ in their distribution, with blue light being highly absorbed in the upper leaf while green light penetrates deeper (Evans *et al.*, 2007; Bellasio and Griffiths, 2014*c*). The light propagation in maize is further complicated by the different structure and function of mesophyll and bundle sheath chloroplasts. Mesophyll chloroplasts are generally smaller than bundle sheath chloroplasts and contain more chlorophyll. Bundle sheath chloroplasts on the other hand are larger, contain less chlorophyll, are specialized in CO_2 fixation and lack significant PSII activity (Dengler and Nelson, 1999; Kanai and Edwards, 1999). Some anatomical features like bundle sheath extensions which lack chlorophyll are suggested to facilitate propagation of light into bundle sheath cells (Bellasio and Lundgren, 2016). The amount of light absorbed and the differences in chloroplasts ultimately determine the amount of ATP generated in mesophyll and bundle sheath cells. The fraction of ATP produced in mesophyll cells is predicted to be around 40 % (von Caemmerer and Furbank, 1999; Yin and Struik, 2012) for maximal rate of photosynthesis. Light absorption is enhanced in maize leaves by maintaining a close spacing of the veins so that more chloroplasts are obtained per unit leaf area (Ehleringer *et al.*, 1997). This short intervenial distance was suggested to result in a higher quantum yield (Ogle, 2003). Movement of mesophyll chloroplasts which maximizes light absorption (Terashima *et al.*,

2011) is rather slow in C_4 plants compared to that of C_3 plants (Yamada *et al.*, 2009). Bundle sheath chloroplasts do not move in response to light intensity (Taniguchi *et al.*, 2003; Yamada *et al.*, 2009).

2.5 Losses of efficiency in C_4 photosynthesis

In C_4 crops, the CCM elevates the concentration of inorganic carbon in bundle sheath cells much higher than that in mesophyll cells (Furbank and Hatch, 1987). This gradient in concentration results in the leakage of CO_2 and bicarbonate from bundle sheath cells to mesophyll cells. The rate of CO_2 leakage relative to the rate of PEP carboxylation, termed leakiness (von Caemmerer and Furbank, 1999), is used to assess the efficiency of C_4 photosynthesis. Leakiness is constrained both by the resistance of bundle sheath cells and the balance of the C_4 and C_3 cycle (Kromdijk *et al.*, 2014). For instance, a higher capacity of the C_4 cycle and a reduced C_3 cycle activity leads to increased leakage due to excess CO_2. This balance is carefully controlled *in vivo* so that leakiness remains low (10 to 30 %) under ambient conditions (Kromdijk *et al.*, 2014).

C_4 photosynthesis is susceptible to low light intensity, low temperature and light quality. Several reports show that leakiness of bundle sheath cells increased at low irradiance (Henderson *et al.*, 1992; Pengelly *et al.*, 2010; Kromdijk *et al.*, 2010). This phenomenon is of critical importance since about half of the maize productivity occurs under low light (Kromdijk *et al.*, 2008). Increased photorespiration and day respiration contribute to CO_2 leak, and an imbalance of the rate of CO_2 delivery by C_4 cycle and fixation rate by C_3 cycle at low light intensities were hypothesized to be the reasons behind the increase in leakiness (Kromdijk *et al.*, 2010, 2014). Low-light grown maize plants reduced their day respiration to avoid the progressive increase of leakiness at low light intensities but not high-light grown plants (Bellasio and Griffiths, 2014*a*). The increase in leakiness in the high-light grown plants was suggested to be due to a short-term imbalance of C_3 and C_4 cycles when the light intensity was reduced. This trend in leakiness could also be an artifact of models used in the estimation of leakiness (Ubierna *et al.*, 2011). In Chapter 5, a new modeling approach is thus applied to examine leakiness in response to light intensity. In addition, in some plants, leakiness has been shown to increase due to the imbalance in CO_2 accumulation and reduction

when the spectral quality of light changed due to fluctuation of light intensity, thereby decreasing the efficiency of the CCM (Sun *et al.*, 2014).

When maize plants were grown under increasing nitrogen supply, the resistance of bundle sheath cells to CO_2 leakage was found to decrease (Yin *et al.*, 2011*b*). While the high nitrogen supply boosted the rate of photosynthesis, the decrease of the resistance to CO_2 leakage suggested that the CCM became less effective. The effect of increased nitrogen supply was thus shown to be counterintuitive. The negative effect of increased nitrogen supply was postulated to be due to possible modification of cell wall, membranes or bundle sheath structure by nitrogen. The role of leaf anatomy should be investigated further by increasing steps of nitrogen application from two extreme levels used in the study (Yin *et al.*, 2011*b*) and by quantification of leaf anatomical properties (Chapter 3).

Growth at elevated CO_2 and temperature results in loss of CCM efficiency: leakiness increased when C_4 plants were grown at elevated CO_2 (Watling, 2000) or temperature (Zheng *et al.*, 2013). In the latter two studies, leakiness increased due to the decrease in bundle sheath resistance resulting from a reduction in the bundle sheath cell wall thickness. On the other hand, growth at elevated CO_2 and temperature may benefit biomass accumulation in C_4 plants, which was attributed to increased water-use efficiency (reviwed by, Anand *et al.*, 2014). In particular, the enhancement of growth at elevated CO_2, although assimilation is believed to be CO_2-saturated, was suggested to be due to reduced stomatal conductance leading to decreased transpiration and elevated CO_2 resulting in high intercellular CO_2 (Ghannoum *et al.*, 2000). In addition, direct gas diffusion to bundle sheath cell in young leaves was suggested as to partly account for this enhancement (Ghannoum *et al.*, 2000). In Chapter 5, the potential of leaf anatomy in supporting such diffusion in relation to bundle sheath photosynthesis is investigated.

C_4 plants are capable of higher photosynthesis both at saturated and limited-light conditions compared with C_3 plants. These are, however, only apparent at high temperature, more than 25 °C (Sage and Pearcy, 2000). Above 30 °C, C_3 plants have a low quantum yield because the oxygenase activity increases more than the carboxylase activity (Furbank *et al.*, 2004). Temperature response is of crucial importance since C_4 bioenergy crops are mostly located at high latitudes where there is a low temperature that severely limits photosynthesis (Sage *et al.*, 2011). Low temperature causes low yields due to the inhibition of enzymes like PEPC and

PPDK (Sage and Kubien, 2007). Mathematical models are useful in discerning the contributions of biochemical and biophysical processes to the temperature response of photosynthesis, which could help in explaining the interspecific differences in the response (Juurola *et al.*, 2005). In Chapter 5, this is examined in more detail.

2.6 Multiscale modeling paradigm

2.6.1 Introduction

Multiscale models are composed of a sequence of interconnected sub models, which describe a biological system at different scales of time, space and physiological function (Walpole *et al.*, 2013; Ho *et al.*, 2013). This implies that a multiscale model must account for more than one spatial scale. They are aimed at analyzing the system behavior at one level making best use of the information available at different levels (Weinan, 2011). In addition, multiscale models must add more information than a model of one level of scale. This is of particular importance in biological systems because cells behave differently in isolation and in tissue (Walpole *et al.*, 2013).

A multiscale model is required when a macroscale model is inaccurate and/or a microscale model is inefficient (Brandt, 2001). For instance, design of food-processing industries becomes more accurate when material properties of food items are known. However, it is cumbersome to estimate these properties due to the expanding number of multicomponent food items. Modeling these items at the scale of actual sizes also overlooks the important intricacies of microstructure (Ho *et al.*, 2013). On the other hand, due to the limitation of computational power, it is impossible to model every detail at scale of the food items. The multiscale modeling paradigm provides an alternative approach that allows a balance between accuracy (due to fine scale) and feasibility (due to less detailed information) of a model (Brandt, 2001; Weinan, 2011; Ho *et al.*, 2013). The analysis of one sub-model at a time while accounting for the microstructure information reduces the demand for computational resources. An interesting feature of such an analysis in applications where the microstructure is important is that parameters lumping microstructural information become well known physical constants due to explicit description of the microstructure. In addition, combination of a continuous (macroscale) and a discrete (microscale) modeling approach renders biological information quite well (Walpole *et al.*, 2013). The modeling is executed in two

approaches depending upon the scale of interest: upscaling and downscaling (Weinan, 2011; Ho *et al.*, 2013). Upscaling is a process of scaling fine scale solutions to coarse solutions until the scale of interest is reached while the opposite, downscaling, is used to examine a particular area of interest that cannot be adequately described by the macroscale model (Weinan, 2011).

2.6.2 Acquisition of microstructure geometry

The application of multiscale modeling for studying transport phenomena in various applications requires knowledge of the internal structure of an object of interest at different scales. A two-dimensional (2-D) geometry of an item of interest could be obtained using CCD cameras, optical microscopy, transmission and scanning electron microscopy among others. A three-dimensional (3-D) geometry may be developed using imaging techniques such as laser scanning microscopy, x-ray tomography and magnetic resonance imaging (Verboven *et al.*, 2008, 2010, 2013; Dhondt *et al.*, 2010).

X-ray micro-computed tomography (X-ray micro-CT) has been widely used in our lab for obtaining anatomical data for quantification of microstructure and gas transport modeling (Mebatsion *et al.*, 2006*a*; Verboven *et al.*, 2008, 2010, 2015; Cantre *et al.*, 2014; Herremans *et al.*, 2015; Ho *et al.*, 2016). In brief, an X-ray source is directed onto a sample positioned at a given distance between the source and the detector of the rays resulting in a 2-D projection of the 3-D volume of the object. To reconstruct the 3-D volume, either the sample or the source and detector are rotated by a certain angle and several projections are made. The resulting stack of images is further processed to gain a clearer view on an object of interest. Post processing of the anatomical data for development of 3-D geometry, quantification of the microstructure and visualization can be done using image processing software tools such as CTAn v1.13.5.1 (Bruker micro-CT, Kontich, Belgium), Avizo Fire (VSG, France) and Matlab (The Mathworks, Natick, MA), among others.

2.6.3 Solving multiscale models

The sub-models in a multiscale model are connected by analytical or numerical solutions (Weinan, 2011) with the numerical solution being the most widely used (Ho *et al.*, 2013). The choice of a particular numerical method depends on the scale of interest. At the microscale

and below, a material is a composite of discrete particles. In this case, methods like Lattice Boltzmann, molecular dynamics or meshless particle methods are required. These methods will not be explained in detail, and readers are referred to the literature (e.g., Shaofan and Wing Kam 2004). Such methods are useful in models of gas transport in leaves when the interaction of water vapor, CO_2 and other trace gases are considered explicitly (Leuning, 1983). However, at length scales much greater than inter-atomic distances, the material can be approximated as continuous. Finite element or finite volume methods may then be used for obtaining solutions. This is the case for transport of gases in fruit and leaves (Ho *et al.*, 2009, 2012, 2016; Fanta *et al.*, 2014).

The finite element method aims to find an approximate solution to boundary value problems described by partial differential equations. In this method, the domain of interest is subdivided into subdomains called finite elements. The number of mesh elements is a compromise between increasing the accuracy in the approximation and reducing the computational resource needed. The variation of a function describing the problem in these elements (where there is no node) is then approximated by local functions that could be linear, quadratic or higher-order polynomials. The function is expressed within each element using nodal values of that element. A set of equations describing the behavior of the elements is then obtained by the method of weighted residuals like Galerkin's method. These element equations, applying the initial values, are assembled to a global system of equations resulting in an approximate solution to the problem. Similar to the finite element method, the finite volume method divides the domain into finite volumes over which the governing equation is integrated to yield a set of discretized equations. These equations describe the flux across the boundaries of the control volume. These fluxes are evaluated at each nodal point within a control volume resulting in a set of algebraic equations. While these differences in the scheme exist, the differences in accuracy and computational efficiency depends on the type of computational fluid dynamics applications (Idelsohn and Oñate, 1994; Molina-Aiz *et al.*, 2010).

Finite element/volume procedure and subsequent post processing of results can be carried out in commercial software packages such as COMSOL Multiphysics (Comsol AB, Stockholm) and ANSYS (ANSYS, Inc., Canonsburg, PA, USA). While COMSOL is a finite-element software, ANSYS can handle both finite-element (ANSYS/FLOTRAN) and finite-volume analysis (ANSYS/FLUENT). Comparison of earlier versions of these software tools in fluid

flow and heat transfer (Salvi *et al.*, 2010; Hysing and Turek, 2015) shows that the accuracy provided by each solver is comparable while COMSOL required significantly less time, but more memory compared to ANSYS. Another point of difference may be ease of use; COMSOL is more intuitive and flexible than ANSYS.

2.6.4 Applications of multiscale models

Multiscale modeling has been applied in plant physiology to investigate postharvest problems such as anoxia and hypoxia (Ho *et al.*, 2010, 2011) and water loss from fruit (Fanta *et al.*, 2014; Aregawi *et al.*, 2014*b*,*a*). It has also been extended to study gas transport in leaves (Ho *et al.*, 2012, 2016; Verboven *et al.*, 2014), roots (Verboven *et al.*, 2012) and seeds (Verboven *et al.*, 2013). In the context of photosynthesis, microscale models that explicitly consider leaf anatomy were able to successfully predict macroscale variables such as net CO_2 assimilation and apparent mesophyll conductance in addition to unraveling the gas exchange pathways of C_3 photosynthesis (Ho *et al.*, 2012, 2016). Application of such models to photosynthesis of C_4 plants is, however, still lacking.

2.7 Fundamentals of leaf gas exchange modeling

Mass transfer occurs within a system consisting of two or more chemical species by a random motion of molecules or by convection. This movement of molecules is driven by the change in the concentration of a species from one point in space to another, thereby reducing the concentration gradient. Many biochemical processes such as photosynthesis, transpiration and respiration involve mass transfer; CO_2, O_2, water vapor and metabolites are exchanged.

2.7.1 Fick's laws of diffusion

A gradient in the concentration of a chemical species in a multicomponent system results in net movement of molecules. At steady-state, this flow of molecules per unit area of a surface, also called flux, is related to the concentration gradient. This relationship is given by Fick's first law of diffusion given as:

$$J_z = -D_z \nabla C_z \tag{2.1}$$

where J_z is the flux of species *z*; D_z is the diffusivity of species *z* in the medium; and ∇C_z is the concentration gradient of species *z*. The negative sign shows that the diffusion is from high to lower concentration.

The change in concentration of *z* with time due to diffusion is given by Fick's second law as:

$$\frac{\partial C_z}{\partial t} = \nabla D_z \nabla C_z \tag{2.2}$$

2.7.2 Fundamentals of reaction-diffusion models

A reaction-diffusion equation describes a system composed of chemical species that spread in space by diffusion and interconvert by chemical reactions. For a system involving *n* chemical species, the change in concentration *C* of a species *z* in time is given by :

$$\frac{\partial C_z}{\partial t} = \nabla D_z \nabla C_z + S_z \ (z = 1, 2, ...n) \tag{2.3}$$

where S_z is a source or a sink term associated with species *z*. The terms at the right side of Eq. 2.3 describe the contribution of a transport and a chemical reaction in determining the change in *C* of species *z* in time. S_z is a non-linear function of concentration.

Gas exchange during photosynthesis is considered as a reaction-diffusion system governed by Eq. 2.3 (Berghuijs *et al.*, 2016). Gases such as CO_2 and O_2 diffuse into or out of a leaf. Photosynthesis, respiration and photorespiration among others are the processes that consume or release CO_2 and O_2. Biochemical models of photosynthesis (see section 2.6.3) provide S_z for Eq. 2.3. The spread of species *z* in gaseous or liquid phase media of leaf tissue by diffusion is given by the Fick's law of diffusion (Eq. 2.1).

2.7.3 Photosynthetic gas exchange in a maize leaf

Gas exchange in leaves is a process by which CO_2 enters and water vapor and O_2 leave the leaf. Diffusion of gases inside a leaf and nitrogen-use and water-use efficiency are related. The gradient of CO_2 inside a leaf, for instance, affects the efficiency of CO_2 assimilating

enzymes, thus nitrogen-use efficiency of the leaf. In addition, due to the drawdown in CO_2, leaves open stomata to increase diffusion but lose water vapor, thus influencing the water-use efficiency (Evans and von Caemmerer, 1996).

Photosynthetic gas exchange in leaves is a function of multiple spatial scales across plant physiology (Fig. 2.3). Leaf scale measurements provide the least mechanistic understanding of photosynthesis. Microscale (10^{-6} – 10^{-3} m) models of photosynthesis gas exchange have been developed to generate detailed information about photosynthesis (Ho *et al.*, 2012, 2016). In these models, altering a microscale parameter (membrane permeability, diffusivities and so on) results in a measurable change in a macroscale (10^{-3} – 10^{0} m) parameter (photosynthesis and CO_2 conductances). This approach provides a useful tool to generate information that cannot be easily generated by experimental measurement techniques.

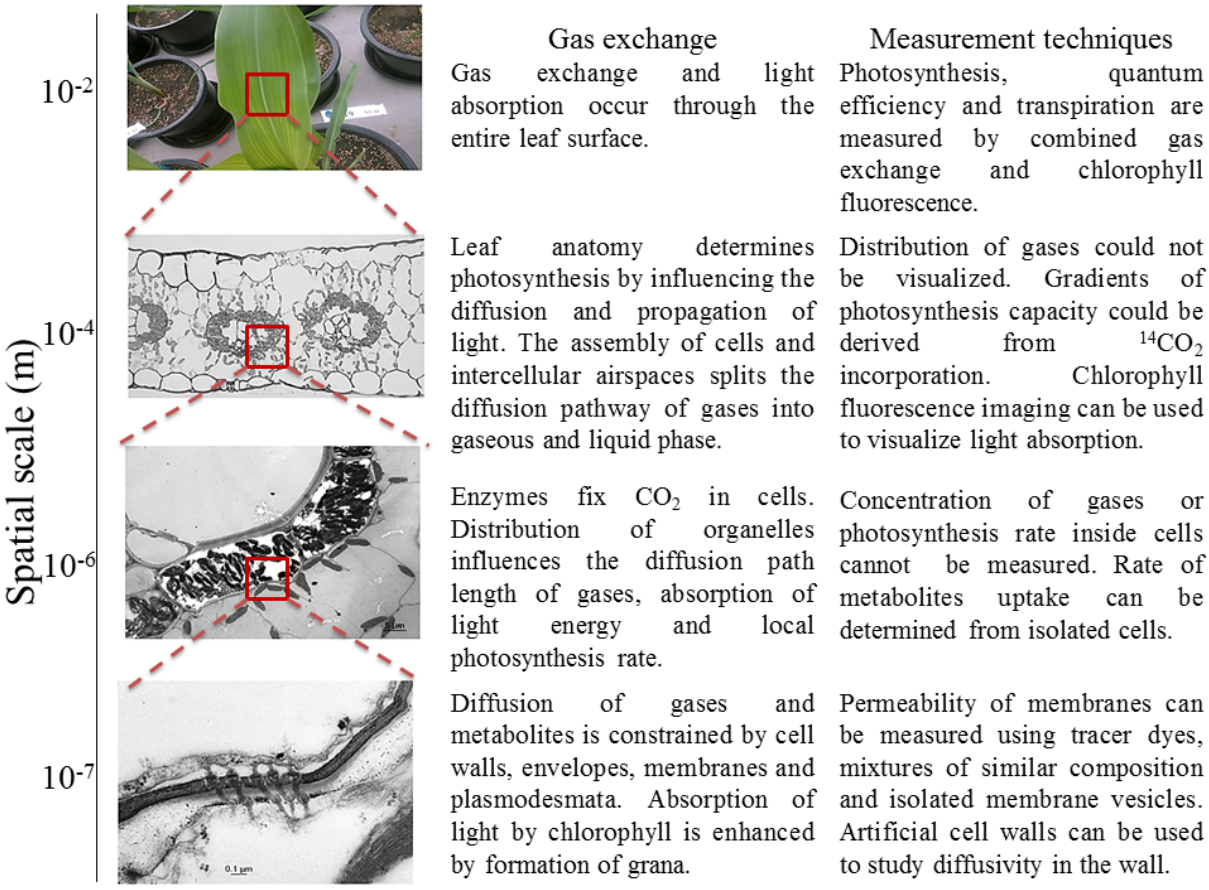

Figure 2.4. A detailed look at how photosynthesis gas exchange is a function of several spatial scales across plant physiology.

Transport of gases in a maize leaf occurs throughout the entire leaf (macroscale), via stomata, to air spaces and cells (microscale) through cell wall and membranes (mesoscale, 10^{-7} – 10^{-6} m) and plasmodesmata (nanoscale, 10^{-9} – 10^{-7} m). A model that accounts for the entire tire of resolution becomes computationally expensive. Models of gas transport in leaves are thus commonly developed accounting for microscale features explicitly while mesoscale and nanoscale features are modeled as resistances (Tholen and Zhu, 2011; Ho *et al.*, 2012, 2016). This approach resulted in computationally less demanding but practical models of gas transport. Microscale models can be simplified by assuming lumped epidermal cells and mesophyll cells as one big chloroplast (Ho *et al.*, 2012). Including further details in mesophyll cells like a chloroplast layer was shown to improve assessment CO_2 transport for C_3 photosynthesis (Ho *et al.*, 2012). Mesophyll chloroplasts of a maize leaf, however, do not fix CO_2 (Kanai and Edwards, 1999). In addition, modeling exchange of metabolites and leakage CO_2 that occurs through plasmodesmata could explicitly increase the complexity of a gas transport model for a maize leaf since simple diffusion alone may not fully explain the exchange (Sowiński *et al.*, 2008). Therefore, for examining C_4 photosynthesis in relation to gas transport, microscale modeling approach is preferred.

2.7.4 Biochemical models of C_4 photosynthesis

The mechanism of C_4 photosynthesis has been modeled extensively (Berry and Farquhar, 1978; Peisker, 1979; Collatz *et al.*, 1992; Laisk and Edwards, 2009; Wang *et al.*, 2014*b*). The complex pathway of the C_4 mechanism was simplified to understand the physiology in earlier biochemical models (Berry and Farquhar, 1978; Peisker, 1979; Collatz *et al.*, 1992; von Caemmerer and Furbank, 1999). By contrast, recent models were developed aiming at systems-level understanding of photosynthesis (Wang *et al.*, 2014*b*). Due to their robustness, the simplified models have a wider use in practical applications such as environmental and physiological studies (Chen *et al.*, 1994; Sellers *et al.*, 1997; Pengelly *et al.*, 2010; Yin *et al.*, 2011*b*; Bellasio and Griffiths, 2014*a*). These models were generalized in the biochemical model presented by von Caemmerer and Furbank (1999). The latter model describes C_4 photosynthesis using two controlling enzymes: PEPC and Rubisco. The rate of PEP carboxylation is assumed to be limited by the enzyme PEPC or the rate of electron transport that determines the rate of regeneration of PEP by PPDK. The initial hydration of CO_2 by carbonic anhydrase is assumed not to limit PEP carboxylation. Decarboxylation of C_4 acids in

the bundle sheath cells, at steady state, is assumed to proceed at the rate of PEP carboxylation. In bundle sheath cells, fixation of CO_2 is assumed to be limited by Rubisco or the rate of electron transport.

The biochemical model (von Caemmerer and Furbank, 1999) indirectly accounts for the influence of a C_4 leaf anatomy and ultrastructure by lumping them into CO_2 conductances, g_m and g_{bs}. As a result, mechanistic understanding of these conductances is limited (von Caemmerer, 2013). In addition, the release of CO_2 through photorespiration is assumed to take place in the same compartment as CO_2 fixation (Farquhar *et al.*, 1980). However, the release of photorespiration occurs in the cytosol where mitochondria are located. The potential re-fixation and/or escape of this photorespiratory CO_2, thus, could not be assessed from this lumped modeling approach. Development of models accounting for leaf anatomy of C_3 plants explicitly has enabled mechanistic understanding of diffusion limitations (Tholen and Zhu, 2011; Ho *et al.*, 2012, 2016). In Chapter 4, a modeling tool for investigating CO_2 conductances in relation to C_4 photosynthesis while explicitly accounting for microstructure is presented.

The kinetics of C_3 photosynthesis are described by the Farquhar, von Caemmerer & Berry (also referred to as FvCB) model (Farquhar *et al.*, 1980). The model states that net rate of photosynthesis is the minimum of the Rubisco-limited-rate or the RuBP-regeneration-limited rate. The model was further extended to include an expression for triose phosphate utilization limited rate observed at very high CO_2 concentrations (Sharkey *et al.*, 2007). Extensions of the RuBP-limited-rate of photosynthesis allowing generalized description of electron transport has also been proposed (Yin *et al.*, 2004; Yin and Struik, 2012). The equations from these biochemical models provide a source/sink term for the reaction-diffusion equations (see Section 2.7.1).

2.7.5 Light propagation in a leaf

Gradients of light inside a leaf exist due to the opaque nature of the leaf. This gradient has been examined using various techniques since photochemistry depends on photons absorbed by pigments (Ichiro *et al.*, 2016). A micro-fiber was inserted in a leaf to measure the space irradiance (the energy flux that enters a small sphere divided by the cross sectional area of the sphere) (Vogelmann and Bjorn, 1984); images of chlorophyll fluorescence emissions from

PSII were also used in C_4 and C_3 plant leaves to determine where the light was absorbed (Evans *et al.*, 2007); ray tracing modeling in which rays are tracked from cell to cell until they are absorbed or leave the leaf boundaries (Govaerts *et al.*, 1996; Ustin *et al.*, 2001; Watté *et al.*, 2015); and the absorption could be determined from distribution of chlorophyll by illuminating transverse leaf sections using vertically incident light. The chlorophyll fluorescence method for C_4 plants is limited by the unequal abundance of PSII in mesophyll and bundle sheath chloroplasts. The space irradiance derived from micro-fibers would not be equal to the absorption profile since a leaf is a heterogeneous medium: optical properties vary in leaf tissue (Lambers *et al.*, 1998). Ray-tracing has been applied using a virtual C_3 leaf tissue geometry to estimate the properties of radiation transfer (Govaerts *et al.*, 1996). In the latter research, cells in a representative three-dimensional leaf geometry were treated as composites of cell wall constituents, chlorophyll and water. Optical properties of these substances were used to derive the light absorption profile. Ustin *et al*. (2001) extended the work of Govaerts *et al*. (1996) to study the relationship between light absorption gradient and photosynthesis gradient. These two researches assumed the leaf tissue to be a homogenous medium, thereby overlooking the distribution of cellular organelles such as grana and mitochondria and represented the leaf structure with simple geometrical shapes. A light propagation model for C_3 leaves that is based on a realistic leaf microstructure (Verboven *et al.*, 2015) was recently developed and validated experimentally (Watté *et al.*, 2015). This method was then coupled with a CO_2 reaction-diffusion model to investigate the profile of carbon fixation inside a C_3 leaf in relation to the light gradient (Ho *et al.*, 2016).

Ray-tracing has limited applications in C_4 plants so far (Baranoski *et al.*, 2012; Bellasio and Griffiths, 2014*b*). Baranoski *et al*. (2012), aiming at estimating optical properties in response to abiotic stress factors, represented the leaf tissue of C_4 monocots using its basic constituents: water, pigments, cellulose, protein and lignin. Each of these constituents was assigned optical properties. A ray was traced through a sequential layer of upper epidermis, adaxial side mesophyll, air, abaxial side mesophyll and lower epidermis to determine leaf transmittance and reflectance profiles. Bellasio and Griffiths (2014*b*) represented the leaf anatomy of maize by square units consisting of mesophyll and bundle sheath cells. Upper and lower epidermis were implicitly treated as a single layer of reflecting elements. Leaf transmittance and reflectance were computed by combining two light absorption profiles differing in an absorption coefficient of bundle sheath cells, assumed equal to or three times that of

mesophyll chloroplasts. The light gradient was derived by calibrating the model using the measured leaf transmittance and reflectance (Woolley, 1971).

2.7.6 Leaf microstructure geometry

CO_2 and O_2 diffuse in the intercellular air space in three dimensions, that is both vertical and lateral because the stomata are discrete and located several mesophyll cells apart (Parkhurst, 1994; Morison & Lawson, 2007). Analysis of gas transport in both the gaseous and liquid phase requires a three-dimensional geometry. Earlier studies of gas exchange of C_3 plant leaves used various simplifications of the leaf microstructure, which have consequences on photosynthesis (Vesala *et al.*, 1996; Pachepsky and Acock, 1996; Aalto and Juurola, 2002). The model of Pachepsky and Acock (1996) incorporated structural differences and the distribution of chloroplasts in palisade and spongy mesophyll, albeit in 2-D, unlike a homogenous media representation of Vesala *et al.* (1995). Aalto and Juurola (2002) accounted for the three-dimensional geometry of a leaf and included epidermis, stoma, mesophyll cells, chloroplasts and intercellular air space. However, the use of spheres to depict leaf tissue in earlier models (Vesala *et al.*, 1996; Aalto and Juurola, 2002) understated the actual irregular shape of the cells and their interconnection (Parkhurst, 1994). These actual intricacies of leaf microstructure were accounted for, to some extent, by digitizing the leaf anatomy directly from light microscopy images (Ho *et al.*, 2012). This innovative technique allows parameterization of the geometry of the leaf anatomy directly from real images. However, it results in a 2-D description of the geometry that underestimates the interconnectivity of air spaces (Ho *et al.*, 2012). Another geometrical description was the consideration of a single mesophyll cell (Tholen and Zhu, 2011). This approach allowed detailed analysis of mesophyll conductance but is limited for analysis of photosynthesis at the tissue level. Recently, there has been remarkable progress in degree of realism in describing the leaf microstructure (Ho *et al.*, 2016). Ho *et al.* (2016) obtained a three-dimensional geometry of tomato leaves using synchrotron tomography equipment that allows excellent contrast at minimum tissue preparation (Verboven *et al.*, 2015). The geometry thus obtained, however, needed to be modified to include chloroplasts and vacuoles, which could not be resolved from the synchrotron images. Unlike simplified description of leaf anatomy described, Ho *et al.* (2016) demonstrated that the actual shapes of cells and organelle positioning matters in determining local light absorption and CO_2 diffusion, thus photosynthesis. In addition, the three-

dimensional description clearly demonstrated that CO_2 gradients in the air space are much more uniform than predicted by a 2-D model (Ho *et al.*, 2012).

Leaf geometry was not explicitly included in mathematical models of C_4 gas exchange (Jenkins *et al.*, 1989*a*; Chen *et al.*, 1994; von Caemmerer and Furbank, 1999). An earlier study simplified the leaf anatomy using concentric cylinders to study the flux of metabolites (Osmond, 1971). These C_4 models lump the effects of leaf microstructural features, such as cell walls and plasma membranes, and overlook the spatial nature of the gas exchange phenomena. Therefore, the mechanistic understanding of gas transport that can be derived from such models is limited. The effect of the unique anatomical arrangement of mesophyll and bundle sheath cells on gas transport and light penetration, thus photosynthesis, may be more mechanistically examined if explicit description of leaf anatomy and ultrastructure is accounted for.

The complexities of a model and the computational resource requirement are affected by the leaf microstructure description. A detailed description of leaf anatomical features (Tholen and Zhu, 2011; Ho *et al.*, 2016) increases the complexity of a model and the computer resource required to solve it (Berghuijs *et al.*, 2016). This may also negatively impact the wide-spread applicability of the model. On the other hand, less detailed models are limited in providing mechanistic and detailed insight into photosynthesis, although may equally predict net photosynthesis in response to ambient changes in CO_2 and light. However, with advancement of computing technology, the resource problem may be diminished.

2.7.7 Model parameterization and validation

A model requires parameterization, which is a process of deciding on and defining the model parameters for complete specification. Reaction-diffusion models of photosynthesis gas exchange require parameters related to gas transport and biochemical models. Gas transport parameters include gas diffusivities and permeability values, and biochemical model parameters are enzyme kinetic properties. The former are usually obtained from literature reports (Gutknecht, 1988; Frank *et al.*, 1996; Uehlein *et al.*, 2008; Evans *et al.*, 2009) and the latter could also be estimated from fitting of combined gas exchange and chlorophyll fluorescence measurement data (Yin *et al.*, 2009, 2011*a*,*b*, Bellasio *et al.*, 2016*a*,*b*).

Combined gas exchange and chlorophyll fluorescence measurements are carried out by enclosing a leaf from a living plant in a small controlled chamber. Air containing nitrogen and a known amount of CO_2 is supplied at one end. The net CO_2 uptake by the leaf which is assumed equal to the net photosynthesis rate is measured by measuring the concentration of CO_2 across the leaf chamber. The rate of transpiration is determined from the concentration of water vapor at the exit of the chamber since that is added to the incoming dry air due to leaf transpiration. The concentration of CO_2 is determined commonly using an infrared gas analyzer (IRGA). The main principle used in IRGA is that CO_2 present between an infrared radiation source and detector results in reduction of transmission of infrared wavebands, which is a function of concentration of CO_2 (LI-COR, 2004). The gas exchange measurement is commonly carried out using portable open gas exchange systems (LI-6400, LI-COR, Lincoln, Nebraska, USA). Photosynthesis measurements should be corrected for leakage of gases (Flexas *et al.*, 2007). An IRGA is usually fitted with a chlorophyll fluorescence head to measure chlorophyll fluorescence during photosynthesis, which can be used to determine the rate of electron transport (Maxwell and Johnson, 2000).

Mathematical models of photosynthesis gas exchange are aimed at interpretation of gas exchange measurements (von Caemmerer, 2013) which result in the responses of net photosynthesis to changes in ambient CO_2 and irradiances. Thus, validation of these models is usually carried out by comparing model predictions of photosynthesis and those derived from gas exchange measurements (Tholen and Zhu, 2011; Ho *et al.*, 2012, 2016). This validation is, however, only primary since this multiscale models need to be validated at each tier of the scale. However, the validation at microscale is difficult since it requires measurements of distribution of gases or their average concentration in various cellular compartments (Fig. 2.3), which cannot be accurately determined from experiments (Walpole *et al.*, 2013). Therefore, the response of macroscale variables like net photosynthesis is used to validate model predictions.

2.7.8 Review of gas exchange models

Gas exchange during photosynthesis in C_3 leaves was described by a set of reaction-diffusion models (Vesala *et al.*, 1996; Pachepsky and Acock, 1996; Aalto and Juurola, 2002; Tholen and Zhu, 2011; Ho *et al.*, 2012, 2016). Some of these models are briefly discussed here as

detailed discussions are available elsewhere (Berghuijs *et al.*, 2016). Vesala *et al*. (1995) developed a reaction-diffusion equation describing diffusion of CO_2, photosynthesis, photorespiration and day-respiration. The leaf geometry was cylindrical and consisted of stoma and mesophyll. The purpose of the study was to investigate stomatal diffusion in relation to CO_2 assimilation in detail. Investigation of stomatal functioning using reaction-diffusion models was extended further by Pachepsky and Acock (1996). They developed a two-dimensional model of transport of CO_2 and water vapor in a leaf. The model showed that changes in stomatal density by elevated CO_2 affects photosynthesis. Aalto and Juurola (2002) developed a three-dimensional model of CO_2 diffusion and light propagation in silver birch leaves to investigate photosynthesis in response to stomatal opening, gradients in photosynthesis capacity and environmental variables such as rising CO_2 and temperature. A two-dimensional reaction diffusion model was also developed to investigate the responses of mesophyll and stomatal conductances to changes in ambient conditions (Ho *et al.*, 2012). Tholen and Zhu (2011b) developed a three-dimensional reaction-diffusion model of gas exchange using a single spherical mesophyll cell to investigate mesophyll diffusion in more detail. The most advanced reaction-diffusion model to date was presented by Ho *et al*. (2016). The leaf anatomy of tomato leaves incorporating realistic shapes of cells was incorporated. The light propagation in the leaf was modeled using an advanced ray-tracing method that could deal with complexity in structure and composition of biological tissues (Aernouts *et al.*, 2014; Watté *et al.*, 2015). The model was applied to investigate photosynthesis in relation to gradients of photosynthesis capacity, recycling of mitochondrial CO_2 and presence or absence of CA. The study showed that scaling of photosynthesis capacity with light penetration in a leaf would increase photosynthesis; a substantial fraction of CO_2 released by respiration was re-assimilated; and, CA was beneficial for achieving a high rate of photosynthesis at low intercellular CO_2 levels.

Photosynthetic gas transport modeling using the actual microstructure of the leaves of C_4 species is an untouched field of research. Models were limited to flux analysis (Jenkins *et al.*, 1989*a*; Chen *et al.*, 1994; von Caemmerer and Furbank, 1999). Chen *et al*. (1994) examined the response of C_4 photosynthesis to elevated CO_2. Jenkins *et al*. (1989) estimated the amount of CO_2 and bicarbonate that would develop at a steady state due to the CCM. In their model, volumes of different cell components were assumed. The amount of CO_2 in each cell part was sensitive to assumptions regarding permeability values (Furbank *et al.*, 1989). A mathematical

model of C_4 photosynthesis was also applied to study bundle sheath resistance in relation to the ratio of biochemical capacity of PEPC and Rubisco (von Caemmerer and Furbank, 2003). The study shows that scaling of bundle sheath resistance to CO_2 leakage with the ratio of the enzyme capacities would avoid loss of efficiency. In addition, the study developed a hypothetical model to assess the implications of introducing a C_4 mechanism in C_3 plants on CO_2 diffusion. Furthermore, various models of the mechanism of C_4 photosynthesis that included individual reactions were developed (Laisk and Edwards, 2000; Bellasio and Griffiths, 2014*b*; Wang *et al.*, 2014*b*,*a*). Although these models are beyond the scope of this research, they are aimed at systems-level understanding of photosynthesis of C_4 plants.

2.8 Conclusion

Multiscale modeling of physiological phenomena has provided detailed insight into postharvest problems related to gas transport in fruit and photosynthesis of C_3 plants. Such models allowed testing the role of the microstructure of fruit and leaves in these metabolic processes. In order to expedite mechanistic understanding of gas transport phenomena in C_4 plant leaves and efficiency losses in C_4 photosynthesis, development of multiscale models accounting for a realistic tissue microstructure must be done. Although the application may not be straightforward due to the complexity of the C_4 mechanism, multiscale models of gas transport in C_3 plants can be extended to that of C_4 plants to increase quantitative insights into photosynthesis of C_4 plants. In addition, parameters of gas transport in C_4 leaves and their response to environmental variables should be investigated widely.

3 Impact of anatomical traits of maize (*Zea mays* L.) leaf as affected by nitrogen supply and leaf age on bundle sheath conductance

This chapter is based on:

Retta M., Yin X., van der Putten P.E.L., Cantre D., Berghuijs H.N.C., Ho Q.T., Verboven, P., Struik, P.C, Nicolai, B.M. (2016). Impact of anatomical traits of maize (*Zea mays* L.) leaf as affected by nitrogen supply and leaf age on bundle sheath conductance. Plant Science 252, 205–214.

3.1 Introduction

In Chapter 2, it was discussed that the association of the mesophyll and bundle sheath cells, combined with highly regulated enzyme activities, creates a CO_2 concentration mechanism (CCM) which enables C_4 plants to be more efficient in solar-radiation use, nitrogen-use and water-use than C_3 plants. The efficiency of the CCM relies on the concerted action of anatomical, biochemical and biophysical mechanisms. It was also mentioned that leakiness is believed to be one of the efficiency losses in C_4 photosynthesis. In particular, the bundle sheath resistance has been shown in the literature to be an important constraint to leakiness. In Chapter 3, the role of changes in leaf anatomy in response to leaf nitrogen content and age on bundle sheath conductance g_{bs} will be quantified.

It has been well known from C_3 photosynthesis studies that leaf anatomy impacts photosynthesis as it influences the physical obstruction to CO_2 diffusion. Fig. 2.3 shows the pathway of CO_2 diffusion in maize leaf and various conductances along the way. The leaf boundary layer and stomatal conductance (g_s) affect diffusion of CO_2 towards the stomatal cavity. The mesophyll conductance (g_m) constrains the diffusion from sub-stomatal cavities into CO_2-fixation sites in mesophyll. The distribution of stomata and the connectivity of intercellular air spaces affect the diffusion of CO_2 in the gaseous phase, while the properties of the cell wall such as thickness and porosity, the plasma membrane and presence of carbonic anhydrase affect the diffusion in the liquid phase (von Caemmerer *et al.*, 2007; Tholen and Zhu, 2011; Ho *et al.*, 2016). While these phenomena occur in C_4 photosynthesis as well, C_4 photosynthesis is also affected by CO_2 retro-diffusion from bundle sheath cells back into mesophyll cells. This retro-diffusion, also called 'CO_2 leakage', partially increases the CO_2 levels of the mesophyll cells (see, Fig. 4.3, Subsection 4.3.2) and is constrained by resistance of the mesophyll-bundle sheath interface (Furbank *et al.*, 1990). The inverse of this resistance is known as the bundle sheath conductance (g_{bs}). The lower g_{bs}, the lower is CO_2 retro-diffusion from bundle sheath cells, and thus the higher is the efficiency of the CCM (Hatch, 1987; Leegood, 2002; Ubierna *et al.*, 2013; Kromdijk *et al.*, 2014). Leakiness, a physiological variable often used to characterize retro-diffusion of CO_2 from bundle sheath cells back to mesophyll cells relative to the rate of PEP carboxylation, depends greatly on g_{bs}.

C_4 photosynthetic efficiency has been proposed to depend on a number of anatomical properties of the leaves. For instance, a low permeability of bundle sheath cell walls to CO_2, a high surface of mesophyll cells to volume ratio and features such as close proximity of mesophyll and bundle sheath cells, among others, are essential to the effectiveness of the CCM (Hatch, 1987; Dengler *et al.*, 1994; von Caemmerer *et al.*, 2007; El-Sharkawy, 2009). Moreover, the shorter vein spacing in C_4 plants than in C_3 plants has been shown to be beneficial for high quantum yields (Ogle, 2003). CO_2 retro-diffusion has also been found to be influenced by the diffusive properties of the stroma and the chloroplast envelope (von Caemmerer and Furbank, 2003). Thus, the significance of leaf anatomy and ultrastructure of C_4 plants to the efficiency of C_4 photosynthesis continues to be extensively studied (El-Sharkawy and Hesketh, 1965; Hattersley, 1984; Dengler *et al.*, 1994; Sowiński *et al.*, 2007; El-Sharkawy, 2009; Pengelly *et al.*, 2011; Griffiths *et al.*, 2013).

CO_2 conductances in C_4 plant leaves were recently estimated using combined gas exchange and chlorophyll fluorescence measurements (Yin *et al.*, 2011*b*; Bellasio and Griffiths, 2014*c*) or with carbon isotope discrimination measurements (Kromdijk *et al.*, 2010, 2014; Ubierna *et al.*, 2013; Bellasio and Griffiths, 2014*c*) in analogy to the methods used to estimate g_m in C_3 leaves (Harley *et al.*, 1992; Evans and von Caemmerer, 1996; Yin *et al.*, 2009). Gas exchange and chlorophyll fluorescence measurements result in CO_2 and irradiance responses of net photosynthesis and quantum efficiency of PSII electron transport, which are then used to parameterize biochemical models of von Caemmerer & Furbank (1999) and estimate g_m and/or g_{bs}. The procedures to estimate these conductances using various software tools are readily accessible (Yin *et al.*, 2011*b*; Bellasio *et al.*, 2016*a*). In addition, the benefits of chlorophyll fluorescence measurements in C_4 plants have been substantiated (Yin *et al.*, 2011*b*, 2014, 2016; Bellasio and Griffiths, 2014*c*). Using these methods, g_{bs} was found to vary with nitrogen supply (Yin *et al.*, 2011*b*), growth light (Pengelly *et al.*, 2010; Kromdijk *et al.*, 2010; Bellasio and Griffiths, 2014*c*), leaf age (He and Edwards, 1996; Kiirats *et al.*, 2002; Yin *et al.*, 2011*b*), and temperature (Yin *et al.*, 2016).

Very few studies measured leaf anatomical properties and estimated g_{bs} or g_m in C_4 plants to examine their relationship (Pengelly *et al.*, 2010; Kromdijk *et al.*, 2010). These properties include the exposed surface area of mesophyll cells per unit of leaf area (S_m), surface area of bundle sheath cells per unit of leaf area (S_b), leaf thickness and diameter of mesophyll and

bundle sheath cells. When maize and *Flaveria bidentis* were grown under contrasting light environment, differences in S_m, S_b (Pengelly *et al*. 2010), leaf thickness and cell diameter (Kromdijk *et al*. 2010) contributed to the variations in g_{bs} or g_m. A negative correlation of bundle sheath resistance with leaf nitrogen content was reported for maize in a recent study (Yin *et al.*, 2011*b*). At that time, it was only presumed to be due to S_b and cell wall thickness being altered by nitrogen treatment. In addition, an increase in g_{bs} was suggested when C_4 plants were grown at elevated CO_2 (Watling, 2000) or temperature (Zheng *et al.*, 2013) due to a decrease in wall thickness of the bundle sheath.

The relationships between photosynthesis and leaf anatomical properties have commonly been investigated using chemically fixed leaf tissue samples (Dengler *et al.*, 1994; Greef, 1994; Moreno-Sotomayor *et al.*, 2002; Pengelly *et al.*, 2010, 2011). X-ray micro-computed tomography (X-ray micro-CT) (principle of operation is stated in Subsection 2.6.2) also gives high-quality images that render the air space between cells at sufficient contrast to allow quantification of anatomical features with the additional advantage of no requirement of intensive sample preparation and thus measurement artefacts are minimized (Verboven *et al.*, 2012, 2013; Herremans *et al.*, 2015). In addition, X-ray micro-CT allows measurements over the intricate three-dimensional leaf geometry of any thickness but has a limitation in resolving leaf ultrastructural components (Verboven *et al.*, 2008, 2015).

In C_3 plants, it is well known that the cell wall strongly influences CO_2 diffusion and hence CO_2 fixation rate (Flexas *et al.*, 2008). Whether and how the cell wall of the bundle sheath contributes to the variations in g_{bs} for C_4 plants with leaf nitrogen content and age have not been investigated. The objectives of this research were (i) to study how bundle sheath conductance is affected by leaf nitrogen content and leaf age, (ii) to quantify leaf anatomical properties as altered by leaf nitrogen and age using combined microscopy and micro-tomography measurements, (iii) to relate these properties to CO_2 conductances of a maize (*Zea mays* L.) leaf. This will be achieved by using gas exchange and chlorophyll fluorescence measurements with biochemical models of C_4 photosynthesis (von Caemmerer and Furbank, 1999) to estimate g_{bs}, and X-ray micro-CT, light and electron microscopy images to obtain microstructure and ultrastructure details of the leaf anatomy.

3.2 Materials and methods

3.2.1 Plants, treatments and photosynthetic measurements

A pot experiment was conducted in a controlled glasshouse compartment at Wageningen University, from 11 April until 1 July in the year 2013. Maize (*Zea mays* L.) plants, hybrid 2-02R10074, were grown in a controlled glasshouse compartment. When the global incident radiation dropped below 150 W m^{-2}, high pressure sodium lamps (Philips MASTER Green Power CG 600W) were automatically switched on. These lamps emit light mainly in the yellow or red portion of the visible light spectrum. When the radiation exceeded 250 W m^{-2}, the lamps were switched off. The ambient CO_2 concentration was about 380 µmol mol^{-1}, the relative humidity was 60–80 % and glasshouse temperature was 21 ± 3 °C during the day and 16 °C during the night. The photoperiod was 16 hours per day. To spread out the measurement work, a weekly staggered sowing was made. The maize seeds were sown in ten liter pots filled with a mixture of sandy soil and perlite (2:3 vol./vol.) (one seed per pot). The initial nitrogen (N) content of the medium in each of the pots was 31 mg N. One week after emergence, the plants received a nutrient solution containing 1M $Ca(NO_3)_2$. $4H_2O$, 2M NH_4NO_3, 0.5M K_2SO_4, 1M KH_2PO_4, 1M $MgSO_47H_2O$ and other micronutrients once a week for four weeks resulting in three nitrogen levels: 0.15, 0.50 and 1.25 g N per pot (for more details, see text A.1, Appendix A) (Vos *et al.*, 2005). Total additions of P, K and Mg were 0.33, 1.25, 0.50 g per pot, respectively. The experiment was designed as a split plot with 4 blocks, 2 harvests as main plots and the nitrogen treatments as sub plots. With one maize plant per pot, the design resulted in 24 of maize plants in total. Each of the N levels was applied to 8 maize plants. The frequency of applying nutrients was increased to twice a week after the fourth week (since nutrition application started) to minimize the decline of leaf nitrogen content with leaf age.

Combined gas exchange and chlorophyll fluorescence measurements were made in four replicates using a LI-6400XT open gas exchange system with an integrated fluorescence chamber head, enclosing 2 cm^2 leaf area. The measurements were done on fully expanded 6^{th} leaves that are 19 days old and 32 days old after emergence of the leaves. The leaf temperature during the measurement was kept at 25 ± 0.2 °C. For the light response of photosynthesis, leaves were first dark adapted for 25 min. Subsequently, light intensity (10 % blue, 90 % red) applied on the upper leaf surface was increased in steps of 20, 40, 60, 80, 100,

200, 500, 1000, 1500 and 2000 µmol m^{-2} s^{-1}. Between the steps, there was a 6 min adaptation time. To create contrasting levels of photorespiration, the ambient CO_2 concentration was maintained at 250 µmol mol^{-1} or 1000 µmol mol^{-1} for 21 % and 2 % oxygen level respectively. The oxygen concentration was maintained at 2 % using gas cylinders containing a mixture of 2 % O_2 and 98 % of N_2. This mixture was moisturized by bubbling it in water before use. The CO_2 response measurements were done by increasing the concentration in the following steps: 380, 200, 100, 90, 80, 70, 60, 50, 380, 380, 500, 1000 and 1500 µmol mol^{-1}, while keeping incident irradiance at 1500 µmol m^{-2} s^{-1}. After CO_2 of 50 µmol mol^{-1}, the leaf was adapted to CO_2 level of 380 µmol mol^{-1} before increasing to higher concentrations. Three minutes were allowed between steps to reach steady state photosynthesis. Leaf-to-air vapor pressure difference was kept between 0.9–1.8 kPa. Simultaneously with the gas exchange measurements, the steady-state fluorescence (F_s) and maximum relative fluorescence (F_m') were also measured. F_s was measured after photosynthesis was allowed to reach steady-state after each of the CO_2 or light steps. F_m' was measured after a saturating light-pulse of intensity greater than 8500 µmol m^{-2} s^{-1} for a duration of 0.8 s. The quantum efficiency of PSII electron transport was calculated as $\Delta F / F_m' = (F_m' - F_s) / F_m'$ (Genty *et al.*, 1989). The measurement data were corrected for leakage using thermally killed leaves (Flexas *et al.*, 2007). To determine the leaf nitrogen content, discs of 17 mm in diameter were taken at the place of measurement. These were then dried to constant weight in an oven at 70 °C for 48 hr. The leaf nitrogen content was determined by the Micro-Dumas combustion method (Thermo Scientific, elemental C/N analyzer, type: Flash 2000) (Steyermark, 1961) using three samples of leaf having an average area of 2.15 cm^2.

3.2.2 X-ray micro-CT imaging

Maize plants of the same cultivar were grown in three replicates simultaneously with those used in the gas exchange measurement to study the leaf anatomy using microscopy and the tomography experiments. The effect of nitrogen on these plants was assessed from readings of a portable chlorophyll meter (SPAD-502, Minolta, Japan) (Ciganda *et al.*, 2009). Maize leaf tissue samples (5 mm × 5 mm), both for young and old leaves, were obtained from the 6th leaf of each plant. Three samples per plant were taken from six plants (2 ages and 3 N levels). Each leaf was mounted on a polystyrene base and wrapped in a parafilm to prevent dehydration during scanning. The samples were placed on a high precision stage where the

sample rotated by 0.4° up to an angle of 196°. The samples were scanned using a high resolution X-ray micro-CT (Skyscan 1172, Bruker micro-CT, Kontich, Belgium) with an operating voltage of 60 kV and a current of 167 µA. Projection images were averaged from three frames. Each frame was captured with a camera size of 2000 × 1048 pixels and 885× 10^{-3} s exposure time. A single scan lasted for about 30 minutes. The samples were imaged at an isotropic voxel size of 2.96 µm.

Reconstruction of the cross-section from the shadow projections was performed using a filtered back projection algorithm (Feldkamp *et al.*, 1984) implemented in NRecon 1.6.6.0 (Bruker micro-CT, Kontich, Belgium). Beam hardening correction, smoothing and ring artifact reduction were set at 35, 2 and 8 % respectively. The linear attenuation coefficient range was set at 0 to 0.1068 to improve contrast and to standardize the grayscale range of the output images. The output file was an 8-bit bitmap with about 950 cross-section slices for each data set. The data sets were cleaned to remove noise and other extraneous materials. The cleaning procedure was implemented in the commercial software CTAn v1.13.5.1 (Bruker micro-CT, Kontich, Belgium).

Before morphometric analysis, the images were segmented into the constituent objects by using Otsu's algorithm (Otsu, 1979) in CTAn. A common global threshold value of 63 was found suitable for segmentation of the intercellular air spaces from cells of the leaf types. The segmented images were subsequently analyzed using a 3-D algorithm to determine the tissue volume, porosity, pore (intercellular air space) surface per volume, connectivity density of the pores and leaf thickness (Herremans *et al.*, 2015).

3.2.3 Light and electron microscopy measurements

Leaf samples from the 6th leaf, both young and old, were fixed in cold 2 % glutaraldehyde, buffered at pH 7.3 with 50 mM Na-cacodylate and 150 mM saccharose. Post fixation was carried out in 2 % osmium tetroxide in the same buffer. After dehydration in a graded acetone series, tissues were embedded in Araldite and sectioned with a Leica EM UC6 ultra-microtome. Serial semi-thin sections with a thickness of 1 µm were stained with methylene blue and thionin and viewed in an Olympus BX-51 microscope at 40x. Double stained 70 nm thin sections were examined in a Zeiss EM900 electron microscope.

Anatomical parameters such as S_m, S_b and the interveinal distance were measured from the light microscopy images while the cell wall thicknesses of mesophyll and bundle sheath were obtained from electron microscopy images. Three image samples were randomly selected for each N treatment × leaf age combination. The images were first digitized using in-house-made software (Mebatsion *et al.*, 2006*a*). The digitized images were then imported into finite-element software Comsol Multiphysics vs. 3.5 (Comsol AB, Stockholm). To calculate S_m and S_b the length of exposed mesophyll surface, perimeter of bundle sheath cells within an interveinal distance and a leaf area, taken as a distance between the centers of two consecutive bundle sheath cells, were measured (Pengelly *et al.*, 2010). Using a curvature correction factor of 1.43 (Thain, 1983; Evans *et al.*, 1994), these dimension measurements were converted into area. The thicknesses of mesophyll and bundle sheath cells wall were taken as the average of the distance between several parallel points on the digitized images of the cell walls. Interveinal distance was measured as the distance between the centers of two successive veins per image sample.

3.2.4 Estimation of bundle sheath conductance and other parameters

We used the procedure of Yin *et al*. (2011*b*) to estimate g_{bs} and other photosynthesis parameters. The underlying model equations of the procedure are listed in text A.1 (Appendix A) while model input parameters are shown in Table A.1.3. Using the method developed previously (Yin *et al.*, 2011*b*), the rate of day respiration (R_d) was estimated as the intercept of the linear relationship between photosynthesis and the term $I_{inc}\Phi_2 / 3$, based on data from the light-response curves at low ranges of an incident light intensity (I_{inc}) ($20 \leq I_{inc} \leq 200$ µmol m^{-2} s^{-1}). The measurements at 2 and 21 % O_2 levels were pooled to estimate a common R_d since the estimate for each O_2 level did not differ significantly ($P > 0.05$). The slope of the same linear regression but using data of 2 % O_2 plus measurements from the CO_2 response curves at high CO_2 ranges ($\geq$ 500 µmol mol^{-1}) at 2 % O_2 could give the lumped calibration factor s' for calculating potential ATP production rate J_{ATP} (Eq. A.1.2, Appendix A), based on fluorescence measurements (Yin *et al.*, 2011*b*). Here, s' was estimated for each leaf type simultaneously with g_{bs} as described below.

Bundle sheath conductance values corresponding to the three N levels × two leaf ages were determined using the SAS (SAS Institute Inc., Cary, NC, USA) code obtained from Yin *et al*.

(2011*b*) (the code is available upon request to the corresponding author of that paper). To avoid overfitting, we assumed a linear relationship between g_m and leaf nitrogen content (LNC) as was also shown to exist for C_4 crops (Weng and Hsu, 2001; Yin *et al.*, 2011*b*). The common slope of linearity (X_{gm}) was estimated (for details, see A.2, Appendix A). In addition, we found a good linear relationship between the quantum efficiency of CO_2 fixation and that of PSII electron transport (Fig. A.5.1, Appendix A) across all light and CO_2 levels. This suggests that (i) the proportion of ATP or energy used for sinks other than CO_2 fixation was not altered during the measurements, and, more importantly, (ii) any enzymatic limitation, if occurred, had a feedback effect on electron transport. Consequently, most of the measured rates of photosynthesis were covered by equations of electron-transport-limited rates of the model (Eqs. A.1.1 and A.1.3, Appendix A). Therefore, the resulting estimates for maximum catalytic rate of PEPc ($V_{p,max}$) and ribulose-1,5-bisphosphate carboxylase/oxygenase (Rubisco) ($V_{c,max}$) were not well constrained and had unreasonably high standard errors. This had little impact as the main aim here was not to estimate $V_{p,max}$ or $V_{c,max}$ but g_{bs}. Thus, we fixed $V_{p,max}$ and $V_{c,max}$ to arbitrarily high values to estimate g_{bs}, s' and X_{gm} only. Furthermore, it was shown recently that the use of a rectangular flash in a chlorophyll fluorescence measurement resulted in an underestimation of quantum efficiency of PSII electron transport, Φ_2 (Loriaux *et al.*, 2013). However, the influence of this underestimation is minimized using our calibration procedure for calculating J_{ATP}. For example, a 20 % higher Φ_2 (Loriaux *et al.*, 2013) would lower the estimated s' by ca. 16 %. As a result, J_{ATP} is minimally affected (see Eq. B.1.2, Appendix B) as s' compensated, to some extent, for an underestimation in Φ_2 (Yin *et al.*, 2014). Thus, the estimated g_{bs} values did not change (Table A.1.4, Appendix A).

3.2.5 Statistical analysis

A number of leaf anatomical properties for the six leaf age × N combinations were measured to determine explanatory variables for variation in g_{bs}. Using principal component analysis, the data of mean values could be summarized into linear combination of a few key variables that contribute to the variability in data while elucidating the relationship between leaf anatomical parameters and the g_{bs} and g_m. ANOVA was carried out using JMP version 12 (SAS Institute, USA) to compare N and leaf age groups. Mean values of the leaf

morphometric parameters were then compared using Student's *t*-test. A significance level of 5 % was used for this analysis.

3.3 Results

3.3.1 Effect of nitrogen supply and leaf age on photosynthesis

The effect of increased N supply and leaf aging on the rate of photosynthesis (*A*) in response to intercellular CO_2 concentration (C_i) and I_{inc} are shown in Fig. 3.1 and Fig. 3.2, respectively.

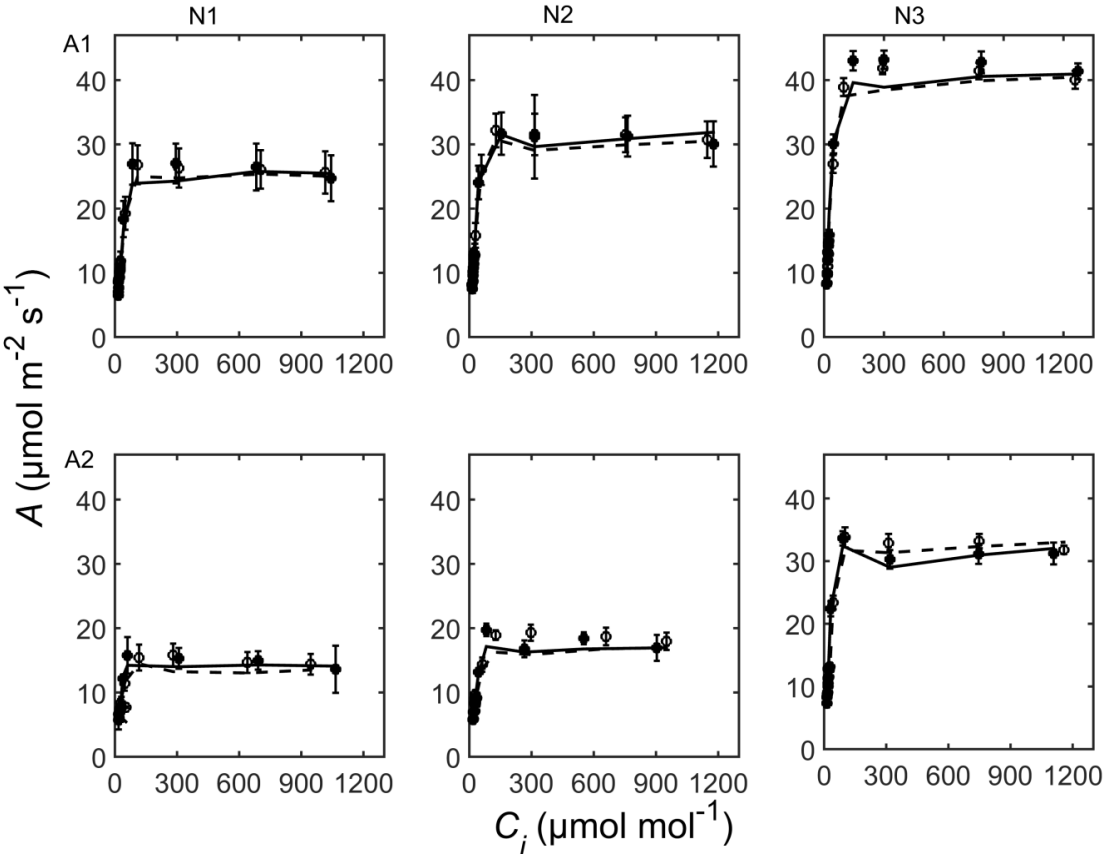

Figure 3.1. The response of photosynthesis to intercellular CO_2 concentration (C_i) for young (A1) and old (A2) leaves from maize plants grown under three nitrogen (N) levels: 0.15 g N per pot (N1); 0.50 g N per pot (N2) and 1.25 g N per pot (N3). Symbols show measured values while curves show model predicted values connected. Each measurement value is an average of measurements in four replicates (Materials and methods). The bars show standard error of the measurements. The oxygen levels were 21 % (filled circles, solid curves) and 2 % (open circles, dashed curves). The irradiance was kept at 1500 µmol m^{-2} s^{-1}.

Fig. 3.1 and Fig. 3.2 show that *A* increased with the amount of N added to the pots and declined with leaf age. These effects were reflected in the measured responses Φ_2 (Fig. 3.3) which were high for N3 leaves at high I_{inc} values and lower in old leaves than young leaves.

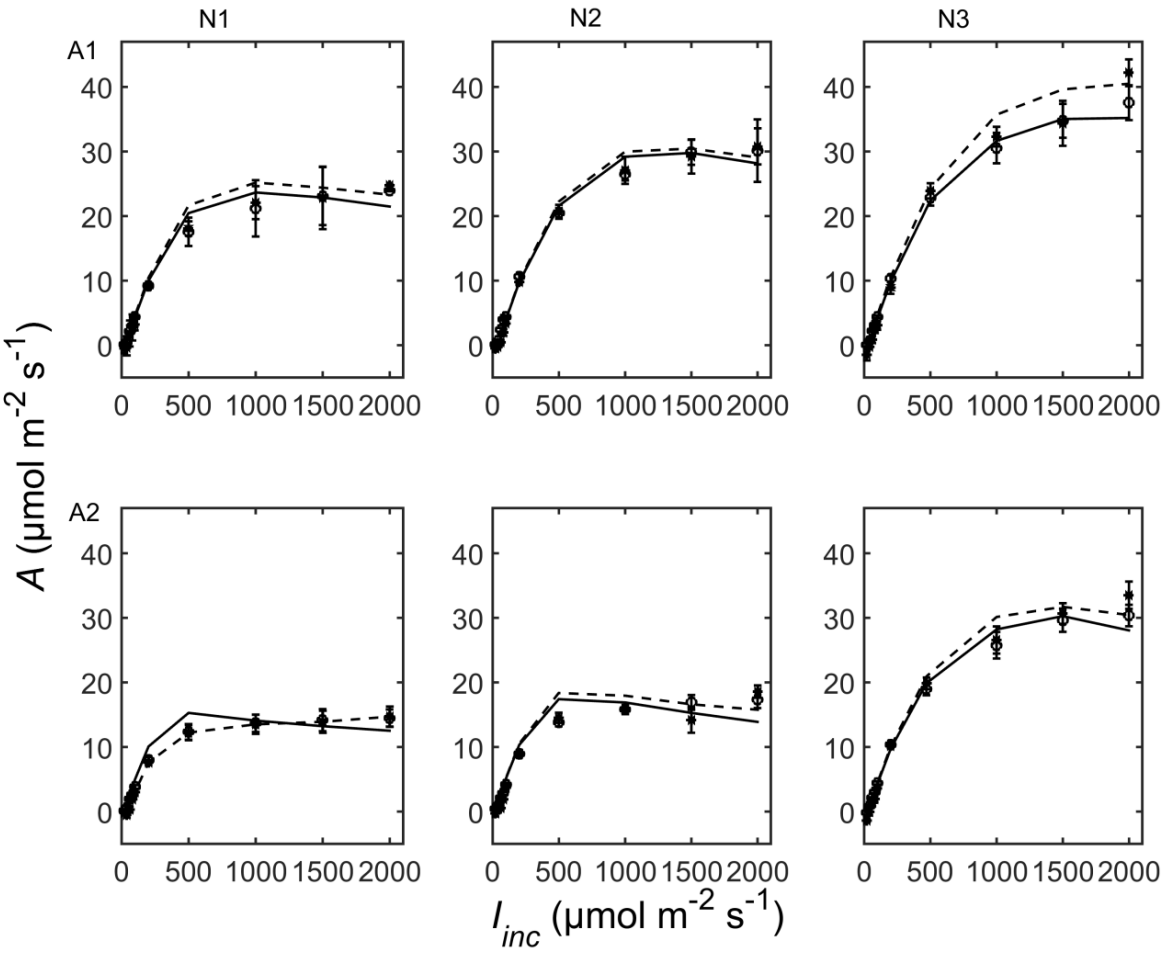

Figure 3.2. The response of photosynthesis to incident irradiance for young (A1) and old (A2) leaves from maize plants grown under three nitrogen (N) levels: 0.15 g N per pot (N1), 0.50 g N per pot (N2) and 1.25 g N per pot (N3). Symbols show measured values while curves show model predicted values connected. Each measurement value is an average of measurements in four replicates (Materials and methods). The bars show standard error of the measurements. The oxygen levels were 21 % (filled circles, solid curves) and 2 % (open circles, dashed curves). The ambient CO_2 was kept at 250 µmol mol^{-1} for 21 % and 1000 µmol mol^{-1} for 2 % oxygen levels.

The oxygen level, 2 % or 21 %, did not affect A and Φ_2 substantially although the differences in A and Φ_2 tend to be more in young N3 leaves suggesting an increased photorespiration.

The contrasting differences in rate of photosynthesis shown in Fig. 3.1 and Fig. 3.2 could be explained in part by significant differences in g_s (Table 3.1). Fig. 3.1 and Fig 3.2 also show that at constant C_i or irradiance level, non-stomatal factors contributed to the differences in rate of photosynthesis. In addition, Fig. 3.1 shows that photosynthesis rate reached saturation at low C_i which implies that stomatal limitation may have not been severe. This is expected in C_4 plants since the CCM mechanism allows them to be less reliant on stomatal conductance compared to C_3 plants. Thus, the discussion in this chapter will be focused more on non-stomatal factors such as g_m and g_{bs}.

Therefore, higher N application increased A and Φ_2 while leaf aging decreased them, as expected.

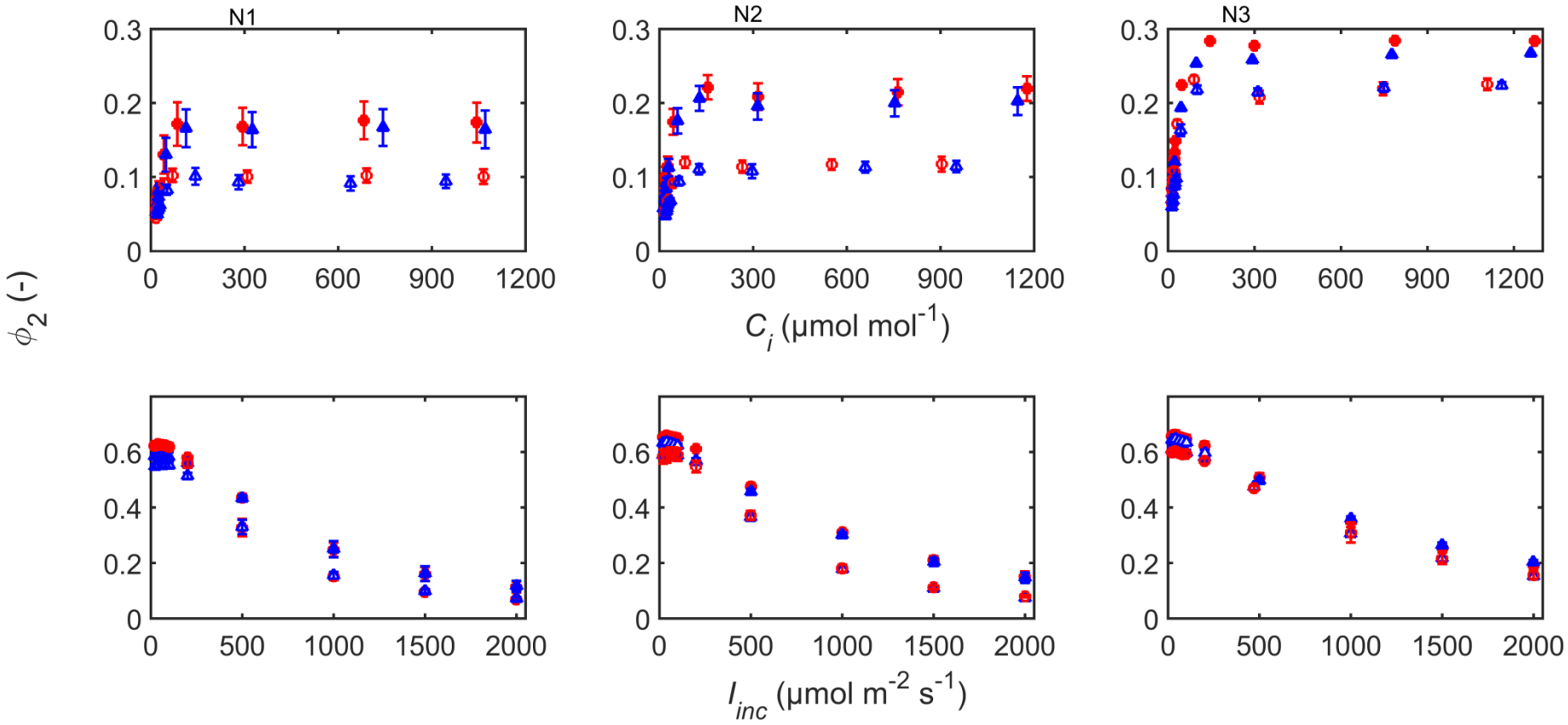

Figure 3.3. The measured response of apparent quantum efficiency of PSII electron transport to intercellular CO_2 concentration (top) and incident irradiance (bottom) for young (filled symbols) and old (open symbols) leaves at three nitrogen (N) levels: 0.15 g N per pot (N1), 0.50 g N per pot (N2) and 1.25 g N per pot (N3). The oxygen levels were 21 % (circles) and 2 % (triangles). The irradiance was kept at 1500 µmol m^{-2} s^{-1}. The bars show standard error of the measurements (n = 4).

3.3.2 The relationship between photosynthetic characteristics and LNC

Table 3.1 shows that the LNC increased when the amount of N added to the pots increased. Leaf aging decreased the LNC, however, less so for N2 and N3 leaves as a result of the more frequent N treatments for the old leaves. All young leaves had significantly higher *A* than all old leaves while all N3 leaves had significantly higher *A* than N2 and N1 leaves (Table 3.1). The relationships between *A*, day respiration rate (R_d), leaf dry mass per leaf area (LMA), light conversion efficiency ($s´$) and LNC are shown in Fig. 3.4. There was a strong positive correlation between *A* and LNC. LMA declined as LNC increased. R_d generally increased with LNC but the correlation was weak. There was also a loose correlation between $s´$ and LNC. The correlation of *A* with LNC was significant. The chlorophyll content of leaves also increased with LNC (Table 3.2).

Table 3.1 shows that all N3 leaves (young and old) have significantly higher g_s than those of N1 leaves while young N2 and N3 leaves have higher g_s than old N2 and N3 leaves.

Table 3.1. Estimated values of R_d, s', g_s and g_{bs} (± standard error) for young (A1) and old (A2) leaves from maize plants grown under three nitrogen (N) levels: low (N1), intermediate (N2) and high (N3). Shown also are leaf nitrogen content (LNC), leaf mass per unit leaf area (LMA) and stomatal conductance (g_s) and net photosynthesis (A) at ambient CO_2 of 380 µmol mol^{-1}, 21 % O_2 and irradiance of 1500 µmol m^{-2} s^{-1}. Means not connected by the same letter are significantly different ($P < 0.05$). Comparisons between leaf ages are indicated by upper case letters while differences among N levels within an age level are indicated by lower case letters. Shown in brackets for LNC, LMA, g_s and A are standard errors (n = 4) of measurement while those for R_d, s' and g_{bs} are standard errors of model fitting.

Leaf age	Leaf type	LNC g m^{-2}	LMA g m^{-2}	A µmol m^{-2} s^{-1}	g_s mol m^{-2} s^{-1}	R_d µmol m^{-2} s^{-1}	s'	g_{bs} mmol m^{-2} s^{-1}
A1	N1	0.64±0.09 a,A	39.01±0.65 a,A	27.05±2.79 a,A	0.17±0.024 a,A	1.70±0.20	0.325±0.004	0.88±0.55
	N2	0.83±0.08 a,A	33.95±0.59 b,A	31.92±2.34 a,A	0.24±0.021 ab,A	2.20±0.23	0.328±0.003	2.33±0.83
	N3	1.16±0.12 b,A	34.27±0.93 b,A	43.04±1.31 b,A	0.35±0.010 b,A	2.16±0.27	0.323±0.006	3.56±0.90
A2	N1	0.34±0.03 a,B	40.60±1.55 a,A	16.78±1.40 a,B	0.09±0.004 a,A	1.68±0.17	0.327±0.007	0.36±0.50
	N2	0.60±0.11 a,A	36.29±1.72 a,A	19.33±0.80 a,B	0.11±0.0080 a,B	1.65±0.21	0.332±0.003	0.51±0.51
	N3	0.74±0.15 a,A	38.70±2.30 a,A	33.74±0.99 b,B	0.21±0.0087 c,B	2.29±0.19	0.321±0.003	1.34±0.62

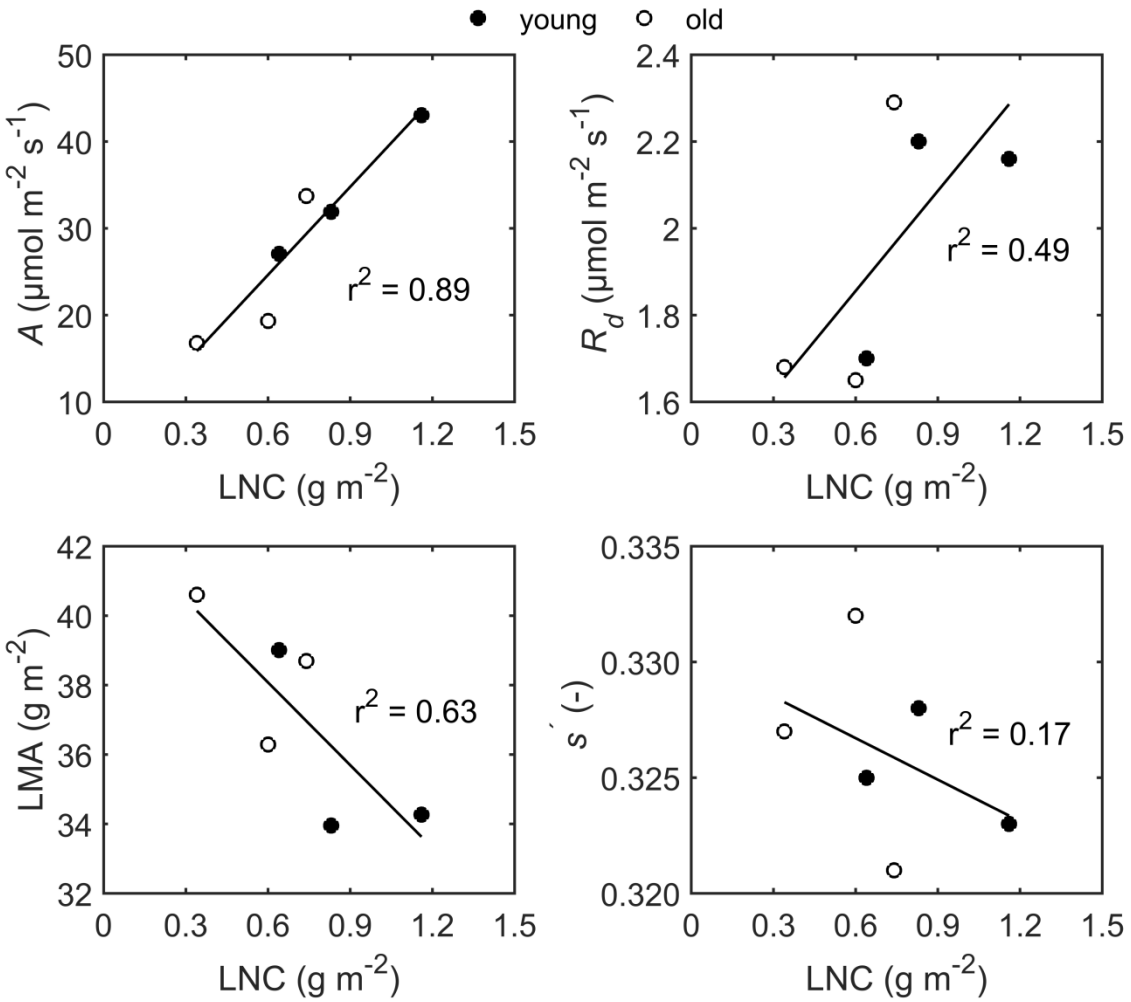

Figure 3.4. Photosynthesis rate (*A*), day respiration (R_d), leaf dry mass per leaf area (LMA) and light conversion efficiency (*s´*) in relation to leaf nitrogen content (LNC) for young (○) and old leaves (●).

3.3.3 Bundle sheath conductance in response to LNC and leaf age

Table 3.1 shows that estimated g_{bs} values were higher for N3 leaves than for N2 and N1 leaves. Old leaves had lower g_{bs} than young leaves. The model to estimate g_{bs} predicts the rate of photosynthesis well (Fig. 3.1 and Fig. 3.2, $r^2 = 0.98$); however, some of the best-fit values of g_{bs} had high standard errors. Although there is an uncertainty on the actual g_{bs}, the estimated values show a general trend of increasing with LNC and declining with leaf age. In addition, g_{bs} correlated with LNC ($r^2 = 0.90$) (Fig. 3.5). Across N levels and leaf ages, the bundle sheath resistance thus varied from ca. 281 to 2756 m^2 s mol^{-1}. Furthermore, the

estimated X_{gm} was 2.83 ± 0.16 mol (g N)$^{-1}$ s^{-1} resulting in g_m values of 0.54 mol m^{-2} s^{-1} at the lowest LNC and 2.85 mol m^{-2} s^{-1} at our highest LNC.

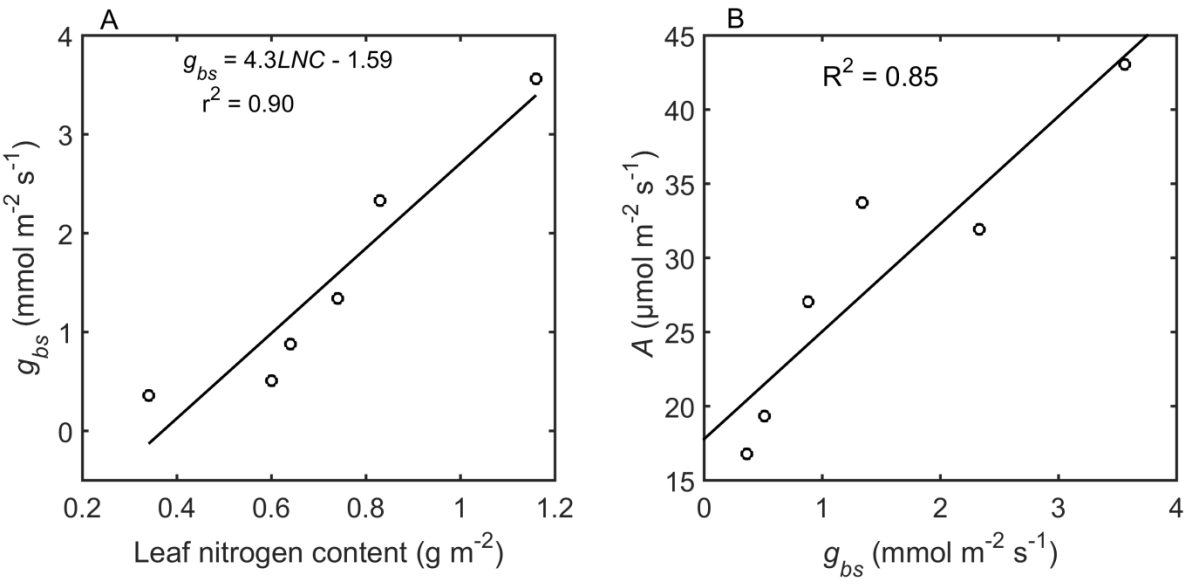

Figure 3.5. A. The estimated bundle sheath conductance (g_{bs}) in relation to leaf nitrogen content (LNC). B. The relationship between photosynthesis (A) and $g_{bs.}$

Fig. 3.5B shows that a good linear relationship between A and g_{bs} exists. As a result of increased g_{bs} with LNC, the mean CO_2 concentration in the bundle sheath (C_c) (Fig. 3.6) was higher for young N1 leaves than for young N2 and N3 leaves across all irradiances. This pattern was the same for the old leaves (Fig. A.3.1, Appendix A).

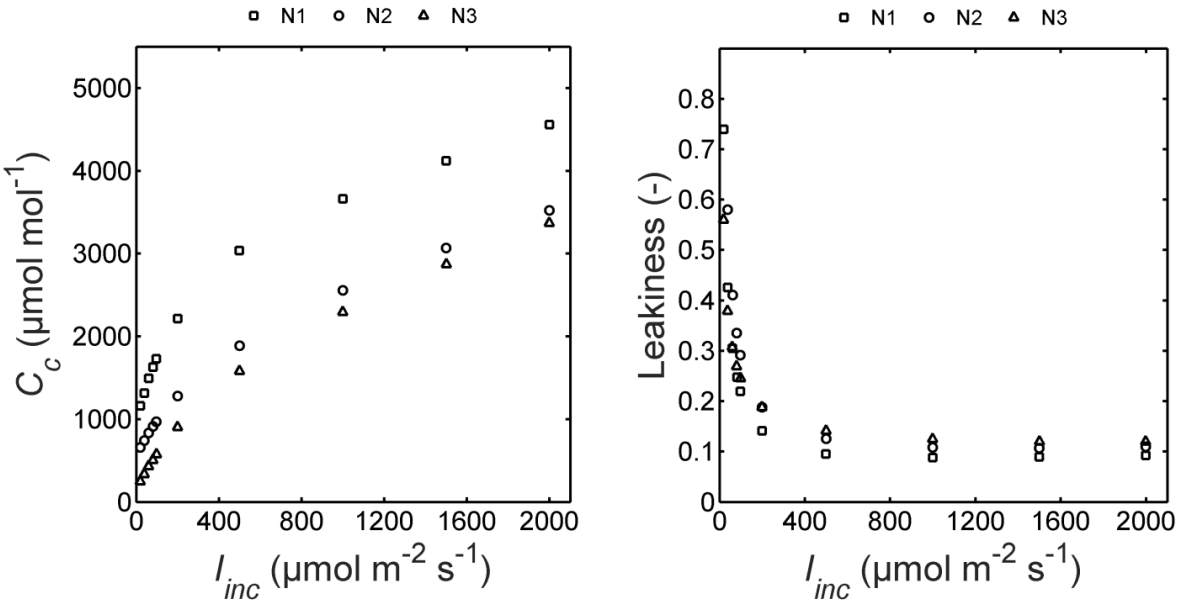

Figure 3.6. The predicted response of mean concentration of CO_2 in bundle sheath cells (C_c) (left panel) and leakiness (right panel) to incident irradiance (I_{inc}) for young leaves grown at three nitrogen (N) levels: 0.15 g N per pot (N1), 0.50 g N per pot (N2) and 1.25 g N per pot (N3). The ambient CO_2 was kept at 250 µmol mol^{-1} and oxygen level was 21 %.

Across leaf ages, C_c was higher in old leaves than in young leaves consistent with differences in g_{bs} (Fig. A.3.1, A.3.2, Appendix A). The efficiency of the CCM as indicated by leakiness, however, was not substantially different within N levels (Fig. 3.6). The predicted leakiness was also similar across leaf ages (Fig. A.3.3, A.3.4, Appendix A).

3.3.4 Sensitivity analysis

The sensitivity of X_{gm}, s' and g_{bs} to the fraction of ATP allocated to the C_4 cycle (x) (Table A.1.3), which is an important determinant of the electron-transport-limited rate of PEP carboxylation and photosynthesis (Eq. A.1.1 and Eq. A.1.3, Appendix A), is shown in Table A.1.5 (Appendix A). The estimated X_{gm} and s' were largely insensitive to various values of x except when it was low (0.35). However, the value x = 0.35 may not be biologically realistic as many modeling studies show that x is very close to 0.40 (von Caemmerer and Furbank, 1999; Yin *et al.*, 2011*b*) under various treatments and ambient conditions. Yin and Struik (2012) estimated that when additional ATP utilizing processes were considered, x varied from 0.399 to 0.385. Optimization analysis showed that the optimum x was ca. 0.4 over a wide

range of conditions, except under extremely low-light conditions (von Caemmerer and Furbank, 1999). Table A.1.4 also shows that g_{bs} was sensitive to x. However, when x was also estimated simultaneously with g_{bs} from our model (not shown), it was 0.43 ± 0.042 which is also close to 0.4. We decided to fix x = 0.4 to improve the estimation of g_{bs} by reducing the number of parameters to be fitted. Fig. A.5.2 (Appendix A) shows that the relationship between g_{bs} and LNC remained strongly linear. Therefore, although the estimated g_{bs} values were sensitive to the choice of x, the relationship between g_{bs} and LNC was minimally affected. The magnitudes of leakiness and C_c were, however, sensitive to x (Fig. A.5.3 and Fig. A.5.4, Appendix A). Therefore, these predictions should be considered as temporary values. However, the trends of C_c and leakiness were not altered. Furthermore, X_{gm}, s' and g_{bs} were expectedly insensitive to Rubisco and PEPc kinetics parameters (Table A.1.5, Appendix A) due to the close link between photosynthesis and electron transport (Fig. A.5.5, Appendix A).

3.3.5 The effects of LNC and leaf age on the anatomy of maize leaves

Table 3.2 shows the measurement results of the leaf morphological properties for young and old leaves. The portable chlorophyll meter readings that correlate with chlorophyll content (Ciganda *et al.*, 2009), were higher for N3 and N2 than for N1 leaves and lower for old leaves than for the young leaves (Table 3.2). This implies that the nitrogen content of maize leaves used for imaging increased with higher N application and decreased with leaf age. The images of transverse sections of the maize leaf samples, cell walls of the bundle sheath and surface rendering of leaves using X-ray micro-CT images are shown in Fig. A.6.1, Fig. A.6.2 and Fig. A.6.3, respectively (Appendix A).

Anatomical parameters such as S_m, S_b, leaf thickness, cell volume and bundle sheath cell wall thickness were not significantly altered by LNC. Old N1 leaves had a significantly thicker mesophyll cell wall than old N2 leaves. The pore surface to volume ratio of young N1 leaves was significantly higher than that of young N2 and N3 leaves while it was significantly larger for old N1 leaves than for the old N2 leaves. Old N3 leaves were significantly more porous than old N2 leaves. The connectivity density was significantly larger in the old N3 leaves than that in the N2 leaves. Both young and old N1 leaves had significantly shorter interveinal distance that N2 and N3 leaves.

The porosity, pore surface per volume and connectivity density values were not significantly different between young and old leaves. Young N1 leaves were significantly thicker than old N1 leaves. Old N1 leaves had significantly thicker cell walls of mesophyll and bundle sheath than young N1 leaves. Comparing across leaf ages, mean values of S_m of old leaves were larger than those of young leaves. However, statistical analysis showed that only old N2 leaves had a significantly larger S_m than young N2 leaves. By contrast, all young leaves had significantly higher S_b than their respective old leaves. The difference in interveinal distance between young and old N1 leaves was significant.

Table 3.2. Leaf anatomical properties of young leaves (A1) and old leaves (A2) (mean ± standard error, n=3) from maize plants grown under three nitrogen (N) levels: low (N1), intermediate (N2) and high (N3). Means not connected by the same letter are significantly different ($P < 0.05$). Comparisons between leaf ages are indicated by upper case letters while differences among N levels within an age level are indicated by lower case letters. Porosity, cell volume, pore surface per volume, connectivity density and leaf thickness were measured from X-ray micro-CT images. Cell wall thicknesses were measured from transmission electron microscopy images. *Sm*, S_b and interveinal distances were measured from light microscopy images.

Parameter	A1			A2		
	N1	N2	N3	N1	N2	N3
Chlorophyll meter readings (SPAD units)	38.1	42.3	48.1	22.1	27.2	39.4
Porosity (%)	36.7 ± 0.39 a,A	38.3 ± 1.1 a,A	38.6 ± 2.5 a,A	37.05 ± 2.6 ab,A	36.3 ± 0.25 a,A	38.4 ± 0.53 b,A
Cell volume (mm^3)	1.79 ± 0.04 a,A	1.66 ± 0.05 a,A	1.68 ± 0.05 a,A	1.46 ± 0.04 a,B	1.58 ± 0.05 a,A	1.61 ± 0.1 a,A
Pore surface/volume (mm^2 mm^{-3})	268 ± 0.60 a,A	255 ± 0.59 b,A	253 ± 5.1 b,A	261 ± 3.7 a,A	258 ± 1.2 b,A	263 ± 7.7 ab,A
Connectivity density ×1000 (mm^{-3})[(1)]	81.9 ± 1.2 a,A	78.9 ± 4.7 a,A	77.8 ± 8.1 a,A	78.5 ± 9.1 ab,A	74.0 ± 1.5 a,A	81.6 ± 2.2 b,B
Leaf thickness (µm)	237 ± 6.87 a,A	217 ± 8.41 a,A	243 ± 7.84 a,A	197 ± 5.22 a,B	209 ± 8.91 a,A	208 ± 5.31 a,A
Bundle sheath cell wall thickness (µm)	0.188 ± 0.0140 a,A	0.245 ± 0.0458 a,A	0.260 ± 0.0331 a,A	0.457 ± 0.0190 a,B	0.445 ± 0.0500 a,A	0.319 ± 0.0150 a,A
Mesophyll cell wall thickness (µm)	0.161 ± 0.0277 a,A	0.119 ± 0.0209 a,A	0.138 ± 0.0288 a,A	0.230 ± 0.0277 a,B	0.139 ± 0.0139 b,A	0.149 ± 0.0144 ab,A
S_m (m^2 m^{-2})	9.10 ± 0.53 a,A	8.93 ± 0.16 a,A	9.01 ± 0.39 a,A	11.19 ± 1.67 a,A	10.60 ± 0.28 a,B	9.66 ± 1.00 a,A
S_b area (m^2 m^{-2})	2.82 ± 0.16 a,A	2.56 ± 0.17 a,A	2.54 ± 0.14 a,A	1.89 ± 0.06 a,B	1.81 ± 0.03 a,B	1.82 ± 0.03 a,B
Interveinal distance (µm)	119 ± 3.96 a,A	142 ± 5.72 b,A	149 ± 14.18 b,A	130 ± 3.13 a,B	146 ± 2.95 b,A	141 ± 5.38 b,A

[(1)] Connectivity density is defined as the number of multiple connections between structures per unit volume.

3.3.6 Bundle sheath conductance in relation to leaf anatomy

The correlation between the measured leaf anatomical parameters and g_{bs} is shown by principal component analysis (PCA) biplot in Fig. 3.7 in analogy to a study on C_3 plants (Galmés *et al.*, 2013). The scores represent young and old leaves. Since a total of six g_{bs} values were estimated for LNC × leaf age combinations, mean values of anatomical parameters were used in the PCA. The direction of correlation loadings which are vectors with origin at (0,0) shows positive or negative correlation. Thus, the vectors in opposite direction are largely negatively correlated while the vectors pointing to the same direction are positively correlated. If the vectors point in the direction of a score (young or old leaves), the score is characterized by a positive value of the corresponding anatomical property or CO_2 conductance. Vectors that are perpendicular to each other are uncorrelated. The corresponding correlation coefficients are shown in Table A.1.6 (Appendix A).

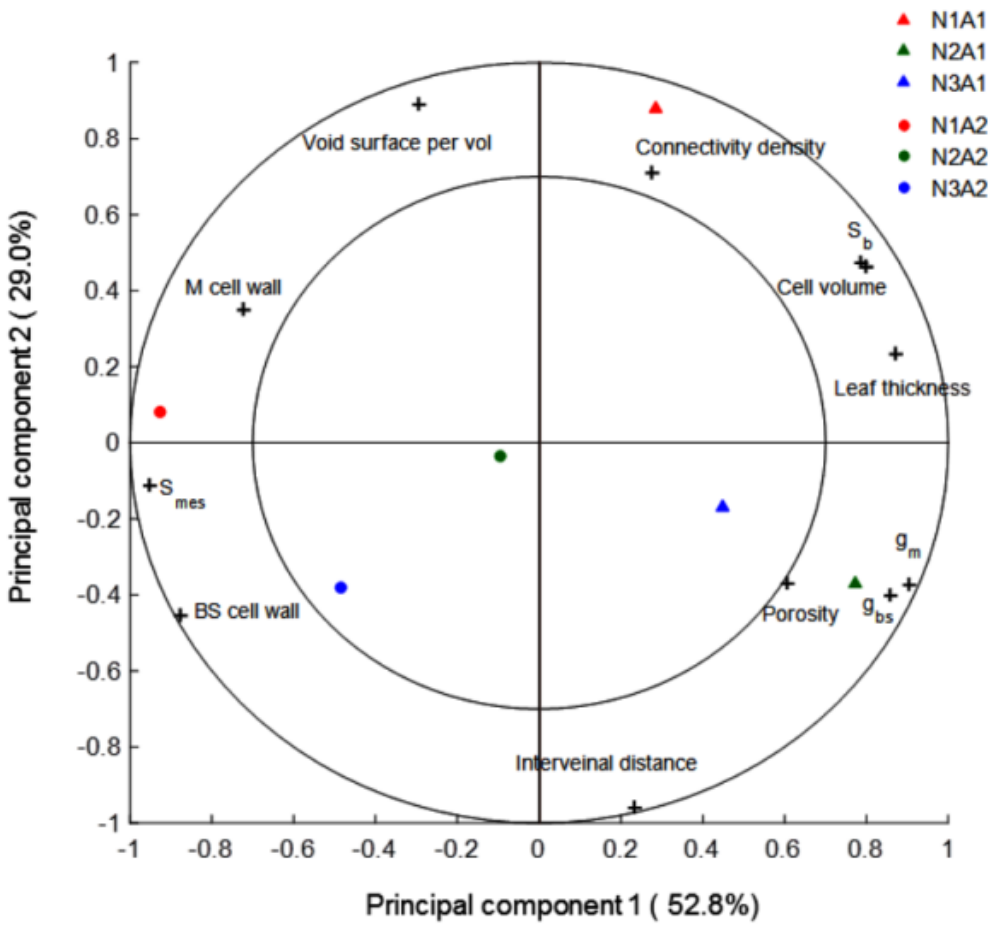

Figure 3.7. Principal component analysis (PCA) biplot of young and old leaves showing the grouping of leaf types in terms of leaf anatomical properties (mean values). Scores of young (A1) and old leaves (A2) grown under three nitrogen (N) levels: low (N1), intermediate (N2) and high (N3) are shown. Variables should be interpreted as vectors with origin in (0,0). Correlation loading (+) located between the circles (70 % and 100 % of the explained variance limits) are considered most important for explaining the variability with respect to the principal component shown. Correlation between variables is as follows; variables with correlation loadings that are close to each other are correlated, loading that are 90° from each other are uncorrelated and loading that are 180° from each other are inversely correlated. Abbreviations: bundle sheath (BS) conductance (g_{bs}), mesophyll (M) conductance (g_m), exposed mesophyll surface per unit leaf area (S_m), bundle sheath surface area per unit leaf area (S_b).

The PCA analysis resulted in two principal components (PCs) that explained 82 % of the total variance. PC1 was well correlated (r > 0.70) to cell wall thickness of mesophyll and bundle sheath cells, S_m, S_b, leaf thickness and tissue volume (Table A.1.6, Appendix A). Thus, PC1 was correlated to the major determinants of g_{bs} and g_m. The first PC was also effective in separating young and old leaves. g_m, g_{bs} and porosity were highly correlated similar to the correlation between leaf thickness, S_b and cell volume. g_{bs} was correlated with interveinal distance and S_b although less strongly than leaf thickness. There was a strong negative correlation between the mesophyll cell wall thickness and g_m but not g_{bs}. The bundle sheath cell wall thickness was inversely related to g_{bs} while S_m was inversely related to g_m. Void surface per volume and connectivity density were correlated to each other but uncorrelated to other anatomical properties and g_m in this biplot. Fig. 3.7 also shows that old leaves in general have thicker cell walls of mesophyll and bundle sheath cells, lower conductances and are thinner than young leaves.

3.4 Discussion

3.4.1 Bundle sheath conductance increased with LNC and declined with leaf age

We have grown maize plants under three nitrogen treatment levels to study how g_{bs} varies with LNC. Previously, it was shown that g_{bs} increased with LNC for two extreme N treatment levels (Yin *et al.*, 2011*b*). Our results confirm that g_{bs} varied in with LNC (Table 3.1). The bundle sheath resistances were mostly in the range 100 to 1600 m^2 s mol^{-1}, reported for various C_4 species (Jenkins *et al.*, 1989*a*; von Caemmerer and Furbank, 2003; Kromdijk *et al.*, 2010; Yin *et al.*, 2011*b*). More importantly, g_{bs} significantly correlated with LNC while the impact of the latter on g_{bs} was much more than that of leaf age as confirmed by a two-variable regression (Table A.7.1, Appendix A). Fig. 3.5B shows that a strong linear relationship exists between A and g_{bs}. The effect of decreased CO_2 concentration in bundle sheath cells due to high g_{bs} with high LNC was reflected in the fraction of assimilation lost due to photorespiration (Eq. A.3.2, Appendix A) which was higher for N3 leaves than for N1 and N2 leaves (Fig. A.3.5, Appendix A). In addition, leakiness was not affected by the LNC since the energy efficiency of CO_2 fixation indicated by

the ratio of quantum yield of CO_2 fixation to quantum yield of PSII electron transport was not significantly different in young and old leaves within N levels (Fig. A.5.6, Appendix A). Consistent with this, the predicted leakiness (Fig. 3.6) also shows that the efficiency of the C_4 cycle was not substantially affected while a strong positive correlation between *A* and LNC was found (Fig. 3.4). This occurs when the increased rate of CO_2 leakage was matched with increased delivery of CO_2 by the higher capacity of the C_4 cycle in leaves having high LNC. Consequently, the bundle sheath resistance of high photosynthesis capacity leaves should decrease (Fig. 3.6B) (von Caemmerer and Furbank, 2003). The corollary to these predictions is that the maize plants grown in low N supply responded by increasing bundle sheath resistance to maintain similar efficiency. This raises the question of how the variation of g_{bs} was achieved.

3.4.2 The combined effect of LNC and leaf age on anatomy may explain the differences in bundle sheath conductance

Our results for the increase of g_{bs} with LNC (Fig. 3.5) confirm the earlier result of Yin *et al.* (2011*b*) based on only two nitrogen treatments. This positive correlation could be examined using the influence of LNC on anatomical components of g_{bs}, S_b, and cellular conductance, which is the CO_2 conductance of the mesophyll-bundle sheath interface (von Caemmerer and Furbank, 1999). The cellular conductance may be expected to be influenced by properties of the bundle sheath cell wall, while g_{bs}, which is expressed per unit leaf area, is influenced by S_b (von Caemmerer and Furbank, 1999). The measured S_b was in the range of values reported in the literature 1.5 to 3.1 m^2 m^{-2} (Brown and Byrd, 1993; Dengler *et al.*, 1994; Pengelly *et al.*, 2010, 2011; Barbour *et al.*, 2016). In addition, the measured values of cell wall thickness of bundle sheath cells are close to the reported values for C_4 plants, including maize, ca. 0.3 to 1.6 µm (Hattersley and Browning, 1981; Rezvani Moghaddam and Wiliman, 1998; Watling, 2000; von Caemmerer and Furbank, 2003). The decline of g_{bs} with leaf aging was accompanied by a significant decline of S_b. Due to this reduction in S_b, old leaves were also significantly thinner than young leaves except for old N2 leaves, where the reduction in S_b accompanied by significantly larger S_m resulted in similar leaf thickness (Table 3.2). In old N1 leaves, particularly, the wall thickness of bundle sheath cells was also thicker. Since LNC also declined with leaf age (Table 3.1), significantly so within young and old N1 leaves, these responses of leaf anatomy and

the resulting differences in g_{bs} are attributed to the combined effects of LNC and leaf age. However, within N levels, it seems that neither S_b nor wall thickness of bundle sheath was responsible for the differences in g_{bs}. The anatomy changed in such a way that only the vein spacing increased with LNC but interveinal distance correlated to g_{bs} less strongly. The lack of association between g_{bs} and cell wall thickness within N levels suggests that other factors may play a role. For instance, the density of plasmodesmata which are considered the main pathway to CO_2 leakage (Hattersley and Browning, 1981; Sowiński *et al.*, 2008) since the suberin layer (for instance, Fig. A.6.4, Appendix A) may restrict the leakage of CO_2 through the cell walls as suggested previously (Dengler and Nelson, 1999; Mertz and Brutnell, 2014). Previous reports show that the abundance of plasmodesmata responded to growth conditions such as low temperature or low irradiance (Sowiński *et al.*, 2003, 2007). Overall, the impact of LNC on g_{bs} was not due to alteration of the anatomical factors while its effect on the anatomy in interaction with leaf age explains for differences in g_{bs} between young and old leaves.

3.4.3 Mesophyll conductance in relation to LNC and leaf age

In C_3 plants, a positive correlation of g_m with exposed mesophyll surface has been reported (Flexas *et al.*, 2008). For C_4 plants, CO_2 assimilation occurs in the mesophyll cytosol, thus the parameter S_m is believed to be positively related to g_m (von Caemmerer and Furbank, 2003). Our measured S_m was in the range of values reported for C_4 species (El-Sharkawy, 2009; Pengelly *et al.*, 2011; Barbour *et al.*, 2016). In relation to g_m, however, *Sm* did not change significantly with LNC. *Sm* had also strong negative correlation with g_m (Fig. 3.7) due to a higher *Sm* in old leaves than young leaves. Thus, the role of S_m in g_m was counter-intuitive. As shown in Fig. 3.7, g_m also correlated with porosity, leaf thickness and mesophyll cell wall thickness. The lack of significant differences in porosity or degree of connectivity of air spaces in many of the leaves, however, rules out the possibility of causal relationship between the parameters and variations in g_m. In addition, since maize is an amphistomatous leaf, the resistance of the intercellular air space is low (Parkhurst and Mott, 1990). Among young and old leaves, the decline of leaf thickness may have been due to reduced S_b not due to changes in S_m. A strong negative correlation of mesophyll cell

wall thickness with g_m in combination with a significantly thicker mesophyll cell wall of old N1 leaves support the decline of g_m across leaf ages.

3.4.4 Implications of conserved leaf anatomy under contrasting LNC on photosynthesis

An increased g_{bs} with LNC reduced the effectiveness of the CCM as the CO_2 concentration in the neighborhood of Rubisco decreased. On the other hand, similar to previous reports (Vos *et al.*, 2005; Tazoe *et al.*, 2006; Feng *et al.*, 2012), higher LNC boosted the rate of photosynthesis. In addition, high LNC leaves had low LMA which is associated with elevated concentration proteins and photosynthesis (Poorter *et al.*, 2009). It is to be noted that our measured photosynthesis was mainly limited by electron transport. This paradox could be explained by the increase in quantum efficiency of electron transport outweighing the increase of g_{bs} with LNC. In conjunction with leaf anatomical data, this implies that the negative impact of decreased bundle sheath resistance was not detrimental to the rate of photosynthesis. Similarly, Yin *et al*. (2011*b*) have shown that the increase of g_{bs} by LNC has less influence on the rate of photosynthesis compared to the effect of LNC on photosynthetic capacity. It could also be that increased CO_2 leak with high LNC may elevate the CO_2 concentration in mesophyll (Fig. 4.3, Subsection 4.3.2), thus, the rate of PEP carboxylation and also maintains the balance of energy supply and demand, boosting photosynthesis (Wang *et al.*, 2014*b*).

In response to growth conditions, some C_4 plants have shown to respond, for instance, through alteration in anatomy (Pengelly *et al.*, 2010; Kromdijk *et al.*, 2010). Similarly, due to leaf aging, which was accompanied by a drop in LNC, old maize leaves had lower g_{bs} than young leaves through lower S_b. However, the anatomy of a maize leaf was generally conserved despite the large differences in LNC (Table 3.2). While accepting that the tissue preparation for the microscopy experiment may have affected our results, the apparent lack of effect of LNC may also be in line with the hypothesis that the C_4 leaf anatomy responds to environmental changes by ensuring intimate contacts of mesophyll and bundle sheath cells which is essential for efficient metabolite transport and CCM (Greef, 1994; Dengler and Nelson, 1999; Sage and McKown,

2005; El-Sharkawy, 2009). These views suggest that the leaf anatomy in C_4 plants may be constrained by the need for rapid metabolite fluxes.

3.5 Conclusion

We investigated the bundle sheath conductance in relation to anatomy of maize leaf as a function of nitrogen and leaf age. g_{bs} appeared to be strongly related to LNC but leaf anatomy was not. Consequently, changes in the leaf anatomy were not the cause of variation in g_{bs} with LNC except in interaction with leaf age. In addition, a high photosynthesis rate occurred simultaneously with a high g_{bs}. These results were unexpected and counter-intuitive. However, since the chloroplast envelope and plasma membrane also contribute to bundle sheath resistance, the possible effect of nitrogen through altered composition, thus permeability, should be accounted for. The CO_2 diffusion in the liquid phase of mesophyll cells is also constrained by the permeability of the plasma membrane which, in maize, contains aquaporins and carbonic anhydrases that may enhance its CO_2 permeability (Utsunomiya and Muto, 1993; Maurel *et al.*, 2008). Therefore, future investigations considering these components along with the roles of suberin and plasmodesmata are recommended to unravel the effect of LNC on g_{bs} further.

4 A two-dimensional microscale model of gas exchange during photosynthesis in maize (*Zea mays* L.) leaves

This chapter is based on:

Retta M., Ho Q.T., Yin X., Verboven P., Berghuijs H.N.C., Struik P.C., Nicolai, B.M. (2016). A two-dimensional microscale model of gas exchange during photosynthesis in maize (*Zea mays* L.) leaves. Plant Science 246, 37–51.

4.1 Introduction

The role of leaf anatomical properties on CO_2 conductances, g_m and g_{bs}, in relation to leaf nitrogen content and age was examined in the Chapter 3. g_{bs} as derived from a biochemical model of C_4 photosynthesis correlated well with many of the anatomical properties. In addition, to examine the influence of LNC and leaf age on g_{bs} further, additional microstructural features should be considered. In Chapter 4, a microscale model of gas exchange will be developed to mechanistically analyze g_m and g_{bs} and thus increase quantitative insight on the role of leaf microstructure to the efficiency of the CO_2 concentration mechanism (CCM).

The mechanisms contributing to the high g_m of C_4 plants are not understood well (von Caemmerer and Furbank, 2003; Weber and von Caemmerer, 2010), but are suggested to be related to the fact that CO_2 has to cross fewer membranes in mesophyll cells of C_4 plants than those of C_3 plants (von Caemmerer *et al.*, 2007), a thinner mesophyll cell wall in C_4 plants (Evans and Loreto, 2000; von Caemmerer *et al.*, 2007), abundant aquaporins in the mesophyll plasma membrane of C_4 plants (Weber and von Caemmerer, 2010) and mesophyll chloroplasts allowing more volume for CO_2 assimilation by covering less of the exposed mesophyll surface (Stata *et al.*, 2014).

Bundle sheath resistance determines the concentration of CO_2 in bundle sheath cells and constrains the rate of retro-diffusion (Hatch, 1987; Leegood, 2002), thereby contributing to an efficient CCM. The inverse of the resistance, the bundle sheath conductance (g_{bs}), has been estimated using mathematical model fitting (see Chapter 3) (von Caemmerer and Furbank, 2003; Yin *et al.*, 2011*b*) or using a plant which lacks the C_4 cycle (Kiirats *et al.*, 2002) or isolated bundle sheath cells (Furbank *et al.*, 1989; Brown and Byrd, 1993). It is reported to vary with growth light (Kromdijk *et al.*, 2010; Bellasio and Griffiths, 2014*c*), nitrogen supply and leaf age (He and Edwards, 1996; Kiirats *et al.*, 2002; Yin *et al.*, 2011*b*). These results came predominantly from resistance-based analytical models (Furbank and Hatch, 1987; Jenkins *et al.*, 1989*b*; Collatz *et al.*, 1992; Brown and Byrd, 1993; Kiirats *et al.*, 2002; Yin *et al.*, 2011*b*). CO_2 diffusion limitations imposed by the intracellular structure in C_4 leaves have also been quantified using resistance models (Longstreth *et al.*, 1980; von Caemmerer and Furbank, 2003). However,

resistance models do not specifically consider distributed sources and sinks of CO_2 in leaves, nor do these models account directly for the effects of leaf anatomy on CO_2 diffusion. Considerable progress was recently made by our group in the development of microscale models of CO_2 exchange that incorporate the leaf microstructure of C_3 plant leaves (Ho *et al.*, 2012, 2016). Such microscale photosynthesis models, if implemented for C_4 leaves, may help in explaining the influences of leaf microstructure on g_{bs}.

The objectives of this research were (i), to include the physical barriers of leaf anatomy and ultrastructure in the microscale model analysis of gas diffusion and photosynthesis in C_4 leaves, and (ii), to quantitatively evaluate the role of components along the CO_2 diffusion and retro-diffusion pathway on CCM.

4.2 Materials and methods

4.2.1 Biochemical model of C_4 photosynthesis

We based our analysis on a photosynthesis kinetics model for C_4 leaves presented by von Caemmerer and Furbank (1999). This model states that in mesophyll cells (*m*), the PEP carboxylation rate V_p is enzyme-limited or electron-transport-limited. V_p is given by (von Caemmerer and Furbank, 1999):

$$V_p = \min\left\{\frac{[CO_2]_m \cdot V_{p,max}}{[CO_2]_m + K_p}, \frac{x J_{ATP}}{2}\right\} \tag{4.1}$$

The first term between the brackets is for the enzyme-limited rate while the second term is for the electron-transport-limited rate of PEP carboxylation. $[CO_2]_m$ is the concentration of CO_2 in the mesophyll cytosol; K_p is the Michaelis-Menten constant of PEPc for CO_2; and $V_{p,max}$ is the carboxylation capacity of PEPc. The partitioning factor, x, is the fraction of ATP allocated to the C_4 cycle. Note that the rate of total electron transport in the model of von Caemmerer and

Furbank (1999) was changed here to J_{ATP}, the rate of ATP production (Yin and Struik, 2012). We calculated J_{ATP} according to Yin *et al*. (2011*b*) (Eq. B.1.1, in Appendix B).

The gross rate of CO_2 fixation in bundle sheath (*bs*) chloroplasts (V_c) limited by the rate of Rubisco carboxylation (w_c) or the rate of electron transport (w_j) is expressed as (Farquhar *et al.*, 1980; von Caemmerer and Furbank, 1999):

$$V_c = \min(w_c, w_j) \tag{4.2}$$

$$w_c = \frac{[CO_2]_{bs} \cdot V_{c,max}}{[CO_2]_{bs} + K_{m,C}(1 + [O_2]_{bs} / K_{m,O})} \tag{4.3}$$

$$w_j = \frac{[CO_2]_{bs} \cdot (1-x) J_{ATP}}{3[CO_2]_{bs} + 7\gamma^*[O_2]_{bs}} \tag{4.4}$$

where $V_{c,max}$ is the carboxylation capacity of Rubisco; $K_{m,C}$ and $K_{m,O}$ are Michaelis-Menten constants of Rubisco for CO_2 and O_2 respectively; γ^* is half the inverse of Rubisco specificity; and $[CO_2]_{bs}$ and $[O_2]_{bs}$ are the concentrations of CO_2 and O_2 in bundle sheath chloroplasts. Symbols, definitions, values, units are listed in Table B.1 and Table B.2 (Appendix B).

4.2.2 Model of CO_2 transport inside a leaf of NADP-ME type C_4 plant

Fig. 4.1 shows the schematic representation of CO_2 transport in a C_4 leaf based on which reaction-diffusion equations for CO_2 transport in a maize leaf were formulated. Transport of various metabolites in the C_4 pathway was not explicitly modeled, for practical purposes; however, their role in the delivery CO_2 to the site of fixation was accounted for.

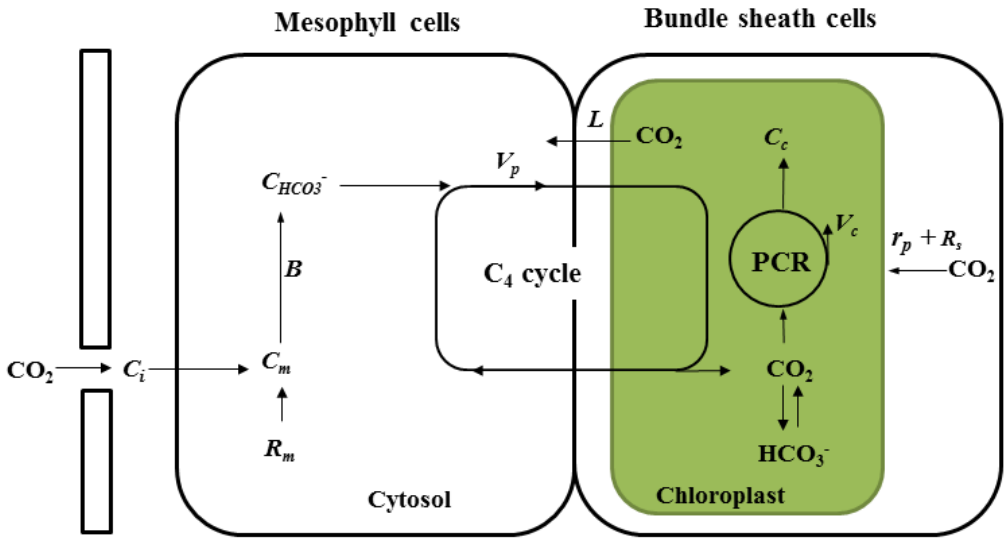

Figure 4.1. Schematic representation of the C_4 pathway of CO_2 fixation. CO_2 is hydrated to bicarbonate ions at a rate B which are then fixed to C_4 acids at rate V_p. It is assumed that at steady state, CO_2 is produced from decarboxylation of C_4 acids in bundle sheath cells at a rate V_p. In bundle sheath chloroplasts, CO_2 is fixed at a rate V_c in the photosynthetic carbon reduction (PCR) cycle, while mitochondria in the cytosol of bundle sheath cells release CO_2 through photorespiration at a rate r_p and through day respiration at a rate R_s. R_m is the rate of CO_2 release by mitochondria in the mesophyll cytosol. A difference in CO_2 concentration between bundle sheath cells (C_c) and mesophyll cells (C_m) creates diffusive leakage (L). Figure was adapted from various sources (von Caemmerer and Furbank, 1999; Leegood, 2004).

CO_2 transport in mesophyll cells

It is usually assumed that CO_2 limits the rate of PEP carboxylation (Peisker, 1979; von Caemmerer and Furbank, 1999). Consequently, V_p (Eq. B.1.1, Appendix B) is expressed using concentrations of CO_2 in the standard biochemical model (Kanai and Edwards, 1999) although the substrate is bicarbonate. Therefore, we set V_p as a sink term for CO_2 and briefly assess the consequences of these assumptions (for details see Appendix B.2). CO_2 is released by mitochondria in the mesophyll cytosol through respiration at a volumetric rate, R_m^* (hereafter, the

superscript * in symbols is used to signify a volumetric rate equivalent of a leaf area-based variable).

The reaction-diffusion equation for CO_2 in the mesophyll cytosol is given by:

$$\frac{\partial [\mathrm{CO_2}]_m}{\partial t} = \nabla \cdot \left(D_{CO_2} \nabla [\mathrm{CO_2}]_m \right) - V_p^* - B_{CA} + R_m^* \tag{4.5}$$

where ∇ is the gradient operator. D_{CO_2} is the diffusion coefficient of CO_2 in the liquid phase; V_p^* is the volumetric rate of V_p (Table B.1, Appendix B). B_{CA}, the rate of CA catalyzed hydration of CO_2 in mesophyll cytosol, is given by (Spalding and Portis, 1985; Tholen and Zhu, 2011):

$$B_{CA} = \frac{k_a X_a \cdot \left([\mathrm{CO_2}]_m - \frac{[\mathrm{HCO_3^-}]_m [\mathrm{H^+}]_m}{K_{eq}} \right)}{K_{CO_2} + \frac{K_{CO_2}}{K_{HCO_3^-}} \cdot [\mathrm{HCO_3^-}]_m + [\mathrm{CO_2}]_m} \tag{4.6}$$

where k_a is the CA turnover rate; X_a is the concentration of CA; K_{CO_2} and $K_{HCO_3^-}$ are Michaelis-Menten constants of CA hydration and dehydration, respectively; K_{eq} is the equilibrium constant for CA; $[\mathrm{HCO_3^-}]_m$ is the concentration of bicarbonate in mesophyll cytosol; and $[\mathrm{H^+}]_m$ is the concentration of H^+ ions in mesophyll cytosol (the pH of the cytosol was assumed to be 7.5 (Evans *et al.*, 2009).

The reaction-diffusion equation for bicarbonate in the mesophyll cytosol is given by:

$$\frac{\partial[\mathrm{HCO_3^-}]_m}{\partial t} = \nabla \cdot \left(D_{HCO_3^-} \nabla[\mathrm{HCO_3^-}]_m \right) + B_{CA} \tag{4.7}$$

where $D_{HCO_3^-}$ is the diffusion coefficient of bicarbonate.

CO_2 transport in bundle sheath cells

In bundle sheath chloroplasts, it is assumed that CO_2 is released from decarboxylation of C_4 acids at the same rate as the rate of PEP carboxylation (Peisker, 1979; von Caemmerer and Furbank, 1999). Therefore, the average rate of PEP carboxylation, $\bar{V}_p$ in the mesophyll cytosol (Eq. B.1.2, in Appendix B) was set equal to the mean rate of CO_2 release in bundle sheath chloroplasts. It was assumed that there is negligible CA activity in bundle sheath cells due to low CA concentrations (Ku and Edwards, 1975; Burnell and Hatch, 1988). In addition, without a model for actual transport of metabolites, a possible CO_2 release in maize bundle sheath cytosol (Pick *et al.*, 2011; Bellasio and Griffiths, 2014*c*) could not be included. Thus, CO_2 was assumed to be released in bundle sheath chloroplasts only. The reaction-diffusion equation for CO_2 in bundle sheath cells, therefore, is given by:

$$\frac{\partial[\mathrm{CO_2}]_{bs}}{\partial t} = \nabla \cdot \left(D_{CO_2} \nabla[\mathrm{CO_2}]_{bs} \right) + \bar{V}_p^* - V_c^* - B_{NCA} + R_s^* + r_p^* \tag{4.8}$$

The second and the third term on the right side of Eq. 4..8 are the volumetric rate of CO_2 release from decarboxylation of C_4 acids (Eq. B.1.3, in Appendix B) and the volumetric rate of CO_2 consumption during carboxylation of Rubisco in the chloroplasts (Table B.1, Appendix B), respectively. The fourth term B_{NCA} is the non-enzymatic CO_2 hydration rate in bundle sheath cytosol and stroma. The last two terms R_s^* and r_p^* on the right side of Eq. 4.8 are the volumetric CO_2 release through respiration (Table B.1, Appendix B) and photorespiration in the cytosol, respectively. The photorespiration in bundle sheath chloroplast was integrated over its volume but used as a source of CO_2 in the cytosol (Eq. B.1.4, in Appendix B).

B_{NCA} is given by (Ho *et al.*, 2012):

$$B_{NCA} = k_1 \cdot [CO_2]_{bs} - \frac{k_2 \cdot [HCO_3^-]_{bs} [H^+]_{bs}}{K} \tag{4.9}$$

where k_1 is the CO_2 hydration rate constant; k_2 is the CO_2 dehydration rate constant; K is the acid dissociation constant for H_2CO_3; and $[HCO_3^-]_{bs}$ is the concentration of bicarbonate in bundle sheath cells. $[H^+]_{bs}$ is calculated from pH of the bundle sheath cytosol (7.5) or stroma (7.8) (the pH values were assumed equal to those reported for cytosol and stroma of C_3 plants (Evans *et al.*, 2009)).

The reaction-diffusion equation for bicarbonate ions in the bundle sheath cells is given by:

$$\frac{\partial [HCO_3^-]_{bs}}{\partial t} = \nabla \cdot \left(D_{HCO_3^-} \nabla [HCO_3^-]_{bs} \right) + B_{NCA} \tag{4.10}$$

In NADP-ME subtype C_4 plants like maize, Photosystem II associated O_2 evolution is low (Kanai and Edwards, 1999). Consequently, a reaction-diffusion equation for O_2 was not included. Thus, concentration of oxygen in the leaf tissue was assumed equal to that in the ambient air.

The mean concentrations of CO_2, in the mesophyll cells ($\bar{C}_m$) and in the bundle sheath chloroplasts ($\bar{C}_c$), were determined by integrating the concentration over the volume (area in 2-D) of the respective compartments and divide them by the volume of these components (Eq. B.1.5 and Eq. B.1.6 respectively, in Appendix B). g_{bs} was calculated by dividing the leakage flux (Eq. B.1.7, in Appendix B) by the difference in mean CO_2 concentration between bundle sheath and mesophyll cells (Eq. B.1.8, in Appendix B).

The net rate of photosynthesis $\bar{A}$ was calculated from:

$$\bar{A} = \bar{V}_c - \bar{r}_p - R_d \tag{4.11}$$

The mean fixation of CO_2, $\bar{V}_c$, was calculated by integrating V_c (Eq. 4.2) over the bundle sheath chloroplast (using a similar expression as Eq. B.1.2, in Appendix B). R_d is the total rate of CO_2 release from the leaf through respiration. The mean photorespiration rate, $\bar{r}_p$ on leaf area basis, was calculated by integrating photorespiration over the volume of bundle sheath chloroplasts (Eq. B.1.9, in Appendix B).

4.2.3 Boundary conditions

Equations 4.5 to 4.10 describe the diffusion of CO_2 only in the liquid phase media of mesophyll and bundle sheath cells. Since diffusion in the gas phase of the intercellular air spaces could not be realistically modeled in a 2-D geometry, we assumed a uniform CO_2 concentration, equal to the measured intercellular CO_2 concentration at the outer surface of mesophyll cell wall that were exposed to intercellular air spaces. A Neumann (or insulated) boundary condition was applied at the boundary where epidermal and mesophyll cells contact since CO_2 from the atmosphere mainly enters the leaf through the stomata.

The resistance to CO_2 diffusion imposed by a cell wall was defined as the thickness of the wall divided by the effective diffusivity of CO_2 in the wall (Evans *et al.*, 2009). We assumed a value of one for tortuosity and solvent to water partitioning coefficient for CO_2 in the wall (Evans *et al.*, 2009). The contact boundaries among mesophyll cells and bundle sheath cells were modeled as a thin boundary layer with thickness of twice the thickness of both the respective cell walls and plasma membranes. The resistance of a plasma membrane was calculated as the inverse of its CO_2 permeability (Evans *et al.*, 1994).

Diffusion of CO_2 through the plasmodesmata at the mesophyll-bundle sheath interface was considered by accounting for the fraction of the interface occupied by the plasmodesmata. The flux of CO_2 per unit area of the interface $J_{CO_2,pd}$, is defined as:

$$J_{CO_2,pd} = \frac{D_{CO_2}\theta}{L_{pd}}([CO_2]_{bs} - [CO_2]_m) \tag{4.12}$$

where L_{pd} is the length of the mesophyll-bundle sheath interface and θ is the ratio of the bundle sheath surface area covered by plasmodesmata to the total area of the mesophyll-bundle sheath interface. The parameter θ quantifies the fraction of area available for CO_2 diffusion. Since leakage flux occurs mainly at the mesophyll-bundle sheath interface, an insulated boundary condition was assumed at the surface of the bundle sheath cells exposed to the intercellular air spaces (Evert *et al.*, 1977; Furbank and Hatch, 1987). We also carried out a separate simulation where leakage of CO_2 through the exposed surface was allowed to assess the role of suberin in restricting apoplastic leakage towards the air space (Text B.3, Appendix B). The diffusion of bicarbonate ions through the plasmodesmata was defined using similar expression as Eq. 4.12.

CO_2 diffuses through the envelope of bundle sheath chloroplast at a flux J_{CO_2} that is given by:

$$J_{CO_2} = -P_{CO_2} \Delta[CO_2] \tag{4.13}$$

where P_{CO_2} is the CO_2 permeability of the chloroplast envelope and $\Delta[CO_2]$ is the difference in CO_2 concentration across a membrane. In addition, the flux of bicarbonate ions through the envelopes of bundle sheath chloroplast was defined similarly. The CO_2 concentration in the gas and liquid phases were assumed to be in equilibrium, thus, Henry's law was used.

4.2.4 Gas exchange and chlorophyll fluorescence measurement

Plants, treatments and photosynthetic measurements were described in the subsection 3.2.1. We used the measurement data for the 32-day old leaf having a N content of 1.16 g m^{-2} to compare model predictions of the responses of photosynthesis.

4.2.5 Parameterization of the model

Parameters of the biochemical model of C_4 photosynthesis such as x, K_p, $K_{m,C}$ and $K_{m,O}$ were obtained from literature (Cousins *et al.*, 2010; Yin *et al.*, 2011*b*) (Table B.2, Appendix B). $V_{p,max}$ and $V_{c,max}$ could not be estimated from our gas exchange and chlorophyll fluorescence measurement data due to limitation of CO_2 fixation mainly by electron transport (for details, see

Appendix B.3 in Appendix B). However, a linear relationship between $V_{p,max}$, $V_{c,max}$ and leaf nitrogen content was reported previously (Sage *et al.*, 1987; Tazoe *et al.*, 2006). The slopes of linearity were reported for maize leaves of the same cultivar as ours to be 242.2 ± 95.3 µmol CO_2 (g N)$^{-1}$ s^{-1} and 96 ± 10.7 µmol CO_2 (g N)$^{-1}$ s^{-1} for $V_{p,max}$ and $V_{c,max}$ respectively (Yin *et al.*, 2011*b*). Our leaf N content of 1.16 g m^{-2} was higher than the base leaf N content of 0.242 ± 0.045 g N m^{-2} above which the linear relationship was assumed (Yin *et al.*, 2011*b*). Therefore, $V_{p,max}$ and $V_{c,max}$ were calculated using these values and the measured leaf N content (Table B.2, Appendix B). Parameters R_d and s' were estimated from our gas exchange measurement using the procedures of Yin *et al*. (2011b) in Microsoft Excel.

The Michaelis-Menten constant of CA for CO_2 was reported for maize (Hatch and Burnell, 1990) (Table 2). However, constants such as $K_{HCO_3^-}$, K_{eq} and the concentration of CA have not been reported. Here we used the equilibrium constants reported for spinach leaves (Pocker and Miksch, 1978) on the ground that comparable activities exist between spinach and maize (Poincelot, 1972). The concentration of CA in leaves of various C_3 plants was suggested to be between 0.14 and 0.69 mol m^{-3} (Tholen and Zhu, 2011). In our model, a default CA concentration of 0.69 mol active sites m^{-3} was assumed as mesophyll conductance is generally higher in C_4 plants than in C_3 plants (Longstreth *et al.*, 1980; Pengelly *et al.*, 2010; Yin *et al.*, 2011*b*).

The presence of CA and aquaporins in plasma membrane have been suggested to enhance the diffusion of CO_2 in mesophyll cells (Utsunomiya and Muto, 1993; Evans and Loreto, 2000; Weber and von Caemmerer, 2010). Accounting for those membrane components, the CO_2 permeability has been reported to be 1.6×10^{-2} m s^{-1} (Missner *et al.*, 2008). Since the plasma membrane of a maize leaf contains considerable CA and aquaporins (Utsunomiya and Muto, 1993; Maurel *et al.*, 2008), we adopted the aforementioned value for permeability of the plasma membrane of the mesophyll cells. It has also been proposed that aquaporins may be found to a lesser extent in the plasma membrane of the bundle sheath cells (Hatch, 1987; Weber and von Caemmerer, 2010). Thus, we assumed a CO_2 permeability of 3.5×10^{-3} m s^{-1} for plasma membrane of the bundle sheath cells (Gutknecht, 1988; Weber and von Caemmerer, 2010). The

outer and inner envelop of a chloroplast may have different permeability, although the permeability values were not reported (Weber and von Caemmerer, 2010). Here, we halved the permeability bundle sheath plasma membrane to account for the double layer. The diffusion coefficient of CO_2 in the liquid phase of the cells was assumed to be equal to that in water (Aalto and Juurola, 2002). The apparent diffusivity of CO_2 in the bundle sheath cell wall was calculated assuming an effective porosity of 0.1 (0.05-0.2 (Evans *et al.*, 2009)). Diffusion coefficient of CO_2 in pure water was used for the aqueous media filling the cell wall pores (Table B.2, Appendix B) (Evans *et al.*, 2009). We assumed that in the mesophyll cell wall, CO_2 has an apparent diffusivity equal to that of pure water to account for rapid diffusion towards cytosol expected in C_4 leaves (von Caemmerer *et al.*, 2007). This resulted in conductance of combined the mesophyll cell wall and plasma membrane of 0.25 mol m^{-2} s^{-1} which is within the range of values previously reported (Evans *et al.*, 2009). The thickness of the mesophyll cell wall was 0.16 µm, an average value reported for C_4 plants (Stata *et al.*, 2014), and the thickness of bundle sheath cell wall was assumed to be 0.4 µm (von Caemmerer and Furbank, 2003). A plasmodesmata fraction (θ) of 0.03 m^2 m^{-2} (Sowiński *et al.*, 2008) was assumed at the mesophyll-bundle sheath interface. L_{pd} was assumed equal to the sum of the thickness of the mesophyll and the bundle sheath cell wall. The role of the suberin layer around the bundle sheath cell wall exposed to air space was accounted for by the insulated boundary condition. Thus, its thickness was not explicitly included.

4.2.6 Geometry of maize leaf microstructure

Samples of maize leaf blades from the plants used in the gas exchange measurements were fixed in cold 2 % glutaraldehyde, buffered at pH 7.3 with 50 mM sodium cacodylate and 150 mM saccharose. After dehydration in a graded acetone series, tissues were embedded in Araldite and sectioned with a Leica EM UC6 ultra-microtome. Serial semi-thin sections which were 1 µm thick were stained with methylene blue and thionin, and viewed in an Olympus BX-51 microscope at 40× magnification.

The 2-D geometry of maize leaf microstructure was constructed from the light microscopic images of the 6th leaf. The image was digitized in the Matlab programming environment version

7.0 (The Mathworks, Natick, MA) by in house developed software (Mebatsion *et al.*, 2006*b*). Since CO_2 fixation by Rubisco is assumed to be restricted to bundle sheath cells only (Kanai and Edwards, 1999) and CO_2 assimilation by PEPc occurs in the cytosol, chloroplast layers in mesophyll cells were not included in the geometry. Clusters of bundle sheath chloroplasts were digitized as layers of chloroplasts (Fig. B.5.1, Appendix B). Plasmodesmata was accounted for in the calculation of the apparent diffusivity of CO_2 through the mesophyll-bundle sheath interface. Preliminary results showed that the vacuole did not affect the rate of photosynthesis. It was, therefore, not included in the leaf microstructure geometry.

4.2.7 Numerical solution

The CO_2 transport model equations were solved by the finite-element method. Eq. 4.5 to Eq. 4.10 were discretized over the 2-D geometry of leaf microstructure (Fig. B.6.1, Appendix B). The resulting equations were solved at a steady-state condition using Matlab (The Mathworks, Inc., Natick, USA) integrated with Comsol Multiphysics vs. 3.5 (Comsol AB, Stockholm). Simulations of the response of photosynthesis to changes in CO_2 and light intensity were carried out.

4.3 Results

4.3.1 Comparison of model predictions of photosynthesis with experimental data

Fig. 4.2 shows the model predicted and the measured responses of net photosynthesis to irradiance and intercellular CO_2 concentration.

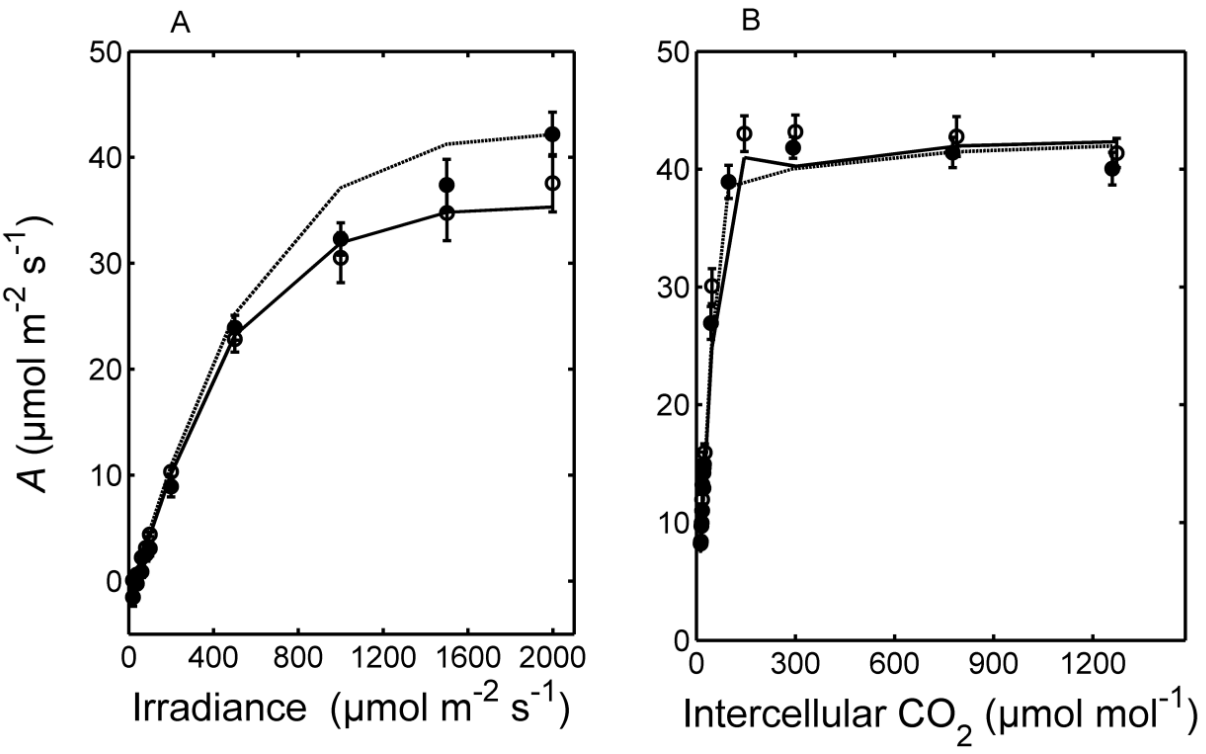

Figure 4.2. Simulated response of rate of photosynthesis (*A*) to changes in irradiance (panel A) and intercellular air space CO_2 concentrations (panel B). For the irradiance response curve, ambient CO_2 was 250 µmol mol^{-1} for 21 % O_2 and 1000 µmol mol^{-1} for 2 % O_2. For the CO_2 response curve, irradiance was 1500 µmol m^{-2} s^{-1} for 21 % and 2 % O_2. Symbols indicate measurement values and curves show model predicted values. 2 % O_2 (open symbols, dashed curve) and 21 % O_2 (filled symbols, solid curves). The bars indicate the standard error, n = 4.

In general, the simulations agreed with the experimental data. However, the light response curve of photosynthesis at 2 % O_2 for high light intensities was overestimated by the model. This

discrepancy was due to *s'* determined only from low light intensities and was assumed to be constant for the high light levels also (for details, see Text B.5 in Appendix B). In Fig. 4.2A, the rates of photosynthesis at high light intensities (measured or predicted) were higher at 2 % O_2 than at 21 % O_2 since at the ambient CO_2 was 1000 µmol mol^{-1} at 2 % O_2 and 250 µmol mol^{-1} at 21 % O_2.

4.3.2 Microscale CO_2 concentration profile

Biochemical CCM results in an elevated CO_2 in bundle sheath cells: this is shown in the computed microscale CO_2 concentration profile in Fig. 4.3 (C_a = 380 µmol mol^{-1}, I_{inc} = 1500 µmol m^{-2} s^{-1} and 21 % O_2). Consequently, the ratio $\bar{C}_c / \bar{C}_m$ was found to be 17 while the CO_2 leakage flux was about 11 % of the net photosynthesis rate.

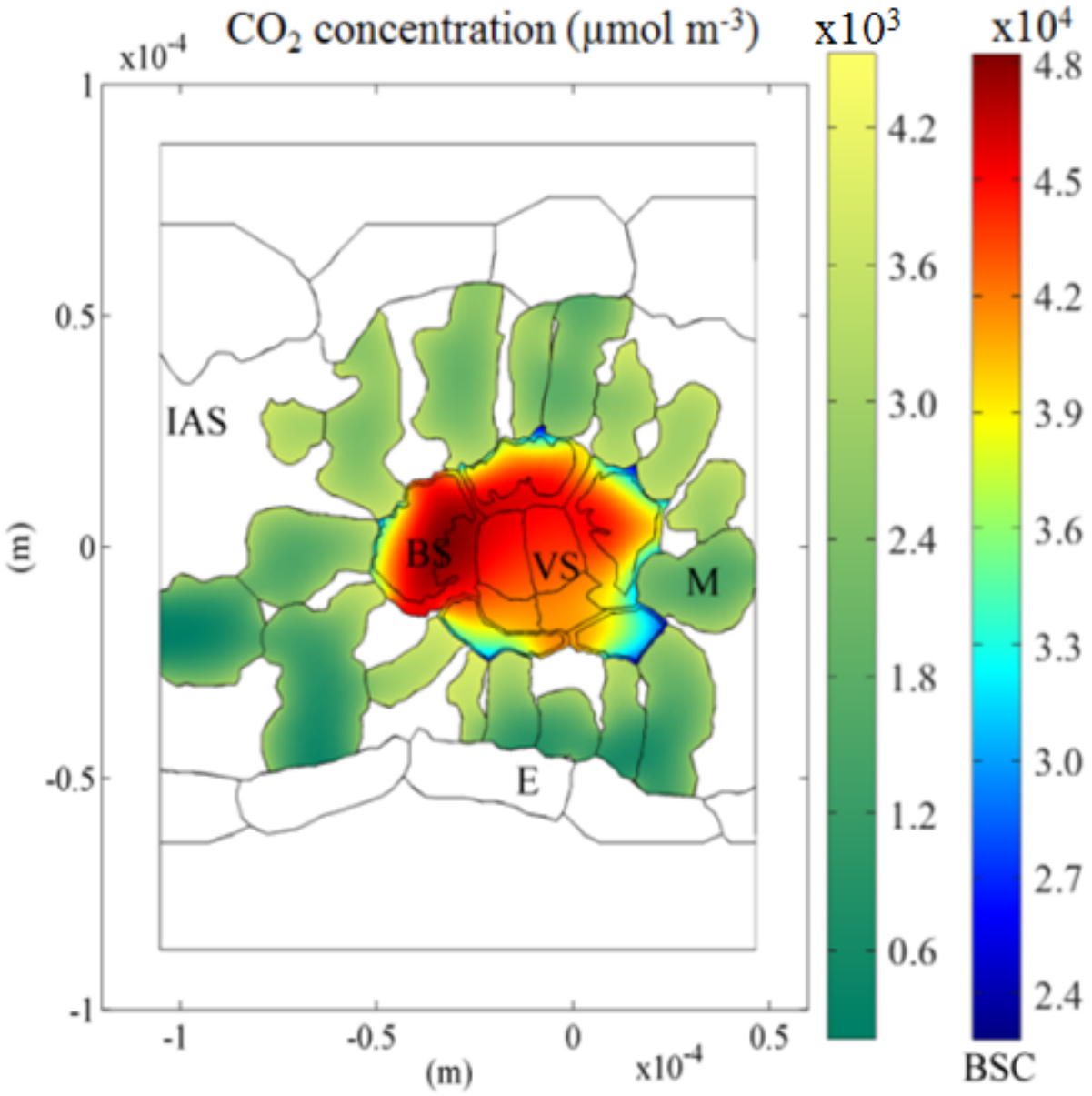

Figure 4.3.Carbon dioxide concentration profile in the leaf tissue (C_a = 380 µmol mol^{-1}, intercellular CO_2 = 145.38 µmol mol^{-1}, irradiance= 1500 µmol m^{-2} s^{-1}, temperature =25 °C). The color bar labeled BSC (bundle sheath CO_2concentration) corresponds to the CO_2 profile in bundle sheath cells. Separate color bars are used for the purpose of clarity as the high concentrations in bundle sheath cells mask the concentration profile in mesophyll cells if the same color bar would be used.BS: bundle sheath; E: epidermis; IAS: intercellular air space; M: mesophyll; VS: vasculature.

The computed g_{bs} was 3.52×10^{-3} mol m^{-2} s^{-1}. Furthermore, we also examined the responses of leakiness (Eq. B.1.10, in Appendix B) and $\bar{C}_c$ to changes in intercellular CO_2 and irradiance (Fig. 4.4) to test whether the model could predict the trends reported in the literature (von Caemmerer and Furbank, 1999; Kromdijk *et al.*, 2010; Yin *et al.*, 2011*b*).

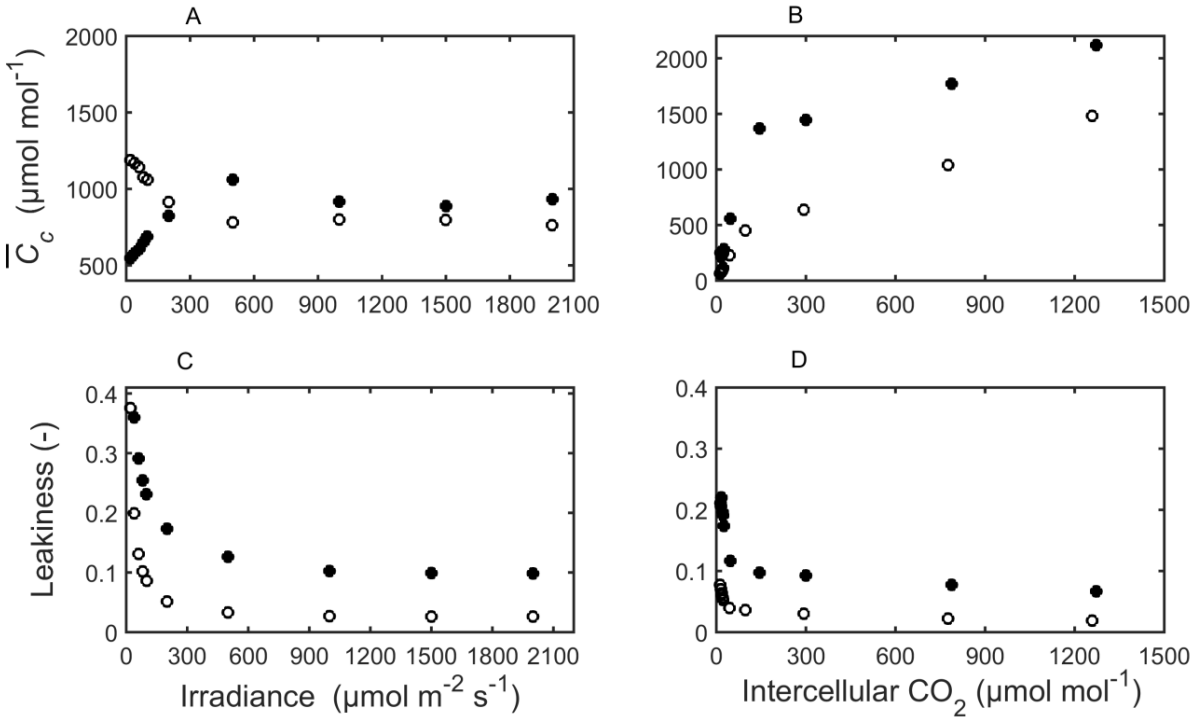

Figure 4.4. Simulated response of mean CO_2 concentration in bundle sheath chloroplasts ($\bar{C}_c$) (top; A, B) and leakiness (bottom; C, D) to changes in irradiance (left; A, C) and intercellular air space CO_2 concentrations (right; B, D). For CO_2 responses, irradiance was 1500 µmol m^{-2} s^{-1} at 21 % and 2 % O_2. For irradiance responses , C_a was 250 µmol mol^{-1} at 21 % O_2 or 1000 µmol mol^{-1} at 2 % O_2. Open symbols represent 2 % O_2 while filled symbols represent 21 % O_2. Leakiness was calculated using Eq. B.1.10, in Appendix B.

There was a rise in $\bar{C}_c$ (Fig. 4.4; A, B) with an increase in CO_2 availability while it remained largely stable at high irradiances (500 µmol m^{-2} s^{-1} and higher). In Fig 4.4 (A, B), $\bar{C}_c$ was higher at 21 % O_2 than at 2 % O_2 due to photorespiration. Fig. 4.4 (C, D) also shows that the leakiness

was high at low irradiances or low intercellular CO_2. At high irradiance or intercellular CO_2, however, leakiness decreased and became stable. Moreover, in Fig. 4.4A at 2 % O_2 , except at very low light intensities, $\bar{C}_c$ dropped below the ambient CO_2 concentration of 1000 µmol mol^{-1} similar to findings of a previous study (Yin *et al.*, 2011*b*).

4.3.3 Physical barriers at air space-mesophyll interface

Fig. 4.5 shows that both the rate of photosynthesis and bundle sheath conductance were highly sensitive to the apparent diffusivity of CO_2 in the mesophyll cell wall and the CO_2 permeability of the plasma membrane of mesophyll cells. Assuming an effective diffusivity of CO_2 in the mesophyll cell wall that was 0.2 times the diffusion coefficient of CO_2 in pure water at 25 °C (Evans *et al.*, 2009) and the commonly used membrane permeability of 3.5×10^{-3} m s^{-1}, only about 80 % of the measured photosynthesis rate could be achieved. Fig. 4.5A also shows that higher permeability values could not increase the predicted rate photosynthesis. Fig. 4.5B also shows that the effective diffusivity of CO_2 in the cell wall has a larger effect than the permeability. When the permeability was assumed to be less than 3.5×10^{-3} m s^{-1} or the porosity was less than 0.2, the bundle sheath conductance (Eq. A.8, in Appendix A) increased by about 10 fold (Fig. 5; C, D) due to a low $\bar{C}_m$ elevating $\bar{C}_c$ / $\bar{C}_m$.

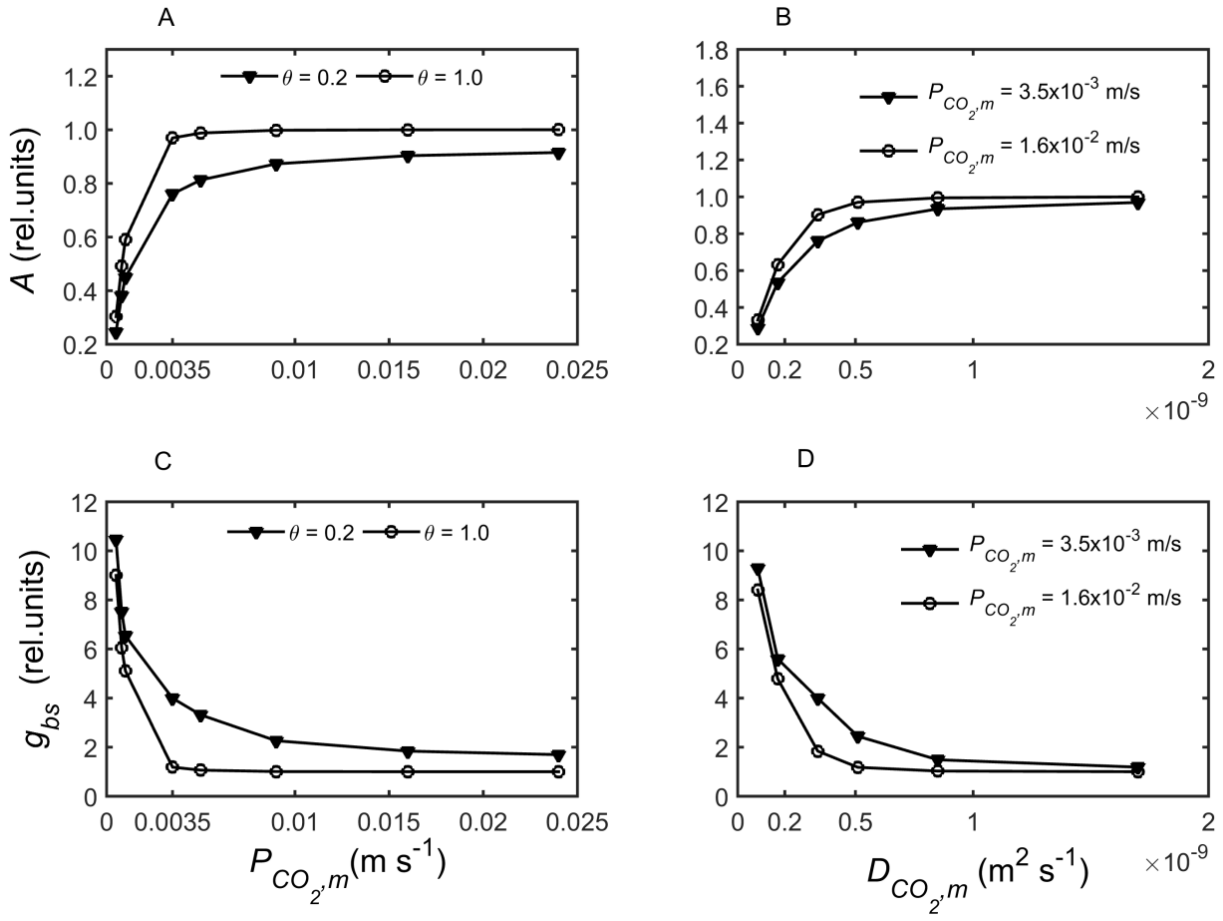

Figure 4.5. Sensitivity of photosynthesis (*A*) (top; A, B) and bundle sheath conductance (g_{bs}) (bottom; C, D) to changes in the CO_2 permeability of mesophyll (m) plasma membrane $P_{CO_2,m}$ (A, C) and apparent diffusivity of CO_2 in mesophyll cell wall ($D_{CO_2,m}$) (B, D). The responses were evaluated for two effective porosities of the mesophyll cell wall (A, C) and for two $P_{CO_2,m}$ values (B, D). Conditions for simulation were: C_a = 380 µmol mol^{-1}, irradiance = 1500 µmol m^{-2} s^{-1} and 21 % O_2. Relative values were calculated by dividing *A* and g_{bs} with their default value (g_{bs} = 3.52×10^{-3} mol m^{-2} s^{-1}, *A* = 40 µmol m^{-2} s^{-1}).

4.3.4 Resistances to CO_2 retro-diffusion

Resistances imposed by microstructural components along the CO_2 retro-diffusion pathways were calculated for the condition of C_a of 380 µmol mol^{-1}, I_{inc} of 1500 µmol m^{-2} s^{-1} and 21 % O_2, by dividing the difference in average concentrations across a compartment by the leakage flux expressed per leaf area (Table 4.1). The resistances calculated in this way are apparent as they depend on conditions of CO_2 and irradiance. Table 4.1 shows that the mesophyll-bundle sheath interface imposes a considerable resistance to diffusive leakage of CO_2 (213 m^2 s mol^{-1}) followed by stromal resistance (33 m^2 s mol^{-1}) consistent with a previous report (von Caemmerer and Furbank, 2003).

Table 4.1. Resistances (m^2 s mol^{-1}) to CO_2 diffusion in each liquid phase compartment in bundle sheath cells, calculated from a microscale model (C_a = 380 µmol mol^{-1}, I_{inc} = 1500 µmol m^{-2} s^{-1} and 21% O_2). The resistances were calculated by dividing the difference in average concentration across a compartment by the leakage flux expressed per leaf area (Eq. B.1.7, in Appendix B). Values in brackets show the percentage contribution of the individual resistances to the total resistance.

Microstructure component	**Resistance (m^2 s mol^{-1})**
Mesophyll-bundle sheath interface	212.70 (75.0 %)
Chloroplast envelope	6.98 (2.5 %)
Cytosol	31.80 (11.2 %)
Stroma	32.57 (11.5 %)
Total	284.06 (100 %)

The CO_2 permeability of the bundle sheath chloroplast envelope affected both the rate of photosynthesis and g_{bs} (Fig. 4.6; A, C). At the low end of the permeability, g_{bs} was more sensitive than photosynthesis. The permeability of the bundle sheath chloroplast envelope to bicarbonate ions had no influence on photosynthesis and bundle sheath conductance (Fig. B.4.2; A, C,

Appendix B). CO_2 leakage occurs through the plasmodesmata abundant at the mesophyll-bundle sheath interface. Fig. 4.6B and Fig. 4.6D respectively show that the rate of photosynthesis and g_{bs} were strongly affected when the area of plasmodesmata per unit area of the interface, θ, was changed. For θ of 0.8 % (Sowiński *et al.*, 2008), g_{bs} decreased by 73 % while photosynthesis changed by 5 %.

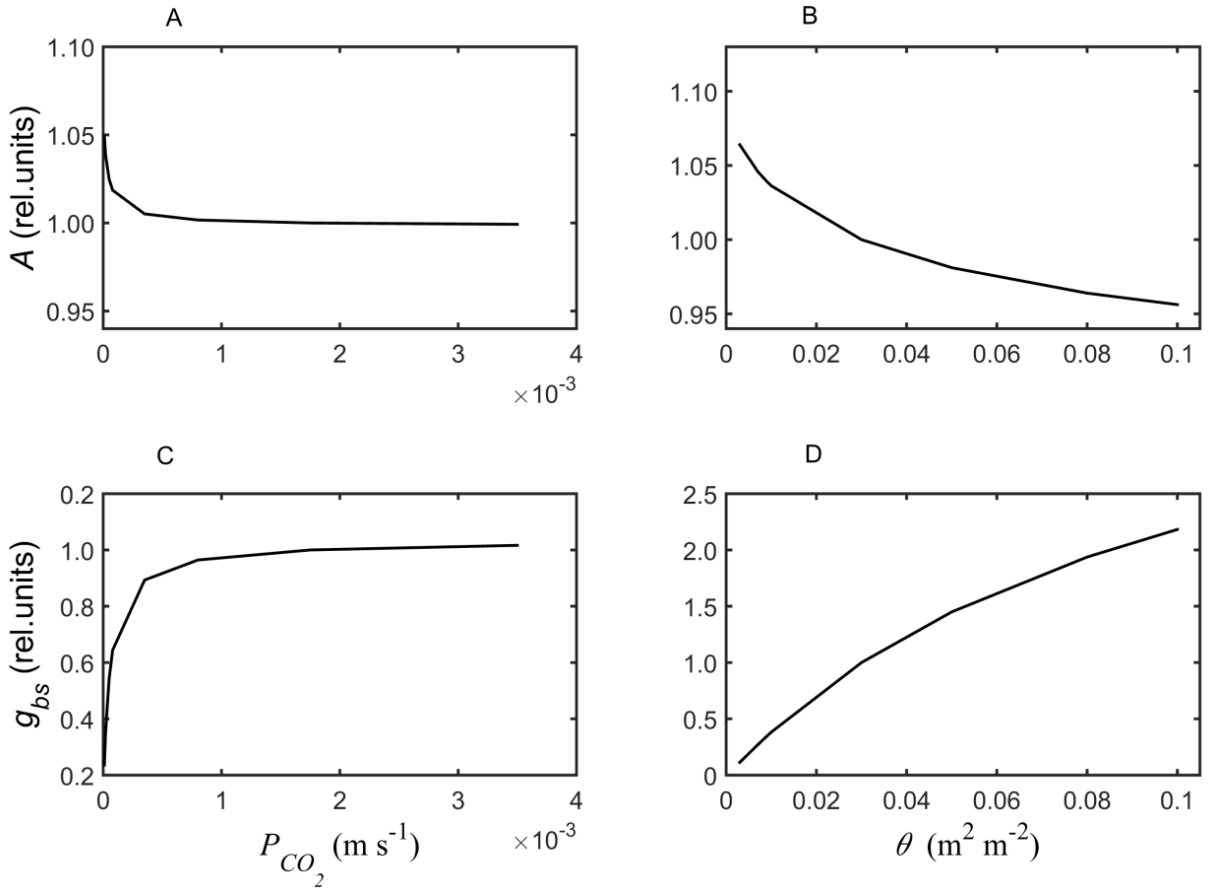

Figure 4.6. Sensitivity of photosynthesis (A) (top; A, B) and bundle sheath conductance (g_{bs}) (bottom; C, D) to changes in the CO_2 permeability of bundle sheath chloroplast envelope (P_{CO_2}) (left; A, C) and the area of plasmodesmata per surface area of bundle sheath cells (θ) (right; B, D). Conditions for simulation were: C_a = 380 µmol mol^{-1}, irradiance = 1500 µmol m^{-2} s^{-1} and 21 % O_2. Relative values were calculated by dividing A and g_{bs} with their default value (g_{bs} = 3.52 10-3 mol m^{-2} s^{-1}, A = 40 µmol m^{-2} s^{-1}).

Fig. 4.7 (A, C) shows the effect of changing the cell wall thickness of bundle sheath cells on the rate of photosynthesis and bundle sheath conductance. The bundle sheath cell wall constitutes the largest fraction of the total length of the mesophyll-bundle sheath interface assumed in our model. When the thickness of the cell wall increased (L_{pd} increased), the rate of photosynthesis increased and the bundle sheath conductance decreased.

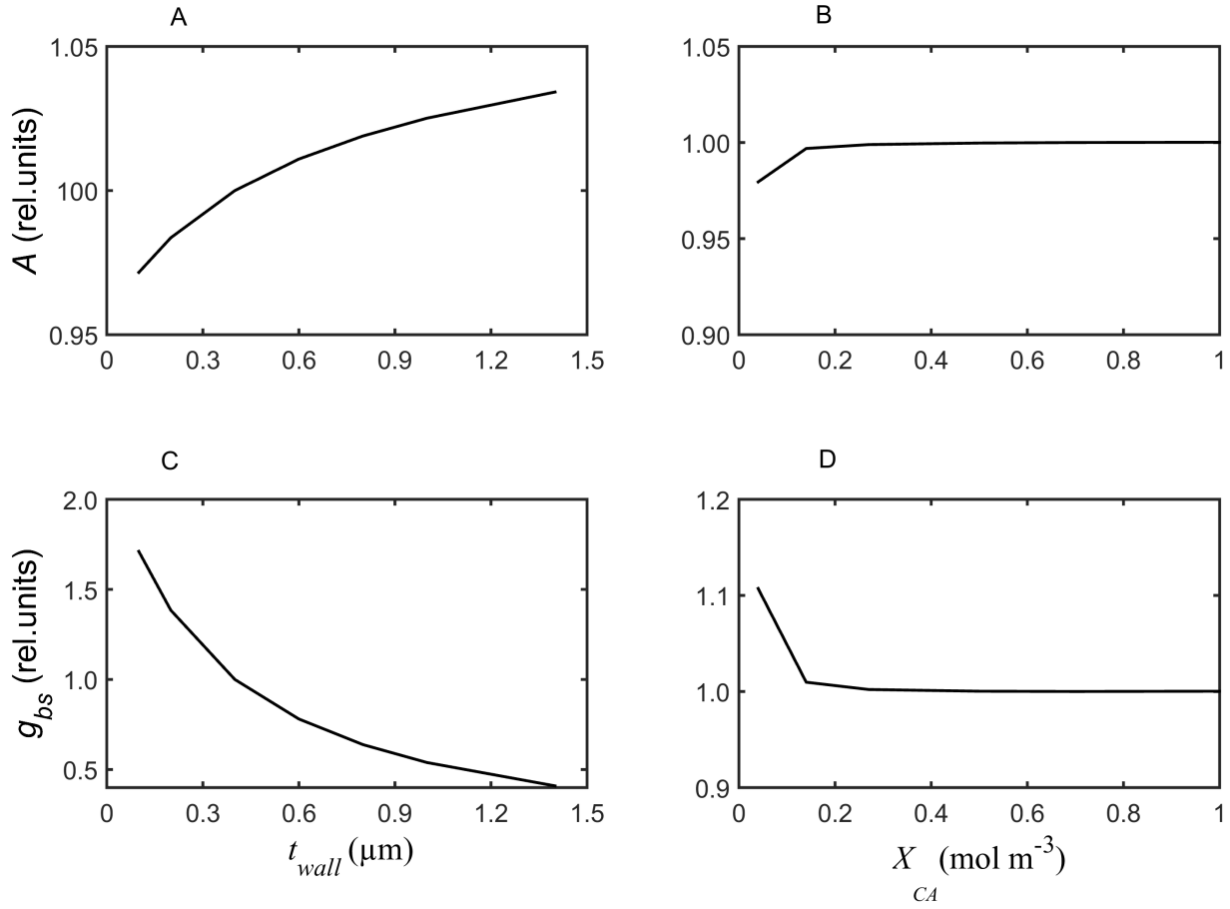

Figure 4.7. Sensitivity of photosynthesis (top; A, B) and bundle sheath conductance (g_{bs}) (bottom; C, D) to the thickness of bundle sheath cell wall (t_{wall}) (A, C) and concentration of CA in mesophyll cells (B, D). Conditions for simulation were: C_a = 380 µmol mol^{-1}, irradiance = 1500 µmol m^{-2} s^{-1} and 21 % O_2. Relative values were calculated by dividing A and g_{bs} with their default value ($g_{bs} = 3.52 \times 10^{-3}$ mol m^{-2} s^{-1}, A = 40 µmol m^{-2} s^{-1}).

For thickness of the cell wall that is 1.44 µm (Rezvani Moghaddam and Wiliman, 1998), g_{bs} decreased by 60 % while photosynthesis changed by less than 5 %.

The fraction of surface of bundle sheath cells exposed to the intercellular air spaces to the total surface of bundle sheath cells measured from the digitized leaf microstructures was 0.34. When the suberin at this surface was assumed to allow for leakage of CO_2 to the air space, the leakage rate increased by a factor of two compared to the rate at which the suberin restricted diffusive leakage through the exposed surface (calculated at C_a = 380 µmol mol^{-1} and irradiance = 1500 µmol m^{-2} s^{-1}). Consequently, $\bar{C}_c$ decreased by about 30 % and the predicted net photosynthesis rate dropped by 12 %.

4.3.5 Effects of the ratio of $V_{p,max}$ to $V_{c,max}$

The relative capacity of the C_4 and the C_3 cycle, $V_{p,max} / V_{c,max}$, varies from two to eight (von Caemmerer and Furbank, 1999). Both the rate of photosynthesis and g_{bs} (calculated at C_a = 380 µmol mol^{-1}, I_{inc} = 1500 µmol m^{-2} s^{-1}) decreased (Fig. B.4.2; B, D, Appendix B) when the $V_{p,max} / V_{c,max}$ was increased. Increasing $V_{p,max} / V_{c,max}$ at a constant $V_{p,max}$ was the same as reducing the $V_{c,max}$ which decreased the rate of photosynthesis and increased leakage as a result of increased $\bar{C}_c$. Consequently, the calculated bundle sheath conductance (Eq. B.1.8, in Appendix B) decreased (Fig. B.4.2; D, in Appendix B). Moreover, $V_{p,max} / V_{c,max}$ greater than three increased the rate of leakage. Similarly, through modeling, it has been shown that $V_{p,max}$ to $V_{c,max}$ ratios greater than four would produce the same result (von Caemmerer and Furbank, 1999).

4.3.6 Effects of CA in mesophyll and bundle sheath

The predicted photosynthesis was not sensitive to the assumed concentration of CA in mesophyll cells (Fig. 4.8B) while the bundle sheath conductance increased by 10 % for very low concentration of CA (Fig. 4.8D). We also examined the role of CA on CCM by doing simulations with and without CA (Fig. 4.8). The results show that the predicted rate of photosynthesis (Fig.

4.8A) and $\bar{C}_c$ (Fig. 4.8C) were highly affected except when the ambient CO_2 level was high (1000 µmol mol^{-1} or higher). To evaluate the effect of CA present in bundle sheath chloroplasts, simulations with assumed CA concentration values were additionally carried out at C_a of 380 µmol mol^{-1} and irradiance of 1500 µmol m^{-2} s^{-1}) (Fig. 4.8; B, D).

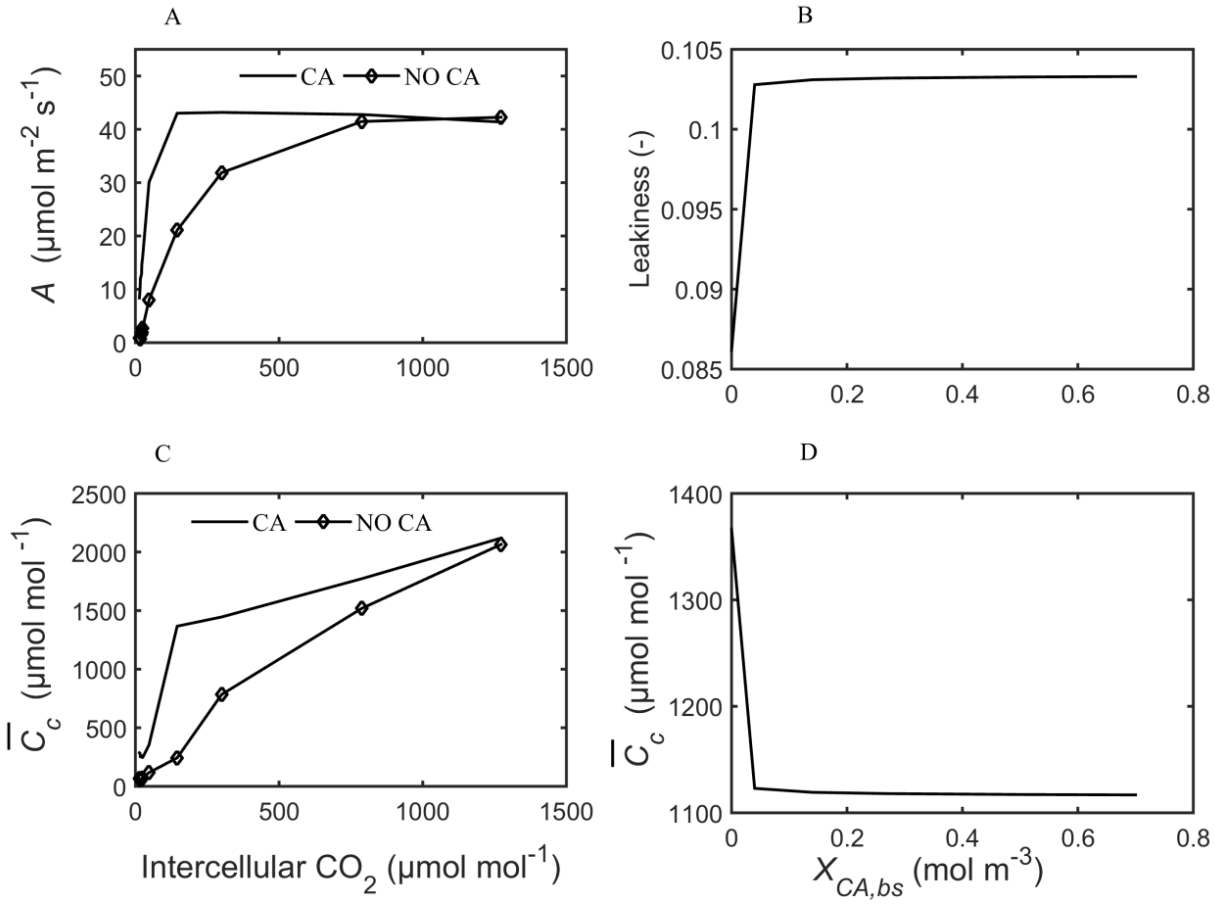

Figure 4.8. Effect of carbonic anhydrase on the rate of photosynthesis (top; A) and mean CO_2 concentration in bundle-sheath cells (bottom; C). The effect of concentration of carbonic anhydrase ($X_{CA,bs}$) in bundle-sheath (bs) cells on leakiness (top; B) and mean CO_2 concentration in bundle-sheath cells (bottom; D). Conditions for simulation in panels B and D were: C_a = 380 µmol mol^{-1}, irradiance = 1500 µmol m^{-2} s^{-1} and 21 % O_2.

In bundle sheath cells, the presence of low CA activity decreased $\bar{C}_c$ by 18 % (Fig. 4.8D) and increased leakiness by 17 % (Fig. 4.8B) resulting in 30 % higher g_{bs}. However, the net photosynthesis rate was not affected by the presence of CA (< 3%). Further increases in CA concentration did not dramatically change the leakiness and $\bar{C}_c$.

4.4 Discussion

4.4.1 A reaction-diffusion model is able to predict important CCM parameters well

Microscale models that account for the actual microstructure of plant organs have demonstrated their potential to investigate gas transport (Ho *et al.*, 2009, 2011, Verboven *et al.*, 2012, 2013, 2014), water transport in fruit (Fanta *et al.*, 2014) and photosynthetic gas exchange in C_3 plant leaves (Ho *et al.*, 2012, 2016). Here, we have developed and applied such a model for the first time in the context of photosynthesis of C_4 plants to quantify the importance of leaf microstructural features on the CO_2 transport, thus, CCM. Our model allowed mechanistic understanding of retro-diffusion and bundle sheath conductance in contrast to previous C_4 models that estimate lumped conductances (He and Edwards, 1996; Yin *et al.*, 2011*b*). The microstructure geometry implemented in our model is much more realistic in capturing the intricate features of the Kranz-anatomy than concentric cylinder approximation used previously (Hatch and Osmond, 1976). Our approach does not require assumptions about volumes of cell compartments essential in models using flux analysis (Jenkins *et al.*, 1989*b*; Wang *et al.*, 2014*b*) and a predefined effective diffusion path length in organelles such as chloroplasts (von Caemmerer and Furbank, 2003).

The model predicted responses of photosynthesis to changes in CO_2 and irradiance compared well with experimental data. It should be noted that the curves were not smooth because J_{ATP} (Eq. B.1.1, in Appendix B) calculated from chlorophyll fluorescence measurements was used in the model instead of the non-rectangular hyperbolic irradiance response of electron transport. In addition, the predicted decline of leakiness with increased irradiance (Fig. 4.4C) was consistent

with previous observations (Kromdijk *et al.*, 2010; Ubierna *et al.*, 2013). The decrease of leakiness with increased CO_2 (Fig. 4.4A) has been suggested to be due to the regulation of rates of the C_4 and C_3 cycle being accounted for by the use of experimentally determined J_{ATP} as a model input (Yin *et al.*, 2011*b*). The computed bundle sheath conductance is within the range of values reported for maize (Yin *et al.*, 2011*b*; Bellasio and Griffiths, 2014*c*). Moreover, the predicted responses of the concentration of CO_2 in bundle sheath cells during steady state photosynthesis for various ambient CO_2 and irradiance levels agreed with previous reports (von Caemmerer and Furbank, 1999; Yin *et al.*, 2011*b*). Therefore, the model could predict important parameters of CCM: bundle sheath conductance, leakiness and mean CO_2 concentration in bundle sheath cells over ranges of ambient CO_2 and irradiance levels. The model was subsequently used to evaluate the effect of a model parameter on photosynthesis and bundle sheath conductance. The bundle sheath conductance in this study is considered as the diffusion conductance between mesophyll cytosol, where CO_2 is assimilated, and the bundle sheath chloroplast, where CO_2 released from decarboxylation of C_4 acids (Eq. B.1.8, in Appendix B).

4.4.2 The mesophyll cell wall is the most significant limitation to CO_2 conductance

Rapid transport of CO_2 from the air spaces to mesophyll cytosol is essential for CCM in C_4 crops (Leegood, 2002; von Caemmerer *et al.*, 2007; Weber and von Caemmerer, 2010). In line with this, our results suggest that the diffusive properties of the interface between the air spaces and mesophyll cells may considerably constrain the rate of photosynthesis. In particular, the apparent diffusivity of CO_2 in the mesophyll cell wall was critical. For instance, using the highest value of effective porosity reported (0.05 – 0.2 (Evans *et al.*, 2009)), the rate of photosynthesis was underestimated. Additionally, if the porosity of the cell wall was assumed to be as low as 0.05 (Evans *et al.*, 2009), irrespective of the membrane permeability (see Fig. 4.5B), the predicted rate of photosynthesis was very low due to elevated diffusive resistance to CO_2 by the wall. These findings also imply that the presence of only cell wall and plasma membrane along the CO_2 diffusion pathway towards mesophyll cytosol does not necessarily result in high mesophyll conductance in C_4 plants. Furthermore, a previous study (von Caemmerer *et al.*, 2007)

commented that a combined conductance of cell wall and plasma membrane of 0.14 mol m^{-2} s^{-1} could be enough to get a rapid flux of CO_2 towards the mesophyll cytosol in C_4 plants (von Caemmerer *et al.*, 2007). However, we found that only a conductance of about 1.8 times the aforementioned one could explain the rate of photosynthesis that we measured well. Such a high conductance was obtained partly by assuming a CO_2 permeability of plasma membrane in the higher range of values reported previously (Evans *et al.*, 2009). In fact, the plasma membrane of maize leaf contains a substantial amount of CA (Utsunomiya and Muto, 1993), which is proposed to contribute to CO_2 diffusion (Evans *et al.*, 2004; Weber and von Caemmerer, 2010). In addition, the permeability value also lumps membrane components such as aquaporins for which there is a growing evidence that they may facilitate CO_2 transport in air space-mesophyll interface (Maurel *et al.*, 2015). By contrast, a CO_2 permeability two orders of magnitude lower than our model value reported previously (Uehlein *et al.*, 2008), if existent *in vivo* for mesophyll plasma membrane of maize, would not enable operation of CCM. Nevertheless, the diffusivity of CO_2 in the cell wall and permeability of membranes are less well known (Evans *et al.*, 2009). More research on these properties will improve our understanding of CO_2 diffusion in leaves as has been also highlighted recently (Raven and Beardall, 2016). Overall, not only fewer resistances but also enhanced diffusive properties of the air space-mesophyll interface may be essential for the high rate of CO_2 transport, thus effective CCM.

4.4.3 CO_2 retro-diffusion in maize leaf may mainly be constrained by plasmodesmata

The pathway of CO_2 leakage by diffusion in a maize leaf is complicated by several physical barriers such as the stroma, chloroplast envelope, cytosol, plasma membrane, cell wall, suberin and plasmodesmata. It is believed that the extensive connection of mesophyll and bundle sheath cells (Weiner *et al.*, 1988; Botha, 1992) through plasmodesmata provides the main pathway to leakage (Hattersley and Browning, 1981; Furbank and Hatch, 1987; Sowiński *et al.*, 2008). Our analysis shows that the mesophyll-bundle sheath interface provides a major resistance to the CO_2 retro-diffusion (See Table 4.5.1), indicative of the substantial importance of the abundance of plasmodesmata at this interface. In addition, the computed bundle sheath conductance (Fig. 4.7)

was highly sensitive to the thickness of bundle sheath cell wall, which influences the diffusion length through the plasmodesmata. Furthermore, the area of plasmodesmata available for transport may be one to two orders of magnitude less than 3 % of the mesophyll-bundle sheath interface assumed in our model (Sowiński *et al.*, 2008). In this case, our simulations suggest that lower plasmodesmata fractions could be beneficial for high rate of photosynthesis; however, this must be interpreted with caution as the metabolite transport might be constrained. For instance, Wang *et al*. (2014b) showed through modeling that the benefit of a reduced plasmodesmata fraction depends on length of the mesophyll-bundle sheath interface. Moreover, the CO_2 conductance of the interface was one to two order of magnitude lower than the values of mesophyll conductance in C_3 plants (Flexas *et al.*, 2008). This implies that introduction of C_4 pathway of photosynthesis in C_3 plants (Sheehy *et al.*, 2007) especially in one cell compartment may require high CO_2 retro-diffusion resistance for an efficient CCM (von Caemmerer and Furbank, 2003).

The bundle sheath conductance was reported to be scale positively with leaf nitrogen content (Yin *et al.*, 2011*b*). A previous study (Botha, 1992) found a positive correlation between abundance of plasmodesmata and the rate of photosynthesis. In addition, maize also adjusts the number of plasmodesmata at the mesophyll-bundle sheath interface to maintain a high rate of photosynthesis in response to growth temperature and irradiance (Sowiński *et al.*, 2003, 2007). Our results also show that an increased plasmodesmata fraction led to a higher bundle sheath conductance. Based on these, the reported increase in bundle sheath conductance, thus less effective CCM, with leaf nitrogen (Yin *et al.*, 2011*b*) (see also Chapter 3) might be due to the requirement of more plasmodesmata to accommodate a greater metabolite flux. Moreover, Yin *et al*. (2011*b*) hypothesized that the variation of bundle sheath conductance with leaf nitrogen content may be due to the effect of nitrogen on the wall thickness of the bundle sheath cells. Our results show that the thickness strongly influences the computed bundle sheath conductance (Fig. 4.7D) supporting the hypothesis of Yin *et al*. (2011*b*). In addition, g_{bs} was found to be negatively correlated with cell wall thickness (Chapter 3) although cell wall thickness was not statistically different among many of the leaf types discussed in Chapter 3 (Subsection 3.3.3).

The suberin layer in NADP-ME type C_4 plants is suggested to restrict the apoplastic diffusion pathway of CO_2 leakage (Dengler and Nelson, 1999; von Caemmerer *et al.*, 2007). It is also reported that C_4 plants lacking suberin compensated for it by releasing CO_2 in their bundle sheath cell remotely so that the leakage path is long (von Caemmerer and Furbank, 2003) or by minimizing the contact of bundle sheath surface with intercellular air spaces (Dengler *et al.*, 1994). Consistent with these views, we found that the suberin layer at the exposed surface of bundle sheath cells reduced retro-diffusion of CO_2 directly to intercellular air space considerably since 34 % of the wall area of bundle sheath cells was rendered impermeable by suberin layer. When it is assumed that the suberin layer at the mesophyll-bundle sheath interface is fully permeable, the porosity of the interface would be 0.1, which is the mean value of cell wall porosity reported previously (Evans *et al.*, 2009). In this case, the bundle sheath conductance increased drastically through high rate of leakage while photosynthesis changed by about 5 % (Fig. 4.6B; D). This implies that if permeability of suberin shown for tracer dyes (Eastman *et al.*, 1988) is also valid for CO_2, effectiveness of CCM would be reduced due to highly increased leakage. In general, therefore, a suberin layer may contribute to high rate of photosynthesis by allowing the bundle sheath cells to retain the accumulated CO_2.

4.4.4 CA is essential for high rate of photosynthesis at low intercellular CO_2

CA resides alongside PEPc in the mesophyll cytosol, contributing to a strong sink for CO_2, thereby leading to rapid CO_2 diffusion at the interface between air spaces and mesophyll cells of C_4 plants (Evans and von Caemmerer, 1996; von Caemmerer *et al.*, 2007). The low rates of photosynthesis in the absence of CA at low intercellular CO_2 concentrations (Fig. 4.8) confirms the suggestion in previous reports (Hatch and Burnell, 1990; Studer *et al.*, 2014). However, the substantial decline of the predicted rate of photosynthesis at our ambient CO_2 was not observed in a recent study on the role of CA in maize leaf for comparable ambient CO_2 (Studer *et al.*, 2014). This could be explained by large differences in our measured photosynthesis, which was about twice more, thus requiring higher CO_2 availability, than the experimental values at the ambient CO_2 in the later study. Furthermore, our simulation results indicated that CA activity in bundle sheath cells would decrease the CO_2 concentration and increase leakiness. These predictions

support the view that the presence of CA in the bundle sheath cells would reduce the effectiveness of CCM (Burnell and Hatch, 1988; Badger and Price, 1994).

4.5 Conclusion

The 2-D model presented here is an important first step towards microscale models explicitly incorporating a realistic leaf microstructure of a C_4 plant. It could be used to analyze the effect of leaf microstructure on the biochemical CCM, thus C_4 photosynthesis. However, there are limitations worth noting. The 2-D leaf geometry assumes that the leaf is infinitely long on the paradermal direction; it could not fully capture the 3-D nature of gas diffusion in leaves. Moreover, diffusion of CO_2 through the stomata and intercellular air spaces could not be realistically modeled using a 2-D geometry as it is impossible to include the distribution of stomata and the extent of connectivity of air spaces. Instead, we assumed uniform intercellular CO_2 concentration treating the air spaces as fully connected. This assumption may be true in thin and porous leaves (Parkhurst, 1994). It has also been shown that abaxial and adaxial air spaces could be separated in maize leaves (Long *et al.*, 1989). Furthermore, the photon flux in the leaf was assumed constant. However, light gradients exist in a maize leaf and mesophyll cells shade the deeper bundle sheath cells (Evans *et al.*, 2007), ultimately affecting the ATP partitioning between mesophyll and bundle sheath cells and the CO_2 fixation (Bellasio and Griffiths, 2014*b*). In addition, the quantum efficiency may not be uniform in a leaf as implied by our use of a constant electron transport rate calculated from chlorophyll fluorescence measurements (Terashima *et al.*, 2009). These limitations could be dealt with by using a realistic 3-D geometry (Verboven *et al.*, 2015), and combining a CO_2 transport and light penetration model in future research.

5 A three-dimensional model of gas transport and light propagation improves mechanistic understanding of C_4 photosynthesis

This chapter is based on:

Retta M., Ho Q.T., Yin X., Watte R., Berghuijs H.N.C., Struik P.C., Verboven P., Saeys W., Nicolai, B.M. (2016). A three-dimensional model of gas transport and light propagation improves mechanistic understanding of C_4 photosynthesis. Submitted.

5.1 Introduction

In Chapter 4, a two-dimensional microscale model of CO_2 transport was developed. The significance of leaf anatomical and biochemical factors was investigated in addition to verifying the possibility of combining leaf microstructure and gas transport at tissue level for photosynthesis of C_4 plants. Next, the shortcomings of a two-dimensional model were identified. In Chapter 5, these will be addressed by developing a full three-dimensional model of gas transport.

Mechanistic understanding of C_4 photosynthesis as provided by models helps to unravel potential bottlenecks of photosynthesis efficiency in C_4 plants due to the phenomenon of CO_2 leakage (Kromdijk *et al.*, 2008; Bellasio and Griffiths, 2014*c*) and to examine the responses of photosynthesis and growth to environmental conditions such as low temperature, low light intensity, rapid and momentary increases in light intensity by sunflecks, and elevated CO_2 (Kim *et al.*, 2007; Kromdijk *et al.*, 2010; Sage *et al.*, 2011; Sun *et al.*, 2014).

The high efficiency of C_4 photosynthesis is due to the CO_2 concentration mechanism (CCM) associated with a specialized leaf anatomy (Hatch, 1987). During CCM, CO_2 diffuses from the ambient air towards the mesophyll cytosol where it is hydrated by carbonic anhydrase (CA) to bicarbonate. Phosphoenolpyruvate (PEP) carboxylase (PEPC) fixes the bicarbonate into C_4 acids such as aspartate and malate, which are mass-transported to bundle sheath cells through plasmodesmata (Leegood, 2004; Sowiński *et al.*, 2008). Decarboxylation of the acids by the NADP-malic enzyme (NADP-ME) or PEP carboxykinase (PEPCK) releases CO_2, elevating its concentration in bundle sheath cells, and produces pyruvate. PEP is regenerated from pyruvate by pyruvate, phosphate dikinase (PPDK). Ribulose-1,5-bisphosphate (RuBP) carboxylase/oxygenase (Rubisco) in bundle sheath chloroplasts fixes CO_2 and, to some extent, O_2. The accumulation of CO_2 by CCM allows Rubisco to operate near its saturation, reduces photorespiration and thus results in an efficient photosynthesis (Kanai and Edwards, 1999).

In addition to the leaf biochemistry, the leaf anatomy plays a crucial role in the CCM by allowing for rapid entry of CO_2 into mesophyll cells, in minimizing the leakage of accumulated CO_2 from

the bundle sheath cells and by determining the distribution of light energy (Hatch, 1987; von Caemmerer *et al.*, 2007; Yin *et al.*, 2011*b*). The amount of light energy absorbed by mesophyll and bundle sheath cells determines the balance of CO_2 delivery and reduction in these cells (von Caemmerer and Furbank, 1999; Wang *et al.*, 2014*a*; Bellasio and Lundgren, 2016). For instance, at low light intensities, a sub-optimal energy distribution is one of the causes that reduce CCM efficiency: leakiness, the ratio of the rate of CO_2 leakage to PEP carboxylation, increases rapidly as light intensity decreases (Bellasio and Griffiths, 2014*a*). The absorption of light energy is constrained by the nature of the chloroplasts, the distribution of chlorophyll between mesophyll and bundle sheath cells and the position of these cells in the leaf anatomy, among others (Kanai and Edwards, 1999; Evans *et al.*, 2007). The change in amount of PSII and the total concentration of chlorophyll of some C_4 plants when grown under low light intensity has been hypothesized to benefit them to flexibly control energy availability to mesophyll and bundle sheath cells (Furbank, 2011). Is there an optimal distribution of chlorophyll between mesophyll and bundle sheath cells that results in maximal rate of photosynthesis?

A number of biochemical and anatomical properties of C_4 plant leaves adapt when environmental factors such as CO_2, temperature and light intensity change (Anand *et al.*, 2014). Elevated CO_2 levels stimulated growth and photosynthesis in some C_4 plants (Ghannoum *et al.*, 2000; Anand *et al.*, 2014). Potential mechanisms for this enhancement have been proposed by Ghannoum *et al.* (2000). These authors suggested that the contribution of direct diffusion of CO_2 to bundle sheath cells, particularly in young leaves, to photosynthesis at elevated [CO_2] should be investigated. This is because juvenile leaves may not have a structurally mature bundle sheath cell wall as it was shown that plasmodesmata and suberin layer fully develop later in leaf development (Evert *et al.*, 1996; Mertz and Brutnell, 2014). The extent of the contribution of this diffusion pathway was not, however, tested directly. In addition, some NADP-ME subtype C_4 plants decarboxylate C_4 acids by PEPCK in the bundle sheath cytosol, which helps them maintain efficiency under diverse environmental conditions (Furbank, 2011; Pick *et al.*, 2011; Wang *et al.*, 2014*a*). Through modeling, this cytosolic CO_2 release has been shown to increase leakiness (Wang *et al.*, 2014*a*). Furthermore, increased PSII content in bundle sheath cells promotes photorespiration, which releases CO_2 in the cytosol from mitochondria (von Caemmerer and Furbank, 1999).

However, the role of cytosolic CO_2 release to an increase in leakiness could be overestimated by models based on flux-balance analysis (Sweetlove and Ratcliffe, 2011) since the positioning of organelles like chloroplasts cannot be accounted for (Wang *et al.*, 2014*a*).

In C_3 plants, temperature dependency of diffusion and dissolution of gases were predicted to contribute to the temperature response of photosynthesis while the estimated maximal activities of Rubisco and electron transport were more sensitive to temperature when the 3-D leaf structure was accounted for (Juurola *et al.*, 2005). The contribution of temperature dependency of biochemical and biophysical processes to the temperature response of C_4 photosynthesis and leakiness was not investigated. The importance of the physiological phenomena mentioned thus far to CCM might properly be assessed by a microscale reaction-diffusion model of gas transport and light propagation that incorporates the 3-D leaf microstructural geometry, including organelle positioning (Berghuijs *et al.*, 2016).

Recently, we built a 2-D microscale modeling of gas transport in C_4 leaves by assuming a uniform light environment (Chapter 4). However, a 3-D leaf anatomy is more accurate in capturing the gas exchange and light propagation in leaves (Aalto and Juurola, 2002; Ho *et al.*, 2016). A 3-D geometry may also be essential for modeling maize leaf anatomy since the intercellular air spaces at the abaxial and adaxial leaf side are suggested to be poorly connected (Long *et al.*, 1989). In addition, light penetration and ATP production was modeled using a 2-D leaf anatomy model (Bellasio and Lundgren, 2016) to investigate the evolution of C_4 photosynthesis in relation to leaf anatomy and energetics. A 3-D model of C_4 metabolism in the anatomy of rice was developed to assess the prospects for improving photosynthesis by introducing a C_4 pathway in rice (Wang *et al.*, 2017). However, a model of gas transport and light distribution in a realistic 3-D leaf anatomy of maize, as was previously done for C_3 leaves (Ho *et al.*, 2016), was not developed so far. In addition, to assess the relevance of PSII content in bundle sheath cells to photosynthesis in relation to O_2 production and photorespiration (von Caemmerer and Furbank, 1999; Furbank, 2011), a reaction-diffusion model for O_2 transport is required for a C_4 leaf. The objectives of this study were thus to use the reaction-diffusion model: (i) to test whether optimizing chlorophyll distribution between mesophyll and bundle sheath cells improves C_4 photosynthesis; (ii) to assess the contribution of direct CO_2 diffusion on the rate of C_4

photosynthesis at elevated CO_2; (iii) to investigate the role of biophysical and biochemical processes on the temperature dependence of C_4 photosynthesis; and, (iv) to systematically evaluate the influence of cytosolic CO_2 release on the efficiency of C_4 photosynthesis.

5.2 Materials and methods

5.2.1 Gas exchange and chlorophyll fluorescence measurements

Maize (*Zea mays* L.) plants were grown in controlled conditions in a greenhouse at the facilities of Wageningen University and Research. Plant growth conditions and treatments were described in detail previously (section 3.2.1). To compare model predicted responses of photosynthesis and estimate photosynthesis parameters, gas exchange and chlorophyll fluorescence measurements of 19 d old leaves having an average nitrogen content of 0.64 g m^{-2} were used (Table 3.1).

5.2.2 Geometry of leaf microstructure

The leaf geometry was developed from maize plants whose growth conditions, treatments, fixation and measurement of anatomical properties were reported previously (section 3.2.1). We first attempted to obtain 3-D images using X-ray micro computed tomography (Verboven *et al.*, 2015), but initial tests showed that identification of individual cells was difficult because of insufficient contrast due to lack of air spaces in the vascular bundles (Fig. A.6.3, Appendix A). Light microscopy images were thus used instead.

Light microscopy images (857× 643 µm) of 120 leaf slices at 1 µm intervals were taken covering a section across several parallel vascular bundles (Fig. A.6.1, Appendix A). Using the 3-D image-processing software Avizo Fire (VSG, France) the images were first aligned. The images showed three consecutive bundle sheath cells, each of which was surrounded by a single layer of mesophyll cells forming a repetitive concentric arrangement of mesophyll and bundle sheath cells (Fig. A.6.3, Appendix A). Therefore, using the symmetry of the geometry, only one concentric arrangement of mesophyll and bundle sheath cells along with the epidermis and air spaces was considered by cropping the images to a representative region of interest, resulting in 3-D images

having a pixel resolution of 0.67 µm. Segmentation of leaf anatomical features was carried out semi-automatically due to a less distinct grayscale intensity distribution among microstructural features. Chloroplasts of mesophyll cells were identified clearly due to their random arrangement while numerous clustered chloroplasts of bundle sheath cells were segmented as a layer of centrifugally arranged chloroplasts. Other microstructural features such as mitochondria, cytosol and vacuole could not be identified due to insufficient resolution and contrast. Thus, mitochondria were assumed as uniformly distributed in the cytosol, and vacuoles were created using a Matlab script (The Mathworks, Inc., Natick, USA) as volumes obtained by shrinking cells relative to their geometric center assuming that vacuoles occupy 60 % of the cell volume (Taiz, 1992). Quantification of volume fractions of the cells, exposed surface of mesophyll cells per unit leaf area, surface area of bundle sheath cells per unit leaf area and porosity in comparison to literature values for various C_4 plants is described in Table C.4, Appendix C.

5.3 Microscale model

The microscale model of gas exchange for a C_4 plant leaf was developed by extending a 2-D model of gas exchange in a C_4 leaf (Chapter 4), similar to the 3D-C_3 model by Ho *et al*. (2016). The light profile in a maize leaf was computed (Text C.1., Appendix C) using a meshed Monte Carlo photon transport method (Watté *et al.*, 2015), which was validated for tomato leaves with an experimentally determined absorption profile (Watté *et al.*, 2015; Ho *et al.*, 2016). The rates of electron transport and ATP production were computed from the light profile (see further) and used as an input to the biochemical model of C_4 photosynthesis (Eqs. C.2.1, C.2.2 and C.2.14). The temperature dependency of biophysical and biochemical parameters was also included within the model using an Arrhenius equation (Eqs. C.2.24 and C.2.25). Diffusion through the stomata in relation to the extent of stomatal opening was modeled by adjusting the effective diffusivity of CO_2 through the stomatal pore to match the measured stomatal conductance (Fig. C.1). Transport of metabolites across the mesophyll-bundle sheath interface may not be explained by diffusion alone (Sowiński *et al.*, 2008). Also, proteins facilitating metabolite transport across various envelopes are not fully identified (Brautigam and Weber, 2011). For practical reasons, transport of intermediate metabolites was assumed to be instantaneous and non-limiting and was not

explicitly modeled. Symbols, values and units of the physical properties, photosynthetic parameters and their temperature dependencies are given in supplementary Tables C.1 to C.3.

5.3.1 CO_2 transport inside a C_4 leaf

The reaction-diffusion equation for CO_2 transport in all compartments except the bundle sheath cells (the intercellular air space, stomatal air, epidermis, vasculature and mesophyll cells) at a steady-state is given by:

$$\nabla \cdot \left(D_{CO_2} \nabla [\mathrm{CO_2}] \right) - B_{CA} - B_{NCA} + R^* = 0 \tag{5.1}$$

where ∇ is the gradient operator; [CO_2] is the concentration of CO_2; D_{CO_2} is the diffusivity of CO_2; B_{CA} is the rate of CA catalyzed hydration of CO_2 to bicarbonate ions in the mesophyll cytosol (Eq. 5.2); B_{NCA} is the non-enzymatic CO_2 hydration rate (Eq. 5.4); and, R^* is the volumetric rate of CO_2 release through respiration by mitochondria (Table C.1, Appendix C). The symbol * represents a volumetric rate equivalent of leaf area-based variables. B_{CA} is zero everywhere except in the mesophyll cytosol. B_{NCA} and R^* are zero in the gaseous phase.

B_{CA} is given by (Spalding and Portis, 1985; Tholen and Zhu, 2011):

$$B_{CA} = \frac{V^*_{CA,max} \cdot \left([\mathrm{CO_2}] - \frac{[\mathrm{HCO_3^-}][\mathrm{H^+}]}{K_{eq}} \right)}{K_{CO_2} + \frac{K_{CO_2}}{K_{HCO_3^-}} \cdot [\mathrm{HCO_3^-}] + [\mathrm{CO_2}]} \tag{5.2}$$

where $V^*_{CA,max}$ is the volumetric maximum catalytic activity of CA; [HCO_3^-] is the concentration of bicarbonate; K_{CO_2} and $K_{HCO_3^-}$ are Michaelis-Menten constants of CA hydration and dehydration, respectively; K_{eq} is the equilibrium constant for CA; and, [H^+] is the concentration of H^+ ions.

In bundle sheath cells, the reaction-diffusion equation for CO_2 transport is written as:

$$\nabla \cdot \left(D_{CO_2} \nabla [CO_2] \right) - \min(w_c^*, w_j^*) + \bar{V}_p^* - B_{NCA} + R^* + r_p^* = 0 \tag{5.3}$$

where $\min(w_c^*, w_j^*)$ is the gross volumetric fixation rate of CO_2; w_c^* is the volumetric rate of Rubisco-limited carboxylation (Eq. C.2.1, Appendix C); w_j^* is the volumetric rate of electron-transport-limited carboxylation given by the biochemical model of C_4 photosynthesis (von Caemmerer and Furbank, 1999) (Eq. C.2.2, Appendix C); $\bar{V}_p^*$ is the average (indicated by the overscore) volumetric rate of CO_2 production through decarboxylation of C_4 acids in the chloroplasts (Eq. C.2.15, Appendix C); and, r_p^* is the volumetric rate of CO_2 release through photorespiration in bundle sheath cytosol (Eq. C.2.12, Appendix C). The first three terms from the left after the diffusion term are applicable in the chloroplasts while the next two apply in the cytosol.

Since bundle sheath cells of maize contain little CA, it is assumed that hydration of CO_2 proceeds non-enzymatically (Burnell and Hatch, 1988). The net volumetric hydration rate of CO_2, B_{NCA}, in mesophyll or bundle sheath cell is given by (Ho *et al.*, 2016):

$$B_{NCA} = k_1 \cdot [CO_2] - \frac{k_2 \cdot [HCO_3^-]\,[H^+]}{K} \tag{5.4}$$

where k_1 is CO_2 hydration rate constant; k_2 is CO_2 dehydration rate constant; K is the acid dissociation constant for H_2CO_3; and $[H^+]$ is calculated from pH of the cytosol, vacuole, vasculature or stroma.

It is to be noted that in our previous 2-D model (Chapter 4), the rate of PEP carboxylation which was expressed based on CO_2 as proposed in the standard biochemical model of C_4 photosynthesis (von Caemmerer and Furbank, 1999) was coupled to CO_2 diffusion (section B.4, Appendix B). Since more information has recently become available on kinetic parameters of PEP carboxylation (Boyd *et al.*, 2015), it was rewritten using its substrate bicarbonate and applied in a reaction-diffusion equation for bicarbonate (Eq. C.2.14, Appendix C). Diffusion of bicarbonate

ions in epidermis, mesophyll cells, vasculature or bundle sheath is given by the following general equation:

$$\nabla\cdot\left(D_{HCO_3^-}\nabla[\mathrm{HCO_3^-}]\right)+B_{NCA}+B_{CA}-V_p^*=0 \tag{5.5}$$

where $D_{HCO_3^-}$ is the diffusivity of bicarbonate in respective cell compartments. V_p^* is the rate of PEP carboxylation in the mesophyll cytosol (Eq. C.2.14, Appendix C).

5.3.2 O_2 transport inside a C_4 leaf

The steady state reaction-diffusion equation for O_2 transport is given by:

$$\nabla\cdot\left(D_{O_2}\nabla[\mathrm{O_2}]\right)+E_o^*-r_{p,O_2}^*-r_p^*-R^*=0 \tag{5.6}$$

where $[O_2]$ is the concentration of O_2; D_{O_2} is the diffusivity of O_2; E_o^* is the volumetric rate of oxygen evolution in chloroplasts of mesophyll or bundle sheath cells and zero elsewhere. r_{p,O_2}^* is the volumetric rate of oxygen consumption by photorespiration in the bundle sheath chloroplast (Eq. C.2.13, Appendix C). r_p^* accounts for the consumption of 0.5 mol of O_2 by glycolate oxidase in peroxisomes during photorespiration (Somerville, 2001). r_p^* is applicable in the bundle sheath cytosol. The rate of oxygen evolution E_o^* associated with the linear electron transport in chloroplasts was set to be equal to the quarter of the rate of linear electron flux (Eq. C.2.6, Appendix C) since evolution of one molecule O_2 is accompanied with the flow of four electrons.

The flux of CO_2, HCO_3^- and O_2 at the boundary of cuticle, mesophyll or bundle sheath cells is given by:

$$J_y=-P_y\Delta[\mathrm{C}_y] \tag{5.7}$$

where *y* stands for CO_2, O_2 and HCO_3^-; P_y is the permeability of cuticle, plasma membrane, chloroplasts envelope or the mesophyll-bundle sheath interface to *y*. For the mesophyll-bundle

sheath interface, $P_y = D_y \theta / L_{pd}$ where D_y is the diffusivity of *y* through the plasmodesmata (assumed equal to that in the liquid phase); θ is the ratio of the bundle sheath surface area covered by plasmodesmata to the total area of the mesophyll-bundle sheath interface; and L_{pd} is the thickness of the mesophyll-bundle sheath interface. $\Delta[C_y]$ is the difference in concentration (C) of *y* across a boundary.

The resistance to gas diffusion imposed by leaf ultrastructure was considered. The resistance of the cell wall was defined as the thickness of the wall divided by the effective diffusivity of the gases in the wall (Evans *et al.*, 2009). The cell wall thickness of the mesophyll and bundle sheath cells was measured from electron microscopy images of the same leaf (Fig. A.6.2, Appendix A). We assumed a value of one for tortuosity and solvent to water partitioning coefficient for gases in the wall (Evans *et al.*, 2009). The diffusivity of CO_2 in the mesophyll cell wall, which was shown to be a major limitation to rapid diffusion expected in C_4 leaves (section 4.4.2), was assumed equal to that in water. The resulting CO_2 conductance of the mesophyll-air space interface was within the range of values reported previously (Evans *et al.*, 2009) (Table C.2, Appendix C). In addition, the contact boundaries among mesophyll cells and bundle sheath cells were modeled as a thin boundary layer with thickness of twice the thickness of both the respective cell walls and plasma membranes. The resistance of a plasma membrane was calculated as the inverse of its permeability to the gases or bicarbonate (Evans *et al.*, 1994). The suberine layer restricts diffusion of the gases through the apoplastic pathway. Thus, an insulated boundary condition was assumed at the surface of the bundle sheath cells exposed to the intercellular air space (Evert *et al.*, 1977; Furbank and Hatch, 1987). Furthermore, Henry's law was applied to describe the vapor-liquid equilibrium at the cell-air interface (Ho *et al.*, 2016).

5.3.3 Light propagation

The propagation of light in maize leaf tissue was modeled using a meshed Monte Carlo method with free phase function choice (Watté *et al.*, 2015). Optical properties of mesophyll and bundle sheath cells were computed from the distribution of organelles in these cells (Table C.5, Appendix C) (Aernouts *et al.*, 2014). A light source that is distributed the light uniformly over the

top surface of the leaf was used. The distribution of light was modeled for blue light (470 nm) and red light (665 nm) separately, and the resulting profiles were combined (10 % blue and 90 % red) to derive an overall light absorption profile. The light profile was obtained using measured transmittance and reflectance (Woolley, 1971) by adjusting the absorption coefficient of chloroplasts and the scattering coefficient of cytoplasm to fit the measured overall light absorption (see Appendix C Text C.1 for more details). The resulting light profile was then used to compute the potential rate of electron transport and ATP production in a leaf. The maximum rate of electron transport was estimated by fitting the modeled rate of ATP production to that obtained from chlorophyll fluorescence measurements (Eqs. C.2.3 to C.2.11, Appendix C).

5.4 Optimization of chlorophyll distribution

To optimize photosynthesis, four light propagation models, as described above, were generated using ratios of absorption coefficients of chloroplasts in the bundle sheath to that in mesophyll cells of 0.30, 0.50 (default value used for simulation), 1.00 and 1.50. It is assumed that light absorbed per unit photosystem is strongly affected by chlorophyll content, which is modeled using an absorption coefficient of mesophyll and bundle sheath chloroplasts (Table C.7, Appendix C). The maximum rate of electron transport was estimated for each scenario as discussed above. The light responses of photosynthesis and leakiness were computed from the microscale model (Eqs. C.2.20 and C.2.23, Appendix C). The conditions were an ambient CO_2 concentration of 250 µmol mol^{-1}, 21 % O_2 and a fraction of PSII in bundle sheath cells of 0.10.

5.5 Photosynthesis at an elevated CO_2

To test to what extent direct diffusion alone supports photosynthesis at elevated CO_2 levels, three scenarios were considered. The detailed pathways of CO_2 delivery to bundle sheath chloroplast is shown in Fig. C.7 (Appendix C). CO_2 fixed in bundle sheath cells is assumed to be supplied by (i) decarboxylation of C_4 acids (referred to as "C_4 pump"), (ii) direct diffusion through mesophyll surface (S_m) only (referred to as "Flux-S_m"), and (ii) direct diffusion through mesophyll cells and the entire surface of bundle sheath cells (S_b) (referred to as "Flux-S_m-S_{bs}"). To discern the relative

contribution of direct diffusion pathways, CO_2 supply through the decarboxylation of C_4 acids was neglected. Consequently, for the cases, "Flux-S_m" and "Flux-S_m-S_{bs}", the rate of PEP carboxylation was zero (Eq. C.2.14, Appendix C). The external CO_2 levels were: 380 µmol mol^{-1}, 500 µmol mol^{-1} and 1500 µmol mol^{-1} at irradiance of 1500 µmol m^{-2} s^{-1} and 21 % O_2.

5.6 Temperature dependency

To test the contribution of biophysical and biochemical processes to the temperature response of photosynthesis and leakiness, a sensitivity analysis was carried out. The role of biophysical processes was assessed through diffusion coefficients of CO_2, HCO_3^-, O_2 and Henry's constants of the gases. Maximal catalytic activities of enzymes and their kinetic constants were used to examine the relative importance of biochemical processes. The diffusion coefficients and the parameters of enzyme kinetics are listed in supplementary Tables C.2 and C.3 (Appendix C). Temperature values of 18 °C, 25 °C, 30 °C, 35 °C and 39 °C were chosen. The sensitivity analysis was carried out by considering three scenarios. In the first scenario (referred to as "Base"), the diffusion coefficients, the Henry's constants and the parameters of enzyme kinetics were assumed to depend on temperature. In the second scenario (referred to as "Biochemical"), only the parameters of enzyme kinetics were varied while the diffusion coefficients and Henry's constants were kept constant at those of 25 °C for 18 °C, 30 °C, 35 °C and 39 °C. In the third scenario (referred to as "Biophysical"), only the maximal enzyme activities and kinetic constants were kept constant at those of 25 °C across the temperature ranges. For all the scenarios, the stomatal conductance was assumed constant for various temperature values. Since the quantum efficiency of PSII electron transport at limiting light was quite constant at those temperature values (Yin *et al.*, 2016), together with that of PSI electron transport, it was assumed constant.

5.7 Numerical solution

A 3-D leaf tissue was 124×124×200 µm in dimension and had 9.428×10^6 cube elements with a length of 0.67 µm. The lateral sides of this geometry were assumed to have no net flux while external concentrations of CO_2 and O_2 were assumed at the other sides. The reaction-diffusion

equations were discretized over the finite volumes grid and the resulting linear systems of algebraic equations of the unknown concentrations at the volume nodes were solved by the preconditioned conjugate gradient procedure in Matlab (The Mathworks) using the finite volume method (Versteeg and Malalasekera, 1995; Ho *et al.*, 2016). We used a 16-GB RAM node of the high-performance computer in the VSC – Flemish Supercomputer Center (Belgium).

5.8 Results

5.8.1 Leaf microstructure impacts the light and CO_2 profile

The developed 3-D geometry (Fig. 5.1A) consisted of the epidermis, stomata, the intercellular air space, mesophyll cells, bundle sheath cells and vasculature, as main components of maize leaf tissue. Leaf anatomical properties measured from this geometry were comparable to the literature values for C_4 plants (Table C.4, Appendix C). Fig. 5.1B shows the modeled light absorption profile in the leaf tissue when illuminated from the adaxial leaf side. About 96 % of light absorbed by the leaf tissue (88 % of incident light) was absorbed by chloroplasts. Mesophyll chloroplasts absorbed 52 % while the bundle sheath chloroplasts absorbed 32 % of the total absorbed light (Figs. 5.1B and 5.2A). Due to shading, the abaxial leaf side received much less light (Fig. 5.2A). In addition, the fraction of absorbed photons along leaf depth in Fig. 5.2A shows that halfway the tissue depth the photon absorption was boosted by the numerous chloroplasts of the bundle sheath cells.

The computed light profile was an input in the estimation of the maximum rate of electron transport (Table C.2, Fig. C.2, Appendix C), which was then used to calculate the potential rates of electron transport and ATP production in the chloroplasts. The computed ATP production rates (Eq. C.2.5 to C.2.7, Appendix C) were then used for simulation of the responses of photosynthesis (A) to irradiance and CO_2. Fig. 5.2 (B, C) shows that the predicted responses are generally in agreement with trends observed in the experimental data. The underestimated values, particularly for the irradiance response, are due to the scatter in measured ATP production rate that resulted in an uncertainty in the estimated maximum electron transport rate (Fig. C.2, Appendix C).

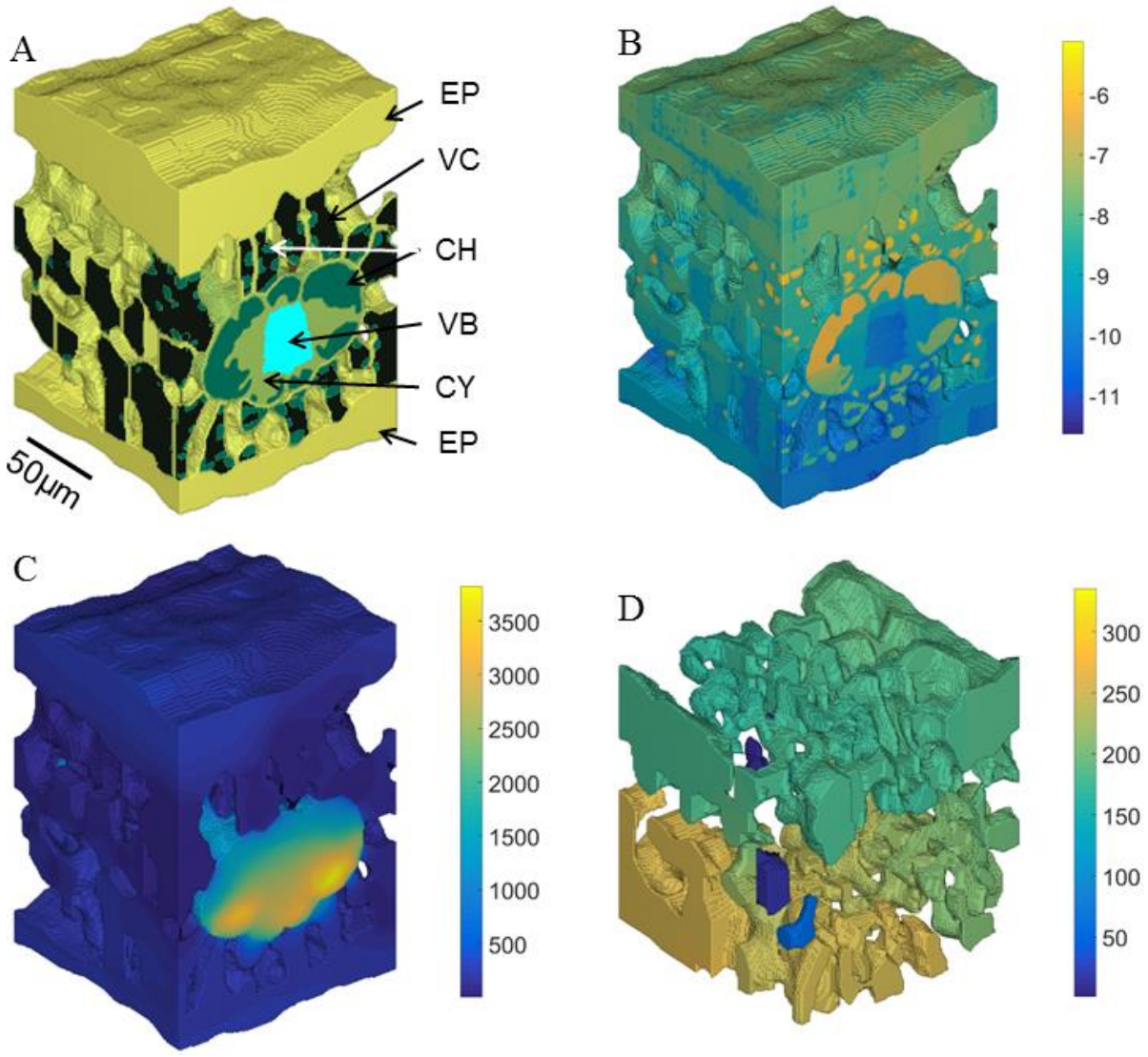

Figure 5.1. Three-dimensional simulation model of light and CO_2 transport in maize leaves. Geometry of maize leaf microstructure (A) including epidermis (EP), vacuole (VC), chloroplasts (CH), vascular bundle (VB) and cytosol (CY); light absorbance of leaf tissue with the color bar showing the logarithm of the fraction of absorbed irradiance (B); computed CO_2 concentration (µmol mol^{-1}) profile in liquid phase (C) and in intercellular air space (D) at irradiance of 1500 µmol m^{-2} s^{-1}, ambient CO_2 of 380 µmol mol^{-1} and 21 % oxygen. Leaf tissue dimensions are 124×124×200 µm.

The fitting of the CO_2 response could improve when the exact PSII content in bundle sheath cells, which was assumed 0.10 (Table C.2, Appendix C), is known for the leaf type used in the experiment (Fig. C.5, Appendix C). In addition, the underestimation of *A* in response to irradiance at 2000 µmol m^{-2} s^{-1} (Fig. 5.2C), despite a high ATP production rate (Fig. C.2, Appendix C), was because of Rubisco limitation (not shown): the response was measured at sub-ambient [CO_2] of 250 µmol mol^{-1} (section 3.2.2).

The CO_2 concentration profile in the liquid phase media (Fig. 5.1C) and in the intercellular air space (Fig. 5.1D) were then computed at an ambient CO_2 concentration (C_a) of 380 µmol mol^{-1}, 21 % O_2 and an irradiance of 1500 µmol m^{-2} s^{-1}. Due to the CCM, the mean CO_2 concentration in the bundle sheath chloroplast was ca. 13 times higher than that in the mesophyll cells. Fig. 5.1D also shows that the concentration profile in the intercellular air space was largely homogenous except in the isolated air spaces, which accounted for less than 1 % of the intercellular air space volume. These air spaces could be connected to air spaces outside the region interest. However, the slightly higher CO_2 concentration in the abaxial-side intercellular air space (Fig. 5.1D) was due to the gradient of light, which resulted in a lower CO_2 assimilation rate than that of the adaxial side, and the low connectivity of the adaxial and abaxial-side intercellular air space (Fig. C.3, Appendix C). The light gradient also resulted in higher CO_2 concentration in the abaxial-side mesophyll than in the adaxial-side (Fig. 5.1C).

The profile of O_2 partial pressure (Fig. 5.3A) shows that the mean partial pressure in bundle sheath chloroplasts was elevated to 26 kPa (C_a of 380 µmol mol^{-1}, 21 % O_2, irradiance of 1500 µmol m^{-2} s^{-1} and at a bundle sheath PSII fraction of 0.10). Fig. 5.3B shows the ratio of bicarbonate to CO_2 concentration in the liquid phase. At equilibrium and a pH of 7.8, this ratio is ca. 48 as calculated from the Henderson–Hasselbalch equation. In bundle sheath chloroplasts, the ratio is close to this value (Fig. 5.3).

At pH 7.5 in mesophyll chloroplasts, the equilibrium ratio is ca. 24 in close agreement with that shown in Fig. 5.3B. In addition, extreme values of this ratio close to mesophyll-epidermis interface are due low CO_2 created by contact of these cells.

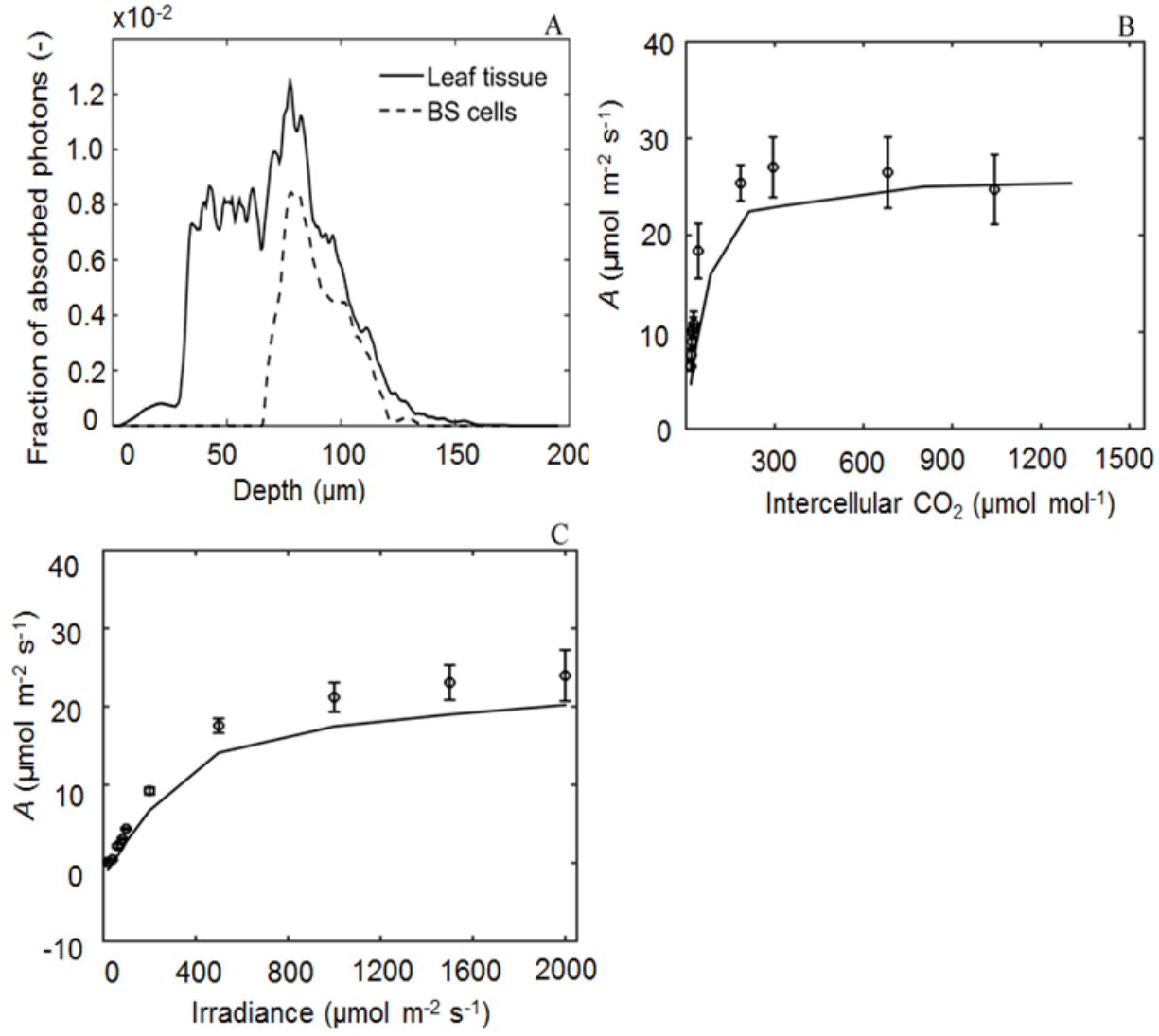

Figure 5.2. Simulations of energy distribution and the responses of photosynthesis. Simulated fraction of absorbed photons by leaf tissue and bundle sheath (BS) cells across leaf depth (top to bottom) (A); response of photosynthesis (*A*) to intercellular CO_2 computed at irradiance of 1500 µmol m^{-2} s^{-1} and 21 % oxygen (B); and the response of *A* to irradiance computed at ambient [CO_2] of 250 µmol mol^{-1} and 21 % oxygen (C). In B and C, symbols indicate measurement data and solid lines show model predictions, while bars show standard error (n = 4).

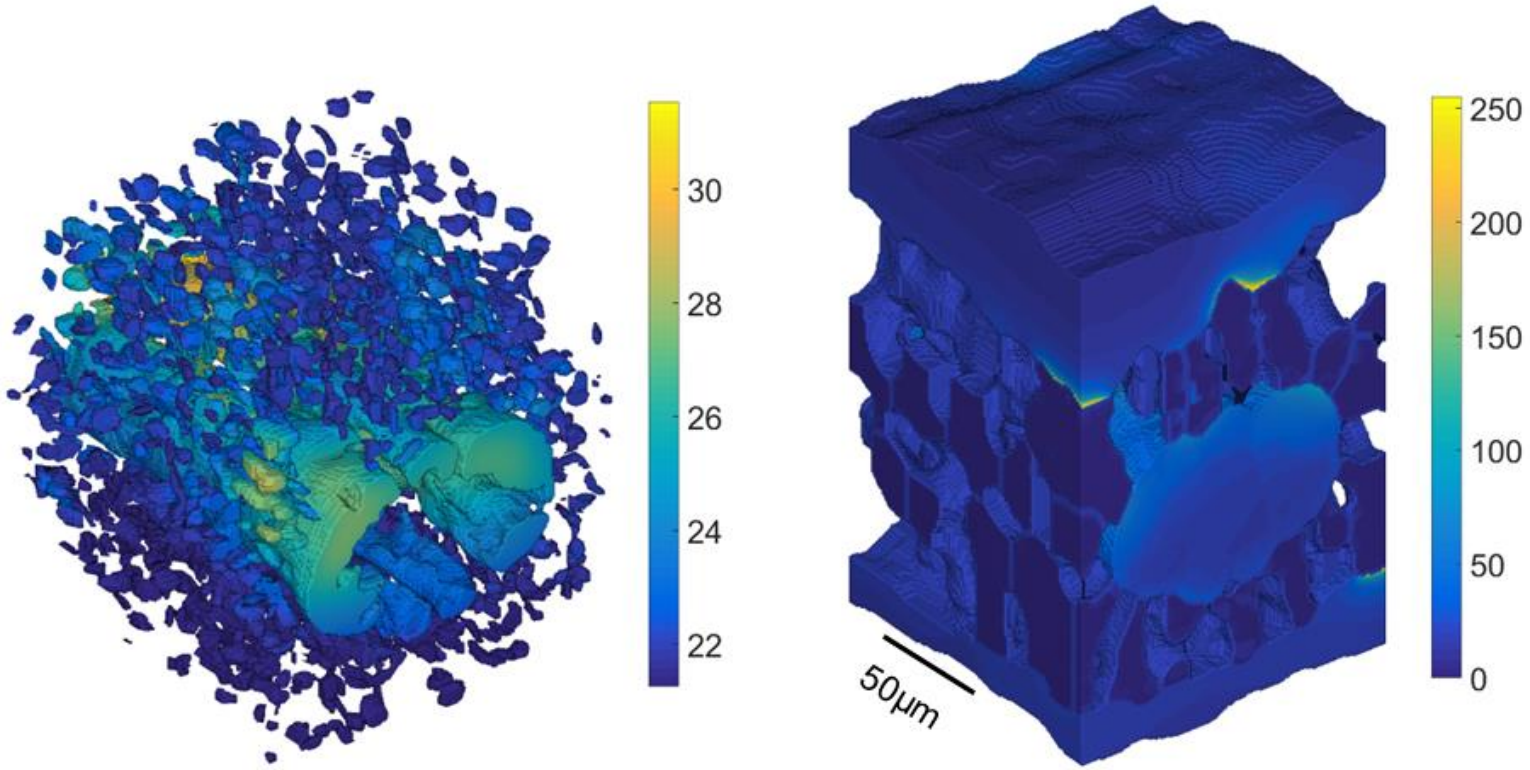

Figure 5.3**.** Three-dimensional profiles of O_2 and bicarbonate. Simulated profile of O_2 partial pressure (kPa) in chloroplasts (A) and the ratio of concentration of bicarbonate to the mean [CO_2] in each leaf component (B) (Eq. C.2.21, Appendix C). Conditions were: irradiance of 1500 µmol m^{-2} s^{-1}, ambient [CO_2] of 380 µmol mol^{-1} and oxygen pressure of 21 kPa. Leaf tissue dimensions are 124×124×200 µm.

5.8.2 Optimization of chlorophyll distribution maximizes photosynthesis rate

Fig. 5.4 shows the effect of various K_{bs}:K_m ratios from which the ratio of chlorophyll (Chl) concentration in bundle sheath to that in mesophyll cells (f_{chl}) can be calculated using $f_{chl} = (K_m / K_{bs}) \times I_{abs,bs} / I_{abs,bs}$ as 3, 2, 1.5 and 1. 2 for K_{bs}:K_m ratios of 0.3, 0.5, 1.0 and 1.5 respectively. Fig. 5.4 shows that a tradeoff between photosynthesis and leakiness exists for various distributions of chlorophyll concentration. Assuming bundle sheath chloroplasts contain 30 % of the total chlorophyll resulted in absorption by bundle sheath cells of ca. 48 % of the total light absorbed (Fig. 5.4A). Consequently, the fraction of ATP production in mesophyll cells ($\bar{x}$) was the highest at low light intensities when electron transport is light-limited (Fig. 5.4B). This is reflected in the response of leakiness at low light intensities, which was also the highest (Fig. 5.4B). As a result of this, the predicted photosynthesis was low. At high light intensities, where the maximum electron transport rate is limiting, $\bar{x}$ leveled at close to 0.40 for various distributions of chlorophyll concentration. Fig. 5.4A also shows that when *Chl bs/m* is 1, the fraction of light absorbed by bundle sheath cells was higher by only 19 %. In this case, $\bar{x}$ remained interestingly close to 0.40 at all irradiances. The predicted ϕ values at low light intensities were very close to the lowest at low light intensities in Fig. 5.4C. However, at light intensities $\geq$ 500 µmol m^{-2} s^{-1}, ϕ was close to the highest in Fig. 5.4C. More importantly, the predicted rate of photosynthesis was the highest (Fig. 5.4D). When the chlorophyll concentration in bundle sheath cells was three times higher than the default, the light absorption was 34 % higher (Fig. 5.4A). At low light intensities, $\bar{x}$ dropped to 0.30 (Fig. 5.4B) leading to lowest ϕ (Fig. 5.4C). However, the predicted photosynthesis was also the lowest due to the low capacity of the C_4 cycle in mesophyll cells, as indicated by $\bar{x}$ (Fig. 5.4D). Overall, an equal photon absorption per unit photosystem of mesophyll and bundle sheath chloroplasts maximized photosynthesis and minimized the loss of CCM efficiency at low light intensities.

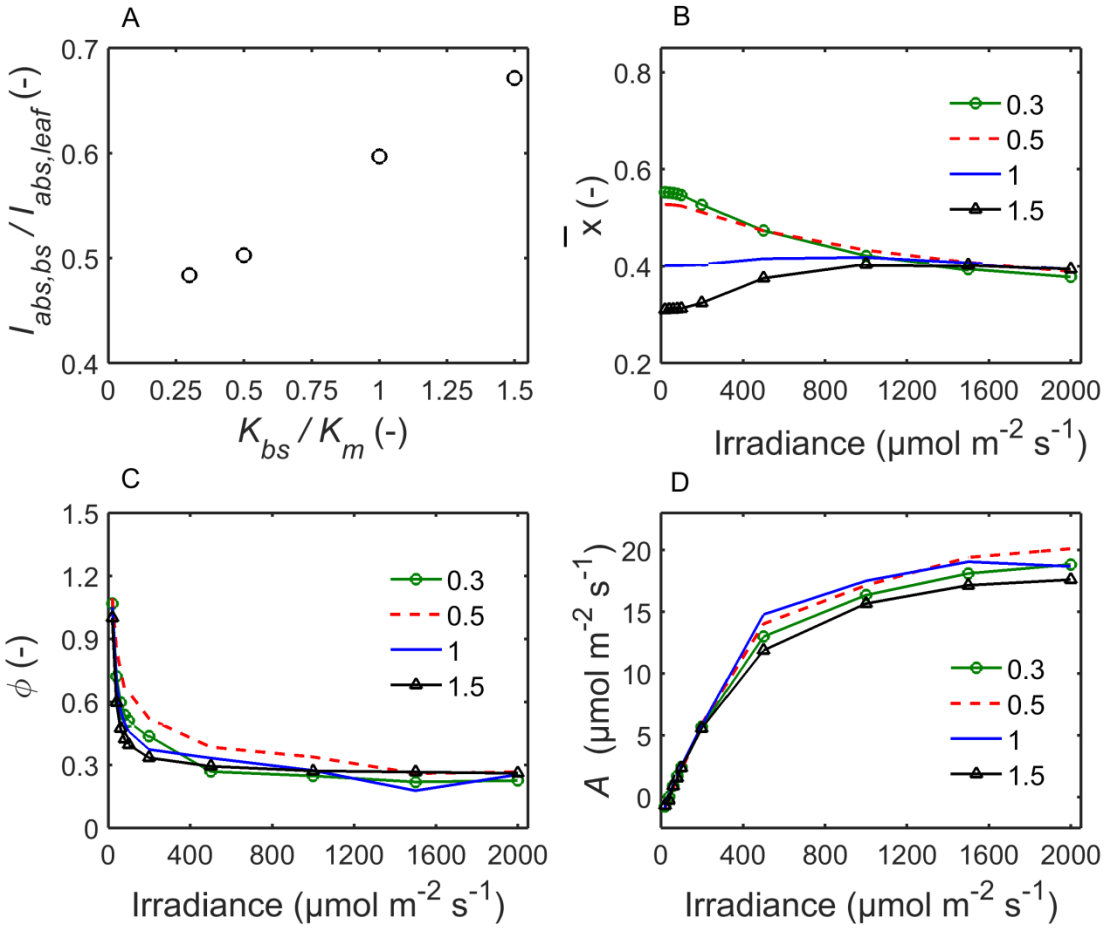

Figure 5.4. Improving of photosynthesis by optimizing the distribution of chlorophyll. Photon absorbed per unit photosystem in bundle sheath (K_{bs}) and mesophyll (K_m) (Eq. C.2.9, Appendix C), which determined the absorbed light in bundle sheath cells ($I_{abs,bs}$) relative to total absorption by leaf tissue ($I_{abs,leaf}$), were varied in steps (A). The resulting ATP production in mesophyll cells relative to the total ATP production ($\bar{x}$) was calculated for various values of K_{bs} : K_m ratio (B). The predicted response of leakiness is shown in C while photosynthesis rate (A) is shown in D. For C and D, ambient [CO_2] was 250 µmol mol^{-1} and [O_2] was 21 %. Legend: K_{bs}:K_m ratio.

5.8.3 Direct diffusion contributes to photosynthesis of young leaves at elevated [CO_2]

Fig. 5.5A shows the contributions of direct diffusion pathways to the rates of photosynthesis at elevated [CO_2].

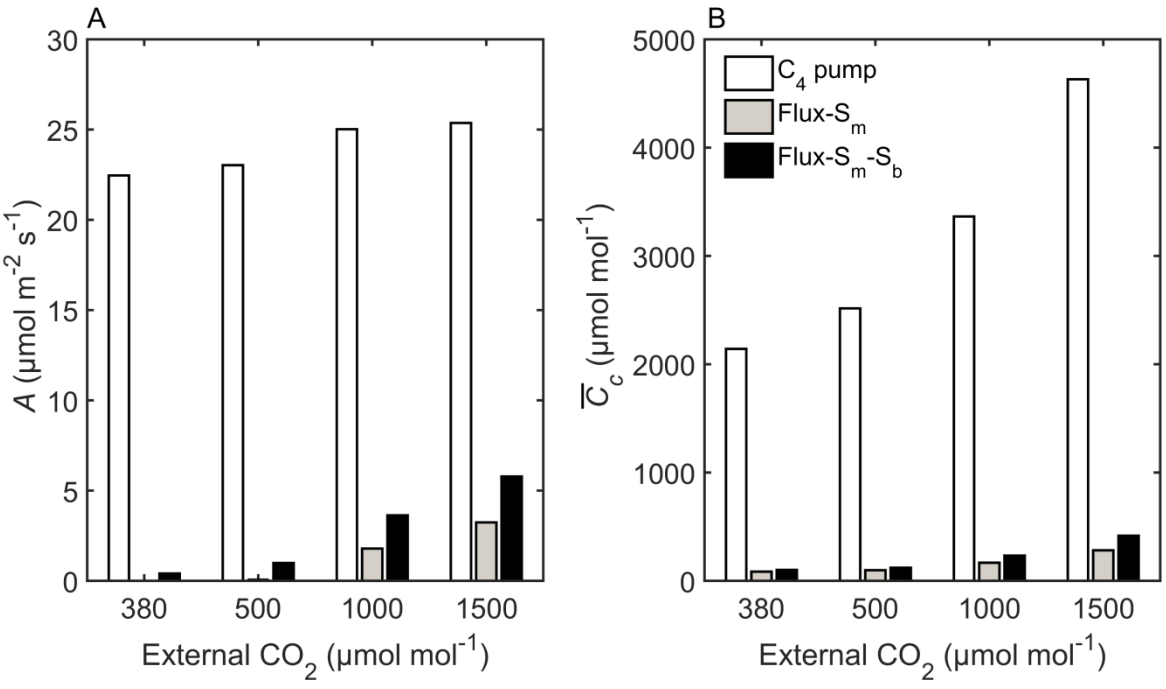

Figure 5.5. The role of direct diffusion on photosynthesis (*A*) and mean CO_2 in bundle sheath cells ($\bar{C}_c$) at elevated [CO_2]. Photosynthesis (A) and $\bar{C}_c$ (B) at various external CO_2 concentration. CO_2 diffuses to bundle sheath cells through plasmodesmata at the mesophyll-bundle sheath interface only (Flux-S_m) or through the entire surface of bundle sheath cells having no suberin layer (Flux-S_m-S_{bs}). "C_4 pump" denotes the scenario where bundle sheath photosynthesis is supplied by decarboxylation of C_4 acids and direct diffusion through plasmodesmata. Irradiance was kept at 1500 µmol m^{-2} s^{-1} and [O_2] was 21 %.

Simulations show that the rate of photosynthesis was not entirely CO_2-saturated at ambient [CO_2]. Consequently, *A* changed by up to 9 % as CO_2 increased (Fig. 5.5A). At an external [CO_2] of 380 µmol mol^{-1}, decarboxylation of C_4 acids is the main source of CO_2 to bundle sheath cells. When

it was assumed that there is no CO_2 supply to bundle sheath cells through decarboxylation of C_4 acids ("Flux-S_m" scenario) and the external [CO_2] was elevated further, the rate of photosynthesis was ca. 6 % and 13 % of the net photosynthesis rate for the "C_4 pump" case at 500 µmol mol^{-1} and 1500 µmol mol^{-1} respectively. The role of the CCM is demonstrated by the respective increase in photorespiration which was about three and four fold since the mean concentration of CO_2 in bundle sheath cells ($\bar{C}_c$) was 5 % (500 µmol mol^{-1}) and 6 % (1500 µmol mol^{-1}) of that for the "C_4 pump" scenario (Fig. 5.5B). If there was no suberin layer around the bundle sheath cell wall, CO_2 and O_2 diffused through the entire surface of the bundle sheath cells. In this case, the rate of photosynthesis was 13 % and 23 % of the "C_4 pump" scenario at 500 µmol mol^{-1} and 1500 µmol mol^{-1}, respectively (Fig. 5.5A). The absence of the suberin layer is detrimental to CCM as it reduced $\bar{C}_c$ by 32 % although the concentration of O_2 in the bundle sheath cells decreased by 8 % compared to "Flux-S_m" scenario at 1500 µmol mol^{-1}. These results show that whenever external [CO_2] exceeds $\bar{C}_c$ during growth in closed systems such as growth chambers and greenhouses, direct diffusion pathways in young leaves will enhance the photosynthesis rate.

5.8.4 CO_2 release in bundle sheath cytosol may increase leakiness moderately

To determine the influence of CO_2 production outside bundle sheath chloroplasts by PEPCK in the cytosol on A and ϕ, we assumed various fractions of CO_2 release in the cytosol (for details, see Appendix C, Text C.3). The fraction of PSII in bundle sheath cells was constant at 0.10 (Chapman and Hatch, 1979). Fig. 5.6 shows that releasing up to 25 % of the CO_2 in bundle sheath cells has a minimal impact on A and ϕ (Fig. 5.6A). At higher fractions, A responded dramatically decreasing by 10 % and ϕ increased by 13 % when all the CO_2 was released in the cytosol (Fig. 5.6A). Simulations showed that this was because $\bar{C}_c$ decreased by ca. 7 % and photorespiration increased by ca. 29 %.

To assess the effect of increased PSII abundance on photosynthesis, the fraction of PSII in bundle sheath cells was increased (Fig. 5.6B). The rate of linear electron transport in bundle sheath cells was calculated for each fraction of PSII in bundle sheath cells (Eqs. C.2.6 and C.2.11, Appendix C). In response to increased PSII content in bundle sheath cells, A and ϕ responded less gradually

(Fig. 5.6B). Tripling the PSII fraction increased $\bar{C}_c$ by ca. 5 %, photorespiration by ca. 12 % and ϕ by ca. 3.6 %.

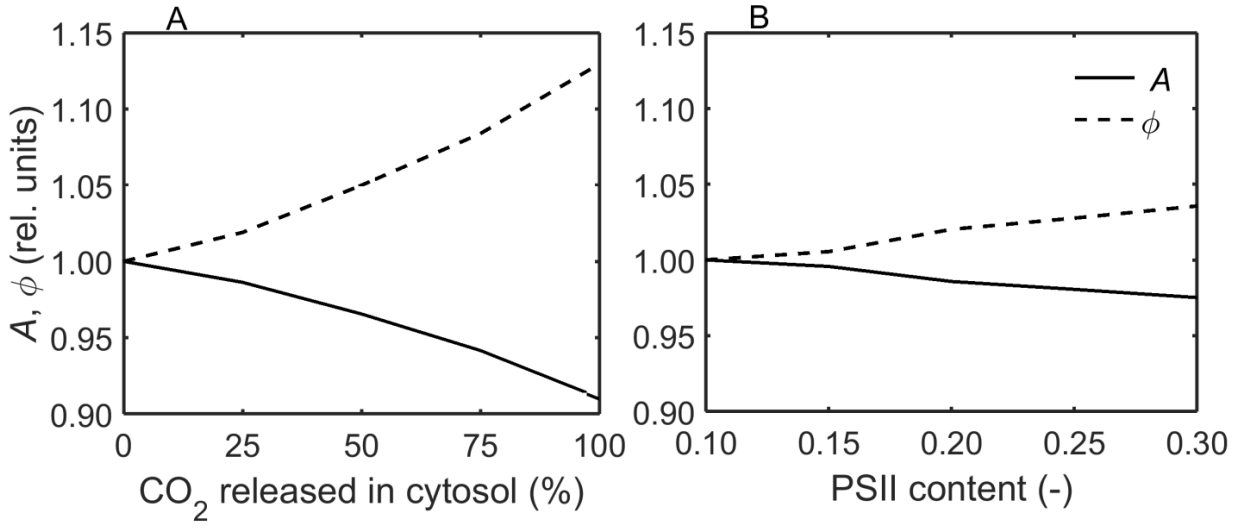

Figure 5.6**.** Effect of cytosolic CO_2 release on photosynthesis and the efficiency of the CO_2 concentration mechanism. Responses of photosynthesis rate (*A*, solid lines) and leakiness (ϕ, dashed lines) for increased fraction of CO_2 released in the bundle sheath cytosol (A) and PSII content in the bundle sheath cells (B). The simulation was done at ambient [CO_2] of 380 µmol mol^{-1}, 21 % oxygen, irradiance of 1500 µmol m^{-2} s^{-1} and at a temperature of 25 °C. *A* and ϕ were divided by their respective values at 0 % fraction of CO_2 release in the bundle sheath cytosol or PSII content of 0.10 (A = 23.5 µmol m^{-2} s^{-1} and ϕ = 0.28). Dashed line represents leakiness and solid lines indicate photosynthesis.

5.8.5 Biophysical processes have little influence on temperature dependency of C_4 photosynthesis and leakiness

Fig. 5.7 shows the relative contribution of temperature dependence of the diffusion and dissolution of gases and biochemical processes to the temperature responses of CO_2 assimilation and leakiness (ϕ) (calculated at C_a of 380 µmol mol^{-1}, 21 % O_2, irradiance of 1500 µmol m^{-2} s^{-1}). The effect of diffusion in the gaseous phases was lumped with that of the liquid phase since temperature dependency of diffusion coefficients of gaseous CO_2 and O_2 were weak (Fig. C.4, Appendix C). *A* did not respond to temperature when temperature dependency of biochemical

processes was ignored (Fig. 5.7A). Temperature responses of *A* for the cases "Base" and "Biochemical" overlapped showing the strong contribution of biochemical processes (Fig. 5.7A). Simulation also showed that the mean CO_2 and O_2 concentration in the bundle sheath chloroplast showed similar trends as the response of *A* while photorespiration increased with temperature continuously (except in the "Biophysical" case where they were constant). Fig. 5.7 (B) also shows that biophysical processes minimally contribute to the temperature response of ϕ (Eq. C.2.23) except for a slight change (< 5 %) at 30 °C. The predicted ϕ was the lowest at 18 °C due to a simultaneous decline of photosynthetic sink and PEP carboxylation (Fig. 5.7B, Fig. C.6, Appendix C). Overall, simulation results suggest that biochemical processes contribute strongly to the temperature response of C_4 photosynthesis and the efficiency of CCM.

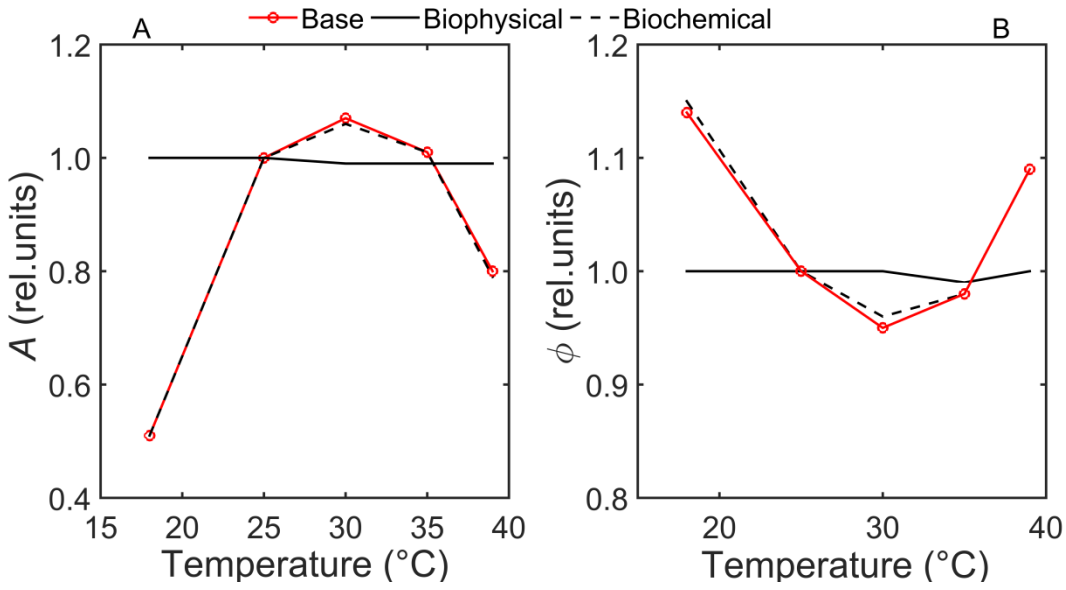

Figure 5.7. Contributions of biophysical and biochemical parameters to temperature responses of photosynthesis and some variables of the CO_2 concentration mechanism. Temperature response of photosynthesis (*A*) (panel A) and leakiness (ϕ) (Panel B). Base represents the case where biochemical and biophysical processes vary with temperature. Biophysical represents the case where only biophysical processes were assumed to vary with temperature. Biochemical represents the case where only biochemical processes were assumed to vary with temperature. *A* and ϕ were divided by their default value at 25 °C (A = 23.5 µmol m^{-2} s^{-1} and ϕ = 0.28).

5.9 Discussion

The leaf anatomy of C_4 crops may influence C_4 photosynthesis by constraining the distribution of light and diffusion of gases. Mechanistic understanding of anatomical and biochemical control of photosynthesis improves through the use of reaction-diffusion models of gas transport that account for a realistic leaf anatomy and distribution of light energy (Berghuijs *et al.*, 2016). Previous C_4-models (Collatz *et al.*, 1992; von Caemmerer and Furbank, 1999) incorporated the role of leaf anatomical features into apparent CO_2 conductances or simplified the diffusion of gases in the gaseous phase due to a 2-D leaf anatomy (Chapter 4). Recently, a three-dimensional model of gas and metabolite transport in C_4 photosynthesis in rice leaf anatomy was developed (Wang *et al.*, 2017). Here we presented a model considering the full 3-D geometry of a C_4 leaf. Diffusion of CO_2 and O_2 in the leaf tissue was modeled while accounting for the light environment provided by the spatial arrangement of mesophyll and bundle sheath cells. The influence of the differences in PSI and PSII content, degrees of grana formation and chlorophyll content of chloroplasts in these cells on light absorption were also accounted for using information from literature. The 3-D model presented here exceled our 2-D model of gas transport in maize leaf (Chapter 4) in several aspects. It described the distribution of light energy between mesophyll and bundle sheath cells (Fig. 5.1B): this has implications in the assessment of the efficiency of CCM at various light intensities (Fig. 5.4B). The 3-D model also revealed that the CO_2 concentration in the intercellular air space (Fig. 5.1D) is not totally uniform as was assumed previously in the 2-D model. In addition, the influence of PSII abundance in bundle sheath cells on photosynthesis in relation to oxygen production, ATP production and photorespiration could now be directly examined (Fig. 5.6B). Modeling oxygen diffusion was also important due to the marked differences in responses of photosynthesis with and without oxygen production (Fig. C.5, Appendix C) even at low PSII fraction of 0.10.

The light profile shows that large gradients exist in the leaf tissue as expected from the Kranz-anatomy when illuminated unilaterally. Even in bundle sheath chloroplasts, the gradient in light absorption (Figs. 5.1B and 5.2A) was substantial in that centrifugally arranged bundle sheath chloroplasts facing the upper epidermis (where the light source was applied) had higher absorption than those facing the lower epidermis. Consequently, there was a considerable

gradient in concentration of CO_2 in liquid phase (Fig. 5.1C) which determines the transition between electron and enzyme limited CO_2 assimilation rates at various depths in the leaf tissue. The light gradient may have consequences in energetics of maize photosynthesis as it implies that the capacity of the C_4 cycle and the efficiency of CCM vary in the leaf tissue. Erect leaves of maize, however, could help in illuminating the abaxial side, probably justify the lack of bundle sheath chloroplast movement and slow movement of mesophyll chloroplasts in response to light intensity (Taniguchi *et al.*, 2003; Ryu *et al.*, 2014). The irradiance response of $\bar{x}$ depends strongly on the relative absorption coefficient of bundle sheath and mesophyll chloroplasts (Fig. 5.4B). At optimal photosynthesis rate, $\bar{x}$ was constant at 0.40 across all irradiances in agreement with previous reports (von Caemmerer and Furbank, 1999; Yin and Struik, 2012).

Photosynthesis was maximized when about 50 % of the light was absorbed in bundle sheath cells. Similarly, about 30 to 40 % absorbed light by bundle sheath cells resulted in optimum photosynthesis (Wang *et al.*, 2014*a*). If leakiness should also be minimized at the same time, our results indicate that bundle sheath cells should absorb about 60 % of the light. The chlorophyll concentration in bundle sheath cells could not be increased more without affecting photosynthesis or the efficiency of CCM (Fig. 5.4). Increasing the chlorophyll concentration in bundle sheath cells compensated for the shading effect of mesophyll cells as it boosted ATP production in bundle sheath cells. Consequently, it also minimized leakiness by reducing the CO_2 delivery into bundle sheath cells (Fig. 5.4C) relative to fixation rate. However, this resulted in low $\bar{C}_c$, which ultimately reduced photosynthesis. In converse, decreasing the chlorophyll content in bundle sheath cells resulted in high $\bar{C}_c$ but Rubisco was light-limited. Therefore, optimal photosynthesis occurred when the photon absorption per unit photosystem in mesophyll and bundle sheath cells was equal. For this to happen, the total amount of photosystem per mole of chlorophyll in bundle sheath cells should be 1.5 times higher than that of mesophyll cells (ratio of absorbed light in the bundle sheath to that in mesophyll is 1.5). This could be possible despite the spatial constraint in the bundle sheath cells (Sage and McKown, 2005) since bundle sheath chloroplasts are usually more dense than mesophyll cells (Dengler *et al.*, 1994; Dengler and Nelson, 1999). Our results support the view that bundle sheath cell size, which determines the content of light harvesting

machinery and thus leaf energetics, may influence the evolution of C_4 photosynthesis (Bellasio and Lundgren, 2016).

The stimulation of growth of C_4 plants was proposed mainly due to increased photosynthesis rate by enhanced intercellular CO_2 (Ghannoum *et al.*, 2000). To test the extent of contribution of direct diffusion of CO_2 to bundle sheath cells, we solved the microscale gas transport model equation using various pathways (Fig. C.7, Appendix C). To simulate the less-developed bundle sheath cell wall in young leaves, suberin lamella was assumed to be not present. Fig. 5.5 shows that diffusion through exposed mesophyll surface and mesophyll-bundle sheath interface could contribute to photosynthesis substantially at about 3.8 times the ambient [CO_2] (380 µmol mol^{-1}), although it was argued that the high resistance to diffusion of this pathway may not allow it (Ghannoum *et al.*, 2000). When the entire surface of bundle sheath cells was assumed to be accessible to CO_2, this contribution became more important. This supports the suggestion that in young leaves, direct diffusion of CO_2 may be a potential mechanism contributing to stimulation of photosynthesis at elevated CO_2 levels (Ghannoum *et al.*, 2000). Coincidentally, maize plant grown at elevated CO_2 levels was reported to reduce the activity of C_4 enzymes, which reduces CO_2 delivery to bundle sheath cells, with little change in the rate of photosynthesis (Maroco *et al.*, 1999). Nevertheless, the atmospheric CO_2 levels may not reach 1000 µmol mol^{-1} in the near future; however, external [CO_2] in growth chambers and greenhouses could easily be elevated beyond this value.

Cytosolic PEPCK activity and photorespiration due to oxygen evolution in bundle sheath cells were suggested to promote leakage (von Caemmerer and Furbank, 1999; Wang *et al.*, 2014*a*). Our results also show that the efficiency of CCM would be reduced in those cases. The extent of reduction might have been lessened due to the centrifugal position of chloroplasts in bundle sheath cells (Fig. 5.1A) which benefits re-assimilation since most of the cytosolic CO_2 has to cross the chloroplast membrane twice before leaking out. This is also supported by abundant mitochondria that are closely associated with chloroplasts in bundle sheath cells (Hylton *et al.*, 1988). Simulation shows that even when all the CO_2 is released outside chloroplasts, leakiness increased only by 15 % (Fig. 5.6A). Flux-balance modeling of C_4 metabolism which does not model bundle sheath chloroplast position predicted that cytosolic CO_2 release impacts leakiness

much more than the aforementioned value (Wang *et al.*, 2014*a*). This implies that prediction of leakiness would be overestimated when organelle positioning is not accounted for.

The temperature dependency of biophysical processes related to CO_2 transport contributed minimally to the temperature response of photosynthesis and the efficiency (ϕ) of CCM at ambient [CO_2] of 380 µmol mol^{-1} and irradiance of 1500 µmol m^{-2} s^{-1}. Neglecting the temperature dependency of dissolution and diffusion of gases did not alter the peaked response of photosynthesis rate implying that the temperature response of the biochemical processes dominates (Fig. 5.7A). In addition, PEP carboxylation and photosynthesis were limited by electron transport across many of the temperature values (Fig. C.6, Appendix C). It should also be noted that the influences of temperature on diffusion of several metabolites that are involved in the delivery of CO_2 were not accounted for here. However, these processes are usually suggested to be fast (Sowiński *et al.*, 2008), and thus their transport may not be limiting. Furthermore, temperature dependency of biochemical processes contributed considerably to the temperature response of the efficiency (ϕ) of CCM (Fig. 5.7). The predicted ϕ resembles the response reported previously for NADP-ME subtype C_4 plants (Henderson *et al.*, 1992; von Caemmerer *et al.*, 2014; Yin *et al.*, 2016). The high dependence on biochemical processes supports the suggestion that ϕ is dominantly controlled by the balance of C_4 and C_3 cycles than by bundle sheath conductance (Kromdijk *et al.*, 2010). This is corroborated by similar responses of ϕ to leaf temperature reported previously (Henderson *et al.*, 1992) and close values of ϕ for a range of C_4 grasses (Cousins, Badger & von Caemmerer 2008).

5.10 Conclusion

A 3-D reaction-diffusion model of gas exchange in C_4 leaves that includes a realistic 3-D leaf anatomy and light transport was developed here. The model improved up on our previous 2-D model (Chapter 4). Photosynthesis was optimized for distribution of chlorophyll between bundle sheath and mesophyll cells. Environmental responses of C_4 plants in relation to photosynthesis were investigated. The results show that direct CO_2 diffusion could support photosynthesis in young leaves at elevated [CO_2]. In addition, cytosolic CO_2 release would result in loss of CCM

efficiency but to a lesser extent than anticipated before. Simulations also suggest that biochemical processes control temperature response of photosynthesis and leakiness while biophysical processes contributed little. The model could serve as a tool to investigate C_4 photosynthesis in relation to gas transport and light propagation further. It is worth nothing that metabolite transport should be included to investigate the role of leaf microstructure and anatomy on C_4 metabolism through metabolite exchange between bundle sheath and mesophyll cells under various light environments. In addition, the role of bundle sheath extensions in light propagation and photosynthesis should be modeled using leaf geometrical anatomy including them.

6 General conclusion and future perspectives

C_4 photosynthesis is a key process driving productivity in food and bioenergy crops such as maize, sugar cane and sorghum. It is the most efficient form of photosynthesis resulting in superior resource use efficiency. The superior resource-use efficiency of C_4 plants is due to suppression of photorespiration by the CO_2 concentration mechanism (CCM). The leaf anatomy impacts CCM by determining the distribution of gases and light energy. The main aim of this dissertation was to develop microscale models that allow mechanistic understanding of the role of leaf anatomical factors, which constrain gas diffusion and light distribution, and biochemical processes that consume or produce gases in photosynthesis of C_4 plants. Maize was used as a model system. In this general discussion, I will summarize and discuss the findings of this dissertation. Then, future perspectives and recommendations for further research will be given.

6.1 Modeling gas transport during photosynthesis of C_4 plants: practices and challenges

Gas exchange models based on a core understanding of a mechanism of photosynthesis have been used to increase quantitative insight in support of research towards improving crop productivity through alteration of leaf anatomical traits in C_3 plants (Tholen and Zhu, 2011; Ho *et al.*, 2012, 2016). However, literature survey showed that application of such models for photosynthesis of C_4 plants has been limited. Since CCM is a concerted action of leaf anatomy, ultrastructure and biochemistry, to examine the individual contributions of these factors to the efficiency of photosynthesis, microscale models of gas transport that incorporate explicit anatomical features are essential. Such models are useful to analyze the bundle sheath conductance; an important limitation to C_4 photosynthesis. Usually, bundle sheath conductance is determined from gas exchange and chlorophyll fluorescence measurements in combination with a biochemical model of C_4 photosynthesis. The conductance thus estimated combines the effects of leaf biochemistry and leaf anatomy. Consequently, the potential limitation of each microstructural and ultrastructural features cannot be individually examined. Therefore,

development of microscale models for photosynthesis of C_4 plant was found timely and beneficial.

Improving upon earlier microscale models of gas transport in a C_3 leaf, it was recently shown that actual intricacies of leaf anatomy are beneficial in elucidating microscale gas profiles (Ho *et al.*, 2016). To extend such approaches to C_4 plants and examine anatomical constraints of gas transport during C_4 photosynthesis, a realistic geometry of leaf anatomy is essential. The leaf microstructure geometry could be obtained from microscopy and X-ray micro-CT images among others (Verboven *et al.*, 2010). X-ray micro-CT images give an excellent contrast between the air and cellular phase with minimal change to leaf structure. However, resolving cell boundaries of cells and cellular organelles requires extensive image processing and is not easy. Although this could be avoided by using microscopy experiments, extensive sample preparation alters leaf anatomy. The leaf tissue could also be approximated using simple geometrical shapes, however, a novel approach is to parametrize the geometry by direct reconstruction from real images thereby avoiding assumptions regarding volumes of compartments. Overall, geometrical simplifications should be avoided and the leaf geometry should be obtained using imaging techniques.

Reaction-diffusion equations of gas transport in leaf tissue are then developed by combining diffusion of gases and kinetics of photosynthesis. The distribution of light energy in leaf tissue is conveniently modeled using ray tracing. In this regard, advanced methods that could effectively deal with structural complexities of biological tissues should be used to model light absorption and scattering accurately. Parameters of photosynthesis kinetics are estimated from measurements of combined gas exchange and chlorophyll fluorescence. The resulting set of reaction-diffusion equations are discretized over the geometry and solved numerically. This approach of solving the model equations requires high capacity computers and licensed software tools which has implications on practicality of the model tools. The computational burden could be minimized by considering 2D. Primary validation of the model is carried out by comparing model predicted responses of photosynthesis to CO_2 and irradiance to those of measurements. Various model output could also be compared to literature reports to verify model outputs. Thorough validation requires measurements of CO_2 and assimilation profiles in leaf tissue, which are not widely available. In conclusion, I have identified practices and challenges of gas transport

modeling in C_4 plants which influenced subsequent planning and execution of model development.

6.2 Bundle sheath conductance in relation to leaf anatomy

Bundle sheath conductance depends on a number of anatomical properties such as cell wall thickness of bundle sheath cell, surface area of bundle sheath cells per unit leaf area and the presence or absence of suberin layer (von Caemmerer and Furbank, 2003). Few studies quantified bundle sheath conductance compared to mesophyll conductance in C_3 plants. In addition, the role of these anatomical properties to bundle sheath conductance in response to physiological variables such as leaf nitrogen content and age were not examined extensively.

In Chapter 3 we increased quantitative information on CO_2 conductances in a maize leaf. The results confirmed positive relationship between g_{bs} and LNC. The cause of such a relationship was not clear although the decline of leaf nitrogen content with ageing have altered leaf anatomy consistent with the trends in g_{bs} across leaf ages. The results imply that increased nitrogen supply to boost growth may decrease the efficiency of CCM. However, this was not detrimental for rate of photosynthesis. The results would improve if advanced leaf anatomy imaging techniques that minimize intensive sample preparation and higher resolution like molecular imaging (Palmer *et al.*, 2015) are used. Future studies should also investigate changes in composition of pectin polysaccharides in bundle sheath cell wall since that influence diffusion through the wall as suggested recently for Miscanthus (Ma *et al.*, 2017). In addition, the possible influence nitrogen on membrane composition and plasmodesmata abundance should be considered before changes in leaf anatomy are ruled out as non-explanatory for trend of g_{bs} with LNC. Recently a method has been developed for quantifying abundance of plasmodesmata in intact leaves of C_4 plants (Danila *et al.*, 2016).

Predictions of leakiness and the ratio of quantum efficiency of CO_2 to that of PSII electron transport have shown that the balance of C_3 and C_4 cycles may have not been altered by LNC and leaf age. Simultaneous carbon isotope discrimination measurement will provide a more direct evidence. In addition, enzyme assay to determine maximal activities of enzymes would allow to

better constrain model parameters required for estimating g_{bs}. Future investigations should also examine directly whether possible underestimation of rate of electron transport by the use of rectangular flash in chlorophyll fluorescence as opposed to multiphase flash have contributed to poor estimates of bundle sheath conductance.

6.3 The roles of leaf microstructure, ultrastructural and biochemistry to the efficiency of CCM

Leaf anatomy and biochemistry are interwoven *in vivo*. To discern the relative contribution of each to photosynthesis, microscale models are good alternatives. In Chapter 3, it was shown that leaf anatomical properties correlated with bundle sheath conductance. Consequently, the effect of permeability of biological membranes, diffusive properties of cell wall and liquid phase media, abundance of plasmodesmata, maximum capacity of enzymes and carbonic anhydrase on CCM needs to be investigated. Such analysis could be carried out more rapidly using microscale models than approaches that involve antisense suppression or overexpression of genes or proteins.

In Chapter 3 and elsewhere in literature reports, bundle sheath conductance was estimated from resistance models that treat diffusion and photosynthesis as sequentially rather than simultaneously occurring processes (von Caemmerer and Furbank, 2003; Yin *et al.*, 2011*b*). In addition, the resulting CO_2 conductances provide the magnitude of the resistances only but not the importance of factors contributing to them. A two-dimensional microscale model of gas exchange accounting for a realistic leaf microstructure was developed for the first time for photosynthesis of C_4 plants in Chapter 4. Due to the agreements of model predictions of photosynthesis rate with that of the experiment and the responses of leakiness and mean concentration of CO_2 in bundle sheath cells to literature values, the model was deemed sufficient to carry out successive analysis. The analysis revealed that the resistance of the mesophyll-bundle sheath interface is a major contributor to bundle sheath resistance. This supported our earlier recommendation that more investigation on bundle sheath cell wall and plasmodesmata would help explain the variation of g_{bs} with LNC. In addition, we learned that the mesophyll cell wall

was the most significant limitation to mesophyll conductance. Furthermore, the suberin layer at the exposed surface of bundle sheath cell wall was found beneficial in reducing leakage. Thus, future investigations should consider CO_2 permeability of mesophyll-air space interface and mesophyll-bundle sheath interface to improve our understanding of the limitation of g_m and g_{bs} on photosynthesis of C_4 plants. The permeability of biological membranes to bicarbonate may not be worth considering since it influenced the rate of photosynthesis or bundle sheath conductance only minimally.

In addition to leaf anatomical properties, biochemical factors such as concentration of carbonic anhydrase and maximal activities of PEPC and Rubisco in relation to the rate of C_4 photosynthesis were investigated. The local carbonic anhydrase was found essential in mesophyll cells but would decrease the efficiency of the CO_2 concentration mechanism if abundant in bundle sheath cells. In particular, at low CO_2, carbonic anhydrase in mesophyll was found essential to high rate of photosynthesis. Since the enzyme contributes to high mesophyll conductance, this result implies that during stress, where intercellular CO_2 drops low, increasing mesophyll conductance can boot C_4 photosynthesis. Furthermore, increasing the ratio of maximal activities of PEPC relative to Rubisco decreases photosynthesis when this ratio is greater than 3. This shows the metabolic robustness of the C_4 pathway. Similar leakiness values predicted in Chapter 2 may have also been due to this ratio not being highly altered by LNC. In conclusion, microscale modeling indeed allowed analysis the limitations provided by leaf ultrastructural properties unlike the lumped conductance model in Chapter 2. Thus, the two-dimensional model was found to be an important tool for mechanistically analyzing CO_2 transport in liquid phase media during C_4 photosynthesis.

6.4 A three-dimensional model of gas transport for photosynthesis of C_4 plants

Diffusion in leaves is three-dimensional in nature due to non-uniform distribution of stomata on epidermis. The two-dimensional model described in Chapter 4 has limitations in describing the three-dimensional nature of diffusion. It ignores the connectivity of air spaces and its role in

affecting the diffusion of gases in gaseous phase. Paradermal diffusion, however, in heterobaric leaves such as maize where bundle sheath cell extensions break the flow, does not contribute to photosynthesis. Furthermore, a three-dimensional leaf geometry is important in modeling the light gradient in the leaf. Because of the importance of the three-dimensional leaf anatomy in diffusion and light propagation, we extended in Chapter 5 the two-dimensional model of Chapter 4 to develop a three-dimensional model for photosynthesis of C_4 plants.

Light microscopy images of leaf anatomy obtained in Chapter 3 were considered. The images were found suitable in resolving the leaf anatomical details unlike images of X-ray micro-CT. Consequently, the 3-D geometrical model was constructed from several series of two-dimensional images. The propagation of light energy inside a leaf was modeled using ray-tracing adapted to deal with structural complexities of leaf tissues so as to obtain a realistic light absorbance profile. Due to the high resistance of bundle sheath cells, the concentration of O_2 in these cells could not be neglected. Consequently, reaction-diffusion models for transport of CO_2 and O_2 were developed. As expected, the 3D model required a high-performance computer with a 16-GB RAM. The model also required a long list of parameters but provided more insights in to photosynthesis. Due to uncertainties in the maximum electron transport rate and some of the gas diffusion parameters there were underestimations. Chlorophyll fluorescence derive electron transport rate may also be uncertain as it is less certain for C_4 plants due to differences in the nature of chloroplasts between mesophyll and bundle sheath cells, which biases the interpretation of chlorophyll fluorescence signals. To improve the accuracy of the fitting, validation of the light absorbance may be beneficial. The light profile shows that large gradients of light intensity exist. This means that chloroplasts at some positions are light saturated while some chloroplasts are light-limited. This may be one of the reasons why the convexity of the light response curve for the whole leaf tissue is less than one (at the level of the chloroplast, the convexity is very close to one). Next, the gas concentration profile in the leaf tissue was computed. As expected from CCM, the mean concentration of CO_2 in bundle sheath cells was higher than that of the ambient air. The concentration profile of CO_2 in the air spaces was largely uniform while in the liquid phase large gradients existed. The mean concentration of oxygen in bundle sheath cell was much higher than in the ambient air and consequently, the response of photosynthesis was impacted when this gradient was neglected.

The three-dimensional model was applied to investigate several physiological questions. It was discussed above that the Kranz-anatomy results in disproportionate distribution of light energy among mesophyll cells and bundle sheath cells. Consequently, the relative rates of CO_2 delivery and reduction are influenced. One way to improve light access to bundle sheath cells is to improve the absorption by increasing chlorophyll content. At the same time, the light absorption and ATP production by mesophyll cells should not be compromised to maintain adequate CO_2 supply to bundle sheath cells. In this regard, it is essential to know whether and how optimizing chlorophyll distribution between mesophyll cells and bundle sheath cells improves photosynthesis. To test this, several light absorbance profile were generated for each assumed chlorophyll content. Simulations show that photosynthesis rate does not increase by simply increasing the chlorophyll content of bundle sheath cells although the light absorption increases. A high photosynthesis rate at low leakiness requires that the chlorophyll content of bundle sheath cells should be such that the light absorbed per unit photosystem is equal in mesophyll cells and bundle sheath cells. This required a higher photosystem per mole of chlorophyll in bundle sheath cells than in mesophyll cells. This result has implications for the evolution of C_4 plants. A large bundle sheath cell in C_3 plants was recently shown to be favorable for evolution of C_4 photosynthesis which requires more energy in bundle sheath cells (Bellasio and Lundgren, 2016). Overall, the leaf anatomy influences C_4 photosynthesis by constraining CO_2 and light availability.

It was shown that the rate of photosynthesis responded to elevated CO_2 although it is believed that photosynthesis is CO_2-saturated (Ghannoum *et al.*, 2000). This was suggested to be due to direct diffusion of CO_2 especially in young leaves that may not have well-developed bundle sheath cell walls. Leaf anatomical measurements in Chapter 3 showed that the total surface area of mesophyll cells and bundle sheath cells was considerable. The model was thus applied to test the potential of leaf anatomy and ultrastructure in allowing direct diffusion of CO_2 to support appreciable photosynthesis. Simulations showed that in matured leaves the contribution of direct diffusion was modest while it was considerable in juvenile leaves. Although direct diffusion may not be responsible for high responsiveness of C_4 photosynthesis to elevated CO_2, its contributions could not be neglected.

The role of leaf three-dimensional leaf anatomy in analyzing temperature response of C_3 photosynthesis showed that maximum enzyme activities at chloroplast level are more temperature sensitive than those estimated without the consideration of the anatomy (Juurola *et al.*, 2005). To discern the contribution of biochemical and biophysical factors to temperature dependency of photosynthesis of C_4 plants, a sensitivity analysis was carried out. Unlike C_3 plants, temperature responses of photosynthesis and leakiness are predominantly controlled by biochemical factors. This explains the smaller variation of the responses of leakiness measured for various C_4 plants as such differences in leaf structure may not be important.

The microscale model was used to examine to what extent cytosolic CO_2 increase due to decarboxylation of C_4 acids in bundle sheath cytosol or photorespiration increases leakiness. When position of organelles like chloroplasts is accounted for by the microscale model, the predicted increase in leakiness was found to be only moderate compared to flux-balance models.

In conclusion, the three-dimensional model provided evidence that leaf anatomy may constrain C_4 photosynthesis by mediating distribution of light and gas transport. Several hypotheses were tested showing the applicability of the model in addressing physiological questions related to gas transport, light propagation and C_4 photosynthesis.

6.5 Future perspectives and recommendations

In Chapter 3, CO_2 conductances were investigated in relation to leaf anatomy. While we addressed how and why bundle sheath conductance responds to leaf nitrogen content and leaf aging, some research questions need to be investigated further. These are:

- Whether and how does the abundance and ultrastructure of plasmodesmata respond to leaf nitrogen content and leaf aging?
- Do permeability values of the chloroplast envelope and the plasma membrane respond to leaf nitrogen content and age?

We recommend a replicate study of the impact of leaf nitrogen content and age on bundle sheath conductance but using advanced methods of leaf anatomy acquisition such as synchrotron micro-

tomography, phase contrast tomography and nano-tomography to minimize leaf anatomy artifacts. Such a study requires careful planning. Measurements of the light and CO_2 response of photosynthesis at two oxygen levels (a total of 42 measurements) takes about 10 h for one plant. At the end of this, the leaf anatomy of the measurement leaf should be imaged subsequently. The leaf nitrogen content must also be measured. However, this results in non-ideal successive use of the same sample for different experiments. Leaf samples nearby the measurement could alternatively be used to avoid this as anatomical properties of the mid-portion of leaves tend to change less dramatically.

We have developed tools to further investigate C_4 photosynthesis in relation to leaf anatomy in Chapters 4 and 5. The models were applied to examine several research questions relating to leaf anatomy and biochemistry. However, the models could be extended further to investigate the following research questions:

- What is the role of leaf anatomical factors on transport of several intermediate metabolites, thus the rate of photosynthesis?
- How does ultrastructural details of plasmodesmata impact the metabolite transport and the efficiency of the CO_2 concentration mechanism?
- What are the effects of bundle sheath extensions, which may improve light propagation in leaf tissue, on the efficiency of photosynthesis?

To address the above questions, a metabolite transport model should be included in the existing leaf anatomical model. A new geometrical model that includes bundle sheath extension is also required. Addition of a metabolite transport model makes the 3-D model even more complex and takes more computational resources to solve it. However, the insights generated from this kind of model will be valuable and accurate since they are derived from a whole system perspective instead of the CO_2 transport aspect alone. This is important since C_4 photosynthesis is also an interplay of several metabolite exchanges. In addition, it is recommended that the light propagation in the leaf used in the gas exchange measurement should be experimentally validated for more accuracy. The light propagation model could be improved by considering a diffuse light source at the leaf surfaces and also light directed on both surfaces since maize leaf has an up-right

leaf. For even more accuracy, the chlorophyll distribution between mesophyll and bundle sheath cells should be determined to constrain the absorption coefficients better.

In general, simplified microscale models of gas exchange provide mechanistic understanding of the gas transport in relation to leaf anatomy of C_4 plants. This would not be possible using lumped conductance based models. In particular, since C_4 plants involve two cell types in CO_2 transport, resistance models would be difficult. More advanced models would excel the microscale models in generating systems level understanding, but are going to be complex and computationally demanding.

Appendix A

A.1. Composition of nutrient solution and model equations

The nutrient solution composition is as shown in Table A.1.1 (below). There were a total of 6 applications of the nutrient solutions prepared for the three nitrogen levels (N1, N2 and N3). Table A.1.2 shows the application spread over the weeks.

Table A.1.1 Composition of nutrient solution used for growing maize plants

Nutrients	Conc. (M)	Amount ($g\ mol^{-1}$)	mg/ml solution				
			N	P	K	Mg	Ca
$Ca(NO_3)_2.4H_2O$	1	236.15	28				40
NH_4NO_3	2	80.04	56				
K_2SO_4	0.5	174.26			39		
KH_2PO_4	1	136.09		31	39		
$MgSO_4.7H_2O$	1	246.47				24	
KNO_3	2	101.11	28		78		

Table A.1.2 Application of nutrient solution spread over weeks. Nitrogen (N), phosphorous (P), potassium (K), magnesium (Mg) and calcium (Ca).

Nutrients	Week 1 to 4 (Mg per pot)	Week 5 and 6 (Mg per pot)
N1	25	50
N2	63	125
N3	156	313
P	55	110
K	208	417
Mg	83	165
Ca	38	75

Bundle sheath conductance (g_{bs}) was estimated from equations of the biochemical model of C_4 photosynthesis (von Caemmerer and Furbank, 1999). Based on this model, in mesophyll cells, phosphoenolpyruvate (PEP) carboxylation rate V_p is enzyme-limited or electron-transport-limited. Values and units of symbols are listed in Table A.1.3.

V_p is given as (von Caemmerer and Furbank, 1999):

$$V_p = \min\left\{\frac{C_m V_{p,max}}{C_m + K_p}, \frac{x J_{ATP}}{2}\right\} \quad \text{(A.1.1)}$$

The first term between the brackets is for the enzyme-limited rate while the second one is for the electron-transport-limited rate. C_m is the concentration of CO_2 in the mesophyll cytosol, K_p is the Michaelis-Menten constant of PEP carboxylase (PEPC) for CO_2, and $V_{p,max}$ is the maximum catalytic rate of PEPc. The parameter x is the fraction of ATP allocated to the C_4 cycle. The rate of total electron transport in the model of von Caemmerer and Furbank (1999) was changed here to J_{ATP}, the rate of ATP production (Yin and Struik, 2012). J_{ATP} is given by Yin *et al.* (2011b) as:

$$J_{ATP} = \frac{s' I_{inc} (\Delta F / F_m')}{(1-x)} \quad \text{(A.1.2)}$$

$$\Delta F / F_m' = (F_m' - F_s) / F_m'$$

where *s´* is the lumped calibration factor, I_{inc} is incident irradiance; F_s is the steady-state relative fluorescence yield; and F_m' is the maximum relative fluorescence yield in a leaf.

The net rate of CO_2 fixation in bundle sheath chloroplasts (*A*), limited by the rate of Rubisco carboxylation (w_c) or the rate of electron transport (w_j) (Farquhar *et al.*, 1980; von Caemmerer and Furbank, 1999) is expressed as:

$$A = \min(w_c, w_j) - R_d \tag{A.1.3}$$

$$w_c = \frac{(C_c - \gamma^* O_c) V_{c,max}}{C_c + K_{m,C}(1 + O_c / K_{m,O})} \tag{A.1.4}$$

$$w_j = \frac{(C_c - \gamma^* O_c)(1-x) J_{ATP}}{3C_c + 7\gamma^* O_c} \tag{A.1.5}$$

where $V_{c,max}$ is the maximum carboxylation rate of Rubisco; $K_{m,C}$ and $K_{m,O}$ are Michaelis-Menten constants of Rubisco for CO_2 and O_2, respectively; γ^* = 0.5/$S_{c/o}$, $S_{c/o}$ is Rubisco specificity; C_c and O_c are the concentrations of CO_2 and O_2 in the bundle sheath chloroplast; R_d is the rate of CO_2 release through respiration.

The concentration of oxygen in the bundle sheath was calculated as (von Caemmerer and Furbank, 1999):

$$O_c = \alpha A / (0.047 g_{bs}) + O_i \tag{A.1.6}$$

where α is the fraction of O_2 evolution in bundle sheath cells; O_i is the concentration of oxygen in the intercellular air space (assumed 210 mbar); g_{bs} is bundle sheath conductance; and 0.047 takes in a lumped coefficient accounting for solubility and diffusivity of O_2 and CO_2 at 25 °C.

A could also be written as (von Caemmerer and Furbank, 1999):

$$A = V_p - L - R_m \tag{A.1.7}$$

where the rate of CO_2 release through respiration in mesophyll (R_m) is taken as half R_d, and L is the rate of CO_2 leakage. L is given by:

$$L = g_{bs}(C_c - C_m) \tag{A.1.8}$$

where C_c is the mean CO_2 concentration in bundle sheath chloroplasts and C_m is the mean CO_2 concentration in mesophyll cytosol.

C_m was calculated as:

$$C_m = C_i - A / g_m \tag{A.1.9}$$

where g_m is mesophyll conductance and C_i is the measured concentration of CO_2 in the intercellular air space.

C_c was calculated as:

$$C_c = C_m + L / g_{bs} \tag{A.1.10}$$

The procedure of Yin *et al*. (2011*b*) expresses net CO_2 assimilation as limited by four combinations of enzyme and electron transport limitations. The combinations are as follows: (1) when V_p and A are enzyme-limited, (2) when V_p and A are electron-transport-limited, (3) when V_p is enzyme-limited and A is electron-transport-limited, and (4) when A is enzyme-limited and V_p is electron-transport-limited. Combining Eq. A.1.3, Eq. A.1.7 to Eq. A.1.9 and the enzyme-limited-rate of V_p (Eq. A.1.1) results in cubic equations for net CO_2 assimilation for Cases 1 and 3. In addition, combining Eq. A.1.3, Eq. A.1.7 to Eq. A.1.9 and the electron-transport-limited V_p (Eq. A.1.1) results in quadratic equations that allow determining net CO_2 assimilation for the Cases 2 and 4. The quadratic and cubic equations with their solutions are given in Yin *et al*. (2011b). g_{bs} is determined by minimizing the difference between the measured net photosynthesis (main text) and net CO_2 assimilation expressed by this four-limitation model. The minimization was carried out in SAS (SAS Institute Inc., Cary, NC, USA).

Table A.1.3. Parameters of the model

Symbol	Definition	Values	References
K_p	Michaelis-Menten constant of PEPc for CO_2	40 µbar	(Pfeffer and Peisker, 1998)
$K_{m,C}$	Michaelis-Menten constant of Rubisco for CO_2	485 µbar	(Cousins *et al.*, 2010)
$K_{m,O}$	Michaelis-Menten constant of Rubisco for O_2	146 mbar	(Cousins *et al.*, 2010)
$S_{c/o}$	Relative CO_2/O_2 specificity factor for Rubisco	2826 dimensionless	(Cousins *et al.*, 2010)
α	Fraction of Photosystem II activity in bundle sheath	0.1	(von Caemmerer and Furbank, 1999)
R_m	Rate of respiratory CO_2 release from mitochondria in mesophyll	0.5 R_d	(von Caemmerer and Furbank, 1999) R_d is given in Table 1 (main text)
$s´$	Lumped calibration factor	Table 1	Estimated
x	Partitioning factor of J_{ATP} to the C_4 cycle	0.4	(von Caemmerer and Furbank, 1999)

Table A.1.4. Estimates of day respiration (R_d), light conversion efficiency (s') and bundle sheath conductance (g_{bs}) when the quantum efficiency of PSII electron transport was increased by 20 % (Loriaux *et al.*, 2013). The estimates of R_d did not change since Loriaux *et al*. (2013) show that the quantum efficiency of PSII electron transport changed by 6 % at low irradiance levels, for which we estimated R_d.

Leaf age	Leaf type	R_d µmol m^{-2} s^{-1}	s' Original	s' Sensitivity	g_{bs} Original mmol m^{-2} s^{-1}	g_{bs} Sensitivity mmol m^{-2} s^{-1}
A1	N1	1.70±0.20	0.325±0.004	0.271±0.003	0.88±0.55	0.88±0.55
	N2	2.20±0.23	0.328±0.003	0.274±0.003	2.33±0.83	2.33±0.83
	N3	2.16±0.27	0.323±0.006	0.270±0.002	3.56±0.90	3.56±0.90
A2	N1	1.68±0.17	0.327±0.007	0.272±0.005	0.36±0.50	0.36±0.50
	N2	1.65±0.21	0.332±0.003	0.277±0.005	0.51±0.51	0.51±0.51
	N3	2.29±0.19	0.321±0.003	0.267±0.003	1.34±0.62	1.34±0.62

Table A.1.5. Sensitivity of parameters, slope of linearity between mesophyll conductance and leaf nitrogen content (Xg_m), lumped calibration factor (s') and bundle sheath conductance (g_{bs}) for assumed values of fraction of ATP allocated to the C_4 cycle (x). The leaf nitrogen (N) contents are represented by low (N1), intermediate (N2) and high (N3) for young (A1) and old (A2) leaves.

		$s'/s'_{x=0.4}$						$g_{bs}/g_{bs,x=0.4}$					
x	Xg_m	N1A1	N1A2	N2A1	N2A2	N3A1	N3A2	N1A1	N1A2	N2A1	N2A2	N3A1	N3A2
0.35	1.00	1.16	1.14	1.14	1.14	1.14	1.15	1.47	0.93	0.77	0.73	0.77	0.77
0.40	1.00	1.00	1.00	1.00	1.00	1.00	1.00	1.00	1.00	1.00	1.00	1.00	1.00
0.45	1.01	0.98	0.99	0.99	0.99	0.99	0.99	2.19	2.82	2.29	3.07	2.40	2.40
0.50	1.02	0.98	0.99	0.98	0.99	0.98	0.98	3.59	4.99	3.81	5.61	4.25	3.95

Table A.1.6. Linear correlation coefficients between leaf anatomical parameters and CO_2 conductances. M stands for mesophyll cell and BS for bundle sheath cells. A correlation value of 0.70 or greater is deemed important.

Parameters	g_{bs}	g_m	Porosity	Void surface per volume	Connectivity density	M cell wall thickness	S_m	Leaf thickness	S_b	Interveinal distance	BS cell wall thickness	Cell volume
g_{bs}	1.00	0.95	0.81	-0.65	0.04	-0.58	-0.70	0.66	0.51	0.55	-0.56	0.45
g_m	0.95	1.00	0.72	-0.56	0.02	-0.73	-0.80	0.75	0.48	0.58	-0.61	0.54
Porosity	0.81	0.72	1.00	-0.44	0.34	-0.38	-0.52	0.25	0.19	0.49	-0.42	0.05
Void surface per volume	-0.65	-0.56	-0.44	1.00	0.67	0.44	0.11	-0.08	0.05	-0.87	-0.16	0.11
Connectivity density	0.04	0.02	0.34	0.67	1.00	0.14	-0.37	0.21	0.39	-0.60	-0.63	0.30
M cell wall thickness	-0.58	-0.73	-0.38	0.44	0.14	1.00	0.81	-0.46	-0.34	-0.56	0.51	-0.46
S_m	-0.70	-0.80	-0.52	0.11	-0.37	0.81	1.00	-0.78	-0.73	-0.15	0.91	-0.79
Leaf thickness	0.66	0.75	0.25	-0.08	0.21	-0.46	-0.78	1.00	0.83	-0.02	-0.80	0.92
S_b	0.51	0.48	0.19	0.05	0.39	-0.34	-0.73	0.83	1.00	-0.33	-0.88	0.93
Interveinal distance	0.55	0.58	0.49	-0.87	-0.60	-0.56	-0.15	-0.02	-0.33	1.00	0.23	-0.27
BS cell wall thickness	-0.56	-0.61	-0.42	-0.16	-0.63	0.51	0.91	-0.80	-0.88	0.23	1.00	-0.87
Cell volume	0.45	0.54	0.05	0.11	0.30	-0.46	-0.79	0.92	0.93	-0.27	-0.87	1.00

A.2. Determination of mesophyll conductance

A linear relationship between g_m and leaf nitrogen content (LNC) in C_4 plants was reported (Weng and Hsu, 2001; Yin *et al.*, 2011*b*). To fix g_m while estimating g_{bs}, we assumed such a relationship given by $g_m = X_{gm}$ (LNC – n_b). X_{gm} is the slope of linearity, and n_b is the base nitrogen content above which such a relationship holds, assumed to be 0.15 g N m^{-2} (Yin *et al.*, 2011*b*).

A.3. Calculation of model variables

After model parameters were estimated, the equations of von Caemmerer & Furbank (1999) model can be used to solve for V_p (Eq.A.1.1), L (A.1.8), C_c (Eq.A.1.10) and O_c (similar to Eq.A.1.10). Then, leakiness, ϕ, was calculated from:

$$\phi = \frac{L}{V_p} \tag{A.3.1}$$

The fraction of CO_2 assimilated that is lost due to photorespiration, f, was calculated as (von Caemmerer and Furbank, 1999):

$$f = \frac{O_c}{S_{c/o} \times C_c} \tag{A.3.2}$$

The responses of C_c (Eq.A.1.10) to irradiance and CO_2 are shown in Fig. A.3.1 and A.3.2. The response of leakiness (Eq. A.3.1) to irradiance and CO_2 are shown in Fig. A.3.3 and Fig. A.3.4.

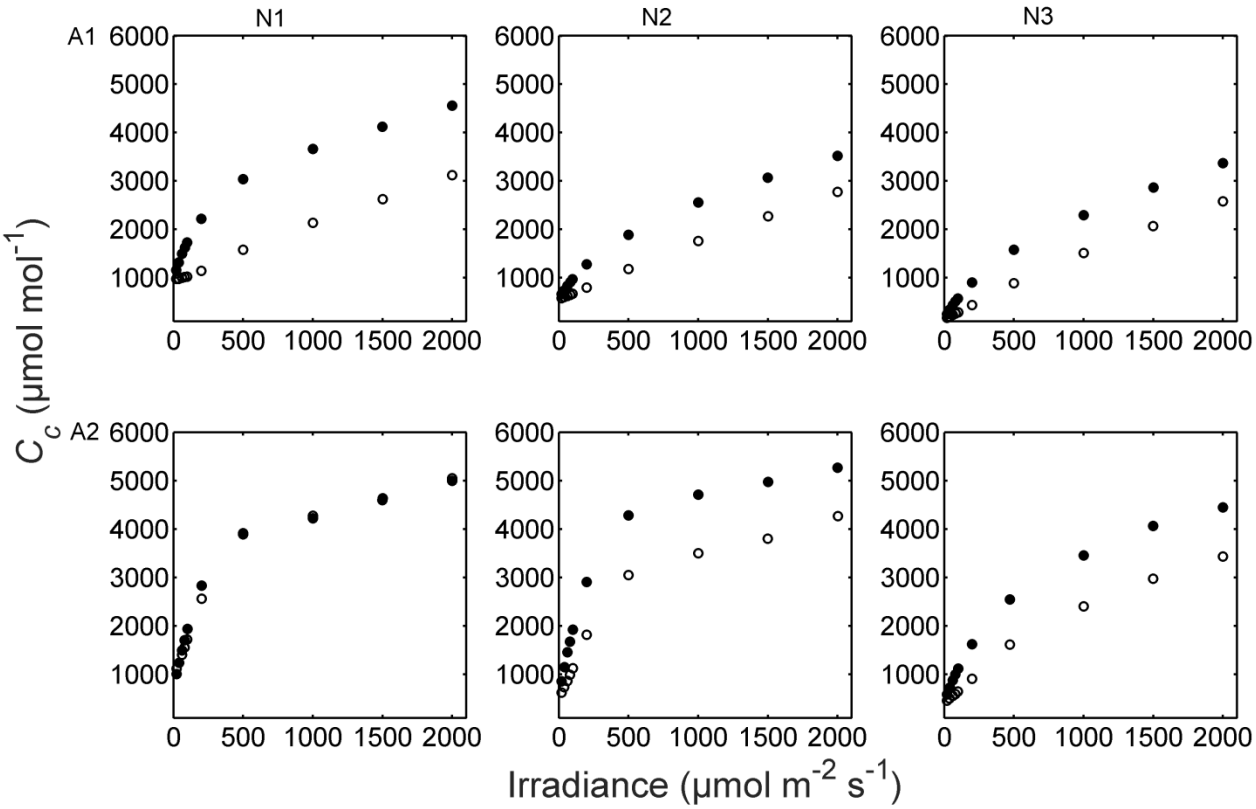

Figure A.3.1. The predicted response of mean concentration of CO_2 in bundle sheath cells to incident irradiance for young (A1) and old (A2) leaves at three nitrogen (N) levels: low (N1), intermediate (N2) and high (N3). The ambient CO_2 was kept at 250 µmol mol^{-1} for 21 % oxygen level (filled circles) and at 1000 µmol mol^{-1} for 2 % oxygen level (open circles).

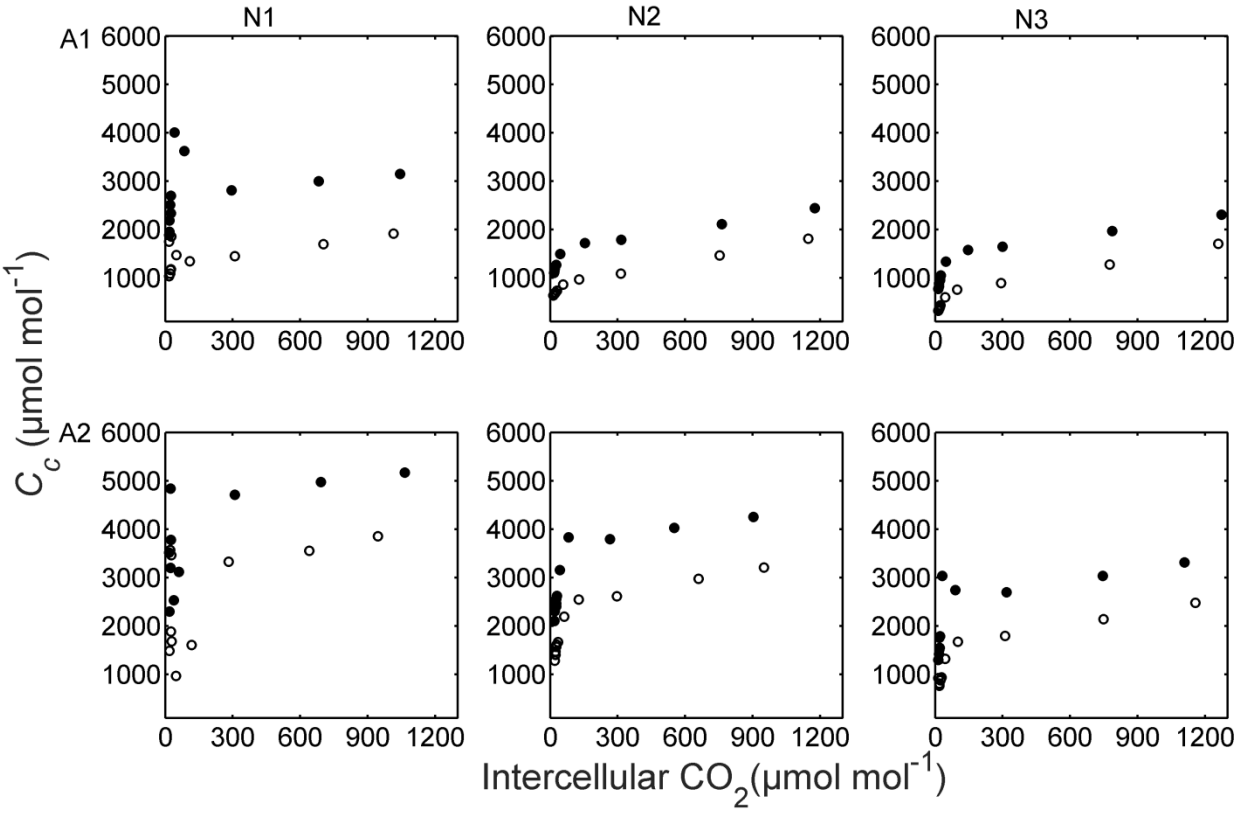

Figure A.3.2. The predicted response of mean concentration of CO_2 in bundle sheath cells to intercellular CO_2 concentration for young (A1) and old (A2) leaves from maize plants grown under three nitrogen (N) levels: low (N1), intermediate (N2) and high (N3). The oxygen levels were 21 % (filled circles) and 2 % (open circles). The irradiance was kept at 1500 µmol m^{-2} s^{-1}.

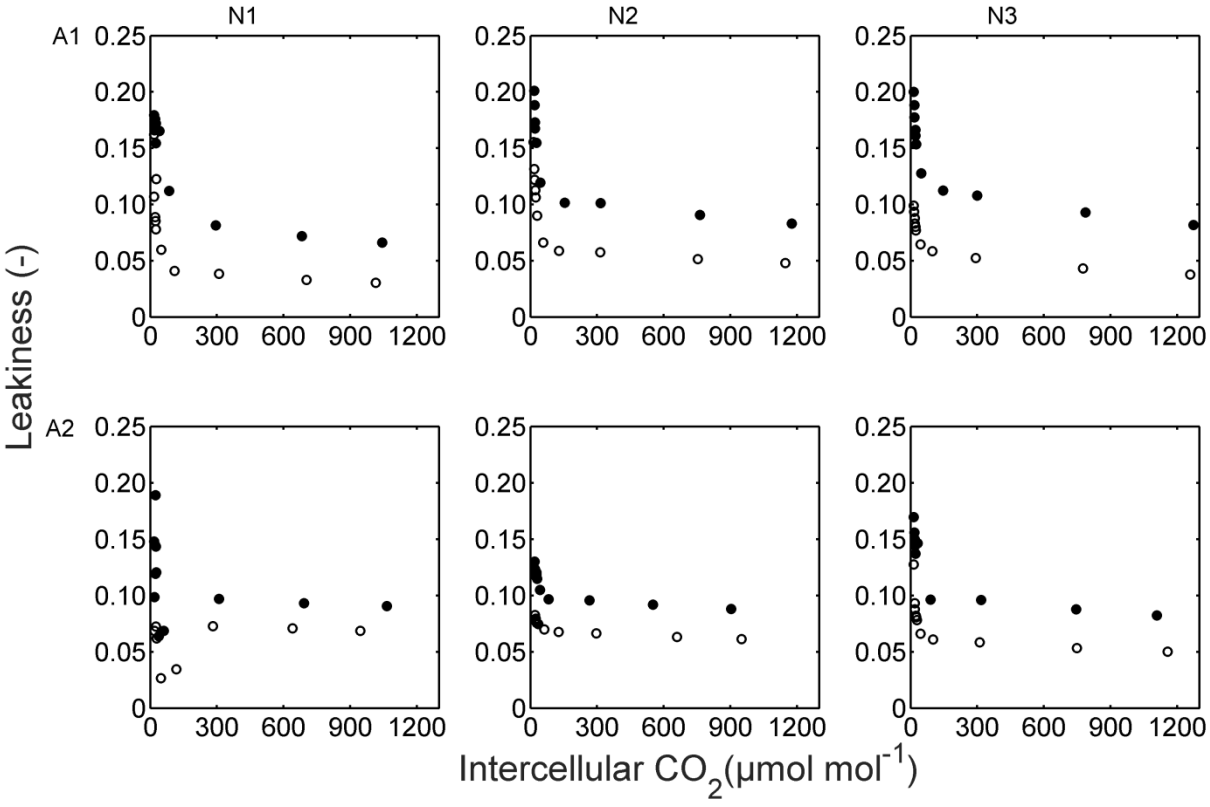

Figure A.3.3. The predicted response of leakiness to intercellular CO_2 concentration for young (A1) and old (A2) leaves from maize plants grown under three nitrogen (N) levels: low (N1), intermediate (N2) and high (N3). The oxygen levels were 21 % (filled circles) and 2 % (open circles). The irradiance was kept at 1500 µmol m^{-2} s^{-1}.

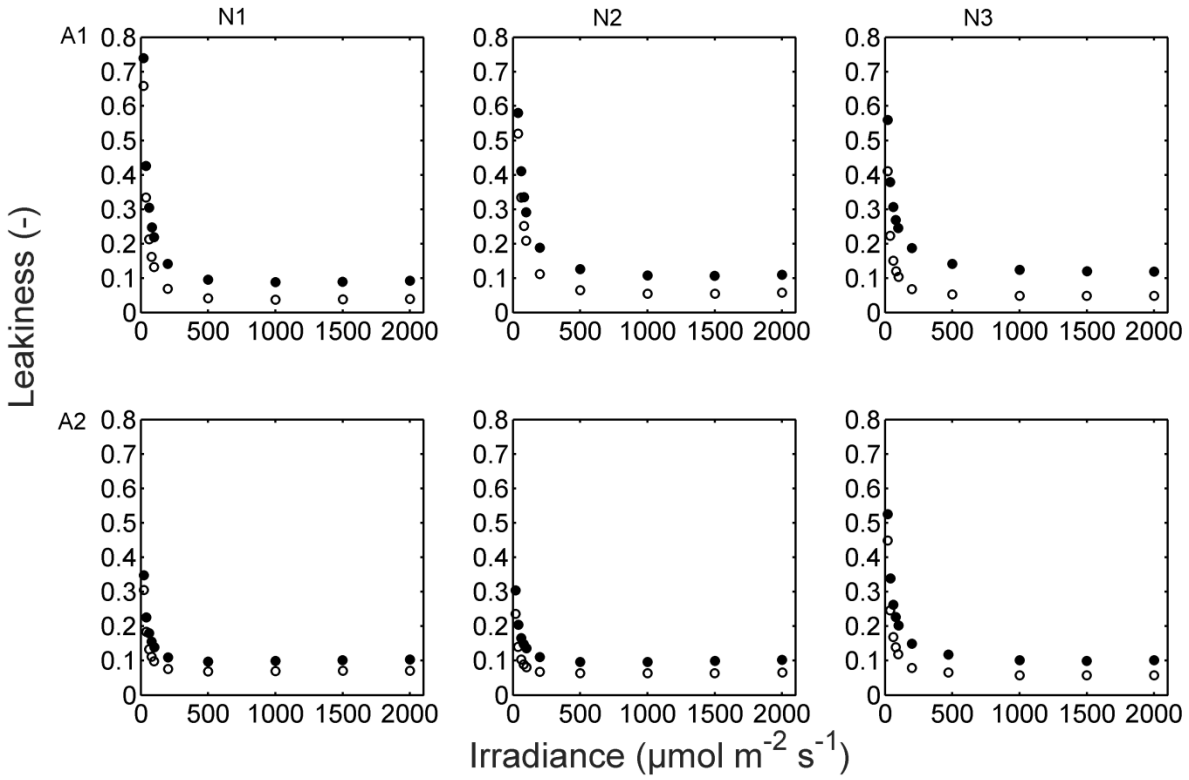

Figure A.3.4. The predicted response of leakiness to incident irradiance for young (A1) and old (A2) leaves at three nitrogen (N) levels: low (N1), intermediate (N2) and high (N3). The oxygen levels were 21 % (filled circles) and 2 % (open circles). The irradiance was maintained at 1500 µmol m^{-2} s^{-1}.

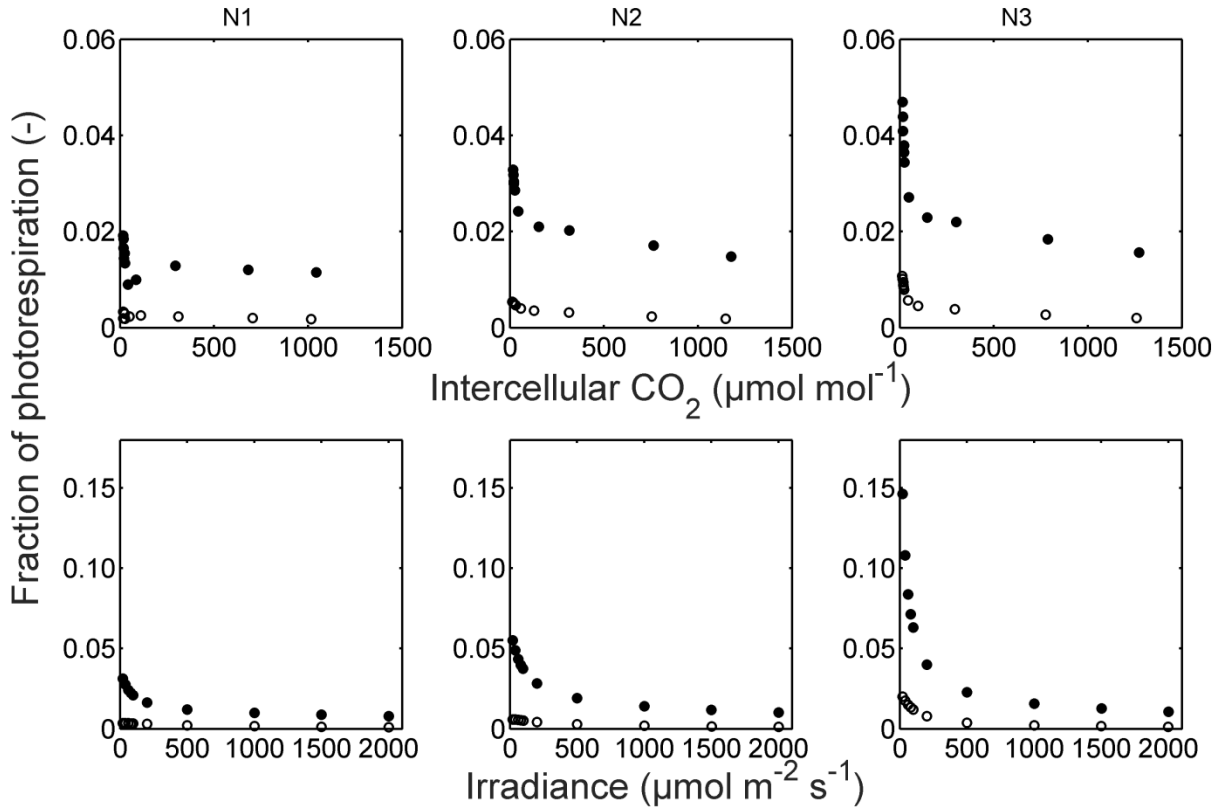

Figure A.3.5. Response of fraction of CO_2 assimilation lost due to photorespiration to intercellular CO_2 concentration (top) and incident irradiance (bottom) for young leaves (filled circles) and old leaves (open circles) at three nitrogen (N) levels: low (N1), intermediate (N2) and high (N3). The irradiance was kept at 1500 µmol m^{-2} s^{-1} for CO_2 responses while for irradiance responses, the ambient CO_2 was kept at 250 µmol mol^{-1}. The oxygen level was 21 %.

A.4. Notes about *s´*

The lumped calibration factor *s´* could be estimated as the slope of the linear relationship between photosynthesis (*A*) and the term $I_{inc}\Phi_2/3$ (Yin *et al*. 2011) for the low incident light intensity ranges at 2 % O_2. Measurements of CO_2 response of *A* (ambient $CO_2 \geq 500$ µmol mol^{-1}) for 2 % O_2 could also be added to determine *s´* as long as these points have the same slope as those of the low irradiance values. Fig. A.4.1 shows this estimation procedure and the values of *s´*. For old N1 and N2 leaves, Fig. A.4.1 shows some deviations from the linear relationship.

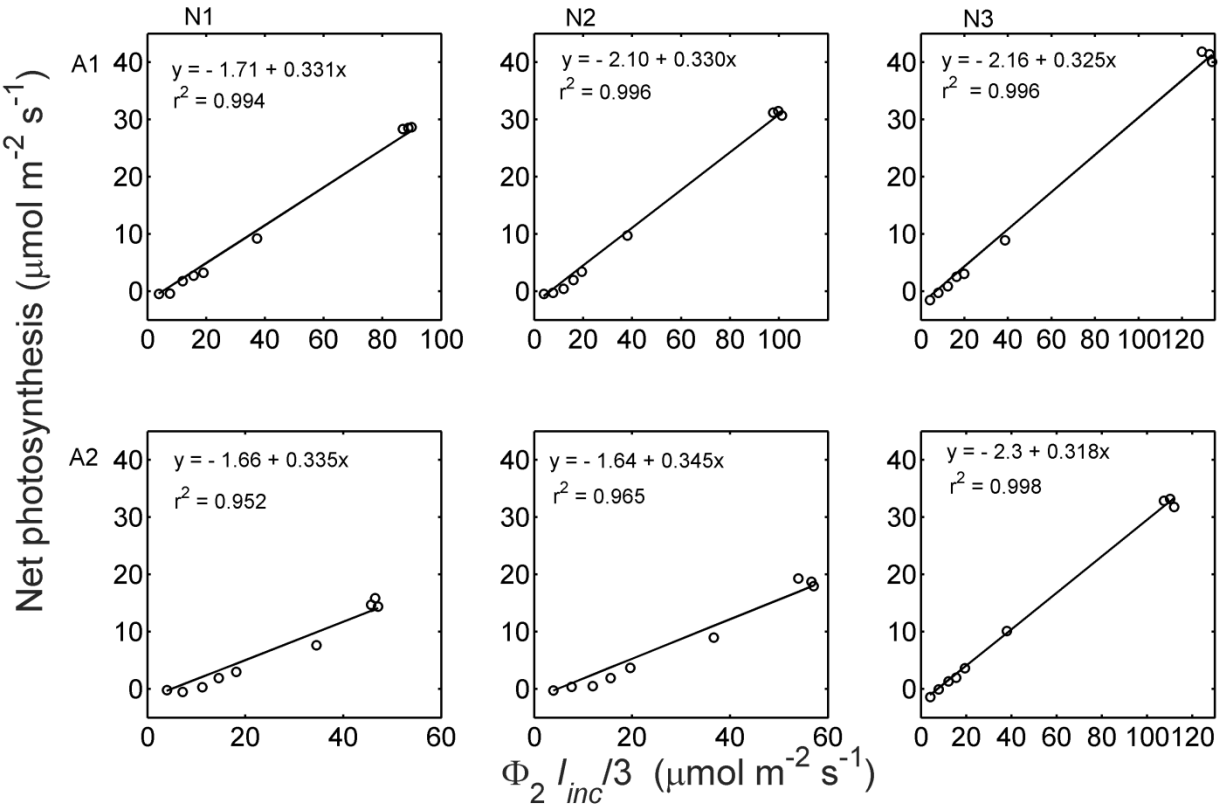

Figure A.4.1. Determination of lumped calibration factor *s´* using measurements of photosynthesis (*A*) and the calculated $I_{inc}\Phi_2/3$ for low irradiance ($20 \le I_{inc} \le 200$ μmol m^{-2} s^{-1}) at 2% O_2. Measurements of *A* at 2 % O_2 and ambient CO_2 of 500 to 1500 μmol mol^{-1} were also added. Measurements were made using young (A1) and old (A2) leaves from maize plants grown under three nitrogen (N) levels: low (N1), intermediate (N2) and high (N3).

A.5. Limitation of photosynthesis by light

Fig. A.5.1 shows that there is linear relationship between quantum efficiency of CO_2 fixation and quantum efficiency of PSII electron transport across all CO_2 and irradiance levels. This strongly suggests that assimilation is mainly limited by electron transport. Fig. A.5.2 shows the ratio of these two quantities in response to irradiance.

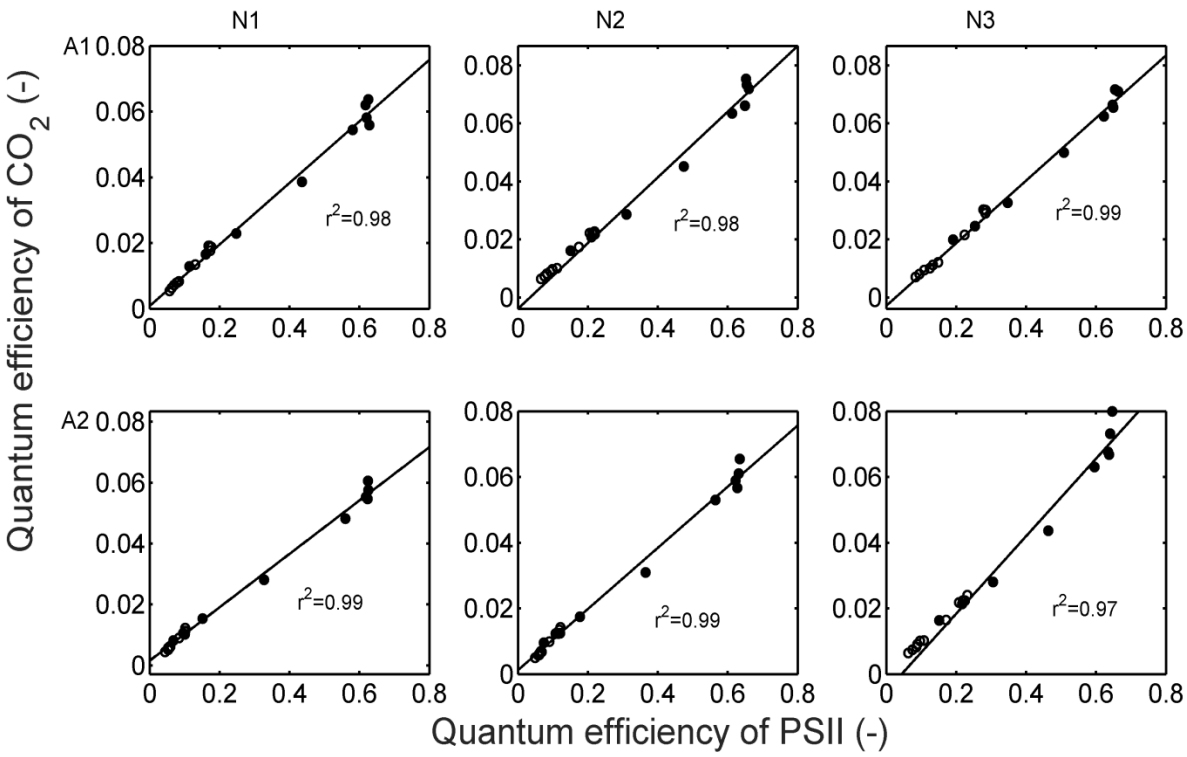

Figure A.5.1. Quantum efficiency of CO_2 fixation versus quantum efficiency of PSII electron transport across all CO_2 levels (open circles) and light levels (filled circles) for young (A1) and old (A2) leaves from maize plants grown under three nitrogen (N) levels: low (N1), intermediate (N2) and high (N3).

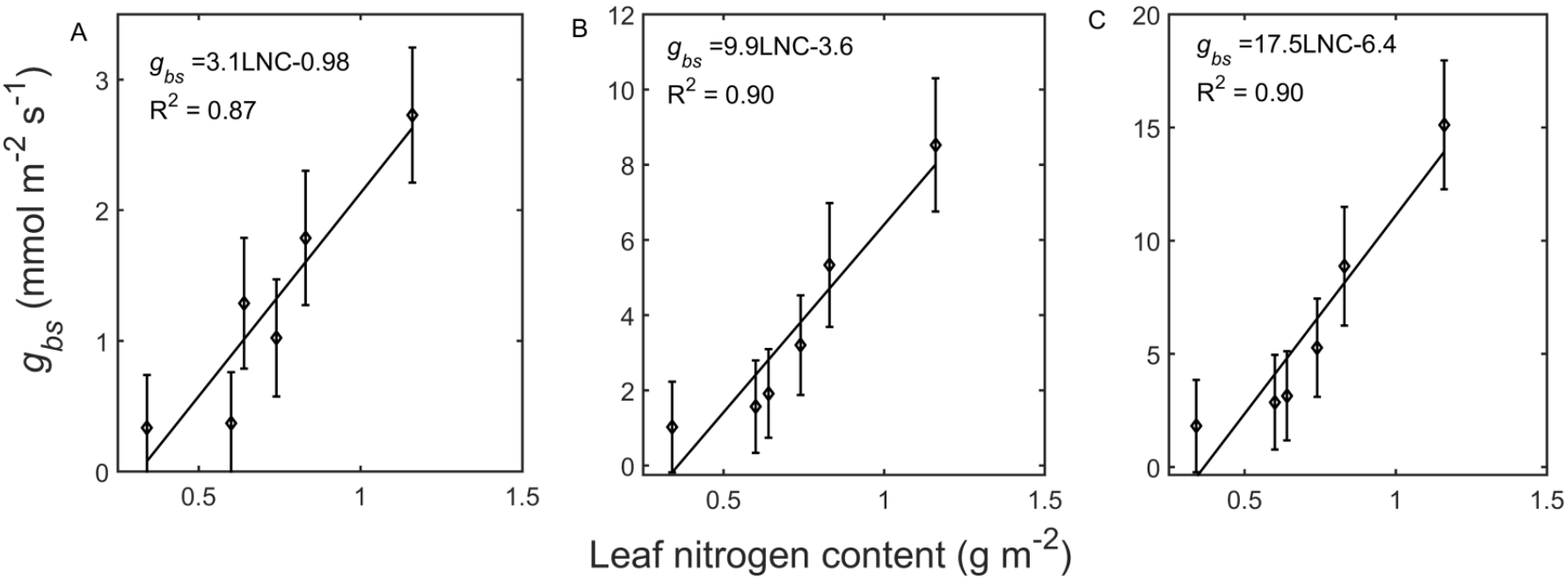

Figure A.5.2. Relationship between bundle sheath conductance (g_{bs}) and leaf nitrogen content (LNC) for various fractions of ATP partitioned to C_4 cycle (x): x = 0.35 (panel A), x = 0.45 (panel B) and x = 0.50 (panel C). Bars represent standard error (n=4).

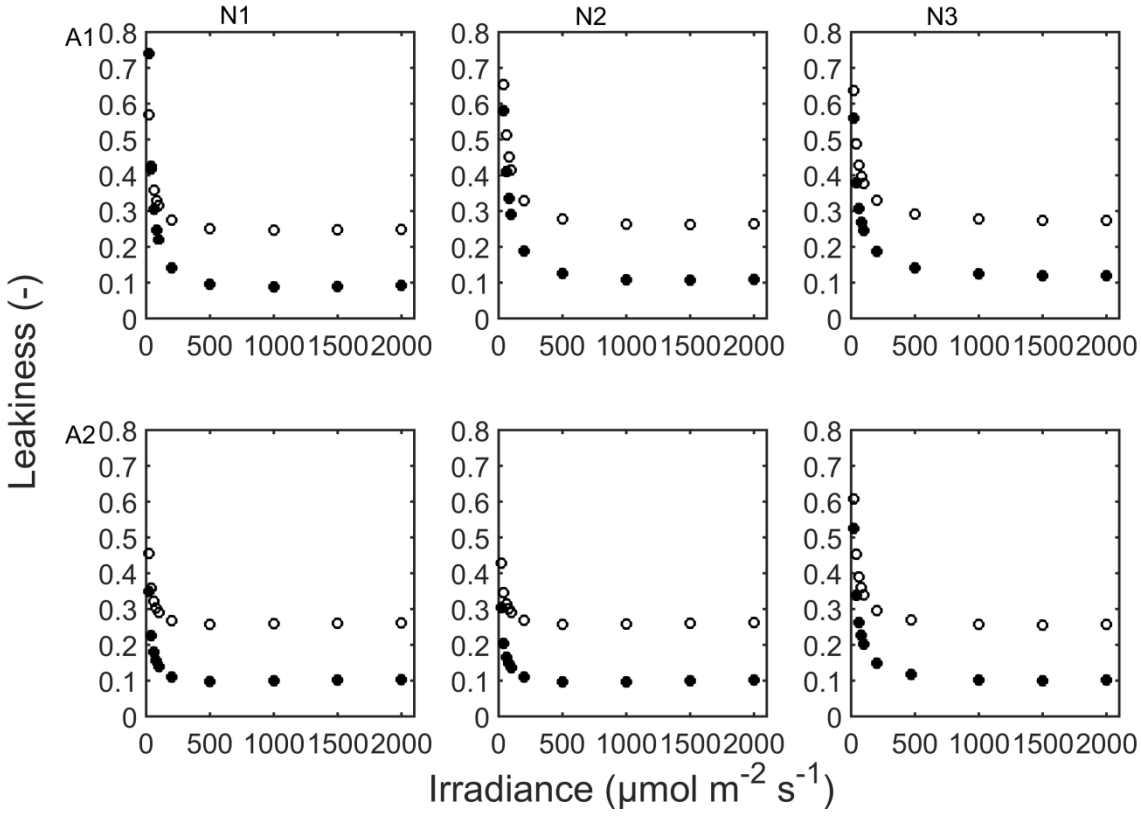

Figure A.5.3. Sensitivity of estimated leakiness in response to irradiance for fraction of ATP allocated to the C_4 cycle (x): x = 0.4 (filled circles) and x = 0.45 (open circles). Leaf types were: young (A1) and old (A2) leaves from maize plant grown under low (N1), intermediate (N2) and high (N3) nitrogen supply. The oxygen concentration was 21 %.

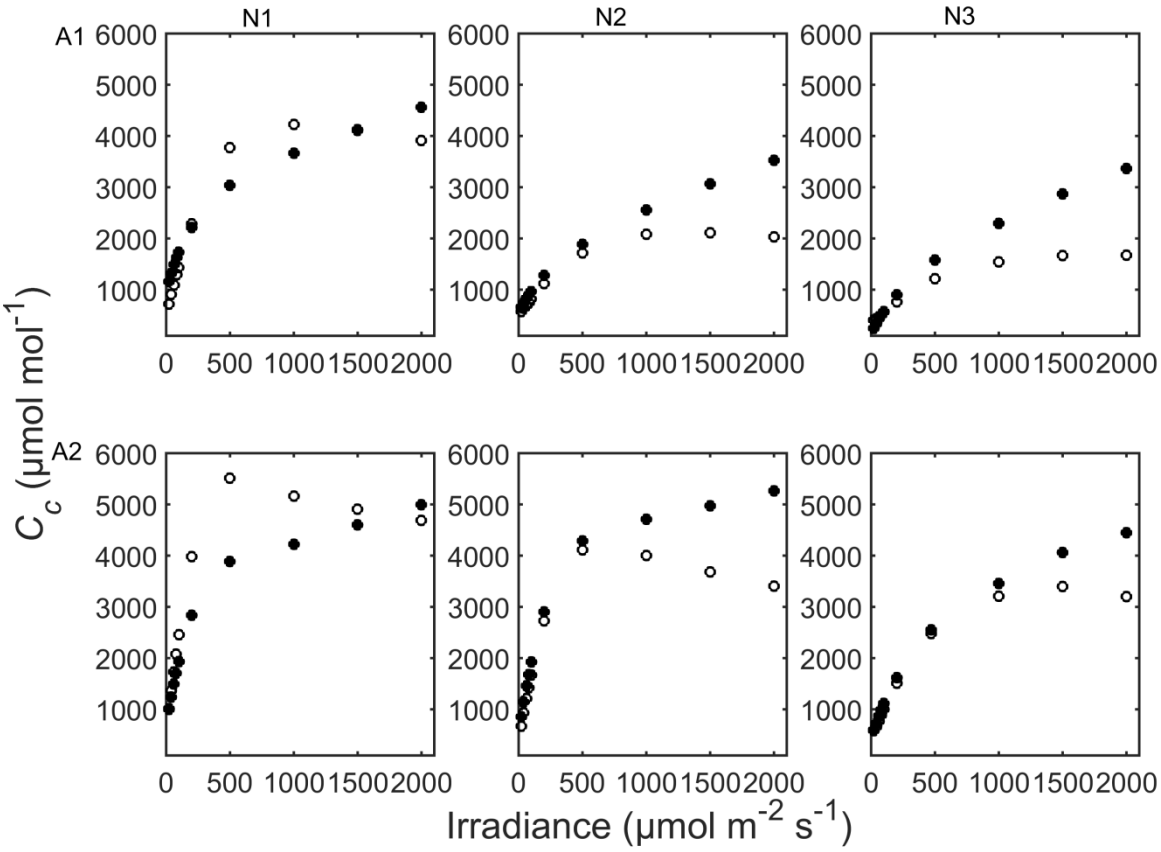

Figure A.5.4. Sensitivity of estimated mean concentration of CO_2 in bundle sheath cells (C_c) in response to irradiance for fraction of ATP allocated to the C_4 cycle (x): x = 0.4 (filled circles) and x = 0.45 (open circles). Leaf types were: young (A1) and old (A2) leaves from maize plant grown under low (N1), intermediate (N2) and high (N3) nitrogen supply. The oxygen concentration was 21 %.

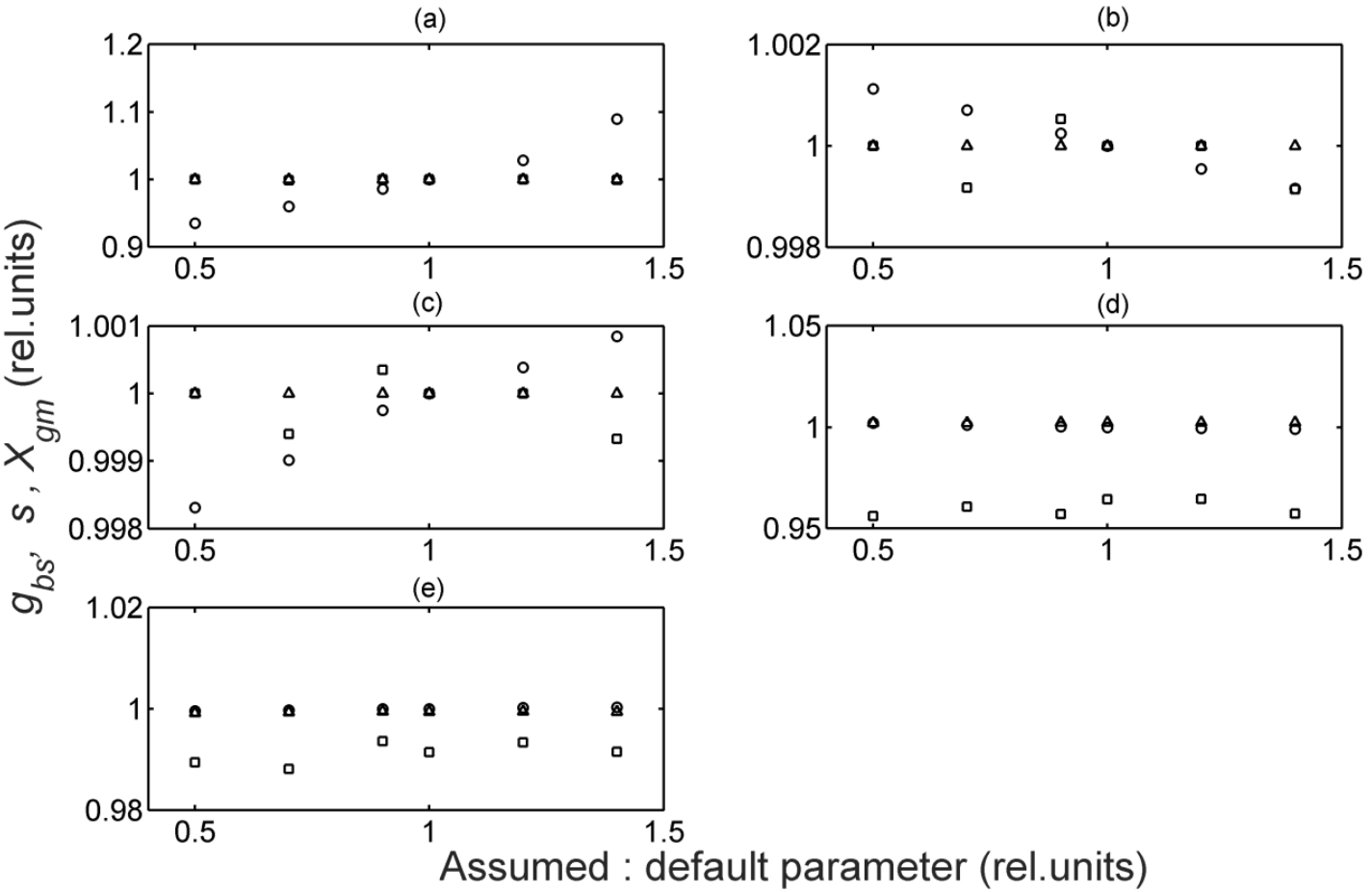

Figure A.5.5. Sensitivity of the estimated values of g_{bs} (square), s' (triangle) and X_{gm} (circle) to input parameters such as K_p (a), $K_{m,C}$, (b) $K_{m,O}$, (c) $S_{c/o}$, (d) and α (e). The changes in the estimated parameters were expressed by dividing the new parameter by the default value given in Table S1. The parameters g_{bs} and s' were an average of the estimates for all leaf types corresponding to each change in the input parameters.

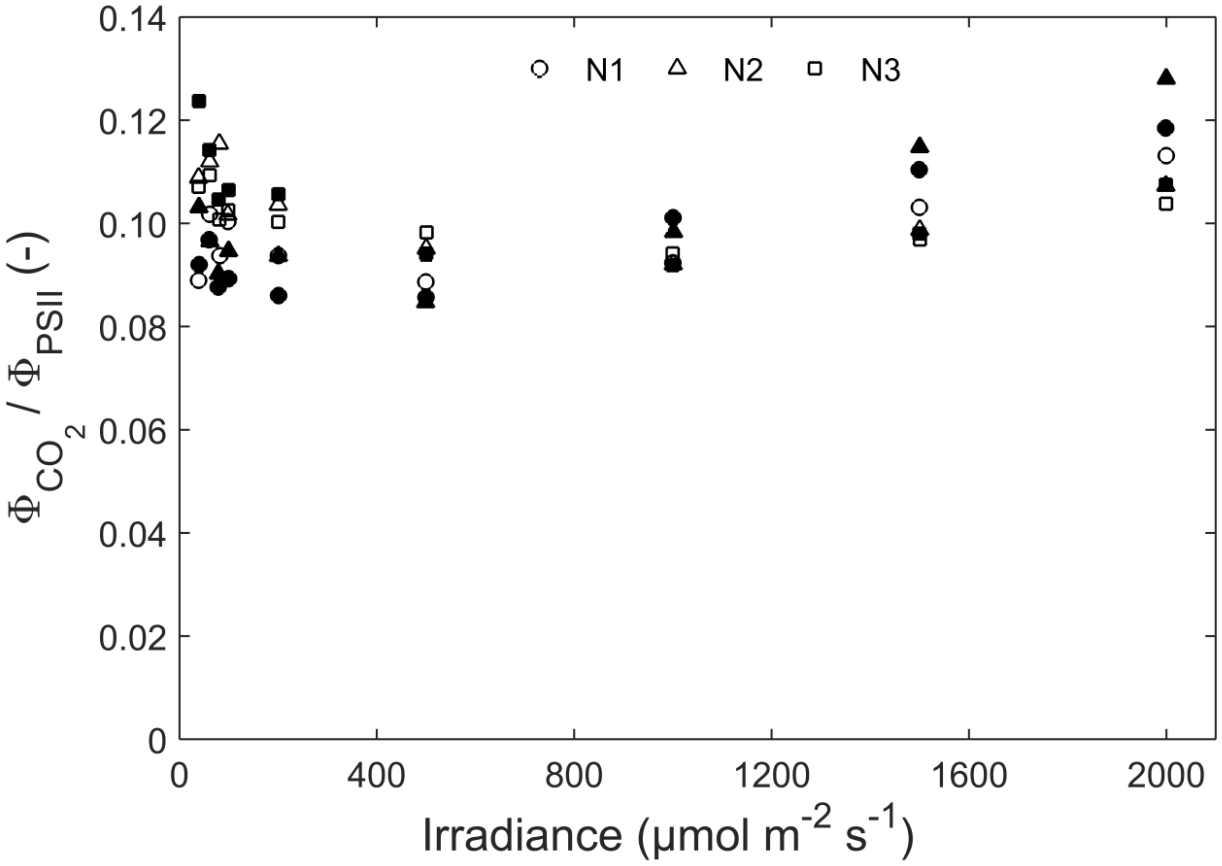

Figure A.5.6. Ratio of quantum yield of CO_2 fixation (Φ_{CO2}) and quantum yield of PSII electron transport (Φ_{PSII}) in response to irradiance for young leaves (open symbols) and old leaves (filled symbols) grown at low nitrogen (N1), intermediate nitrogen (N2) and high nitrogen (N3). Error bars were not included to make the plots clearer. Φ_{CO2} was calculated based on incident irradiance level rather than on light absorbed by PSII, thus, the mean value may seem less than 0.12 reported previously (Edwards and Baker, 1993).

A.6. Light microscopy and X-ray micro-CT images of leaf microstructure

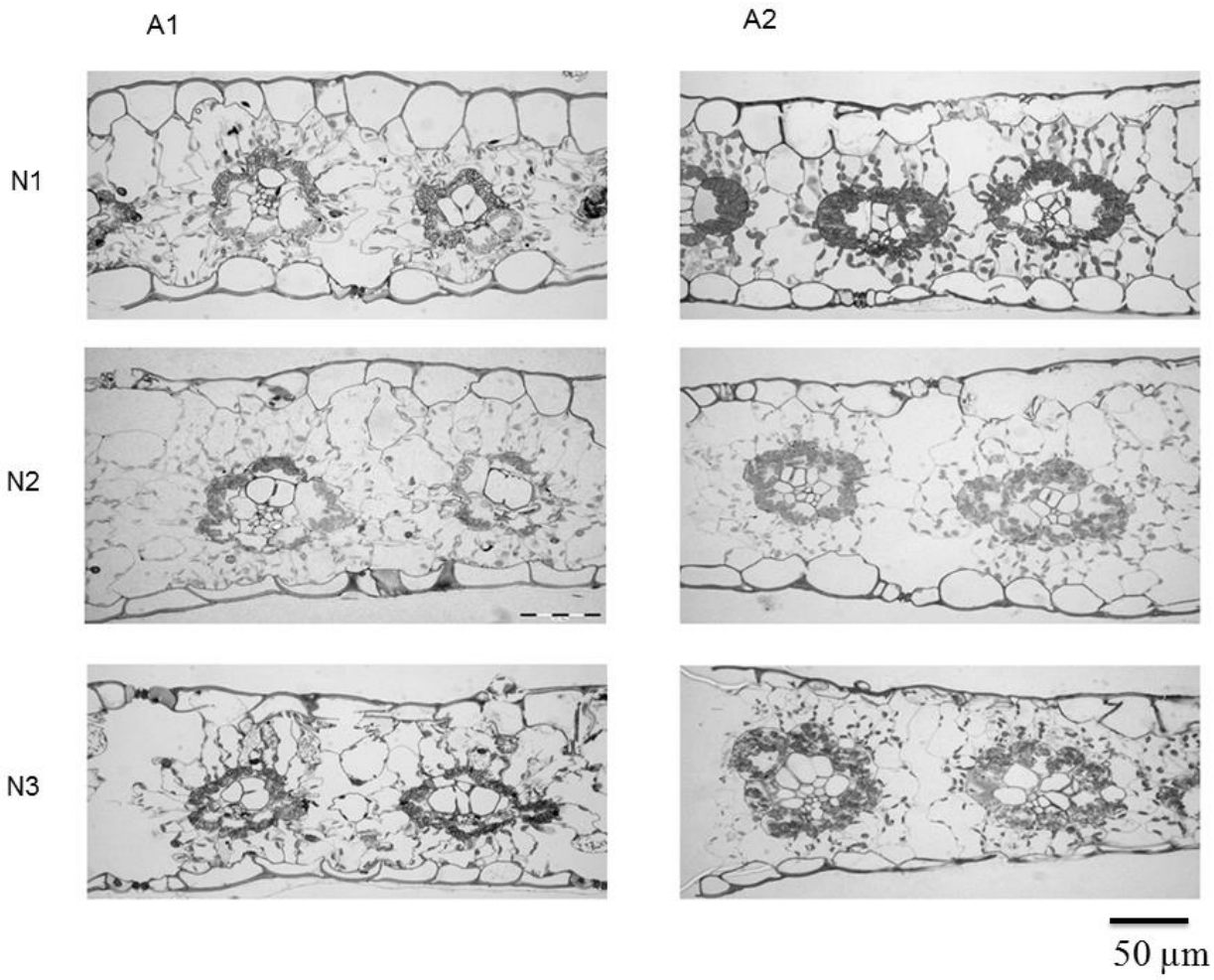

Figure A.6.1. Cross sections of young (A1) and old (A2) leaves from maize plants grown under three nitrogen (N) levels: low (N1), intermediate (N2) and high (N3). Scale bar denotes 50 µm.

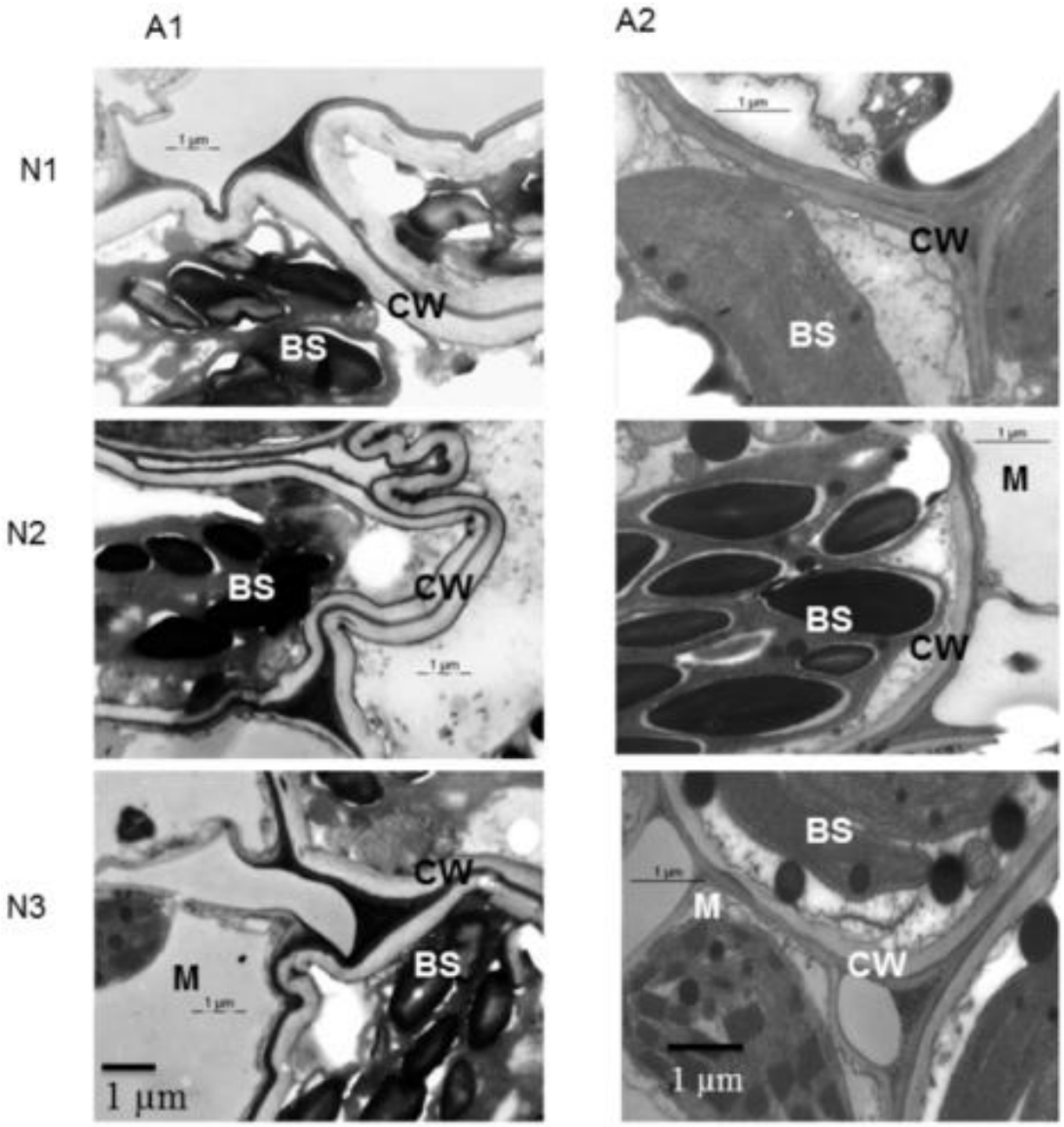

Figure A.6.2. Cross sections of young (A1) and old (A2) leaves from maize plants showing the cell walls of bundle sheath cells. The plants were grown under three nitrogen (N) levels: low (N1), intermediate (N2) and high (N3). Mesophyll cells (M), bundle sheath cells (BS) and bundle sheath cell wall (CW) are also indicated. Note that the scale bars are slightly different for the left panels and the right panels.

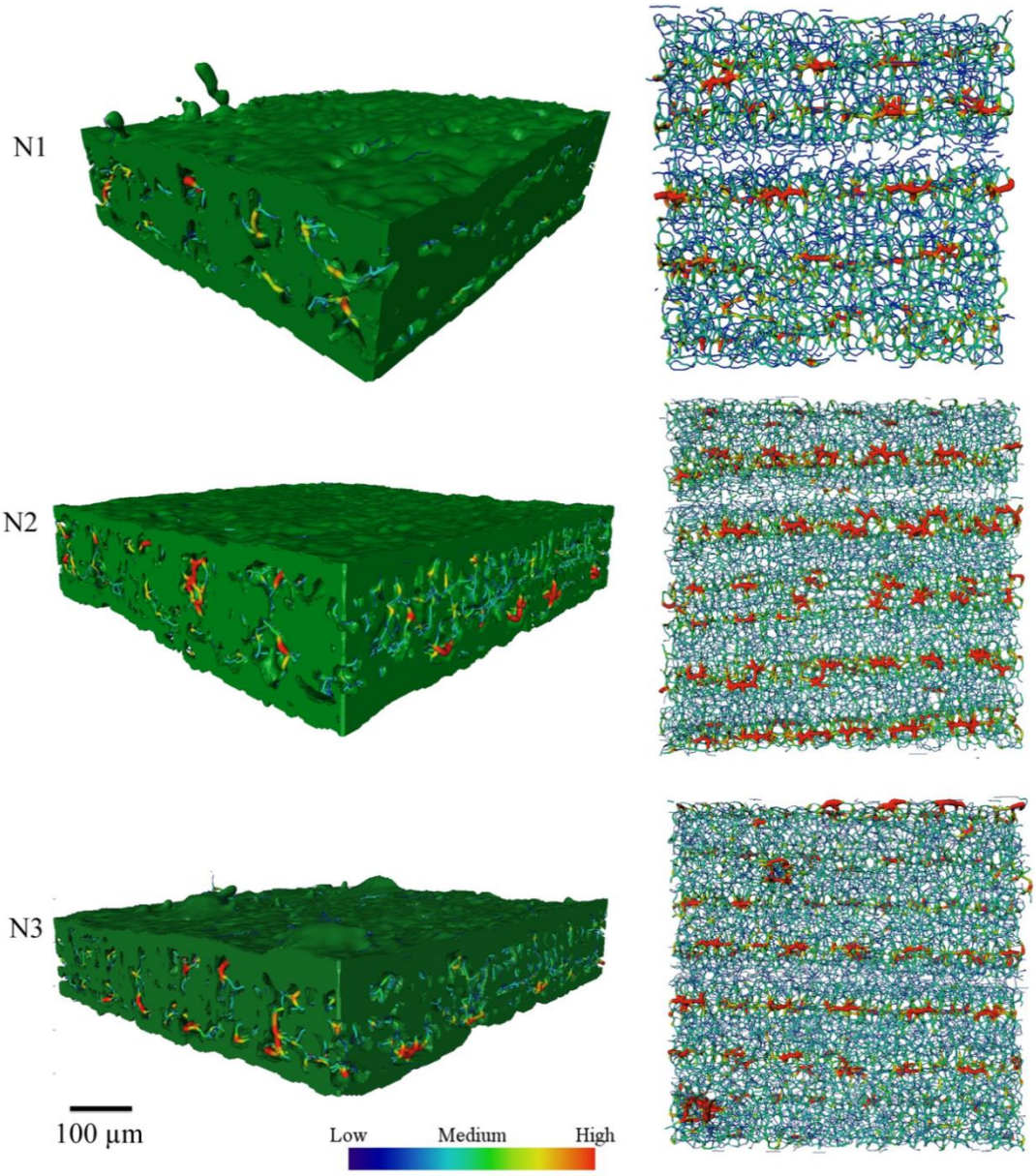

Figure A.6.3. Surface rendering of young maize leaf tissues (right) at three nitrogen (N) levels: low (N1), intermediate (N2) and high (N3). The skeleton of the intercellular air space network is superimposed in the surface rendering. The skeleton of the intercellular air spaces viewed in paradermal direction (left) shows the thickness of the air spaces. The large diameter air spaces (left) are usually associated with the presence of stomata. The color bar shows the diameter of the air spaces (µm). Scale bar is 100 µm. Sample size 200×200×200 pixel at resolution 2.96 µm/pixel.

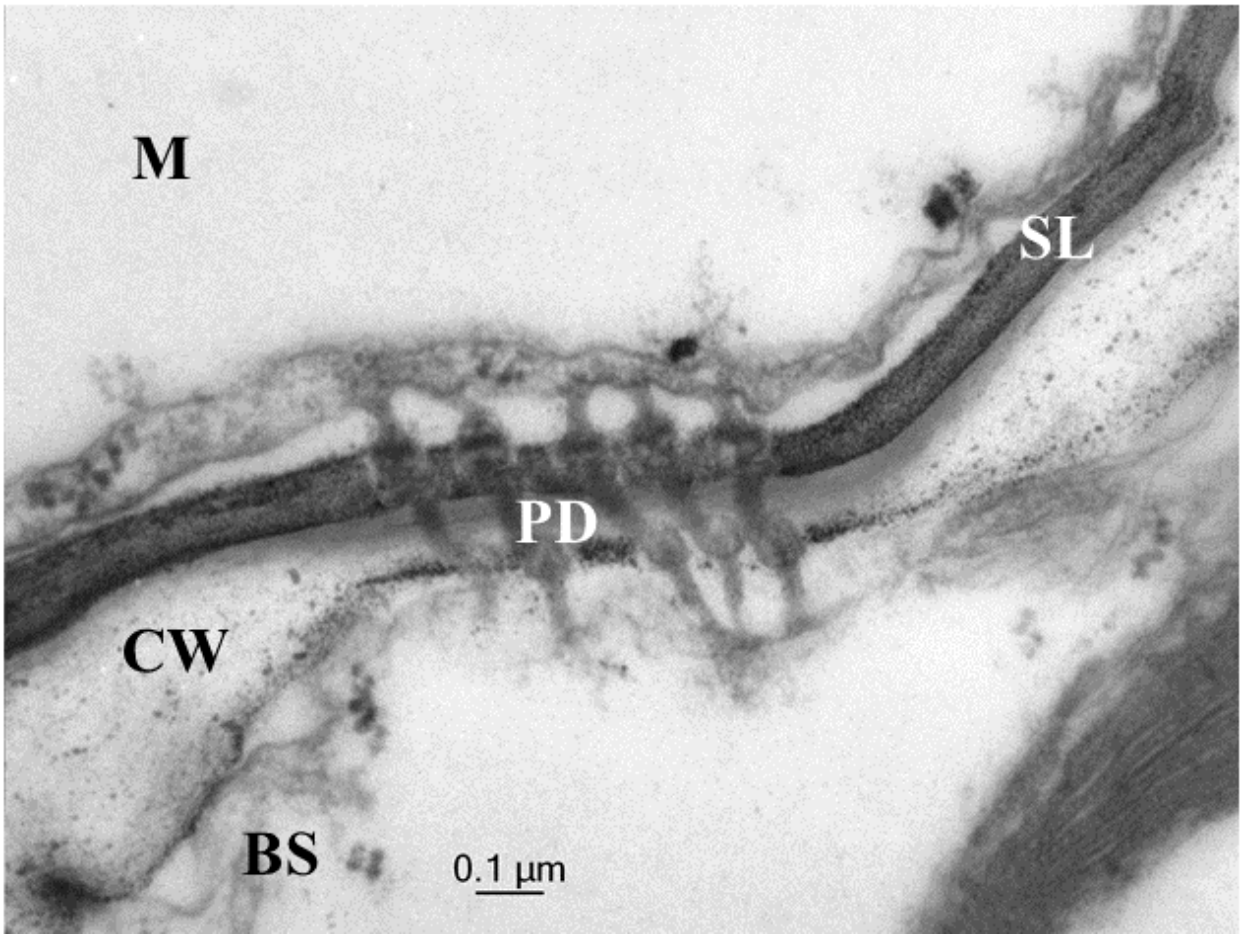

Figure A.6.4. Cross section of the bundle sheath-mesophyll interface showing the mesophyll cell (M), plasmodesmata (PD), suberin layer (SL), bundle sheath cell wall (CW) and bundle sheath cell (BS). Scale bar is 0.1 µm.

A.7. Two-variable regression

To discern the relative importance of leaf age and leaf nitrogen content (LNC) to variation in g_{bs}, a two-variable regression was carried out in Microsoft Excel (2010). Table A.7.1 shows that leaf nitrogen content impacted g_{bs} more than leaf age. Table A.7.1 shows that the mode explains 85 % of the observed variation.

Table A.7.1 ANOVA table outputs of a two-variable linear regression of leaf nitrogen content and leaf age on bundle sheath conductance. A total of six g_{bs} values were estimated for three nitrogen and two leaf age levels.

Regression Statistics	
Multiple R	0.952604
R^2	0.907454
Adjusted R^2	0.845756
Standard Error	0.484574
Observations	6

ANOVA

	Degree of freedom	*Sum of square*	*Mean square*	*F*	*Significance F*
Regression	2	6.907282	3.45364	14.7	0.028154
Residual	3	0.704436	0.23481		
Total	5	7.611718			

	Coefficients	*Standard Error*	*t Stat*	*P-value*	*Lower 95%*	*Upper 95%*	*Lower 95.0%*	*Upper 95.0%*
Intercept	-0.8194	1.59655	-0.5132	0.64	-5.90033	4.2615	-5.90033	4.26152
Leaf age	-0.02055	0.03946	-0.5207	0.63	-0.14613	0.1050	-0.14613	0.10503
Leaf N	3.95157	1.03108	3.83243	0.03	0.670198	7.2329	0.67019	7.23295

Appendix B

B.1. Calculation of microscale model variables

The rate of ATP production, J_{ATP} was calculated from chlorophyll fluorescence measurements (Yin *et al.*, 2011*b*) as:

$$J_{ATP} = \frac{s' I_{inc} (\Delta F / F_m')}{(1-x)} \qquad \text{(B.1.1)}$$

$$\Delta F / F_m' = (F_m' - F_s) / F_m',$$

where F_s is the steady-state relative fluorescence yield and F_m' is the maximum relative fluorescence yield in the leaf.

The average rate of PEP carboxylation in mesophyll cytosol was calculated as:

$$\bar{V}_p = \frac{\int_{V_{mc,cyto}} V_p \, dv}{\int_{V_{mc,cyto}} dv} \qquad \text{(B.1. 2)}$$

where the differential elemental *dv* is integrated over the volume (V) of bundle sheath chloroplast and mesophyll cytosol to determine the total volume (area in 2D) of these compartments. We defined the volume *V* as: $V = \int_G dv = \iiint_G dx dy dz$. The product of differential elements, *dx*, *dy* and *dz* of the region *G* are summed to find the total volume *V* of the region. Since our geometry is two dimensional, *dz* is 1.

The volumetric rate of CO_2 release from decarboxylation of C_4 acids, $\bar{V}_p^*$ was given by:

$$\bar{V}_p^* = \frac{\bar{V}_p}{d \times f_{bs,ch}} \tag{B.1. 3}$$

where $f_{bs,ch}$ is the volume fraction of bundle sheath chloroplasts of the leaf and *d* is the average thickness of the leaf tissue.

Release of photorespired CO_2 occurs in the mitochondria which are located in the cytosol although photorespiration starts in bundle sheath chloroplasts. These cell compartments may have different volumes. Thus, the total volumetric rate of photorespiration in bundle sheath chloroplasts is multiplied by the ratio of volume of bundle sheath chloroplasts, $V_{bs,ch}$, to the volume of bundle sheath cytosol (bs,cy), $V_{bs,cy}$, to calculate volumetric rate of CO_2 release in bundle sheath cytosol, $\bar{r}_p^*$.

$$\bar{r}_p^* = \frac{\int_{V_{bs,ch}} V_c^* \cdot \frac{\gamma^* [\mathrm{O_2}]_{\mathrm{bs}}}{[\mathrm{CO_2}]_{\mathrm{bs}}} dv}{\int_{V_{bs,cy}} dv} \tag{B.1. 4}$$

The mean concentration of CO_2 in mesophyll cells, $\bar{C}_m$ (µmol mol^{-1}) and in bundle sheath chloroplast, $\bar{C}_c$ (µmol mol^{-1}), needs to be determined to calculate the bundle sheath conductance. The equivalent gas phase concentration was calculated using Henry's law (constants *R, T, P,* and *H* are given in Table B. 2).

$\bar{C}_c$ was calculated as:

$$\bar{C}_c = \frac{RT}{P} \frac{1}{H} \frac{\int_{V_{bs,ch}} [\mathrm{CO_2}]_{bs} dv}{\int_{V_{bs,ch}} dv} \tag{B.1. 5}$$

$\bar{C}_m$ was calculated as:

$$\bar{C}_m = \frac{RT}{P}\frac{1}{H}\frac{\int_{V_{mc,cyto}} [\mathrm{CO_2}]_m \, dv}{\int_{V_{mc,cyto}} dv} \quad \text{(B.1. 6)}$$

The rate of leakage, *L* is the rate of leakage (von Caemmerer and Furbank, 1999) was given by:

$$L = \bar{V}_p - \bar{A} - R_m \quad \text{(B.1. 7)}$$

The bundle sheath conductance, g_{bs}, was calculated as:

$$g_{bs} = \frac{L}{\bar{C}_c - \bar{C}_m} \quad \text{(B.1. 8)}$$

The mean photorespiration rate in bundle sheath chloroplasts, $\bar{r}_p$ on leaf area basis, was calculated as:

$$\bar{r}_p = \frac{\int_{V_{bs,ch}} V_c \cdot \frac{\gamma^*[\mathrm{O_2}]}{[\mathrm{CO_2}]} \, dv}{\int_{V_{bs,ch}} dv} \quad \text{(B.1. 9)}$$

The leakiness, ϕ, was calculated from:

$$\phi = \frac{L}{\bar{V}_p} \quad \text{(B.1. 10)}$$

Table B.1. List of symbols, their definitions and units

Variable	**Definition**	**Units**
A	Net photosynthesis rate	μmol m^{-2} s^{-1}
$\bar{A}$	Mean net photosynthesis rate	μmol m^{-2} s^{-1}
B_{CA}	Net hydration of CO_2 in presence of carbonic anhydrase	μmol m^{-3} s^{-1}
B_{NCA}	Non enzymatic net hydration of CO_2	μmol m^{-3} s^{-1}
C_a	Ambient air CO_2 concentration	μmol mol^{-1}
$\bar{C}_m$	Mean concentration of CO_2 in mesophyll cytosol	μmol mol^{-1}
$\bar{C}_c$	Mean concentration of CO_2 in bundle sheath chloroplasts	μmol mol^{-1}
$\bar{C}_i$	Mean intercellular CO_2 concentration	μmol mol^{-1}
D_{CO_2}	CO_2 diffusivity in the liquid phase media	m^2 s^{-1}
$D_{HCO_3^-}$	Diffusivity of HCO_3^-	m^2 s^{-1}
d	Average thickness of tissue	μm
$f_{mc,cy}$	Volume fraction of mesophyll cytosol of the leaf	m^3 m^{-3}
$f_{bs,ch}$	Volume fraction of bundle sheath chloroplasts of the leaf	m^3 m^{-3}
$f_{bs,cy}$	Volume fraction of bundle sheath cytosol of the leaf	m^3 m^{-3}
$f_{resp.}$	Total volume fraction of mesophyll cytosol and bundle sheath cytosol $f_{resp.} = f_{mc,cy} + f_{bs,cy}$	m^3 m^{-3}
g_{bs}	Bundle sheath conductance	mol m^{-2} s^{-1}

H	Henry's constant for CO_2 (25°C)	Dimensionless
$[H^+]$	H^+ concentration	mol L^{-1}
I_{inc}	Photon flux density incident to leaves	μmol m^{-2} s^{-1}
J_{ATP}	ATP production rate	μmol m^{-2} s^{-1}
k_a	Turnover rate of carbonic anhydrase enzyme	s^{-1}
k_1	CO_2 hydration velocity constant	s^{-1}
k_2	CO_2 dehydration velocity constant	s^{-1}
K_{CO_2}	Michaelis-Menten constant for carbonic anhydrase hydration	μmol m^{-3}
K_{eq}	Equilibrium constant of carbonic anhydrase	μmol m^{-3}
K	Acid dissociation constant for H_2CO_3	mol L^{-1}
$K_{m,C}$	Michaelis-Menten constant of Rubisco for CO_2	μbar
$K_{HCO_3^-}$	Michaelis-Menten constant for carbonic anhydrase dehydration	μM
$K_{m,O}$	Michaelis-Menten constant of Rubisco for O_2	Mbar
K_p	Michaelis-Menten constant of PEPc for CO_2	μbar
L	Rate of CO_2 leakage from bundle sheath cells	μmol m^{-2} s^{-1}
L_{pd}	Length of mesophyll-bundle sheath interface	μm
P_m	CO_2 permeability of plasma membrane	m s^{-1}
R_d	Total respiratory CO_2 release from leaf $R_d = R_m + R_s$	μmol m^{-2} s^{-1}
R_m	Rate of respiratory CO_2 release from mitochondria in mesophyll	μmol m^{-2} s^{-1}

	cytosol $R_m = R_d \times \left(f_{m,cy} / f_{resp.} \right)$	
R_m^*	Volumetric rate of respiration in mesophyll cytosol $R_m / \left(f_{resp.} \times d \right)$	μmol m^{-3} s^{-1}
$\bar{r}_p$	Mean rate of photorespiratory CO_2 release from mitochondria in bundle sheath cytosol	μmol m^{-2} s^{-1}
$\bar{r}_p^*$	Volumetric rate of photorespiratory CO_2 release from mitochondria in bundle sheath cytosol	μmol m^{-3} s^{-1}
R_s	Rate of respiratory CO_2 release from mitochondria in bundle sheath cytosol, $R_s = R_d \times \left(f_{bs,cy} / f_{resp.} \right)$	μmol m^{-2} s^{-1}
R_s^*	Volumetric respiration rate in bundle sheath cytosol, $R_s / \left(d \times f_{bs,cy} \right)$	μmol m^{-3} s^{-1}
s'	Lumped calibration factor	Dimensionless
$S_{C/O}$	Relative CO_2/O_2 specificity factor for Rubisco	μbar μbar^{-1}
V_c	Gross rate of CO_2 fixation	μmol m^{-2} s^{-1}
$\bar{V}_c$	Average rate of gross CO_2 fixation	μmol m^{-2} s^{-1}
$V_{c,max}$	Maximum rate of Rubisco activity-limited carboxylation	μmol m^{-2} s^{-1}
V_p	Rate of PEP carboxylation based on CO_2	μmol m^{-2} s^{-1}
$\bar{V}_p$	Average rate of PEP carboxylation	μmol m^{-2} s^{-1}
V_p^*	Volumetric rate of V_p calculated from $V_p / (d * f_{m,cy})$	μmol m^{-3} s^{-1}
$\bar{V}_p^*$	Volumetric rate of CO_2 release from decarboxylation of C_4 acids	μmol m^{-3} s^{-1}

$V_{p,max}$	Maximum rate of PEP carboxylation based on CO_2	μmol m^{-2} s^{-1}
w_c	Rubisco-limited rate of carboxylation	μmol m^{-2} s^{-1}
w_j	Electron-transport-limited rate of carboxylation	μmol m^{-2} s^{-1}
x	Partitioning factor of J_{ATP} to the C_4 cycle	Dimensionless
X_a	Concentration of carbonic anhydrase in cytosol	mol m^{-3}
J_{CO_2}	CO_2 flux through chloroplast envelope	μmol m^{-2} s^{-1}
$J_{CO_2,pd}$	CO_2 leak flux through mesophyll-bundle sheath interface	μmol m^{-2} s^{-1}
ϕ	Leakiness $\phi = L/\overline{V}_p$	Dimensionless
θ	Ratio of the total area of plasmodesmata to the total area of the mesophyll-bundle sheath interface.	m^2 m^{-2}
γ^*	0.5/ $S_{C/O}$	μbar μbar^{-1}

Table B.2. Values of parameters used in the microscale model

Variable	**Symbol**	**Units**	**Value**	**Notes and references**
Diffusivity of CO_2 liquid phase (25 °C)	D_{CO_2}	$m^2\ s^{-1}$	1.7×10^{-9}	(Lide, 1999)
Diffusivity of CO_2 Mesophyll (m) cell wall	$D_{CO_2,m}$	$m^2\ s^{-1}$	1.7×10^{-9}	Assumed
Diffusivity of CO_2 Bundle sheath (bs) cell wall	$D_{CO_2,bs}$	$m^2\ s^{-1}$	$1.7\times10^{-9}\times0.1$	Effective porosity was assumed 0.1
Diffusivity of HCO_3^-	$D_{HCO_3^-}$	$m^2\ s^{-1}$	1.17×10^{-9}	(Geers and Gros, 2000)
Average thickness of tissue	d	µm	165	Measured from image of leaf microstructure
Henry's constant for CO_2 (25 °C)	H	Dimensionless	0.83	(Lide, 1999)
Length of mesophyll-bundle sheath interface	L_{pd}	µm	0.56	Sum of thickness of cell walls (main text)
Turnover rate of	k_a	s^{-1}	3×10^5	(Pocker and

carbonic anhydrase				Miksch, 1978)
CO_2 hydration velocity constant	k_1	s^{-1}	0.039	(Jolly, 1985)
CO_2 dehydration velocity constant	k_2	s^{-1}	23	(Jolly, 1985)
Michaelis-Menten constant for carbonic anhydrase hydration	K_{CO_2}	mol m^{-3}	2.8	(Hatch and Burnell, 1990)
Equilibrium constant of carbonic anhydrase	K_{eq}	mol m^{-3}	5.6×10^{-7}	(Pocker and Miksch, 1978)
Acid dissociation constant for H_2CO_3	K	mol L^{-1}	2.5×10^{-4}	(Jolly, 1985)
Michaelis-Menten constant of Rubisco for CO_2	$K_{m,C}$	μbar	485[(a)]	(Cousins *et al.*, 2010)
Michaelis-Menten constant for carbonic anhydrase hydration	$K_{HCO_3^-}$	mol m^{-3}	34	(Pocker and Miksch, 1978)
Michaelis-Menten constant of Rubisco for O_2	$K_{m,O}$	mbar	146[(a)]	(Cousins *et al.*, 2010)
Michaelis-Menten	K_p	μbar	40[(a)]	(Pfeffer and

constant of PEPC for CO_2				Peisker, 1998)
CO_2 permeability of bundle sheath chloroplast envelopes	P_{CO_2}	m s^{-1}	1.75×10^{-3}	Half of the value reported for plasma membrane (Gutknecht, 1988)
CO_2 permeability of bundle sheath cells plasma membrane	$P_{CO_2,bs}$	m s^{-1}	3.5×10^{-3}	Assumed equal to the reported membrane CO_2 permeability (Gutknecht, 1988)
CO_2 permeability of mesophyll plasma membrane	$P_{CO_2,m}$	m s^{-1}	1.6×10^{-2}	(Missner *et al.*, 2008)
Mitochondrial respiration	R_d	μmol m^{-2} s^{-1}	2.16 ± 0.27	Estimated
Lumped calibration factor	s'		0.329 ± 0.05	Estimated
Rubisco specificity	$S_{C/O}$	μbar μbar^{-1}	2862	(Cousins *et al.*, 2010)
Carboxylation capacity	$V_{c,max}$	μmol m^{-2} s^{-1}	$V_{p,max}$/2.33	(Yin *et al.*,

of Rubisco				2011*b*)
Carboxylation capacity of Rubisco PEP	$V_{p,max}$	µmol m^{-2} s^{-1}	222.3	(Yin *et al.*, 2011*b*)
Partitioning factor of J_{ATP} to the C_4 cycle	x	Dimensionless	0.4	(von Caemmerer and Furbank, 1999)
Concentration of carbonic anhydrase	X_a	mol m^{-3}	0.69	(Tholen and Zhu, 2011)
Half the Inverse of Rubisco specificity	γ^*	µbar µbar^{-1}	Calculated	

[a] These parameters were converted into µmol m^{-3} liquid by multiplying with PH/RT, where P = 101325 Pa, H = 0.83, R = 8.314 m^3 Pa K^{-1} mol^{-1} and T = 298 K.

B.2. A reaction-diffusion model based on a modified biochemical model

We based the reaction-diffusion model presented in the main text on the biochemical model of von Caemmerer and Furbank (von Caemmerer and Furbank, 1999). This biochemical model assumes CO_2 availability limits the rate of phospho*enol*pyruvate (PEP) carboxylation. Consequently, the enzyme limited rate of PEP carboxylation, V_p (Eq. 4.3.1.1, main text) was expressed using CO_2. Therefore, to link the rate of PEP carboxylation with limitations of CO_2 availability, V_p was assumed to be a sink term in the reaction-diffusion equation for CO_2 (Eq. 4.3.2.5, main text).

The substrate for PEP carboxylation is a bicarbonate ion (Hatch and Burnell, 1990). This requires an expression for V_p which shows the role of concentrations of bicarbonate ions. However, the most commonly used biochemical model of C_4 photosynthesis (von Caemmerer and Furbank, 1999) and other biochemical models express V_p based on concentration of CO_2 (Peisker, 1979; Collatz *et al.*, 1992). It is not a common practice to express V_p based on bicarbonate ions in a similar expression for enzyme limited rate of V_p as in the model of von Caemmerer and Furbank (von Caemmerer and Furbank, 1999). Under these limitations, we could only show the consequences of using V_p as a sink term for CO_2 on our simulation results and conclusions. In this case, we used the same expression for the enzyme-limited rate of V_p as that of von Caemmerer and Furbank (von Caemmerer and Furbank, 1999), except that we rewrote it using the concentrations of bicarbonate ions.

The rate of PEP carboxylation rate, V_p, therefore, could be rewritten as:

$$V_p = \min\left\{\frac{V_{p,max}[\mathrm{HCO_3^-}]}{K_h + [\mathrm{HCO_3^-}]}, \frac{x J_{ATP}}{2}\right\} \tag{B.2.1}$$

where $[\mathrm{HCO_3^-}]$ is the concentration of bicarbonate ions in the mesophyll cytosol, K_h is the Michaelis-Menten constant of PEPc for bicarbonate ions, and $V_{p,max}$ is the maximum catalytic rate of PEPc with bicarbonate ions as a substrate (assumed equal to the maximum catalytic rate of PEPc for CO_2). K_h was reported to be 20 µM (Bauwe, 1986). The first expression between the brackets is for the enzyme-limited rate while the second one is for the electron-transport limited rate of PEP carboxylation. The partitioning factor, *x*, is the fraction of ATP allocated to C_4 cycle. J_{ATP} is the rate of ATP production (Eq. B.1.1, Appendix B).

When V_p was used as a sink term for bicarbonate ions the reaction-diffusion equation for CO_2 is given by:

$$\frac{\partial[\mathrm{CO_2}]_m}{\partial t} = \nabla\cdot\left(D_{CO_2}\nabla[\mathrm{CO_2}]_m\right) - B_{CA} + R_m^* \tag{B.2.2}$$

where ∇ the gradient operator; D_{CO_2} is the diffusion coefficient of CO_2 in the liquid phase; $[HCO_3^-]$ is the concentration of CO_2 in mesophyll cells; V_p^* is the volumetric rate of V_p (Table B.1.1); and B_{CA}, the rate of CA catalyzed hydration of CO_2 in mesophyll cytosol (Spalding and Portis, 1985; Tholen and Zhu, 2011), is given by Eq. 4.6 (main text).

The reaction-diffusion equation for bicarbonate is given by:

$$\frac{\partial [HCO_3^-]_m}{\partial t} = \nabla \cdot \left(D_{HCO_3^-} \nabla [HCO_3^-]_m \right) + B_{CA} - V_p^* \tag{B.2.3}$$

where $D_{HCO_3^-}$ is the diffusion coefficient of bicarbonate.

The reaction-diffusion equations for CO_2 and bicarbonate in bundle sheath cells remains the same as in Eq. 4.3.2.8 to Eq. 4.3.2.10 (main text).

We solved the reaction-diffusion equations after including the equations, B.2.2 and B.2.3 (the model hereafter called Model-two). The responses of photosynthesis to changes in intercellular CO_2 and irradiance were compared with those predicted from the model presented in the main text (hereafter called Model-one). Fig. B.2.4 shows that the response of photosynthesis to light (A) and CO_2 (B) were not affected. There was less than 3 % change in the rates of photosynthesis. This is because, in our model, V_p (Eq. B.2.1) was electron transport limited even at low CO_2 levels (see Fig. B.2.1). In addition, Fig. B.2.2 (C, D) shows that there was a one to one relationship between mean concentration of CO_2 in mesophyll and bundle sheath cells calculated from Model-one and Model-two. Interestingly, at the condition used for the sensitivity analysis (ambient CO_2 of 380 µmol mol^{-1} and irradiance of 1500 µmol m^{-2} s^{-1}), both photosynthesis and the mean concentrations changed by less than 1 %.

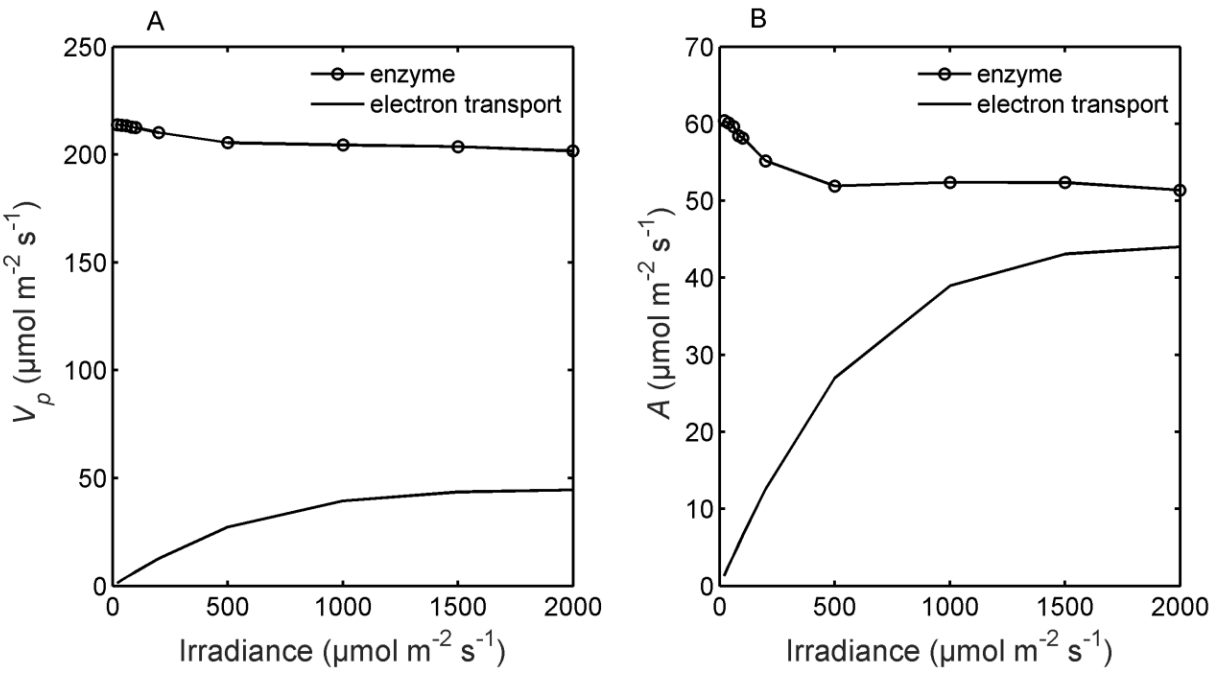

Figure B.2.1. Response of the rate of PEP carboxylation (A) and photosynthesis (B) to irradiance. Enzyme-limited rates are labeled as enzyme limited while electron-transport-limited rates are labeled as e^- transport limited. The equations for each limitation are shown in Eq. 1 and Eq. 2-4 in the main text. Conditions for the simulation were: C_a = 1000 µmol mol^{-1} and 2 % O_2.

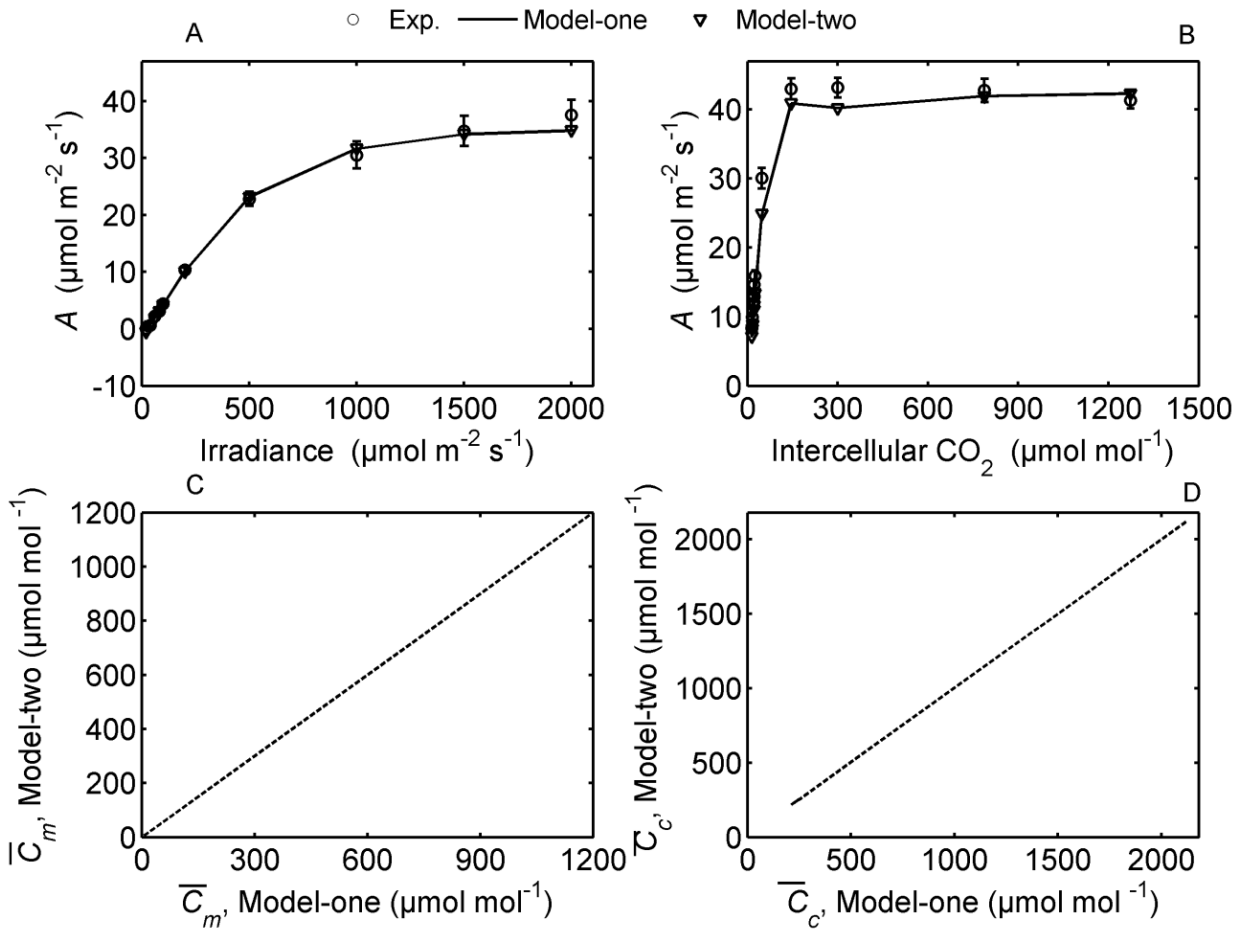

Figure B.2.2. Responses of photosynthesis to irradiance (panel A) and intercellular CO_2 (panel B) when the rate of PEP carboxylation was used as a sink term in the reaction-diffusion equation for CO_2 (Model-one) or that for bicarbonate ions (Model-two). Panel C and D show the plot of mean concentration of CO_2 in mesophyll cell ($\overline{C}_m$) and in bundle sheath cells ($\overline{C}_c$) calculated from Model-one and Model-two. Conditions for the simulation were: C_a = 380 μmol mol^{-1}, irradiance = 1500 μmol m^{-2} s^{-1} and 21 % O_2 except for the irradiance response curve where C_a = 250 μmol mol^{-1}.

In conclusion, we did not find substantial effect on our results (less than 5 % change) due to the modification of V_p. Therefore, a change in the position of V_p as a sink term would not change the conclusions. It should be noted that we could not propose the modified biochemical model (Eq. B.2.1) along with the reaction-diffusion model in the main text as this would lead to complexity.

B.3. Assessing the role of suberin

Bundle sheath cells of maize leaves are suberized (Dengler *et al.*, 1994; Mertz and Brutnell, 2014). The suberin layer is proposed to restrict CO_2 leakage through the apoplastic pathway directly towards the intercellular air spaces (Dengler *et al.*, 1994). To assess this role of suberin at the exposed surface of the bundle sheath cells, we carried out a separate simulation where the suberin layer was assumed fully permeable to CO_2. The insulated boundary condition was changed. Subsequently, the CO_2 concentration at the boundary in contact with the air space was assumed equal to the measured intercellular CO_2 concentration. The resistance of the interface at the exposed bundle sheath interface was the sum of the resistance of bundle sheath cell wall and plasma membrane. The default model parameters were as described in the main text and in Table B.2. The rate of leakage (Eq. B.1.7, Appendix B) was compared to that calculated when the exposed surface was assumed insulated.

B.4. Model parameters $V_{p,\,max}$ and $V_{c,\,max}$

Parameters of the biochemical models such as $V_{p,max}$ and $V_{c,max}$ could be estimated from a combined measurements of gas exchange and chlorophyll fluorescence using the procedures of Yin *et al.*(2011b). Based on this procedure, however, we found out that $V_{p,max}$ and $V_{c,max}$ were inestimable from the measurement data explained in materials and methods. This was due to good linear relationships between quantum yield of CO_2 fixation, $(A + R_d)/I_{inc}$, and quantum yield of PSII electron transport across all CO_2 and all irradiance levels (I_{inc}). The relationships are shown in Fig. B.4.1. This implies that the rate of photosynthesis was limited by electron transport across irradiance and CO_2 levels. In this case, therefore, $V_{p,max}$ and $V_{c,max}$ could not be estimated.

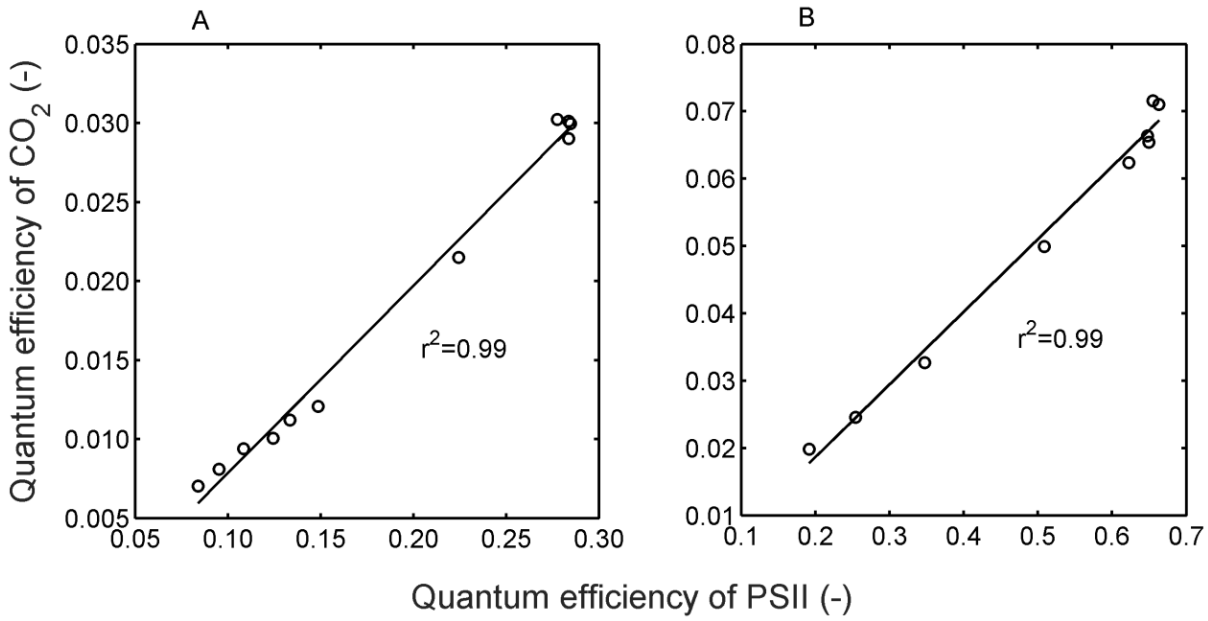

Figure B.4.1 Quantum efficiency of CO_2 fixation versus quantum efficiency of PSII electron transport across all CO_2 levels (A) and all irradiance levels (B).

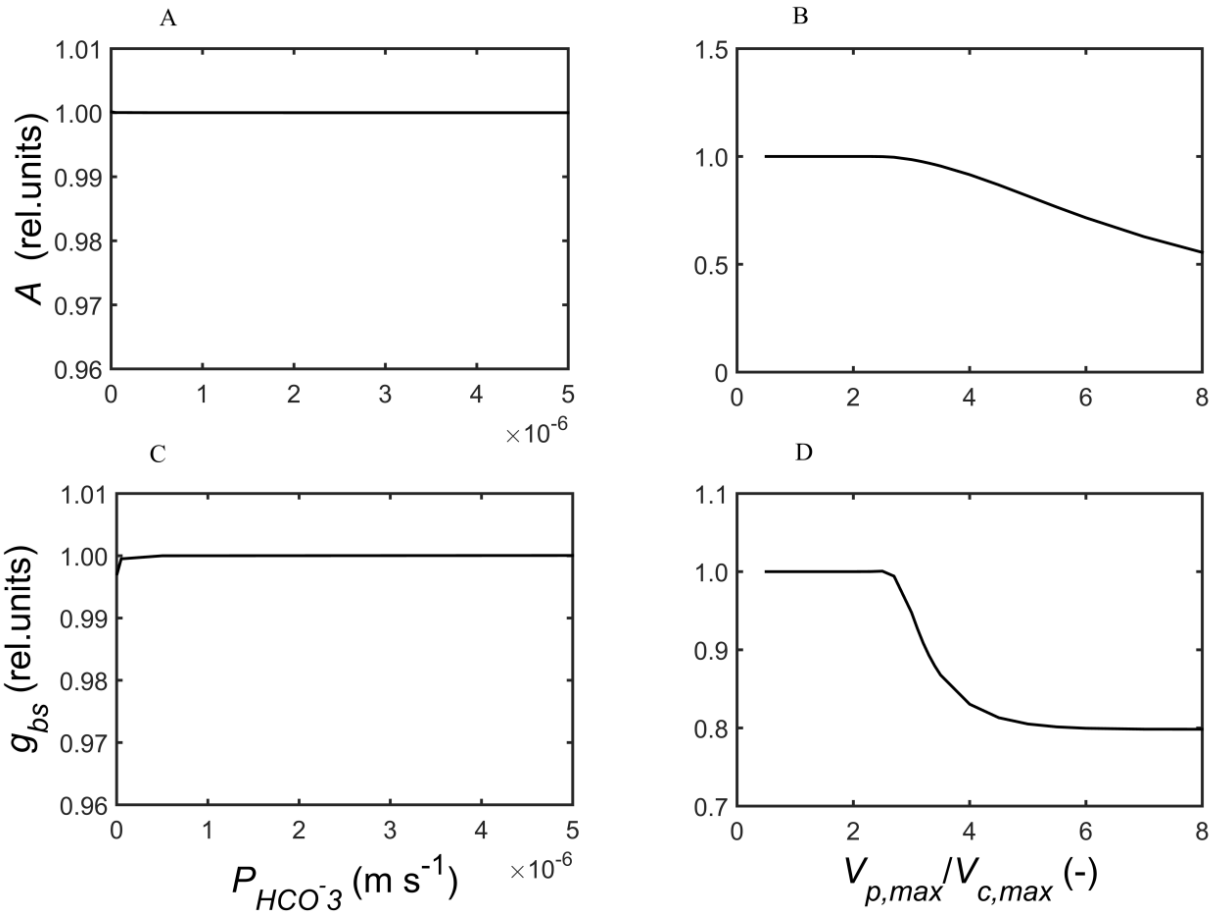

Figure B.4.2. Sensitivity of rate of photosynthesis (top; A, B) and bundle sheath conductance (bottom; C, D) to bicarbonate permeability of chloroplast envelope (A, C) and the ratio $V_{p,max} / V_{c,max}$ (B, D). Conditions for the simulation were: C_a = 380 µmol mol^{-1}, irradiance = 1500 µmol m^{-2} s^{-1} and 21 % O_2. Relative values were calculated by dividing A and g_{bs} with their default value ($g_{bs} = 3.52 \times 10^{-3}$ mol m^{-2} s^{-1}, A = 40 µmol m^{-2} s^{-1}).

B.5. Limitation of photosynthesis by rate of electron transport

The biochemical model of C_4 photosynthesis (Eqs. 4.1, 4.2 to 4.4, main text) express photosynthesis as limited by enzyme or the rate of electron transport. It is believed that enzyme-limited rate of PEP carboxylation largely limits photosynthesis at low CO_2 concentrations, while the maximum rate is limited by regeneration of phospho*enol*pyruvate (PEP) or ribulose-1,5-

bisphosphase (von Caemmerer and Furbank, 1999). We compared the enzyme and electron-transport limited rates of CO_2 assimilation in mesophyll cells and CO_2 reduction in bundle sheath cells. We choose the irradiance response curve of photosynthesis at 2 % O_2 and ambient CO_2 of 1000 µmol mol^{-1} since our model predictions (Fig. 2A, main text) show overestimations for this condition. Fig. B.2.1 shows the electron transport limited both PEP carboxylation and photosynthesis across irradiance and intercellular CO_2 levels.

It was assumed that CO_2 is produced from decarboxylation of C_4 acids in bundle sheath chloroplast at the same rate as the rate of PEP carboxylation in mesophyll cells (Materials and methods, main text). Fig. B.2.1 shows that PEP carboxylation was limited by the rate of electron transport. Therefore, the rate of photosynthesis in bundle sheath cells is influenced by the electron-transport-limited rate of PEP carboxylation.

Eq. 4.4 (main text) shows that the electron-transport-limited rate of photosynthesis is dependent on J_{ATP}, which was determined from chlorophyll fluorescence measurements using lumped calibration factor s' (Eq. B.1.1, in Appendix B). The parameter s' was estimated by fitting photosynthesis and $\Phi I_{inc}/3$ using data points at low irradiance ranges ($20 \leq I_{inc} \leq 200$ µmol m^{-2} s^{-1}) and 2 % O_2 pooled with those at high intercellular CO_2 (500 µmol mol^{-1} and higher) (Yin *et al.*, 2011*b*). This procedure assumes that s' is constant across all light and CO_2 levels. Fig. B.5.1 shows the result of the estimation.

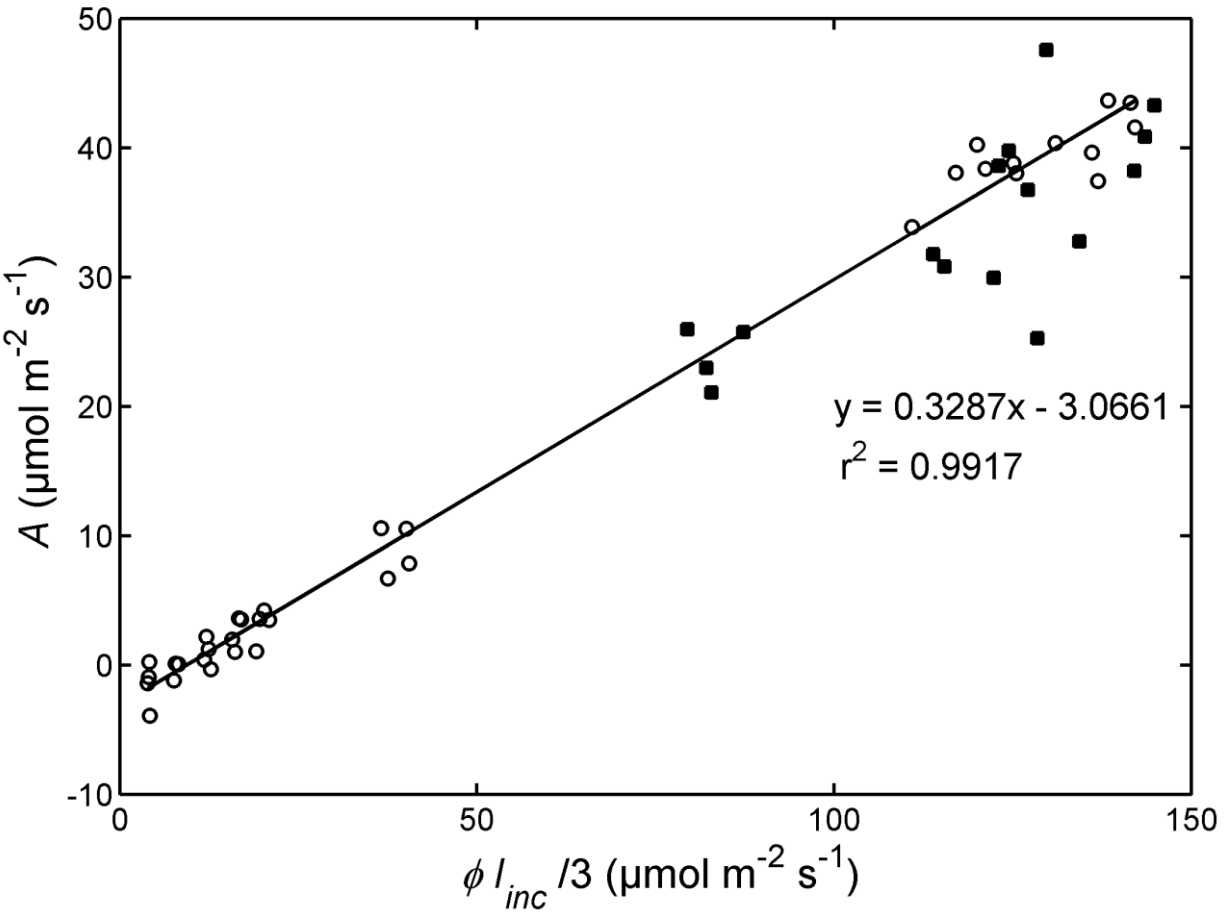

Figure B.5.1. Estimation of parameter s'. The rate of photosynthesis measured at low light intensity ($20 \leq I_{inc} \leq 200$ µmol m^{-2} s^{-1}) pooled with those measured at high intercellular CO_2 are shown in circles. The rate of photosynthesis at high light intensity ($500 \leq I_{inc} \leq 2000$ µmol m^{-2} s^{-1}) are shown in filled rectangles. The solid line shows the linear fit. The oxygen level was 2 %.

The estimated s' was used to calculate the J_{ATP} for high irradiance levels also (500 µmol m^{-2} s^{-1} and higher). However, Fig. B.5.1 shows that the measured rate of photosynthesis at the those irradiances (filled rectangles) were largely below the linear line. This was suggested to be due to the effect of pseudo cyclic electron transport at the high irradiance levels (Yin *et al.*, 2009). Thus, J_{ATP} was higher for the high irradiance levels due to the constant s' assumption. Since in our model, photosynthesis was mainly electron-transport-limited, the parameter s' through J_{ATP} influenced the predictions. Therefore, the overestimations at high light levels for 2 % O_2 were due to higher J_{ATP} brought about by the assumption of a constant s'.

B.6. Leaf microstructural geometry

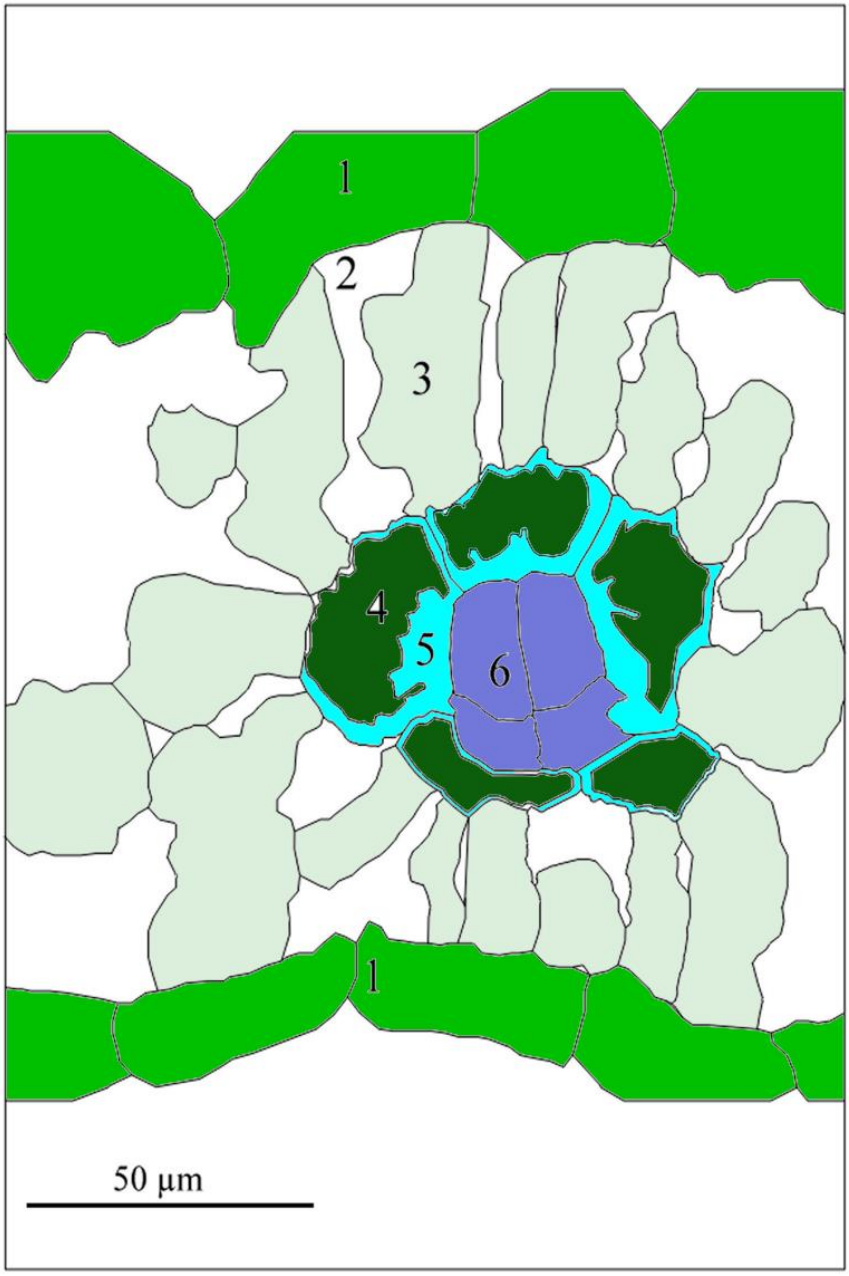

Figure B.6.1. Geometry of a maize leaf microstructure showing the epidermis (1), air spaces (2), mesophyll cells (3), bundle sheath chloroplasts (4), bundle sheath cytosol (5) and vasculature (6).

Appendix C

C.1. Modeling light distribution in maize leaf

The propagation of light in maize leaf tissue was modeled using a meshed Monte Carlo method (Watté *et al.*, 2015) which is an adaption of the classical Monte Carlo method of photon transport to suit structural intricacies of biological tissues. The three-dimensional geometry of a maize leaf (Fig. 5.1A, main text) which was voxel based was meshed using a tetrahedral mesh for use in the light propagation model. The scattering properties of cell types in the tissue were determined from size distribution of organelles in the cells and total number of organelles per unit volume (Table C.2) using a tool developed previously (Aernouts *et al.*, 2014; Ho *et al.*, 2016). A light source uniformly spread over the top side of the mesh was assumed for our simulation. Since the gas exchange measurement used 10 % blue (470 nm) and 90 % red (665 nm) light, two independent simulations of light propagation were done and the resulting two absorption profiles were combined (Table C.2). The distribution of chlorophyll obtained from literature is variable. For instance, maize mesophyll contains 65 % (Ghannoum *et al.*, 2005) or 50 % to 70 % of total chlorophyll (Furbank *et al.*, 1985; Leegood, 1985). An early report shows that the distribution of chlorophyll is 63 % in mesophyll and 38 % in bundle sheath (Ku *et al.*, 1974). Due to this uncertainty, we tentatively assumed that the absorption coefficient of bundle sheath chloroplasts is half that of mesophyll chloroplasts. Consequently, a sensitivity analysis was carried out by varying the chlorophyll distribution between mesophyll and bundle sheath cells (see Table C.7 and Materials and methods, main text). Optical properties that resulted in a match of total reflectance and transmittance computed from the model with those previously measured for a maize leaf (Woolley, 1971) are shown in Table C.6 for the default chlorophyll distribution of 0.50.

C.2. Calculation of microscale model variables

The gross volumetric rate of CO_2 fixation in bundle sheath chloroplasts is given by the minimum of Rubisco-limited carboxylation rate, w_c^*, and electron-transport-limited carboxylation rate, w_j^*, according to the biochemical model of C_4 photosynthesis (von Caemmerer and Furbank, 1999):

$$w_c^* = \frac{[CO_2]\cdot V_{c,max}^*}{[CO_2]+ K_{m,C}(1+[O_2]/ K_{m,O})} \tag{C.2.1}$$

$$w_j^* = \frac{[CO_2]\cdot j_{ATP,bs}^*}{3[CO_2]+ 7\gamma^*[O_2]} \tag{C.2.2}$$

where $K_{m,C}$ and $K_{m,O}$ are Michaelis-Menten constants of Rubisco for CO_2 and O_2, respectively; γ^* = 0.5/$S_{c/o}$ where $S_{c/o}$ is Rubisco specificity to carboxylation and oxygenation; $V_{c,max}^*$ is the maximum capacity of Rubisco carboxylation; and, $j_{ATP,bs}^*$ is the potential rate of ATP production in bundle sheath cells.

The total ATP production rate, j_{ATP} is calculated as the sum of rate of ATP production due to linear electron transport (LET) j_{LET} in mesophyll (subscript *m*) chloroplasts, bundle sheath (subscript *bs*) chloroplasts and that due to the rate of cyclic electron transport (CET) in bundle sheath chloroplasts (j_{CET}). The volumetric rate, j_{ATP}^* is given as:

$$j_{ATP}^* = \frac{3}{4} j_{LET,m}^* + \frac{3}{4} j_{LET,bs}^* + \frac{2}{4} j_{CET,bs}^* \tag{C.2.3}$$

where coefficients 3/4 and 2/4 are ATP produced per electron by LET and CET, respectively. Based on the generally accepted stoichiometry, 1 electron gives rise to 3 H^+ for LET and 2 H^+ for CET, and 4 H^+ are required to synthesize 1 ATP (Yin and Struik, 2012).

The potential volumetric rate of electron transport in mesophyll chloroplast or bundle sheath chloroplast, j^* is given by the hyperbolic minimum of light-limited (LL) rate j^*_{LL} and light-saturated rate, $j^*_{\max}$ (Buckley and Farquhar, 2004) as:

$$j_i^* = \min h\left(j^*_{LL,i}, j^*_{max,i}\right) = \frac{j^*_{LL,i} + j^*_{max,i} - \sqrt{\left(j^*_{LL,i} + j^*_{max,i}\right)^2 - 4\Theta \cdot j^*_{LL,i} \cdot j^*_{max,i}}}{2\Theta} \quad \text{(C.2.4)}$$

where Θ is a measure of co-limitation of electron transport by light and capacity (Buckley & Farquhar, 2004), and *i* refers to the above three electron transport types (Eq. C.2.3).

The parameter $j_{\max}$ was estimated by minimizing the difference between the total ATP production rate determined from chlorophyll fluorescence measurement (Eq. C.2.16) and that modeled from the potential electron transport rate at the whole leaf level (Eq. C.2.17). To facilitate the estimation, it was assumed that $j_{max,LET}$ is the same for mesophyll and bundle sheath chloroplasts since j_{max} is a physiological parameter. It is also assumed that $j_{max,LET}$ in mesophyll cells and $j_{max,CET}$ in bundle sheath cells were equal.

For LET, one needs to take into account the commonly observed difference in electron transport efficiency between PSI and PSII (Yin and Struik, 2012), so the term j^*_{LL} in Eq. C.2.4 is written for the three electron-transport types as:

$$j^*_{LL,LET,m} = \frac{\Phi_{2LL}}{1+\Phi_{2LL}/\Phi_{1LL}} I^*_{abs,m} \quad \text{(C.2.5)}$$

$$j^*_{LL,LET,bs} = \frac{\Phi_{2LL}}{1+\Phi_{2LL}/\Phi_{1LL}} \nu I^*_{abs,bs} \quad \text{(C.2.6)}$$

$$j^*_{LL,CET,bs} = \Phi_{1LL}(1-\nu) I^*_{abs,bs} \quad \text{(C.2.7)}$$

where $I^*_{abs,m}$ and $I^*_{abs,bs}$ are the volumetric rates of photon absorption by mesophyll and bundle sheath cells, respectively, calculated by the product of actinic irradiance and the fraction of that

irradiance absorbed by the chloroplasts in these cells. □□$_{1LL}$ and □$_{2LL}$ are the electron transport efficiency under limiting light for PSI and PSII, respectively. *v* is the fraction of light for LET in bundle sheath chloroplasts, which would be solved as function of other parameters (see next).

Expressing v as a function of other parameters

Let *T* be the total amount of PSII in bundle sheath and mesophyll cells; then αT will be the amount of PSII in bundle sheath cells (where □ is the parameter as used in the standard model of C_4 photosynthesis von Caemmerer & Furbank (1999) for the fraction of PSII in bundle sheath cells), and $(1-\alpha)T$ will be the amount of PSII in mesophyll cells (Table C.2.1).

Table C.2.1. Amounts of PSII and PSI for LET in bundle sheath cells and mesophyll cells, and of PSI for CET in bundle sheath cells.

Electron transport types	Bundle sheath chloroplast		Mesophyll chloroplast	
	PSII	PSI	PSII	PSI
LET	αT	$\frac{\phi_{2LL}}{\phi_{1LL}}\alpha T$	$(1-\alpha)T$	$\frac{\phi_{2LL}}{\phi_{1LL}}(1-\alpha)T$
CET		C_x		

To account for the difference in the electron transport efficiency between PSI and PSII, the amount of PSI in bundle sheath cells has to be $\frac{\phi_{2LL}}{\phi_{1LL}}\alpha T$ to enable an equal electron transport flux passing through PSI and PSII for LET; similarly the amount of PSI in mesophyll cells has to be $\frac{\phi_{2LL}}{\phi_{1LL}}(1-\alpha)T$ (Table C.2.1). It is to be noted that LET dominates in mesophyll cells for maize, thus CET was assumed negligible (Kanai and Edwards, 1999).

Let the amount of PSI in bundle sheath for CET be C_x. Then C_x could be solved based on ATP requirement for C_4 physiology. ATP produced from total LET and CET should be $\frac{3}{4}[K_{bs}\alpha T + K_m(1-\alpha)T]\phi_{2LL}$ and $\frac{2}{4}k_{bs}C_x\phi_{1LL}$, respectively (where K_{bs} and K_m are mol photon absorbed per unit photosystem in BS and M chloroplasts, respectively). It is recognized that ATP generated from

LET is used for the C_3 cycle and ATP from CET is used for the C_4 cycle (Takabayashi *et al.*, 2005) and that per mol CO_2 fixation requires 3 mol of ATP for the C_3 cycle and 2 mol ATP C_4 cycle, respectively (von Caemmerer & Furbank 1999). Therefore the following equation can be written as:

$$\frac{\frac{3}{4}[K_{bs}\alpha T + K_m(1-\alpha)T]\Phi_{2LL}}{\frac{2}{4}K_{bs}C_x\Phi_{1LL}} = \frac{3}{2} \tag{C.2.8}$$

This results in $C_x = \frac{[K_{bs}\alpha + K_m(1-\alpha)]\Phi_{2LL}}{K_{bs}\Phi_{1LL}}T$.

The total amount of light absorbed by bundle sheath cells ($I_{abs,bs}$) can be written, based on Table C.2.1, as:

$$I_{abs,bs} = K_{bs}\left(\alpha T + \frac{\Phi_{2LL}}{\Phi_{1LL}}\alpha T + C_x\right) = K_{bs}\left(\alpha T + \frac{\Phi_{2LL}}{\Phi_{1LL}}\alpha T + \frac{[K_{bs}\alpha + K_m(1-\alpha)]\Phi_{2LL}}{K_{bs}\Phi_{1LL}}T\right) \tag{C.2.9}$$

The amount of light absorbed by bundle sheath cells ($I_{abs,bs,LET}$) that is used for LET can be written, based on Table C.2.1, as:

$$I_{abs,bs,LET} = K_{bs}\left(\alpha T + \frac{\Phi_{2LL}}{\Phi_{1LL}}\alpha T\right) \tag{C.2.10}$$

The parameter v, by definition, is the ratio of $I_{abs,bs,LET}$ to $I_{abs,bs}$, which can be solved from the above two equations as:

$$v = \frac{1+\frac{\Phi_{2LL}}{\Phi_{1LL}}}{1+\frac{\Phi_{2LL}}{\Phi_{1LL}}\left(1+\frac{\alpha K_{bs}+K_m(1-\alpha)}{\alpha K_{bs}}\right)} \tag{C.2.11}$$

The volumetric rate of photorespiration (r_p^*) in bundle sheath chloroplast is multiplied by the ratio of volume of bundle sheath chloroplast, $V_{bs,ch}$, to the volume of the cytosol of bundle sheath (subscript *bs, cy*), $V_{bs,cy}$, to calculate the volumetric rate of CO_2 release in bundle sheath cytosol. r_p^* is given by:

$$r_p^* = \frac{\int_{V_{bs,ch}} V_c^* \cdot \frac{\gamma^*[O_2]}{[CO_2]}\, dv}{\int_{V_{bs,cy}} (\cdot) dv} \tag{C.2.12}$$

where $V_c^* = \min(w_c^*, w_j^*)$ (von Caemmerer and Furbank, 1999) and volume is calculated by $\int_G (\cdot) dv = \iiint_G dx dy dz$ for region *G* (cytosol or chloroplast).

Consumption of 1 mol of O_2 by photorespiration results in the release of 0.5 mol of CO_2. Thus, the volumetric rate of oxygen consumption by photorespiration (r_{p,O_2}^*) in a bundle sheath chloroplast is given by:

$$r_{p,O_2}^* = \frac{\int_{V_{bs,ch}} 2V_c^* \cdot \frac{\gamma^*[O_2]}{[CO_2]}\, dv}{\int_{V_{bs,ch}} (\cdot) dv} \tag{C.2.13}$$

The rate of PEP carboxylation (V_p) is given as a minimum of enzyme-limited rate (first term in bracket, Eq. C.2.14) and electron-transport-limited rate of PEP carboxylation (second term in the bracket, Eq. C.2.14) (von Caemmerer and Furbank, 1999). Note that the enzyme-limited rate in the biochemical model (von Caemmerer and Furbank, 1999) is expressed using concentration of CO_2 under the assumption that CA activity does not limit photosynthesis. However, at low intercellular CO_2 this assumption may not be valid (Studer *et al.*, 2014; Boyd *et al.*, 2015).

Therefore, as proposed in a recent study (Boyd *et al.*, 2015), we adopted the enzyme-limited rate and rewrite V_p^* as:

$$V_p^* = \min\left\{\frac{[HCO_3^-]\cdot V_{p,max}^*}{[HCO_3^-]+K_h}, \frac{j_{ATP,m}^*}{2}\right\} \quad \text{(C.2.14)}$$

where K_h is the Michaelis-Menten constant of PEPC for bicarbonate and $V_{p,max}^*$ is the maximum catalytic rate of PEPC. The potential rate of electron transport in mesophyll cells, $j_{ATP,m}^*$ was determined from Eq. C.2.4.

The average rate of CO_2 production from decarboxylation of C_4 acids, assumed to proceed at the same rate as PEP carboxylation (Eq. C.2.14) in mesophyll cytosol (subscript *m,cy*) (von Caemmerer and Furbank, 1999), was calculated as:

$$\bar{V}_p^* = \frac{\int_{V_{m,cy}} V_p^* \, dv}{\int_{V_{bs,ch}} (\cdot) dv} \quad \text{(C.2.15)}$$

where $V_{bs,ch}$ is the volume of bundle sheath chloroplast (subscript *bs,ch*) and $V_{m,cy}$ is the volume of mesophyll cytosol.

The rate of total ATP production computed from chlorophyll fluorescence (CF) measurements $j_{ATP,CF}$ was given by (Yin *et al.*, 2011*b*) as:

$$j_{ATP,CF} = \frac{s' I_{inc} (\Delta F / F_m')}{(1-x)} \quad \text{(C.2.16)}$$

$$\Delta F / F_m' = (F_m' - F_s) / F_m',$$

where *s'* is the lumped light conversion efficiency; F_s is the steady-state relative fluorescence yield; F'_m is the maximum relative fluorescence yield in the leaf; and, *x* is the fraction of ATP allocated to the C_4 cycle (Table C.2.2). For this calculation, a constant *x* of 0.40 for all irradiances and mesophyll cells was assumed as is commonly done (Yin *et al.*, 2011*b*; Yin and Struik, 2012).

The potential ATP production rate ($\overline{J}_{ATP}$) at the whole leaf level is given by:

$$\overline{J}_{ATP} = \frac{\int_{V_{leaf}} j^*_{ATP} dV}{A_{leaf}} \tag{C.2.17}$$

where A_{leaf} is the area of a cross section of the computational domain; j^*_{ATP} is the local volumetric rate of ATP production determined from Eq. C.2.3; and, V_{leaf} is the total leaf volume.

The potential ATP production rate ($\overline{J}_{ATP,m}$) in mesophyll cells is given by:

$$\overline{J}_{ATP,m} = \frac{\int_{V_m} j^*_{ATP} dV}{A_{leaf}} \tag{C.2.18}$$

j^*_{ATP} is given by Eq. C.2.3; and, V_m is the total volume of mesophyll chloroplasts.

The apparent fraction of ATP partitioned to the C_4 cycle computed from the light propagation model $\overline{x}$ is given by:

$$\overline{x} = \frac{\overline{J}_{ATP,m}}{\overline{J}_{ATP}} \tag{C.2.19}$$

The rate of net photosynthesis was calculated by integrating the flux of CO_2 over the outer epidermis surfaces. The computed photosynthesis, A is given as:

$$A = \frac{\int_{Ae} |Flux| \, dA}{A_p} \tag{C.2.20}$$

where Flux is a normal diffusive flux defined as, $n \cdot (-D \nabla C)$, n is the normal vector of unit length; A_e is the epidermis surface; and, A_p is a projected area of the leaf.

The volume averaged concentration of gases y (CO_2 or O_2) in components of leaf tissue i (mesophyll cytosol, mesophyll chloroplasts or bundle sheath chloroplast) was calculated from the model as:

$$\overline{C}_{y,i} = \frac{\int_{V_{i,leaf}} [C_{y,i}] dV}{V_{i,leaf}} \tag{C.2.21}$$

where $V_{i,}$ is the volume of component i in the 3-D leaf tissue geometry.

Rate of CO_2 leakage, L is given by:

$$L = \overline{V}_p - A - R_m \tag{C.2.22}$$

where $\overline{V}_p$ is the mean rate of PEP carboxylation calculated from Eq. C.2.14 and R_m is the rate of CO_2 release in mesophyll cytosol through respiration.

Leakiness ϕ is calculated as:

$$\phi = \frac{L}{\overline{V}_p} \tag{C.2.23}$$

Temperature dependency of biophysical parameters such as diffusion coefficients of gases (in air or liquid), solubility of gases, viscosity of cell medium and biochemical parameters such as $V_{c,max}$, γ^*, $K_{m,O}$, $K_{m,C}$, K_h and R_d (Table C.2.3) is defined by the Arrhenius equation normalized to 25 °C as (Juurola *et al.*, 2005; Boyd *et al.*, 2015; Yin *et al.*, 2016):

$$\text{Parameter}(T_k) = \text{Parameter}(298\text{ K}) \cdot e^{\frac{E}{R}\left(\frac{1}{298.15} - \frac{1}{T_k}\right)} \tag{C.2.24}$$

where E is the activation energy for the parameter and R is the universal gas constant.

Temperature dependency of $V_{p,max}$, $V_{CA,max}$ or light-saturated electron transport rate (j_{max}), which has a temperature optimum, is given by (Massad *et al.*, 2007; Boyd *et al.*, 2015):

$$\text{Parameter}(T_k) = \text{Parameter}(298\text{ K}) \cdot e^{\frac{E(T_k - 298.15)}{298.15 R T_k}\left(\frac{1+e^{\left(\frac{298.15S-H}{298R}\right)}}{1+e^{\left(\frac{T_kS-H}{T_kR}\right)}}\right)} \tag{C.2.25}$$

where S is the entropy term and H is the energy of deactivation.

Temperature dependence of CA activity as modeled by Eq. 5.2 (main text) was not reported for maize. Instead, the first order rate constant of CA activity reported for a NADP-ME type C_4 plant (Boyd *et al.*, 2015) was tentatively assumed. In addition, temperature responses of non-enzymatic hydration of CO_2 (Eq. 5.4, main text) reported in Boyd *et al*. (2015) was also adopted here.

C.3. Modeling CO_2 release in bundle sheath cytosol

CO_2 is released in the bundle sheath cytosol due to PEPCK activity and photorespiration. NADP-ME type C_4 plants such as maize decarboxylate aspartate in bundle sheath cells resulting CO_2 release in the cytosol (Pick *et al.*, 2011). In addition to this, increased oxygen evolution due to PSII abundance may increase the potential for photorespiration (von Caemmerer and Furbank, 1999). The CO_2 thus produced feeds the Calvin cycle or diffuses back to mesophyll cells (Furbank, 2011). To systematically evaluate the effect of CO_2 release outside the chloroplast on

the efficiency of CCM, we carried out simulations of photosynthesis and leakiness in response to fractions of CO_2 release by PEPCK and by increasing the abundance of PSII.

When both PEPCK and NADP-ME operate in decarboxylation, we assumed that , at steady state, the total CO_2 assimilation by PEP carboxylation in mesophyll cells equals the total CO_2 released in bundle sheath cells by decarboxylation of aspartate (ASP) and malate (MAL). Assuming a fraction of the total CO_2 is released in the bundle sheath cytosol through aspartate decarboxylation (f_{ASP}), the volumetric rate of CO_2 release by PEPCK ($V^*_{p,ASP}$) in the bundle sheath cytosol and that by NADP-ME ($V^*_{p,MAL}$) are given by:

$$V^*_{p,ASP} = \frac{f_{ASP}}{V_{bs,cy}} \cdot \int_{V_{m,cy}} V^*_p \, dv \tag{C.3.1}$$

$$V^*_{p,MAL} = \frac{(1 - f_{ASP})}{V_{bs,ch}} \cdot \int_{V_{m,cy}} V^*_p \, dv \tag{C.3.2}$$

where V^*_p is the volumetric rate of PEP carboxylation (Eq. C.2.14); $V_{m,cy}$ is the volume of mesophyll cytosol; $V_{b,cy}$ is the volume of the bundle sheath cytosol; and, $V_{b,ch}$ is the volume of bundle sheath chloroplast.

When the fraction of PSII content in bundle sheath cells (α) was increased, the ATP production rate due to linear electron transport increased (Eq. C.2.6). This results in higher rate of oxygen evolution (Eq. 5.6, main text). The rate of electron transport (Eq. C.2.4) and ATP production (Eq. C.2.3) are thus updated for each value of α. The possible change in the light absorbance profile due to increased α was not accounted for here. The change in the rate of ATP production was because *v* increased (Eq. C.2.11).

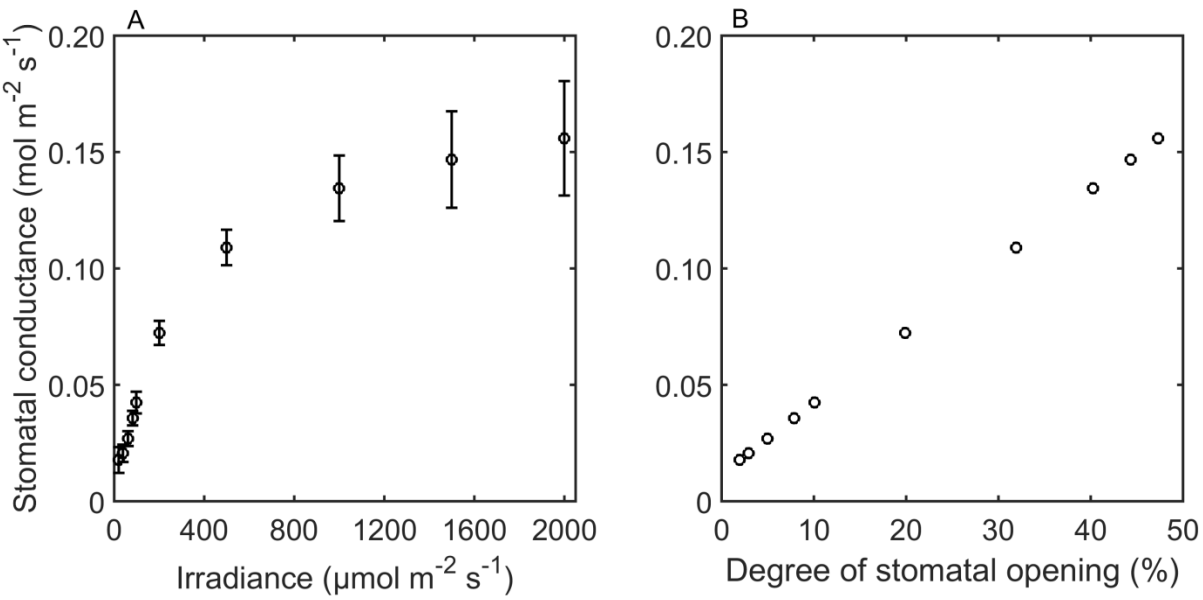

Figure C.1. Stomatal conductance in response to irradiance and degree of stomatal opening. Response of stomatal conductance to irradiance (A) measured at 21 % O_2 and ambient CO_2 of 250 µmol mol^{-1}, leaf temperature of 25 °C and leaf-to-air vapor pressure difference within 1.0-1.6 kPa. Stomatal conductance was modeled by adjusting the diffusion coefficient of gases in the stomata to simulate various degrees of stomatal opening (B). Error bars represent standard error (n = 4).

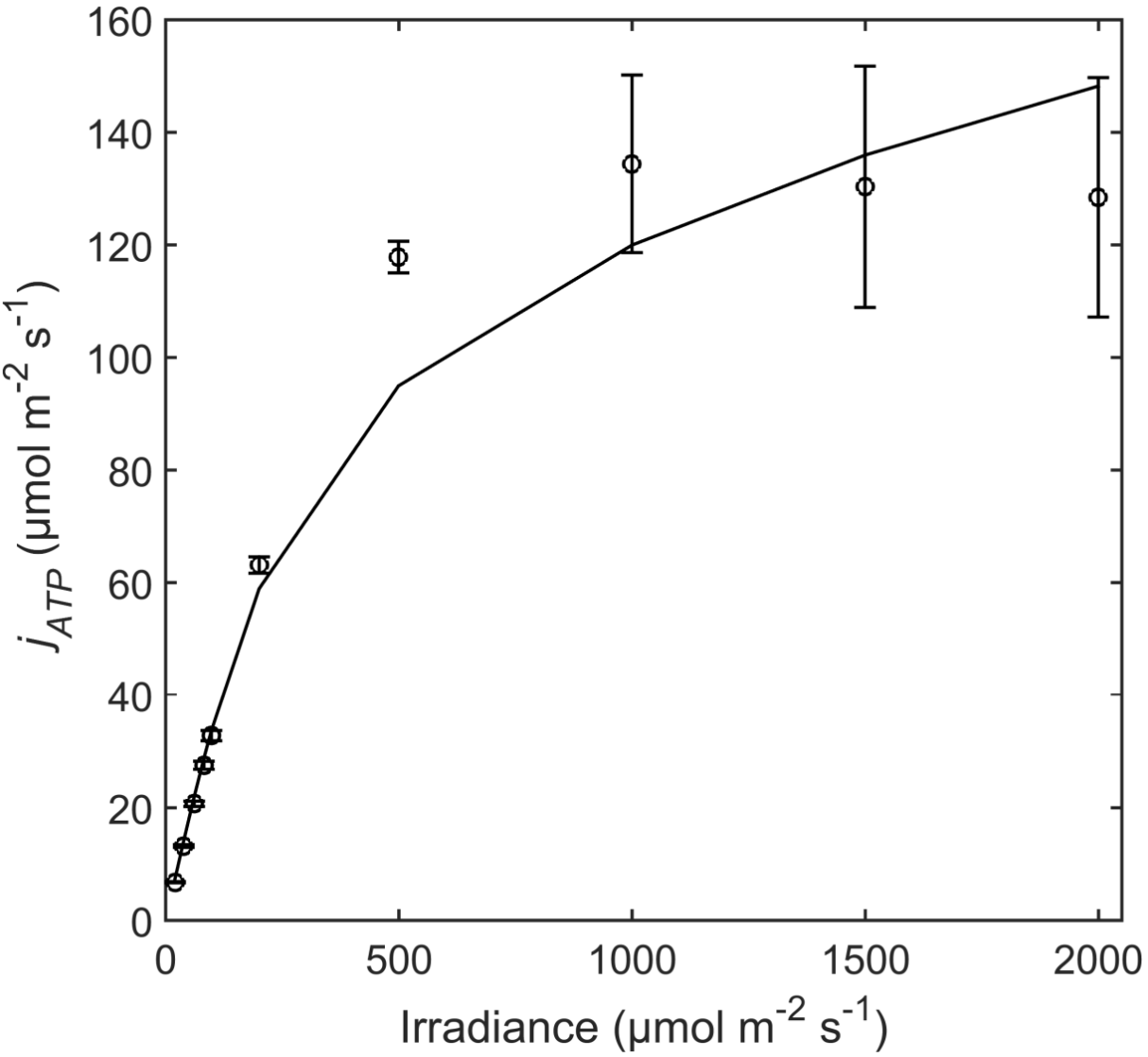

Figure C.2. Responses of the total ATP production rate (j_{ATP}) to irradiance. The computed total ATP production rate (solid line) and that obtained from chlorophyll fluorescence (CF) measurements (circles). ATP production calculated from Eq. S3 using maximum rate of electron transport in Table C.2. The ambient CO_2 was 250 µmol mol^{-1} and ambient oxygen was 21 % while temperature was 25 °C. Bars represent standard error (n = 4).

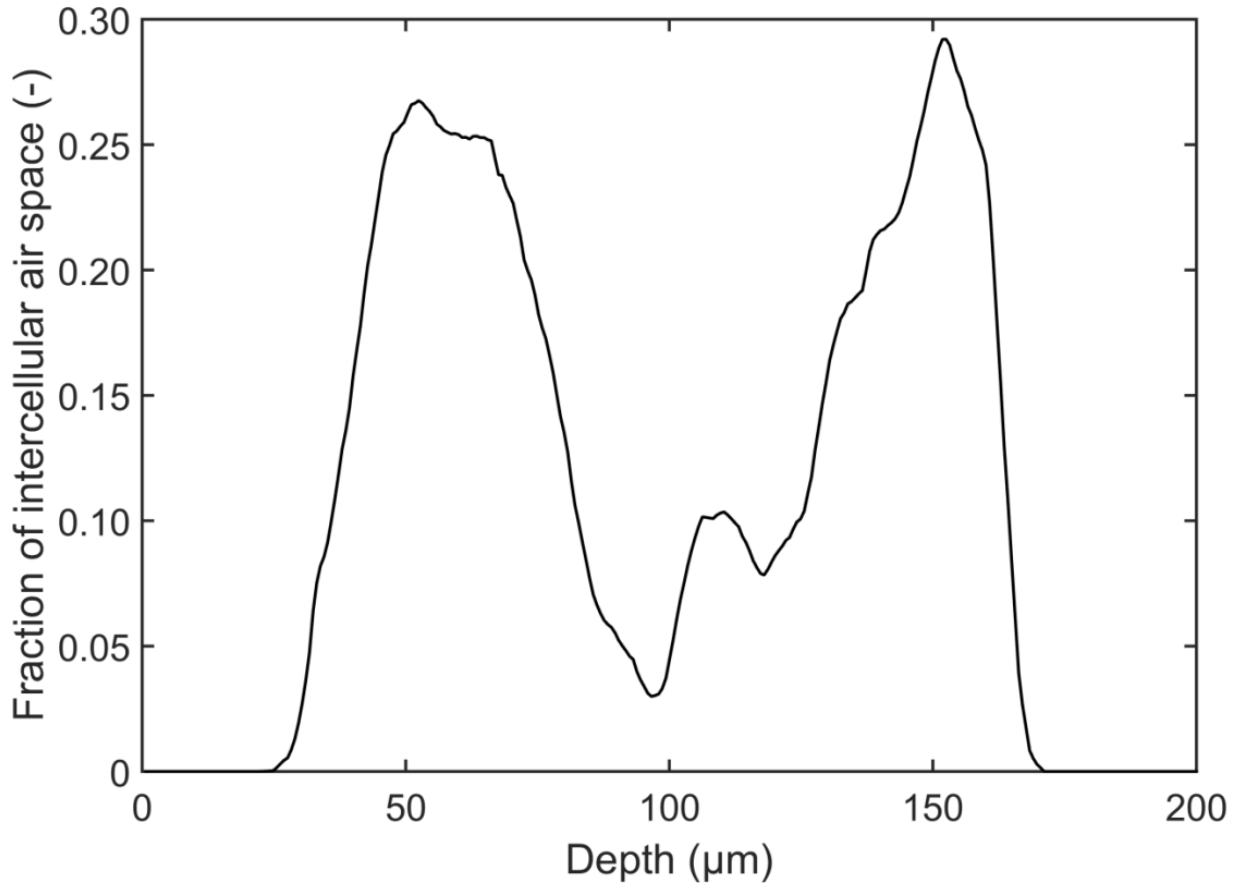

Figure C.3. Fraction of intercellular air space in leaf tissue across leaf depth. Using paradermal leaf sections, the total area of the air space is divided by the total area of the section to calculate the fraction area occupied by air spaces. Nearby 100 μm depth is where bundle sheath cells tissue are located. The fraction drops low near this region indicating poor connection of the adaxial side (25 to 100 μm depth) and abaxial side (100 – 180 μm depth) intercellular air space.

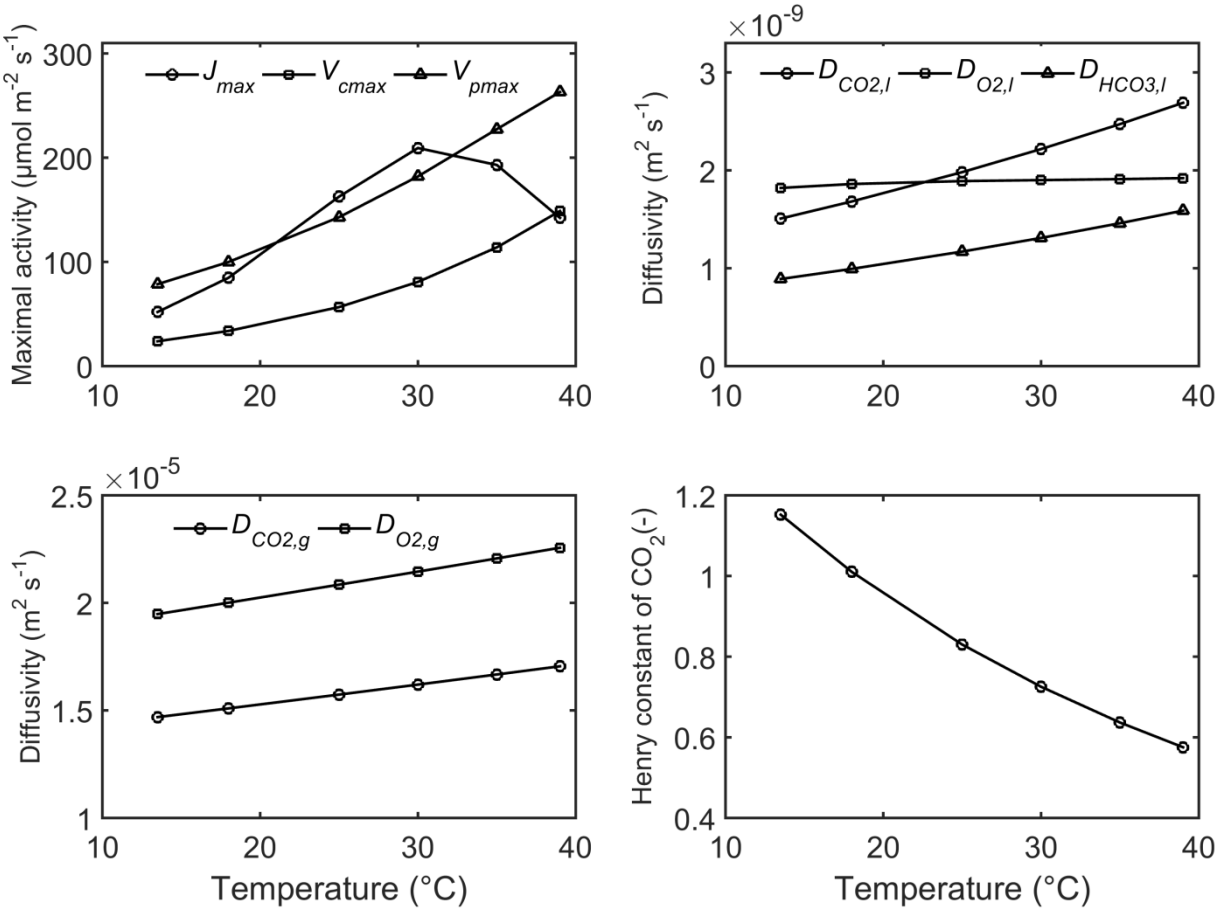

Figure C.4. Temperature response of biochemical and biophysical parameters. Temperature response of biochemical parameters (A) such as the maximum rate of electron transport ($j_{\max}$), maximum capacity of Rubisco-limited carboxylation ($V_{c,max}$) and maximum rate of PEP carboxylation ($V_{p,max}$). Temperature response of diffusion coefficients of CO_2 (D_{CO_2}), O_2 (D_{O_2}) and HCO^-_3 ($D_{HCO_3^-}$) liquid (subscript l) phase (B) and gas (subscript g) (C). Temperature response of Henry constant of CO_2 (D). Temperature dependencies are given in Table C.2.

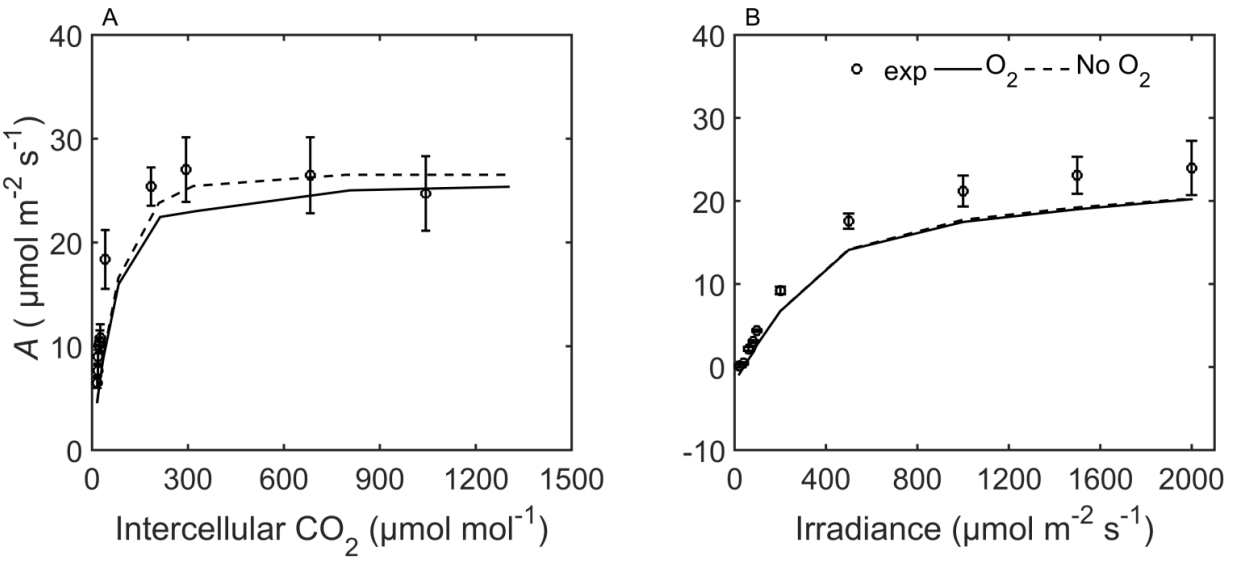

Figure C.5. Comparison of the response of photosynthesis (*A*) with and without oxygen evolution. Response of *A* to intercellular CO_2 (A) and irradiance (B). Symbols indicate experimental data and solid lines show model predictions with oxygen evolution (O_2, $\alpha = 0.10$) and dashed lines show predictions with no oxygen evolution (No O_2). Conditions for simulations in panel A were irradiance of 1500 µmol m^{-2} s^{-1} and 21 % oxygen while those in panel B were ambient CO_2 of 250 µmol mol^{-1} and 21 % oxygen. Bars show standard error (n = 4).

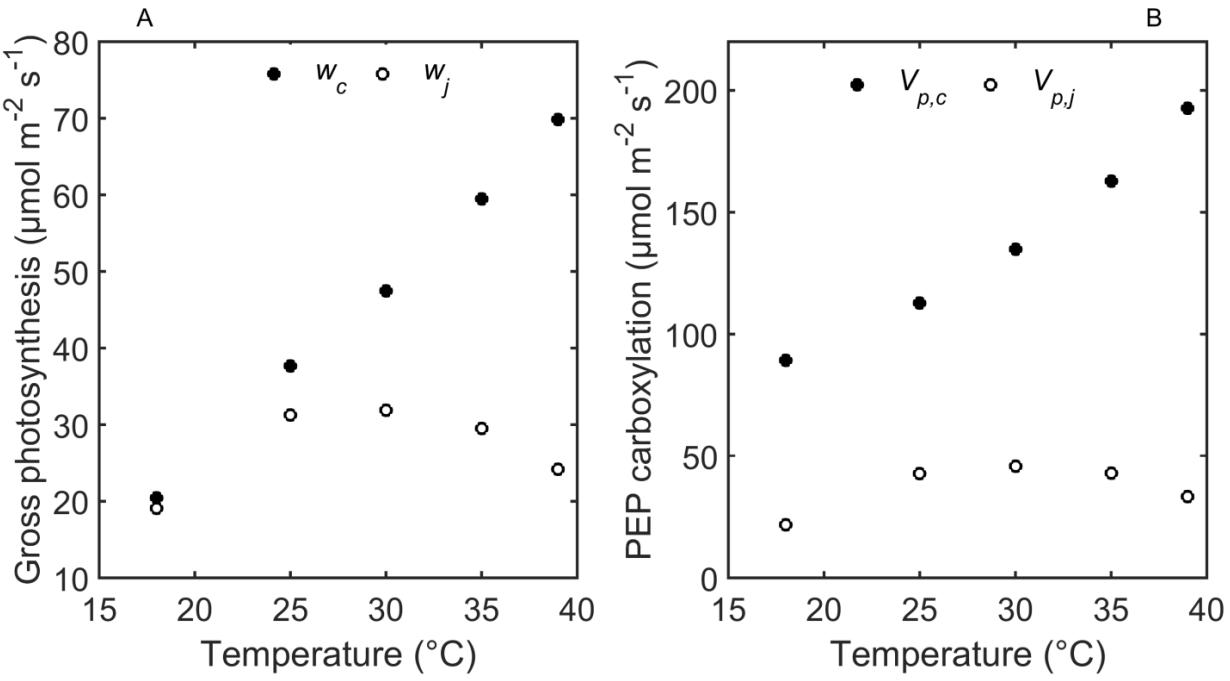

Figure C.6. Limitations of rate of photosynthesis and PEP carboxylation in response to temperature. Temperature response of Rubisco-limited gross photosynthesis (w_c, filled symbols) (A) and that of electron-transport-limited gross photosynthesis (w_j, open symbols). PEP carboxylation limited by enzyme ($V_{p,c}$, filled symbols) or by electron transport ($V_{p,j,}$ open symbols). Simulation conditions were; ambient CO_2 was 380 µmol mol^{-1}, irradiance was 1500 µmol m^{-2} s^{-1} and ambient O_2 of 21 %.

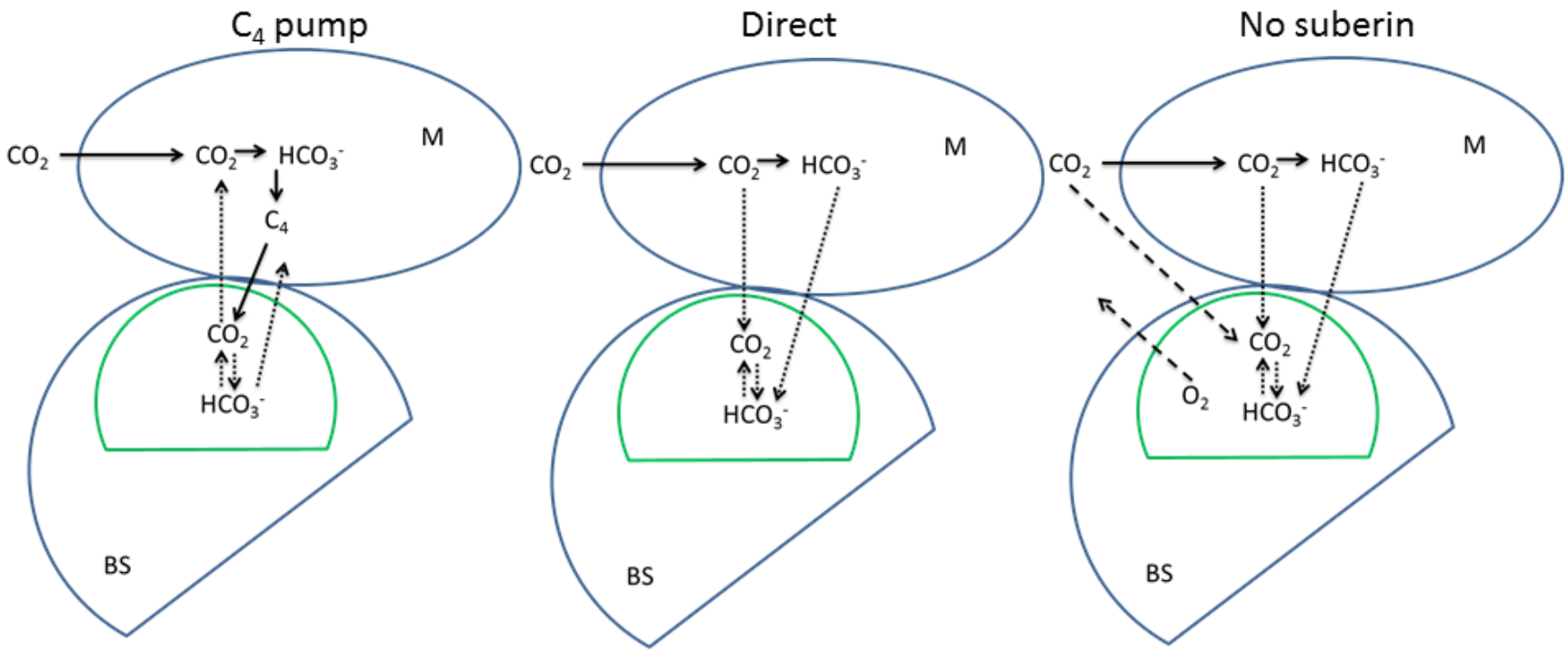

Figure C.7. Pathways of CO_2 donation to bundle sheath cells. In the pathway "C_4 pump", CO_2 is produced in bundle sheath chloroplasts by decarboxylation of C_4 acids. Exchange of CO_2 and bicarbonate occurs through plasmodesmata at the mesophyll-bundle sheath interface only. During direct diffusion, it was assumed that CO_2 diffuses to bundle sheath photosynthesis directly and indirectly through dehydration of bicarbonate. Transport of CO_2 and bicarbonate occurs through the plasmodesmata. The pathway referred as "No suberin" additionally involves exchange of CO_2 and O_2 through the entire surface of bundle sheath cells. Plasmodesmata and water filled pores of bundle sheath cell wall provide the resistance to diffusion at the mesophyll-bundle sheath and mesophyll-air space interface. M stands for mesophyll and BS for bundle sheath cells. The truncated circle inside BS is the chloroplast layer.

Table C.1. List of symbols, their definitions and units

Variable	Definition	Units
A	Net photosynthesis rate	μmol m^{-2} s^{-1}
B_{CA}	Net hydration of CO_2 in presence of carbonic anhydrase	μmol m^{-3} s^{-1}
B_{NCA}	Non enzymatic net hydration of CO_2	μmol m^{-3} s^{-1}
C_a	Ambient air CO_2 concentration	μmol mol^{-1}
$\bar{C}_c$	Mean concentration of CO_2 in bundle sheath chloroplasts	μmol mol^{-1}
$\bar{C}_m$	Mean concentration of CO_2 in mesophyll cytosol	μmol mol^{-1}
D_{CO_2}	CO_2 diffusivity in cell or gas	m^2 s^{-1}
$D_{HCO_3^-}$	Diffusivity of HCO_3^-	m^2 s^{-1}
D_{O_2}	O_2 diffusivity in cell or gas	m^2 s^{-1}
D	Average thickness of leaf tissue	μm
E_o^*	Volumetric rate of oxygen evolution	μmol m^{-3} s^{-1}
f_{epi}	Volume fraction of epidermis of the leaf	m^3 m^{-3}
$f_{bs,ch}$	Volume fraction of bundle sheath chloroplasts of the leaf	m^3 m^{-3}
$f_{bs,cy}$	Volume fraction of bundle sheath cytosol of the leaf	m^3 m^{-3}
$f_{mc,cy}$	Volume fraction of mesophyll cytosol of the leaf	m^3 m^{-3}
f_{vs}	Volume fraction of vascular bundles of the leaf	m^3 m^{-3}

$f_{resp.}$	Total volume fraction of respiratory tissue in the leaf: $f_{resp.} = f_{mc,cy} + f_{bs,cy} + f_{epi} + f_{vs}$	$m^3\ m^{-3}$
H_{CO_2}	Henry's constant for CO_2	Dimensionless
H_{O_2}	Henry's constant for O_2	Dimensionless
$[H^+]$	H^+ concentration	$mol\ L^{-1}$
$i_{abs,bs}$	Volumetric rate of photon absorption in bundle sheath	$\mu mol\ m^{-3}\ s^{-1}$
$i_{abs,m}$	Volumetric rate of photon absorption in mesophyll	$\mu mol\ m^{-3}\ s^{-1}$
j_{ATP}	Total rate of ATP production	$\mu mol\ m^{-2}\ s^{-1}$
$j_{ATP,CF}$	Total rate of ATP production calculated from chlorophyll fluorescence measurement	$\mu mol\ m^{-2}\ s^{-1}$
j^*_{ATP}	Volumetric rate of total rate of ATP production	$\mu mol\ m^{-3}\ s^{-1}$
$\overline{J}_{ATP}$	Computed potential rate of ATP production in the leaf	$\mu mol\ m^{-2}\ s^{-1}$
j^*	Volumetric rate of potential electron transport	$\mu mol\ m^{-3}\ s^{-1}$
$j^*_{CET,bs}$	Volumetric rate of potential cyclic electron transport (CET) in bundle sheath cells	$\mu mol\ m^{-3}\ s^{-1}$
$j^*_{LET,bs}$	Volumetric rate of potential linear electron transport (LET) in bundle sheath cells	$\mu mol\ m^{-3}\ s^{-1}$
$j^*_{LET,m}$	Volumetric rate of potential linear electron transport (LET) in mesophyll cells	$\mu mol\ m^{-3}\ s^{-1}$
j^*_{LL}	Volumetric rate of potential light-limited (LL) electron transport	$\mu mol\ m^{-3}\ s^{-1}$

$j^*_{LL,CET,bs}$	Volumetric rate of potential light-limited (LL) cyclic electron transport in bundle sheath cells	μmol m^{-3} s^{-1}
$j^*_{LL,LET,bs}$	Volumetric rate of potential light-limited (LL) linear electron transport in bundle sheath cells	μmol m^{-3} s^{-1}
$j^*_{LL,LET,m}$	Volumetric rate of potential light-limited (LL) linear electron transport in mesophyll cells	μmol m^{-3} s^{-1}
$j^*_{\max}$	Volumetric rate of light-saturated electron transport	μmol m^{-3} s^{-1}
$j_{\max,CET}$	Light-saturated rate of cyclic electron transport	μmol m^{-2} s^{-1}
$j_{\max,LET}$	Light-saturated rate of linear electron transport	μmol m^{-2} s^{-1}
K_{bs}	Light absorbed per unit photosystem in bundle sheath cells	mol mol^{-1}
K_m	Light absorbed per unit photosystem in mesophyll cells	mol mol^{-1}
R_d	Total respiratory CO_2 release from leaf $R_d = R_m + R_s + R_v + R_{epi}$	μmol m^{-2} s^{-1}
R_{epi}	Volumetric rate of respiratory CO_2 release from mitochondria in epidermis cells $R_{epi} = R_d / \left(d \times f_{resp.}\right)$	μmol m^{-3} s^{-1}
R^*_m	Volumetric rate of respiratory CO_2 release from mitochondria in mesophyll cytosol $R^*_m = R_d / \left(d \times f_{resp.} \times f_{m,cy}\right)$	μmol m^{-3} s^{-1}
$\overline{r_p}$	Mean rate of photorespiratory CO_2 release from mitochondria in bundle sheath cytosol	μmol m^{-2} s^{-1}
r^*_p	Volumetric rate of photorespiratory CO_2 release from mitochondria in bundle sheath cytosol	μmol m^{-3} s^{-1}

r^*_{p,O_2}	Volumetric rate of O_2 consumption due to photorespiratory in bundle sheath chloroplasts	μmol m^{-3} s^{-1}
s'	Lumped calibration factor	Dimensionless
$S_{C/O}$	Relative CO_2/O_2 specificity factor for Rubisco	μbar μbar^{-1}
$V_{c,max}$	Maximum rate of Rubisco activity-limited carboxylation	μmol m^{-2} s^{-1}
$V^*_{c,max}$	Volumetric rate of maximum rate of Rubisco activity-limited carboxylation	μmol m^{-3} s^{-1}
V_p	Rate of PEP carboxylation based on bicarbonate ions	μmol m^{-2} s^{-1}
V^*_p	Volumetric rate of V_p calculated from $V_p/(d \times f_{m,cy})$	μmol m^{-3} s^{-1}
$\bar{V}^*_p$	Volumetric rate of CO_2 release in bundle sheath cells	μmol m^{-3} s^{-1}
$V^*_{p,max}$	Volumetric rate of maximum rate of enzyme activity-limited PEP carboxylation	μmol m^{-3} s^{-1}
x	Fraction of ATP partitioned to the C_4 cycle	Dimensionless
$\bar{x}$	Computed fraction of ATP partitioned to the C_4 cycle	Dimensionless
A	Fraction of PSII in bundle sheath cells	Dimensionless
ϕ	Leakiness $\phi = L/\bar{V}_p$	Dimensionless
Φ_{1LL}	Quantum efficiency of PSI electron transport at limiting light	Dimensionless
Φ_{2LL}	Quantum efficiency of PSII electron transport at limiting light	Dimensionless
θ	Ratio of the total area of plasmodesmata to the total area of the mesophyll-bundle sheath interface.	m^2 m^{-2}

Θ	Convexity coefficient	Dimensionless
γ^*	$0.5/ S_{C/O}$	Dimensionless
ζ	Effective porosity	Dimensionless
η	Viscosity of cell medium relative to water	Dimensionless

Table C.2. Values of parameters used in the microscale model

Variable	Units	Value	Notes and references
D_{CO_2} liquid phase gas cell wall	$m^2\ s^{-1}$	$1.89\times10^{-9}/\eta$ $0.135\times10^{-4}(T/273.15)^{1.75}$ $1.89\times10^{-9}\times\zeta/\eta$	Frank, Kuipers & van Swaaij 1996; Lide 1999; Juurola *et al.* 2005. η is the relative viscosity of cell medium (see further) ζ : effective porosity is 0.1 for bundle sheath cells (Evans *et al.*, 2009) and 1.0 for mesophyll cells resulting in a conductance of 0.28 mol $m^{-2}\ s^{-1}$ which is within 4 $\times10^{-5}$ - 0.64 mol $m^{-2}\ s^{-1}$ reported previously (Evans *et al.*, 2009).
D_{O_2} in gas phase in liquid phase	$m^2\ s^{-1}$	$1.139\times10^{-9}\times T^{1.724}$ $1.97\times10^{-9}\times\zeta/\eta$	T(K) (Denny, 1993)
$D_{HCO_3^-}$	$m^2\ s^{-1}$	$1.17\times10^{-9}/\eta$	At 25 °C (Geers and Gros, 2000).
d	µm	165	Measured Table 3.2
H_{CO_2}	-	0.83	At 25 °C (Lide, 1999).
H_{O_2}	-	3.2×10^{-2}	At 25 °C (Lide, 1999).

L_{pd}	µm	0.35	Sum of thickness of cell walls (Table 3.2).
$V^{*}_{CA,max}$	mol m^{-3} s^{-1}	2.1×10^{5}	Pocker & Miksch 1978; Wang *et al.* 2014
$j_{\max}$	µmol m^{-2} s^{-1}	122.61 ± 8.21	Estimated, see also Table C.3.
k_1	s^{-1}	0.039	Jolly 1985, see also Table C.3.
k_2	s^{-1}	23	Jolly 1985, see also Table C.3.
K_{CO_2}	mol m^{-3}	2.8	Hatch & Burnell 1990
K_{eq}	mol m^{-3}	5.6×10^{-7}	Pocker & Miksch 1978
K	mol L^{-1}	2.5×10^{-4}	Jolly 1985
$K_{m,C}$	µbar	485[(a)]	Cousins *et al.* 2010, see also Table C.3.
$K_{HCO_3^-}$	mol m^{-3}	34	Pocker & Miksch 1978
$K_{m,O}$	mbar	146[(a)]	Cousins *et al.* 2010, see also Table C.3.
K_h	µM	20	Bauwe 1986
P_{CO_2} of bundle sheath chloroplast envelopes	m s^{-1}	1.75×10^{-3}	CO_2 permeability 3.5×10^{-3} (Gutknecht, 1988) was halved to account for the double layer.

P_{CO_2} of bundle sheath cells plasma membrane	m s^{-1}	3.5×10^{-3}	Gutknecht 1988
P_{CO_2} of mesophyll plasma membrane	m s^{-1}	1.6×10^{-2}	Missner *et al.* 2008
P_{O_2} of: plasma membrane chloroplast envelope	m s^{-1}	 3.6×10^{-2} 1.8×10^{-2}	Oxygen permeability of plasma membranes was calculated by dividing the diffusivity of O_2 by thickness of the membrane. The O_2 permeability of double-layered chloroplasts was assumed half that of the plasma membranes.
pH cytosol stroma vasculature vacuole	-	 7.5 7.8 7.0 4.0	Evans *et al.* 2009
R_d	μmol m^{-2} s^{-1}	1.70 ± 0.27	Estimated (Table 3.1)

s'	-	0.325 ± 0.05	Estimated (Table 3.1)
$S_{C/O}$	-	2862	Cousins *et al.* 2010
$V_{c,max}$	μmol m^{-2} s^{-1}	$V_{p,max}/2.33$	Yin *et al.* 2011
$V_{p,max}$	μmol m^{-2} s^{-1}	96.4	Calculated from slopes of linearity between the parameter and leaf nitrogen content (Yin *et al.*, 2011*b*)
x	-	0.40	von Caemmerer & Furbank 1999
α	-	0.10	Chapman & Hatch 1979
θ	-	0.03	Sowiński, Szczepanik & Minchin 2008
η	-	2.0	Ho *et al.* 2016
Θ	-	0.97	Assumed, at chloroplast level.
Φ_{1LL}	-	0.97	Yin & Struik 2012
Φ_{2LL}	-	0.83	Yin & Struik 2012

[(a)] These parameters were converted into μmol m^{-3} liquid by multiplying with *PH/RT*, where P = 101325 Pa, H = 0.83, R = 8.314 m^3 Pa K^{-1} mol^{-1} and T = 298 K.

Table C.3. Temperature dependency of biophysical and biochemical parameters.

Parameter	Activation energy (kJ mol^{-1})	Entropy term (kJ mol^{-1})	Deactivation energy (kJ mol^{-1})	References
D_{CO_2} in liquid	-16.9	-	-	Frank *et al.* 1996
D_{O_2}in liquid	9.5	-	-	Han & Bartels 1996; Yin *et al.* 2016
$D_{HCO_3^-}$	16.9	-	-	Frank *et al.* 1996
H_{CO_2} H_{O_2}	-20.3 -17.0	- -	- -	Frank *et al.* 1996
η	16.4	-	-	Frank *et al.* 1996
j_{max}	77.9	0.627	191.9	Massad *et al.* 2007
$V_{CA,max}$	40.9	0.210	64.5	Boyd *et al.* 2015
$V_{p,max}$	37.0	0.663	214.5	Yin *et al.* 2016
$V_{c,max}$	53.4	-	-	Yin *et al.* 2016
$K_{m,C}$	35.6	-	-	Yin *et al.* 2016
$K_{m,O}$	15.1	-	-	Yin *et al.* 2016
γ^*	27.4	-	-	Yin *et al.* 2016
K_h	27.2	-	-	Boyd *et al.* 2015
k_1	95.0	-	-	Boyd *et al.* 2015
R_d	41.9	-	-	Yin *et al.* 2016

Table C.4. Anatomical properties of maize leaf measured from segmented images.

Cell types	Anatomical property (Vol. or area ratio)	Literature values
Mesophyll cells	31.6 % tissue	47 (Dengler *et al.*, 1994)
Chloroplasts	5.87 % tissue	
Vacuole	61.6 % cell	50-80 % vol. (Taiz, 1992)
Cytosol	29.8 % cell	
	S_m * = 7.2 m^2 m^{-2}	6-10 m^2 m^{-2} (Dengler *et al.*, 1994; von Caemmerer and Furbank, 2003; El-Sharkawy, 2009)
Bundle sheath cells	16.7 % tissue	12 (Dengler *et al.*, 1994)
Chloroplasts	9.08 % tissue	
Cytoplasm	45.9 % cell	
	S_b ** = 1.9 m^2 m^{-2}	0.6-3.1(von Caemmerer and Furbank, 2003)
Intercellular air spaces	21.0 % of tissue	20-25 (Dengler *et al.*, 1994)

* S_m per volume of mesophyll cells was reported to be 0.12 m^2 m^{-3} for C_4 plants (Dengler *et al.*, 1994) corresponding well to our value of 0.14 m^2 m^{-3}.

** S_b per volume of bundle sheath cells was reported to be 0.050 m^2 m^{-3} for C_4 plants (Dengler *et al.*, 1994) corresponding well to our value of 0.045 m^2 m^{-3}.

Table C.5. Size, shapes and the total number of organelles per volume in mesophyll and bundle sheath cells.

Organelle type	Description	Mean equivalent radius $\bar{r}$ (μm)	Standard deviation (μm)	f_{tot} (number μm^{-3})
Mitochondria	Cylindrical-shaped with 0.42 ± 0.06 μm diameter for those in mesophyll cells and 0.52 ± 0.09 μm diameter for those in bundle sheath cells (Yoshimura *et al.*, 2004). Length is 4±0.035 μm (Dieteren *et al.*, 2011). Number per cell is 2.2 ± 1.5 for mesophyll and 8.0 ± 4.8 for bundle sheath cells (Yoshimura *et al.*, 2004).	0.04 for mesophyll cells and 0.07 for bundle sheath cells	-	0.020 for mesophyll cells and 0.0096 for those in bundle sheath cells
Peroxisomes	Spherical shape with 0.81 ± 0.23 μm diameter for mesophyll cells and 1.03 ± 0.17 μm diameter for those in bundle sheath cells. Number per cell is 0.3 ± 0.5 for mesophyll and 1.3 ± 1.8 for bundle sheath cells (Yoshimura *et al.*, 2004).	-	-	0.00273 for mesophyll cells and 0.00157 for bundle sheath cells
Nuclei	Spherical shape with volume of about 72.4±7.5 μm^3 (Dittmer *et al.*, 2007), assumed to be the same both for mesophyll and bundle sheath cells.	2.57	0.0899	0.000201
Golgi stacks	0.5 to 2.0 μm diameter disks of height of 0.3 μm (Dupree & Sherrier, 1998), number=25 (Dupree & Sherrier, 1998). The calculated total number of Golgi stacks per unit volume is about (1.5-5)×10^{-3} μm^{-3}.	0.42	0.0917	0.002518

Ribosome-like complexes	25-30 nm diameter spheres (Verschoor *et al.*, 1998). Assuming 1250 ribosome-like complexes and volume about 2.8 μm^3 (Henderson *et al.*, 2007).	0.0137	0.000625	445.44
Grana	Cylindrical disks of mesophyll chloroplasts are assumed 14-17 stacks of diameter ca. 1 µm, stack height about 0.25 to 1 µm (Austin and Staehelin, 2011). Number could vary from 40 to 60 grana stacks (Staehelin, 2003). Grana in bundle sheath cells are low, volume fraction varies from 1.6 – 7.4 % compared to 68.2 % of mesophyll cells (Yoshimura *et al.*, 2004; Vicankova and Kutik, 2005) thus they were neglected.	0.472	0.0558	0.68

The equivalent radius of an organelle having volume $\overline{V}_{organelle}$ is given by $\bar{r} = \left(\frac{3\overline{V}_{organelle}}{4\pi} \right)^{1/3}$

The lowest and highest value obtained from literature were used to determine the standard deviation.

f_{tot} is the product of the number of organelles per unit volume and volume.

Table C.6. Computed optical properties of the different compartments of the leaf model. The absorption profile is the result of averaging the absorption profile at 470 nm (10 %) and at 665 nm (90 %). μ_a is an absorption coefficient; μ_s is a scattering coefficient; and, γ is an anisotropy factor. The ratio K_{bs}:K_m = 0.50.

470 nm	$\mu_a\ (cm^{-1})$	$\mu_s\ (cm^{-1})$	$\gamma\ (-)$
Air	0	2000	1
Epidermis	10	730	0.9678
Mesophyll cytosol	10	850	0.9800
Mesophyll vacuole	10	730	0.9556
Mesophyll chloroplast	3800	12700	0.9698
Bundle sheath cytosol	10	730	0.9678
Bundle sheath chloroplast	1900	12700	0.9678
Vascular bundles	10	1000	0.9800
665 nm			
Air	0	2000	1
Epidermis	10	330	0.9400
Mesophyll cytosol	10	450	0.9600
Mesophyll vacuole	10	330	0.9200
Mesophyll chloroplast	3400	10700	0.9698
Bundle sheath cytosol	10	330	0.9500
Bundle sheath chloroplast	1700	10700	0.9678
Vascular bundles	10	500	0.9600

Table C.7. Computed optical properties of mesophyll and bundle sheath chloroplasts of the leaf model for various ratios of K_{bs} to K_m. μ_a is an absorption coefficient; μ_s is a scattering coefficient; and, γ is an anisotropy factor.

	K_{bs}:K_m = 0.30			K_{bs}:K_m = 1.00			K_{bs}:K_m = 1.50		
470 nm	μ_a (cm^{-1})	μ_s (cm^{-1})	γ $(-)$	μ_a (cm^{-1})	μ_s (cm^{-1})	γ $(-)$	μ_a (cm^{-1})	μ_s (cm^{-1})	γ $(-)$
Mesophyll chloroplast	3200	12700	0.9698	3200	12700	0.9698	3200	12700	0.9698
Bundle sheath chloroplast	960	12700	0.9678	3200	12700	0.9678	4800	12700	0.9698
665 nm									
Mesophyll chloroplast	2900	10700	0.9698	2900	10700	0.9698	2900	10700	0.9698
Bundle sheath chloroplast	870	10700	0.9678	2900	10700	0.9678	4350	10700	0.9698

References

Aalto T, Juurola E. 2002. A three-dimensional model of CO2 transport in airspaces and mesophyll cells of a silver birch leaf. Plant, cell & environment **25**, 1399–1409.

Aernouts B, Watté R, Van Beers R, Delport F, Merchiers M, De Block J, Lammertyn J, Saeys W. 2014. Flexible tool for simulating the bulk optical properties of polydisperse spherical particles in an absorbing host: experimental validation. Optics express **22**, 20223.

Anand A, Khetarpal S, Singh MP. 2014. Physiological response of maize under rising atmospheric CO2 and temperature. In: Chaudhary PD,, In: Kumar S,, In: Langyan S, eds. Maize: nutrition dynamics and novel uses. New Delhi: Springer India, 105–115.

Aregawi WA, Abera MK, Fanta SW, Verboven P, Nicolai B. 2014*a*. Prediction of water loss and viscoelastic deformation of apple tissue using a multiscale model. Journal of physics: condensed matter **26**, 464111.

Aregawi W, Defraeye T, Saneinejad S, Vontobel P, Lehmann E, Carmeliet J, Verboven P, Derome D, Nicolai B. 2014*b*. Understanding forced convective drying of apple tissue: Combining neutron radiography and numerical modelling. Innovative food science & emerging technologies **24**, 97–105.

Austin JR, Staehelin LA. 2011. Three-dimensional architecture of grana and stroma thylakoids of higher plants as determined by electron tomography. Plant physiology **155**, 1601–11.

Badger MR, Price GD. 1994. The role of carbonic anhydrase in photosynthesis. Annual review of plant physiology and plant molecular biology **45**, 369–392.

Baranoski GVG, Kimmel B, Chen TF, Yim D. 2012. In silico assessment of environmental factors affecting the spectral signature of C4 plants in the visible domain. International journal of remote sensing **33**, 1190–1213.

Barbour MM, Evans JR, Simonin KA, von Caemmerer S. 2016. Online CO2 and H2O oxygen isotope fractionation allows estimation of mesophyll conductance in C4 plants, and reveals that mesophyll conductance decreases as leaves age in both C4 and C3 plants. New phytologist **210**, 875–889.

Bauwe H. 1986. An efficient method for the determination of Km values for HCO3- of phosphoenolpyruvate carboxylase. Planta **169**, 356–360.

Bellasio C, Beerling DJ, Griffiths H. 2016*a*. Deriving C4 photosynthetic parameters from combined gas exchange and chlorophyll fluorescence using an Excel tool: theory and practice. Plant, cell & environment **39**, 1164–1179.

Bellasio C, Beerling DJ, Griffiths H. 2016*b*. An Excel tool for deriving key photosynthetic parameters from combined gas exchange and chlorophyll fluorescence: theory and practice. Plant, cell & environment **39**, 1180–1197.

Bellasio C, Griffiths H. 2014*a*. Acclimation of C4 metabolism to low light in mature maize leaves could limit energetic losses during progressive shading in a crop canopy. Journal of experimental botany **65**, 1–12.

Bellasio C, Griffiths H. 2014*b*. The operation of two decarboxylases, transamination, and partitioning of C4 metabolic processes between mesophyll and bundle sheath cells allows light capture to be balanced for the maize C4 pathway. Plant physiology **164**, 466–80.

Bellasio C, Griffiths H. 2014*c*. Acclimation to low light by C4 maize: implications for bundle sheath leakiness. Plant, cell & environment **37**, 1046–58.

Bellasio C, Lundgren MR. 2016. Anatomical constraints to C4 evolution: light harvesting capacity in the bundle sheath. New phytologist **212**, 485–496.

Berghuijs HNC, Yin X, Ho QT, Driever SM, Retta MA, Nicolaï BM, Struik PC. 2016. Mesophyll conductance and reaction-diffusion models for CO_2 transport in C_3 leaves; needs, opportunities and challenges. Plant science **252**, 62–75.

Berry J, Farquhar G. 1978. The CO2 concentrating function of C4 photosynthesis a biochemical model. In: Coombs, J H,, In: Goodwin T, eds. Proceedings of the fourth international congress on photosynthesis. London, 119–131.

Botha CE. 1992. Plasmodesmatal distribution, structure and frequency in relation to assimilation in C3 and C4 grasses in southern Africa. Planta **187**, 348–58.

Boyd RA, Gandin A, Cousins AB. 2015. Temperature response of C4 photosynthesis: biochemical analysis of rubisco, phosphoenolpyruvate carboxylase and carbonic anhydrase in Setaria viridis. Plant physiology **169**, 1850–1861.

Brandt A. 2001. Multiscale scientific computation: Review. In: Barth TJ,, In: Chan T,, In: Haimes R, eds. Lecture Notes in Computational Science and Engineering. Multiscale and Multiresolution Methods. Berlin, Heidelberg: Springer Berlin Heidelberg, 3–95.

Brautigam A, Weber APM. 2011. Transport processes: Connecting the reactions of C4 photosynthesis. In: Raghavendra AS,, In: Sage RF, eds. Advances in photosynthesis and respiration. Dordrecht, The Netherlands: Springer, 199–219.

Brown RH, Byrd GT. 1993. Estimation of bundle sheath cell conductance in C4 species and O2 insensitivity of photosynthesis. Plant physiology **103**, 1183–1188.

Buckley TN, Farquhar GD. 2004. A new analytical model for whole-leaf potential electron transport rate. Plant, cell and environment **27**, 1487–1502.

Burnell JN, Hatch MD. 1988. Low bundle sheath carbonic anhydrase is apparently essential for effective C_4 pathway operation. Plant physiology **86**, 1252–6.

Byrt CS, Grof CPL, Furbank RT. 2011. C4 Plants as biofuel feedstocks: Optimising biomass production and feedstock quality from a lignocellulosic perspective. Journal of integrative plant biology

53, 120–135.

von Caemmerer S. 2013. Steady-state models of photosynthesis. Plant, cell & environment **36**, 1617–30.

von Caemmerer S, Evans JR, Cousins AB, Badger MR, Furbank RT. 2007. C4 photosynthesis and CO2 diffusion. In: Sheehy J,, In: Mitchell P,, In: Hardy B, eds. Charting new pathways to C4 rice. Philippines: International Rice Research Institute, 95–116.

von Caemmerer S, Farquhar GD. 1981. Some relationships between the biochemistry of photosynthesis and the gas exchange of leaves. Planta **153**, 376–387.

von Caemmerer S, Furbank RT. 1999. Modeling C4 photosynthesis. In: Sage RF,, In: Monson RK, eds. C4 plant biology. Toronto, ON, Canada: Academic Press, 173–211.

von Caemmerer S, Furbank RT. 2003. The C4 pathway: an efficient CO2 pump. Photosynthesis research **77**, 191–207.

von Caemmerer S, Ghannoum O, Pengelly JJL, Cousins AB. 2014. Carbon isotope discrimination as a tool to explore C_4 photosynthesis. Journal of experimental botany **65**, 3459–3470.

Cantre D, Herremans E, Verboven P, Ampofo-Asiama J, Nicolai B. 2014. Characterization of the 3-D microstructure of mango (Mangifera indica L. cv. Carabao) during ripening using X-ray computed microtomography. Innovative food science and emerging technologies **24**, 28–39.

Chapman KSR, Hatch MD. 1979. Aspartate stimulation of malate decarboxylation in Zea mays bundle sheath cells: Possible role in regulation of C4 photosynthesis. Biochemical and biophysical research communications **86**, 1274–1280.

Chen D-X, Coughenour MB, Knapp AK, Owensby CE. 1994. Mathematical simulation of C4 grass photosynthesis in ambient and elevated CO2. Ecological modelling **61**, 63–80.

Christin P-A, Besnard G, Samaritani E, Duvall MR, Hodkinson TR, Savolainen V, Salamin N. 2008. Oligocene CO2 decline promoted C4 photosynthesis in grasses. Current biology **18**, 37–43.

Ciganda VV, Schepers JS, Gitelsonaj A, Schepersc J, Gitelson A. 2009. Non-destructive determination of maize leaf and canopy chlorophyll content. Journal of plant physiology **166**, 157–67.

Collatz G, Ribas-Carbo M, Berry J. 1992. Coupled photosynthesis-stomatal conductance model for leaves of C4 plants. Australian journal of plant physiology **19**, 519.

Cousins AB, Badger MR, von Caemmerer S. 2008. C4 photosynthetic isotope exchange in NAD-ME- and NADP-ME-type grasses. Journal of experimental botany **59**, 1695–1703.

Cousins AB, Ghannoum O, von Caemmerer S, Badger MR. 2010. Simultaneous determination of Rubisco carboxylase and oxygenase kinetic parameters in Triticum aestivum and Zea mays using membrane inlet mass spectrometry. Plant, cell & environment **33**, 444–452.

Danila FR, Quick WP, White RG, Furbank RT, von Caemmerer S. 2016. The metabolite pathway

between bundle sheath and mesophyll: quantification of plasmodesmata in leaves of C3 and C4 monocots. The Plant cell **28**, 1461–1471.

Dengler NG, Nelson T. 1999. Leaf structure and development in C4 plants. In: Sage RF,, In: Monson RK, eds. C4 plant biology. Toronto, ON, Canada: Academic Press, 133–172.

Dengler N, Ronald D, Petra D, Paul H. 1994. Quantitative leaf anatomy of C3 and C4 grasses (Poaceae): Bundle sheath and mesophyll surface area relationships. Annals of botany **73**, 241–255.

Denny MW. 1993. *Air and water: The biology and physics of life's media*. Princeton, NJ: Princeton University press.

Dhondt S, Vanhaeren H, Van Loo D, Cnudde V, Inzé D. 2010. Plant structure visualization by high-resolution X-ray computed tomography. Trends in plant science **15**, 419–422.

Dieteren CEJ, Gielen SCAM, Nijtmans LGJ, Smeitink JAM, Swarts HG, Brock R, Willems PHGM, Koopman WJH. 2011. Solute diffusion is hindered in the mitochondrial matrix. Proceedings of the national academy of sciences of the United States of America **108**, 8657–62.

Dittmer TA, Stacey NJ, Sugimoto-Shirasu K, Richards EJ. 2007. Little nucleic genes affecting nuclear morphology in Arabidopsis thaliana. The Plant cell **19**, 2793–803.

Driscoll SP, Prins A, Olmos E, Kunert KJ, Foyer CH. 2006. Specification of adaxial and abaxial stomata, epidermal structure and photosynthesis to CO2 enrichment in maize leaves. Journal of experimental botany **57**, 381–90.

Dupree P, Sherrier DJ. 1998. The plant Golgi apparatus. Biochimica et biophysica acta **1404**, 259–70.

Eastman PAK, Peterson C a., Dengler NG. 1988. Suberized bundle sheaths in grasses (Poaceae) of different photosynthetic types. II. Apoplastic permeability. Protoplasma **142**, 112–126.

Edwards GE, Baker NR. 1993. Can CO2 assimilation in maize leaves be predicted accurately from chlorophyll fluorescence analysis? Photosynthesis research **37**, 89–102.

Edwards GE, Voznesenskaya E V. 2010. C4 photosynthesis: Kranz forms and single-cell C4 in terrestrial plants. In: Raghavendra AS,, In: Sage RF, eds. Advances in photosynthesis and respiration. C4 photosynthesis and related CO2 concentrating mechanisms. Dordrecht: Springer Netherlands, 29–61.

Edwards G, Walker D. 1983. *C3, C4: Mechanisms, cellular and environmental regulation of photosynthesis*. Oxford: Blackwell Scientific.

Ehleringer JR, Cerling TE, Helliker BR. 1997. C4 photosynthesis, atmospheric CO2, and climate. Oecologia **112**, 285–299.

El-Sharkawy MA. 2009. Pioneering research on C4 leaf anatomical, physiological, and agronomic characteristics of tropical monocot and dicot plant species: Implications for crop water relations and productivity in comparison to C3 cropping systems. Photosynthetica **47**, 163–183.

El-Sharkawy M, Hesketh J. 1965. Photosynthesis among species in relation to characteristics of leaf anatomy and CO2 diffusion resistance. Crop science **5**, 517–521.

Evans JR, von Caemmerer S. 1996. Carbon dioxide diffusion inside leaves. Plant physiology **110**, 339–346.

Evans JR, von Caemmerer S, Setchell B, Hudson G. 1994. The relationship between CO2 transfer conductance and leaf anatomy in transgenic tobacco with a reduced content of rubisco. Australian journal of plant physiology **21**, 475.

Evans JR, Kaldenhoff R, Genty B, Terashima I. 2009. Resistances along the CO2 diffusion pathway inside leaves. Journal of experimental botany **60**, 2235–2248.

Evans JR, Loreto F. 2000. Acquisition and diffusion of CO2 in higher plant leaves. In: Leegood RC,, In: Sharkey TD,, In: von Caemmerer S, eds. Photosynthesis: physiology and metabolism. Kluwer Academic Publishers, 321–351.

Evans JR, Terashima I, Hanba Y, Loreto F. 2004. Chloroplast to leaf. In: Smith WK,, In: Vogelmann TC,, In: Critchley C, eds. Photosynthetic adaptation: chloroplast to the landscape. Springer, 107–132.

Evans JR, Vogelmann TC, Caemmerer S von. 2007. Balancing light capture with distributed metabolic demand during C4 photosynthesis. In: Sheehy J,, In: Mitchell P,, In: Hardy B, eds. Charting new pathways to C4 rice. Philippines: International Rice Research Institute, 127–144.

Evert RF, Eschrich W, Heyser W. 1977. Distribution and structure of the plasmodesmata in mesophyll and bundle-sheath cells of Zea mays L. Planta **136**, 77–89.

Evert RF, Russin WA, Bosabalidis AM. 1996. Anatomical and ultrastructural associated with changes in sink-to-source transition in developing leaves. International journal of Plant sciences **157**, 247–261.

Fanta SW, Abera MK, Aregawi WA, Ho QT, Verboven P, Carmeliet J, Nicolai BM. 2014. Microscale modeling of coupled water transport and mechanical deformation of fruit tissue during dehydration. Journal of food engineering **124**, 86–96.

FAO. 2013. *FAO Statistical Yearbook 2013*. Rome: Food and agricultural organization of the United Nations.

FAOSTAT. 2016. FAOSTAT.

Farquhar G. 1983. On the nature of carbon isotope discrimination in C4 species. Australian journal of plant physiology **10**, 205.

Farquhar GD, von Caemmerer S, Berry JA. 1980. A biochemical model of photosynthetic CO2 assimilation in leaves of C3 species. Planta **149**, 78–90.

Feldkamp LA, Davis LC, Kress JW. 1984. Practical cone-beam algorithm. Journal of the Optical Society of America A **1**, 612.

Feng XP, Chen Y, Qi YH, YU C-L, Zheng B-S, Brancourt-Hulmel M, Jiang D-A. 2012. Nitrogen enhanced photosynthesis of Miscanthus by increasing stomatal conductance and phosphoenolpyruvate carboxylase concentration. Photosynthetica **50**, 577–586.

Flexas J, Díaz-Espejo A, Berry JA, Cifre J, Galmés J, Kaldenhoff R, Medrano H, Ribas-Carbó M. 2007. Analysis of leakage in IRGA's leaf chambers of open gas exchange systems: quantification and its effects in photosynthesis parameterization. Journal of experimental botany **58**, 1533–43.

Flexas J, Ribas-Carbó M, Diaz-Espejo A, Galmés J, Medrano H. 2008. Mesophyll conductance to CO2: current knowledge and future prospects. Plant, cell & environment **31**, 602–21.

Frank MJW, Kuipers JAM, Swaaij WPM van. 1996. Diffusion coefficients and viscosities of CO2 + H2O, CO2+ CH3OH, NH3+H2O, and NH3+CH3OH liquid mixtures. Journal of chemical & engineering data **41**, 297–302.

Furbank RT. 2011. Evolution of the C4 photosynthetic mechanism: are there really three C4 acid decarboxylation types? Journal of experimental botany **62**, 3103–8.

Furbank RT, Hatch MD. 1987. Mechanism of C4 photosynthesis: The size and composition of the inorganic carbon pool in bundle sheath cells. Plant physiology **85**, 958–964.

Furbank RT, Hatch MD, Jenkins CL. 2004. C4 photosynthesis: mechanism and regulation. In: Leegood RC,, In: Sharkey T,, In: Von Caemmerer S, eds. Photosynthesis: physiology and metabolism. Dordrecht: Kluwer Academic Publishers, 435–453.

Furbank RT, Jenkins CLD, Hatch MD. 1989. CO2 concentrating mechanism of C4 photosynthesis: Permeability of isolated bundle sheath cells to inorganic carbon. Plant physiology **91**, 1364–1371.

Furbank R, Jenkins C, Hatch M. 1990. C4 photosynthesis: Quantum requirement, C4 and overcycling and Q-Cycle involvement. Australian journal of plant physiology **17**, 1–7.

Furbank RT, Stitt M, Foyer CH. 1985. Intercellular compartmentation of sucrose synthesis in leaves of Zea mays L. Planta **164**, 172–178.

Galmés J, Ochogavía JM, Gago J, Roldán EJ, Cifre J, Conesa MÀ. 2013. Leaf responses to drought stress in Mediterranean accessions of Solanum lycopersicum: Anatomical adaptations in relation to gas exchange parameters. Plant, cell and environment **36**, 920–935.

Geers C, Gros G. 2000. Carbon dioxide transport and carbonic anhydrase in blood and muscle. Physiological reviews **80**, 681–715.

Genty B, Briantais J-M, Baker NR. 1989. The relationship between the quantum yield of photosynthetic electron transport and quenching of chlorophyll fluorescence. Biochimica et Biophysica Acta (BBA) - General Subjects **990**, 87–92.

Ghannoum O, von Caemmerer S, Conroy JP. 2001. Carbon and water economy of Australian NAD–ME and NADP–ME C4 grasses. Functional plant biology **28**, 213.

Ghannoum O, Caemmerer S Von, Ziska LH, Conroy JP. 2000. The growth response of C4 plants to rising atmospheric CO2 partial pressure: a reassessment. Plant, cell & environment **23**, 931–942.

Ghannoum O, Evans JR, von Caemmerer S. 2010. Nitrogen and water use efficiency of C4 plants. Advances in photosynthesis and respiration. Springer Netherlands, 129–146.

Ghannoum O, Evans JR, Chow WS, Andrews TJ, Conroy JP, von Caemmerer S. 2005. Faster Rubisco is the key to superior nitrogen-use efficiency in NADP-malic enzyme relative to NAD-malic enzyme C4 grasses. Plant physiology **137**, 638–650.

Gillon JS, Yakir D. 2000. Naturally low carbonic anhydrase activity in C4 and C3 plants limits discrimination against C18OO during photosynthesis. Plant, cell and environment **23**, 903–915.

Govaerts YM, Jacquemoud S, Verstraete MM, Ustin SL. 1996. Three-dimensional radiation transfer modeling in a dicotyledon leaf. Applied optics **35**, 6585.

Greef JM. 1994. Productivity of maize (Zea mays L.) in relation to morphological and physiological characteristics under varying amounts of nitrogen supply. Journal of agronomy and crop science **172**, 317–326.

Griffiths H, Weller G, Toy LFM, Dennis RJ. 2013. You're so vein: bundle sheath physiology, phylogeny and evolution in C3 and C4 plants. Plant, cell & environment **36**, 249–261.

Gutknecht J. 1988. Diffusion of carbon dioxide through lipid bilayer membranes. Effects of carbonic anhydrase, bicarbonate, and unstirred layers. The Journal of general physiology **69**, 779–794.

Han P, Bartels DM. 1996. Temperature dependence of oxygen diffusion in H2O and D2O. The Journal of physical chemistry **100**, 5597–5602.

Harley PC, Loreto F, Di Marco G, Sharkey TD. 1992. Theoretical considerations when estimating the mesophyll conductance to CO2 flux by analysis of the response of photosynthesis to CO2. Plant physiology **98**, 1429–36.

Hatch MD. 1987. C4 photosynthesis: a unique blend of modified biochemistry, anatomy and ultrastructure. Biochimica et Biophysica Acta (BBA) - Reviews on bioenergetics **895**, 81–106.

Hatch MD, Burnell JN. 1990. Carbonic anhydrase activity in leaves and its role in the first step of C4 photosynthesis. Plant physiology **93**, 825–828.

Hatch M, Osmond CB. 1976. Transport in plants III. In: Stocking CR,, In: Heber U, eds. Encyclopedia of Plant Physiology. Berlin, Heidelberg: Springer Berlin Heidelberg, 144–184.

Hatch MD, Slack CR. 1970. Photosynthetic CO2-Fixation Pathways. Annual review of plant physiology **21**, 141–162.

Hattersley PW. 1984. Characterization of C4 type leaf anatomy in grasses (Poaceae). Mesophyll: bundle sheath area ratios. Annals of botany **53**, 163–180.

Hattersley PW, Browning AJ. 1981. Occurrence of the suberized lamella in leaves of grasses of different photosynthetic types. I. In parenchymatous bundle sheaths and PCR ('Kranz') sheaths. Protoplasma **109**, 371–401.

He D, Edwards GE. 1996. Estimation of diffusive resistance of bundle sheath cells to CO2 from modeling of C4 photosynthesis. Photosynthesis research **49**, 195–208.

Heaton EA, Dohleman FG, Long SP. 2008. Meeting US biofuel goals with less land: The potential of Miscanthus. Global change biology **14**, 2000–2014.

Henderson SA, von Caemmerer S, Farquhar GD. 1992. Short-term measurements of carbon isotope discrimination in several C4 species. Australian journal of plant physiology **19**, 263–285.

Henderson GP, Gan L, Jensen GJ. 2007. 3-D ultrastructure of O. tauri: electron cryotomography of an entire eukaryotic cell. PLoS One **2**, e749.

Herremans E, Verboven P, Verlinden BE, Cantre D, Abera M, Wevers M, Nicolaï BM. 2015. Automatic analysis of the 3-D microstructure of fruit parenchyma tissue using X-ray micro-CT explains differences in aeration. BMC plant biology **15**, 264.

Ho QT, Berghuijs HNC, Watté R, *et al.* 2016. Three-dimensional microscale modelling of CO2 transport and light propagation in tomato leaves enlightens photosynthesis. Plant, cell & environment **39**, 50–61.

Ho QT, Carmeliet J, Datta AK, *et al.* 2013. Multiscale modeling in food engineering. Journal of food engineering **114**, 279–291.

Ho QT, Verboven P, Mebatsion HK, Verlinden BE, Vandewalle S, Nicolaï BM, Nicolai BM. 2009. Microscale mechanisms of gas exchange in fruit tissue. New phytologist **182**, 163–174.

Ho QT, Verboven P, Verlinden BE, Herremans E, Wevers M, Carmeliet J, Nicolaï BM. 2011. A three-dimensional multiscale model for gas exchange in fruit. Plant physiology **155**, 1158–68.

Ho QT, Verboven P, Verlinden BE, Nicolaï BM. 2010. A model for gas transport in pear fruit at multiple scales. Journal of experimental botany **61**, 2071–81.

Ho QT, Verboven P, Yin X, Struik PC, Nicolaï BM. 2012. A microscale model for combined CO2 diffusion and photosynthesis in leaves. PLoS One **7**, e48376.

Hylton CM, Rawsthorne S, Smith AM, Jones DA, Woolhouse HW. 1988. Glycine decarboxylase is confined to the bundle-sheath cells of leaves of C3-C4 intermediate species. Planta **175**, 452–459.

Hysing JSR, Turek S. 2015. Evaluation of commercial and academic CFD codes for a two-phase flow benchmark test case. International journal of computational science and engineering **10**, 387.

Ichiro T, Hiroki O, Takashi F, Riichi O. 2016. Light environment within a leaf. II. Progress in the past one-third century. Journal of pant research **129**, 353–363.

Idelsohn SR, Oñate E. 1994. Finite volumes and finite elements: Two 'good friends'. International journal for numerical methods in engineering **37**, 3323–3341.

Jenkins CLD, Furbank RT, Hatch MD. 1989*a*. Inorganic carbon diffusion between C4 mesophyll and bundle sheath cells: Direct bundle sheath CO2 assimilation in intact leaves in the presence of an inhibitor of the C4 pathway. Plant physiology **91**, 1356–63.

Jenkins CLD, Furbank RT, Hatch MD. 1989*b*. Mechanism of C4 photosynthesis: A model describing the inorganic carbon pool in bundle sheath cells. Plant physiology **91**, 1372–1381.

Jolly W. 1985. *Modern inorganic chemistry*. New York : McGraw-Hill.

Juurola E, Aalto T, Thum T, Vesala T, Hari P. 2005. Temperature dependence of leaf-level CO2 fixation: revising biochemical coefficients through analysis of leaf three-dimensional structure. The New phytologist **166**, 205–15.

Kanai R, Edwards GE. 1999. The biochemistry of C4 photosynthesis. In: Sage RF,, In: Monson RK, eds. C4 plant biology. Toronto, ON, Canada: Academic Press, 49–87.

Kiirats O, Lea PJ, Franceschi VR, Edwards GE. 2002. Bundle sheath diffusive resistance to CO2 and effectiveness of C4 photosynthesis and refixation of photorespired CO2 in a C4 cycle mutant and wild-type Amaranthus edulis. Plant physiology **130**, 964–76.

Kim S, Gitz D, Sicher R, Baker J, Timlin D, Reddy V. 2007. Temperature dependence of growth, development, and photosynthesis in maize under elevated CO2. Environmental and experimental botany **61**, 224–236.

Kromdijk J, Griffiths H, Schepers HE. 2010. Can the progressive increase of C_4 bundle sheath leakiness at low PFD be explained by incomplete suppression of photorespiration? Plant, cell & environment **33**, 1935–48.

Kromdijk J, Schepers HE, Albanito F, Fitton N, Carroll F, Jones MB, Finnan J, Lanigan GJ, Griffiths H. 2008. Bundle sheath leakiness and light limitation during C4 leaf and canopy CO2 uptake. Plant physiology **148**, 2144–2155.

Kromdijk J, Ubierna N, Cousins AB, Griffiths H. 2014. Bundle-sheath leakiness in C_4 photosynthesis: a careful balancing act between CO_2 concentration and assimilation. Journal of experimental botany **65**, 3443–57.

Ku SB, Edwards GE. 1975. Photosynthesis in mesophyll protoplasts and bundle sheath cells of various types of C4 plants IV. Enzymes of respiratory metabolism and energy utilizing enzymes of photosynthetic pathways. Zeitschrift für pflanzenphysiologie **77**, 16–32.

Ku SB, Gutierrez M, Kanai R, Edwards GE. 1974. Photosynthesis in mesophyll protoplasts and bundle sheath cells of various types of C4 plants II. Chlorophyll and hill reaction studies. Zeitschrift für pflanzenphysiologie **72**, 320–337.

Laisk A, Edwards GE. 2000. A mathematical model of C(4) photosynthesis: The mechanism of

concentrating CO(2) in NADP-malic enzyme type species. Photosynthesis research **66**, 199–224.

Laisk A, Edwards G. 2009. Leaf C4 Photosynthesis in silico : The CO2 Concentrating mechanism. In: Laisk A,, In: Nedbal L,, In: Govindjee, eds. Photosynthesis in silico. Springer Netherlands, 323–348.

Lambers H, Chapin FS, Pons TL. 1998. Photosynthesis, respiration, and long-distance transport. Plant physiological ecology. New York, NY: Springer New York, 10–153.

Leegood RC. 1985. The intercellular compartmentation of metabolites in leaves of Zea mays L. Planta **164**, 163–171.

Leegood RC. 2002. C4 photosynthesis: principles of CO2 concentration and prospects for its introduction into C3 plants. Journal of experimental botany **53**, 581–590.

Leegood RC. 2004. Transport during C4 photosynthesis. In: Leegwood RC,, In: Sharkey T,, In: von Caemmerer S, eds. Photosynthesis: physiology and metabolism. New York: Kluwer Academic Publishers, 460–469.

Leuning RC. 1983. Transport of gases into leaves. Plant, cell and environment **6**, 181–194.

LI-COR. 2004. *Using the LI-6400 - Version 6*.

Lide DR. 1999. *Handbook of chemistry and physics*. CRC Press.

Long SP, Farage PK, Bolhár-Nordenkampf HR, Rohrhofer U. 1989. Separating the contribution of the upper and lower mesophyll to photosynthesis in Zea mays L. leaves. Planta **177**, 207–16.

Long SP, Zhu X-G, Naidu SL, Ort DR. 2006. Can improvement in photosynthesis increase crop yields? Plant, cell and environment **29**, 315–330.

Longstreth DJ, Hartsock TL, Nobel PS. 1980. Mesophyll cell properties for some C3 and C4 species with high photosynthetic rates. Physiologia plantarum **48**, 494–498.

Loriaux SD, Avenson TJ, Welles JM, Mcdermitt DK, Eckles RD, Reinsche B, Genty B. 2013. Closing in on maximum yield of chlorophyll fluorescence using a single multiphase flash of sub-saturating intensity. Plant, cell & environment **36**, 1755–1770.

Ma J-Y, Sun W, Koteyeva NK, Voznesenskaya E, Stutz SS, Gandin A, Smith-Moritz AM, Heazlewood JL, Cousins AB. 2017. Influence of light and nitrogen on the photosynthetic efficiency in the C4 plant Miscanthus × giganteus. Photosynthesis research **131**, 1–13.

Maroco JP, Edwards GE, Ku MSB. 1999. Photosynthetic acclimation of maize to growth under elevated levels of carbon dioxide. Planta **210**, 115–125.

Massad R-S, Tuzet A, Bethenod O. 2007. The effect of temperature on C4-type leaf photosynthesis parameters. Plant, cell & environment **30**, 1191–204.

Maurel C, Boursiac Y, Luu D-T, Santoni V, Shahzad Z, Verdoucq L. 2015. Aquaporins in plants.

Physiological reviews **95**, 1321–1358.

Maurel C, Verdoucq L, Luu D-T, Santoni V. 2008. Plant aquaporins: membrane channels with multiple integrated functions. Annual review of plant biology **59**, 595–624.

Maxwell K, Johnson GN. 2000. Chlorophyll fluorescence-a practical guide. Journal of experimental botany **51**, 659–68.

Mebatsion HK, Verboven P, Ho QT, Verlinden B, Mendoza F, Nguyen TA, Nicolaï BM. 2006*a*. Modeling fruit microstructure using an ellipse tessellation algorithm. 13th world congress of food science & technology. Les Ulis, France: EDP Sciences, .

Mebatsion HK, Verboven P, Verlinden BE, Ho QT, Nguyen T a., Nicolaï BM. 2006*b*. Microscale modelling of fruit tissue using Voronoi tessellations. Computers and electronics in agriculture **52**, 36–48.

Meiyappan P, Jain AK. 2012. Three distinct global estimates of historical land-cover change and land-use conversions for over 200 years. Frontiers of earth science **6**, 122–139.

Mertz RA, Brutnell TP. 2014. Bundle sheath suberization in grass leaves: multiple barriers to characterization. Journal of experimental botany **65**, 3371–3380.

Missner A, Kugler P, Saparov SM, Sommer K, Mathai JC, Zeidel ML, Pohl P. 2008. Carbon dioxide transport through membranes. Journal of biological chemistry **283**, 25340–25347.

Molina-Aiz FD, Fatnassi H, Boulard T, Roy JC, Valera DL. 2010. Comparison of finite element and finite volume methods for simulation of natural ventilation in greenhouses. Computers and electronics in agriculture **72**, 69–86.

Moreno-Sotomayor A, Weiss A, Paparozzi ET, Arkebauer TJ. 2002. Stability of leaf anatomy and light response curves of field grown maize as a function of age and nitrogen status. Journal of plant physiology **159**, 819–826.

Morison JIL, Lawson T. 2007. Does lateral gas diffusion in leaves matter? Plant, cell & environment **30**, 1072–85.

Muhaidat R, Sage RF, Dengler NG. 2007. Diversity of Kranz anatomy and biochemistry in C4 eudicots. American journal of botany **94**, 362–381.

Nobel PS. 2005. Leaves and fluxes. Physicochemical and environmental pant physiology.351–418.

Ogle K. 2003. Implications of interveinal distance for quantum yield in C4 grasses: A modeling and meta-analysis. Oecologia **136**, 532–542.

Ort DR, Merchant SS, Alric J, *et al.* 2015. Redesigning photosynthesis to sustainably meet global food and bioenergy demand. Proceedings of the national academy of sciences **112**, 201424031.

Osmond CB. 1971. Metabolite transport in C4 photosynthesis. Australian journal of biological sciences **24**, 159–164.

Otsu. 1979. A threshold selection method from gray-level histograms. IEEE transactions on systems, man, and cybernetics **9**, 62–66.

Pachepsky LB, Acock B. 1996. A model 2DLEAF of leaf gas exchange: development, validation, and ecological application. Ecological modelling **93**, 1–18.

Palmer WM, Martin AP, Flynn JR, Reed SL, White RG, Furbank RT, Grof CPL. 2015. PEA-CLARITY: 3D molecular imaging of whole plant organs. Scientific reports **5**, 13492.

Parkhurst DF. 1994. Diffusion of CO2 and other gases inside leaves. New phytologist **126**, 449–479.

Parkhurst DF, Mott KA. 1990. Intercellular diffusion limits to CO2 uptake in leaves: studies in air and helox. Plant physiology **94**, 1024–32.

Peisker M. 1979. Conditions for low, and oxygen-independent, CO2 compensation concentrations in C4 plants as derived from a simple model. Photosynthetica **2**, 198–207.

Pengelly JJL, Kwasny S, Bala S, Evans JR, Voznesenskaya E V, Koteyeva NK, Edwards GE, Furbank RT, von Caemmerer S. 2011. Functional analysis of corn husk photosynthesis. Plant physiology **156**, 503–13.

Pengelly JJL, Sirault XRR, Tazoe Y, Evans JR, Furbank RT, von Caemmerer S. 2010. Growth of the C4 dicot Flaveria bidentis: photosynthetic acclimation to low light through shifts in leaf anatomy and biochemistry. Journal of experimental botany **61**, 4109–22.

Pfeffer M, Peisker M. 1998. CO2 gas exchange and phosphoenolpyruvate carboxylase activity in leaves of Zea mays L. Photosynthesis research **58**, 281–291.

Pick TR, Bräutigam A, Schlüter U, *et al.* 2011. Systems analysis of a maize leaf developmental gradient redefines the current C4 model and provides candidates for regulation. The Plant cell **23**, 4208–20.

Pinto H, Powell JR, Sharwood RE, Tissue DT, Ghannoum O. 2015. Variations in nitrogen use efficiency reflect the biochemical subtype while variations in water use efficiency reflect the evolutionary lineage of C4 grasses at inter-glacial CO2. Plant, cell & environment **39**, 514–526.

Pocker Y, Miksch RR. 1978. Plant carbonic anhydrase. Properties and bicarbonate dehydration kinetics. Biochemistry **17**, 1119–1125.

Pohit S, Biswas PK, Kumar R, Jha J. 2009. International experiences of ethanol as transport fuel: policy implications for India. Energy policy **37**, 4540–4548.

Poincelot RP. 1972. The distribution of carbonic anhydrase and ribulose diphosphate carboxylase in maize leaves. Plant physiology **50**, 336–340.

Poorter H, Niinemets U, Poorter L, Wright IJ, Villar R. 2009. Causes and consequences of variation in leaf mass per area (LMA):a meta-analysis. New phytologist **182**, 565–588.

Pyankov VI, Ziegler H, Akhani H, Deigele C, Lüttge U. 2010. European plants with C4 photosynthesis:

geographical and taxonomic distribution and relations to climate parameters. Botanical journal of the Linnean society **163**, 283–304.

Raven JA, Beardall J. 2016. The ins and outs of CO2. Journal of experimental botany **67**, 1–13.

Rezvani Moghaddam P, Wiliman D. 1998. Cell wall thickness and cell dimensions in plant parts of eight forage species. The journal of agricultural science **131**, 59–67.

Ryu J, Nam H, Kim HK, Joo Y, Lee SJ, Kim KH. 2014. In vivo monitoring of intracellular chloroplast movements in intact leaves of C4 plants using two-photon microscopy. Microscopy research and technique **77**, 806–13.

Sage RF. 2004. The evolution of C4 photosynthesis. New phytologist **161**, 341–370.

Sage RF, Kocaciner F, Kubien DS. 2011. C4 photosynthesis and temperature. In: Raghavendra AS,, In: Sage RF, eds. C4 photosynthesis and related CO2 concentrating mechanisms. Dordrecht: Springer Netherlands, 161–195.

Sage RF, Kubien DS. 2007. The temperature response of C3 and C4 photosynthesis. Plant, cell & environment **30**, 1086–106.

Sage RF, McKown AD. 2005. Is C4 photosynthesis less phenotypically plastic than C3 photosynthesis? Journal of experimental botany **57**, 303–317.

Sage RF, Pearcy RW. 2000. The physiological ecology of C4 photosynthesis. In: Leegood RC,, In: Sharkey TD,, In: von Caemmerer S, eds. Advances in Photosynthesis and Respiration. Advances in photosynthesis and respiration. Dordrecht: Springer Netherlands, 497–532.

Sage RF, Pearcy RW, Seemann JR. 1987. The nitrogen use efficiency of C3 and C4 Plants : III. Leaf nitrogen effects on the activity of carboxylating enzymes in Chenopodium album (L.) and Amaranthus retroflexus (L.). Plant physiology **85**, 355–359.

Sage RF, Wedin DA, Li M. 1999. The Biogeography of C4 photosynthesis: patterns and controlling factors. C4 Plant Biology.313–373.

Salvi D, Boldor D, Ortego J, Aita GM, Sabliov CM. 2010. Numerical modeling of continuous flow microwave heating: a critical comparison of COMSOL and ANSYS. The Journal of microwave power and electromagnetic energy : a publication of the International microwave power institute **44**, 187–97.

Sellers PJ, Dickinson RE, Randall DA, *et al.* 1997. Modeling the exchanges of energy, water, and carbon between continents and the atmosphere. Science **275**, 502–509.

Shaofan L, Wing Kam L. 2004. *Meshfree particle methods*. Berlin, Heidelberg: Springer Berlin Heidelberg.

Sharkey TD, Bernacchi CJ, Farquhar GD, Singsaas EL. 2007. Fitting photosynthetic carbon dioxide response curves for C(3) leaves. Plant, cell & environment **30**, 1035–40.

Sheehy J, Mitchel P., Hardy R. 2007. *Charting new pathways to c4 rice* (J Sheehy, P. Mitchel, and R Hardy, Eds.). Loas Banos,Philippines: International Rice Research Institute.

Somerville CR. 2001. An early Arabidopsis demonstration resolving a few issues concerning photorespiration. Plant physiology **127**, 3.

Sommer M, Bräutigam A, Weber APM. 2012. The dicotyledonous NAD malic enzyme C4 plant Cleome gynandra displays age-dependent plasticity of C4 decarboxylation biochemistry. Plant biology **14**, 621–629.

Sowiński P, Bilska A, Barańska K, Fronk J, Kobus P. 2007. Plasmodesmata density in vascular bundles in leaves of C4 grasses grown at different light conditions in respect to photosynthesis and photosynthate export efficiency. Environmental and experimental botany **61**, 74–84.

Sowiński P, Rudzińska-Langwald A, Kobus P. 2003. Changes in plasmodesmata frequency in vascular bundles of maize seedling leaf induced by growth at sub-optimal temperatures in relation to photosynthesis and assimilate export. Environmental and experimental botany **50**, 183–196.

Sowiński P, Szczepanik J, Minchin PEH. 2008. On the mechanism of C4 photosynthesis intermediate exchange between Kranz mesophyll and bundle sheath cells in grasses. Journal of experimental botany **59**, 1137–47.

Spalding MH, Portis AR. 1985. A model of carbon dioxide assimilation in Chlamydomonas reinhardii. Planta **164**, 308–20.

Staehelin LA. 2003. Chloroplast structure: from chlorophyll granules to supra-molecular architecture of thylakoid membranes. Photosynthesis research **76**, 185–96.

Stata M, Sage TL, Rennie TD, Khoshravesh R, Sultmanis S, Khaikin Y, Ludwig M, Sage RF. 2014. Mesophyll cells of C4 plants have fewer chloroplasts than those of closely related C3 plants. Plant, cell & environment **37**, 2587–2600.

Steyermark A. 1961. Microdetermination of nitrogen by the Dumas method. In: Intergovernmental Panel on Climate Change, ed. Quantitative organic microanalysis. Cambridge: Elsevier, 151–187.

Still CJ, Berry JA, Collatz GJ, DeFries RS. 2003. Global distribution of C3 and C4 vegetation: carbon cycle implications. Global biogeochemical cycles **17**, 6-1-6–14.

Studer AJ, Gandin A, Kolbe AR, Wang L, Cousins AB, Brutnell TP. 2014. A limited role for carbonic anhydrase in C4 photosynthesis as revealed by a ca1ca2 double mutant in maize. Plant physiology **165**, 608–617.

Sun W, Ubierna N, Ma J-Y, Walker BJ, Kramer DM, Cousins AB. 2014. The coordination of C4 photosynthesis and the CO2-concentrating mechanism in maize and Miscanthus x giganteus in response to transient changes in light quality. Plant physiology **164**, 1283–92.

Sweetlove LJ, Ratcliffe RG. 2011. Flux-Balance modeling of plant metabolism. Frontiers in plant science **2**, 1–10.

Taiz L. 1992. The plant vacuole. The Journal of experimental biology **172**, 113–122.

Taiz L, Zeiger E. 2003. *Plant Physiology*. Sunderland, MA: Sinauer Associates Inc.

Takabayashi A, Kishine M, Asada K, Endo T, Sato F. 2005. Differential use of two cyclic electron flows around photosystem I for driving CO2-concentration mechanism in C4 photosynthesis. Proceedings of the national academy of sciences of the United States of America **102**, 16898–16903.

Taniguchi Y, Taniguchi M, Kawasaki M, Miyake H. 2003. Strictness of the centrifugal location of bundle sheath chloroplasts in different NADP-ME type C4 grasses. Plant production science **6**, 274–280.

Taub DR, Lerdau MT. 2000. Relationship between Leaf nitrogen and photosynthetic rate for three NAD-ME and three NADP-ME C4 grasses. American journal of botany **87**, 412.

Tazoe Y, Noguchi K, Terashima I. 2006. Effects of growth light and nitrogen nutrition on the organization of the photosynthetic apparatus in leaves of a C4 plant, Amaranthus cruentus. Plant, cell and environment **29**, 691–700.

Terashima I, Fujita T, Inoue T, Chow WS, Oguchi R. 2009. Green light drives leaf photosynthesis more efficiently than red light in strong white light: Revisiting the enigmatic question of why leaves are green. Plant and cell physiology **50**, 684–697.

Terashima I, Hanba YT, Tholen D, Niinemets Ü. 2011. Leaf functional anatomy in relation to photosynthesis. Plant physiology **155**, 108–16.

Thain JF. 1983. Curvature correction factors in the measuremnet of cell surface areas in plant tissues. Journal of experimental botany **34**, 87–94.

Tholen D, Zhu X-G. 2011. The mechanistic basis of internal conductance: a theoretical analysis of mesophyll cell photosynthesis and CO2 diffusion. Plant physiology **156**, 90–105.

Tyree MT. 1970. The symplast concept a general theory of symplastic transport according to the thermodynamics of irreversible processes. Journal of Theoretical Biology **26**, 181–214.

Ubierna N, Sun W, Cousins AB. 2011. The efficiency of C4 photosynthesis under low light conditions: assumptions and calculations with CO2 isotope discrimination. Journal of experimental botany **62**, 3119–34.

Ubierna N, Sun WEI, Kramer DM, Cousins AB. 2013. The efficiency of C4 photosynthesis under low light conditions in Zea mays, Miscanthus x giganteus and Flaveria bidentis. Plant, cell & environment **36**, 365–381.

Uehlein N, Otto B, Hanson DT, Fischer M, McDowell N, Kaldenhoff R. 2008. Function of Nicotiana tabacum aquaporins as chloroplast gas pores challenges the concept of membrane CO2 permeability. The plant cell **20**, 648–57.

Ustin SL, Jacquemoud S, Govaerts Y. 2001. Simulation of photon transport in a three-dimensional leaf: implications for photosynthesis. Plant, cell and environment **24**, 1095–1103.

Utsunomiya E, Muto S. 1993. Carbonic anhydrase in the plasma membranes from leaves of C3 and C4 plants. Physiologia plantarum **88**, 413–419.

Verboven P, Herremans E, Borisjuk L, Helfen L, Ho QT, Tschiersch H, Fuchs J, Nicolaï BM, Rolletschek H. 2013. Void space inside the developing seed of Brassica napus and the modelling of its function. New phytologist **199**, 936–47.

Verboven P, Herremans E, Helfen L, Ho QT, Abera M, Cloetens P, Carmeliet J, Nicolaï BM. 2015. Synchrotron X-ray computed laminography of the 3-D anatomy of tomato leaves. The plant journal **81**, 169–182.

Verboven P, Ho QT, Herremans E, Mebatsion HK, Nicolaï B, Kerckhofs G, Wevers M, Cloetens P. 2010. Fruit microstructure evaluation using synchrotron X-ray computed tomography. Food engineering interfaces.589–598.

Verboven P, Kerckhofs G, Mebatsion HK, Ho QT, Temst K, Wevers M, Cloetens P, Nicolaï BM, Nicolai BM. 2008. Three-dimensional gas exchange pathways in pome fruit characterized by synchrotron x-ray computed tomography. Plant physiology **147**, 518–527.

Verboven P, Pedersen O, Herremans E, Ho QT, Nicolaï BM, Colmer TD, Teakle N. 2012. Root aeration via aerenchymatous phellem: three-dimensional micro-imaging and radial O2 profiles in Melilotus siculus. New phytologist **193**, 420–31.

Verboven P, Pedersen O, Ho QT, Nicolai BM, Colmer TD. 2014. The mechanism of improved aeration due to gas films on leaves of submerged rice. Plant, cell & environment **37**, 2433–52.

Verschoor A, Warner JR, Srivastava S, Grassucci R a, Frank J. 1998. Three-dimensional structure of the yeast ribosome. Nucleic acids research **26**, 655–61.

Versteeg H, Malalasekera W. 1995. *An introduction to computational fluid dynamics : the finite volume method.* Essex, UK: Longman scientific and technical.

Vesala T, Ahonen T, Hari P, Krissinel E, Shokhirev N. 1996. Analysis of stomatal CO2 uptake by a three-dimensional cylindrically symmetric model. New phytologist **132**, 235–245.

Vicankova A, Kutik J. 2005. Chloroplast ultrastructural development in vascular bundle sheath cells of two different maize (Zea mays L.) genotypes. Plant soil and environment **51**, 491–495.

Vogelmann TC, Bjorn LO. 1984. Measurement of light gradients and spectral regime in plant-tissue with a fiber optic probe. Physiologia plantarum **60**, 361–368.

Vos J, Putten PEL van der, Birch CJ. 2005. Effect of nitrogen supply on leaf appearance, leaf growth, leaf nitrogen economy and photosynthetic capacity in maize (Zea mays L.). Field crops research **93**, 64–73.

Walpole J, Papin JA, Peirce SM. 2013. Multiscale computational models of complex biological systems. Annual review of biomedical engineering **15**, 137–54.

Wang Y, Bräutigam A, Weber APM, Zhu X-G. 2014*a*. Three distinct biochemical subtypes of C4 photosynthesis? A modelling analysis. Journal of experimental botany **65**, 3567–78.

Wang Y, Long SP, Zhu X-G. 2014*b*. Elements required for an efficient NADP-malic enzyme type C4 photosynthesis. Plant physiology **164**, 2231–46.

Wang S, Tholen D, Zhu X-G. 2017. C4 photosynthesis in C3 rice: a theoretical analysis of biochemical and anatomical factors. Plant, cell & environment **40**, 80–94.

Watling JR. 2000. Elevated CO2 induces biochemical and ultrastructural changes in leaves of the C4 cereal sorghum. Plant physiology **123**, 1143–1152.

Watté R, Aernouts B, Van Beers R, Herremans E, Ho QT, Verboven P, Nicolaï B, Saeys W. 2015. Modeling the propagation of light in realistic tissue structures with MMC-fpf: a meshed Monte Carlo method with free phase function. Optics express **23**, 17467.

Weber APM, von Caemmerer S. 2010. Plastid transport and metabolism of C3 and C4 plants - comparative analysis and possible biotechnological exploitation. Current opinion in plant biology **13**, 257–65.

van der Weijde T, Alvim Kamei CL, Torres AF, Vermerris W, Dolstra O, Visser RGF, Trindade LM. 2013. The potential of C4 grasses for cellulosic biofuel production. Frontiers in plant science **4**, 107.

Weinan E. 2011. *Principles of multiscale modeling*. Cambridge, UK: Cambridge university press.

Weiner H, Burnell JN, Woodrow IE, Heldt HW, Hatch MD, Sauer F. 1988. Metabolite diffusion into bundle sheath cells from C4 plants: relation to C4 photosynthesis and plasmodesmatal function. Plant physiology **88**, 815–22.

Weng J-H, Hsu F-H. 2001. Gas exchange and epidermal characteristics of Miscanthus populations in Taiwan varying with habitats and nitrogen application. Photosynthetica **39**, 35–41.

Woolley JT. 1971. Reflectance and transmittance of light by leaves. Plant physiology **47**, 656–662.

Yamada M, Kawasaki M, Sugiyama T, Miyake H, Taniguchi M. 2009. Differential positioning of C4 mesophyll and bundle sheath chloroplasts: aggregative movement of C4 mesophyll chloroplasts in response to environmental stresses. Plant & cell physiology **50**, 1736–49.

Yin X, Belay DW, van der Putten PEL, Struik PC. 2014. Accounting for the decrease of photosystem photochemical efficiency with increasing irradiance to estimate quantum yield of leaf photosynthesis. Photosynthesis research **122**, 323–335.

Yin X, Van Oijen M, Schapendonk AHCM. 2004. Extension of a biochemical model for the generalized stoichiometry of electron transport limited C3 photosynthesis. Plant, cell and environment **27**, 1211–1222.

Yin X, van der Putten PEL, Driever SM, Struik PC. 2016. Temperature response of bundle-sheath conductance in maize leaves. Journal of experimental botany **67**, 2699–2714.

Yin X, Struik PC. 2012. Mathematical review of the energy transduction stoichiometries of C4 leaf photosynthesis under limiting light. Plant, cell & environment **35**, 1299–312.

Yin X, Struik PC, Romero P, Harbinson J, Evers JB, Van Der Putten PEL, Vos J. 2009. Using combined measurements of gas exchange and chlorophyll fluorescence to estimate parameters of a biochemical C3 photosynthesis model : a critical appraisal and a new integrated approach applied to leaves in a wheat (Triticum aestivum) canopy. Plant, cell & environment **32**, 448–64.

Yin X, Sun Z, Struik PC, Gu J. 2011*a*. Evaluating a new method to estimate the rate of leaf respiration in the light by analysis of combined gas exchange and chlorophyll fluorescence measurements. Journal of experimental botany **62**, 3489–99.

Yin X, Sun Z, Struik PC, Van der Putten PEL, Van Ieperen W, Harbinson J. 2011*b*. Using a biochemical C4 photosynthesis model and combined gas exchange and chlorophyll fluorescence measurements to estimate bundle-sheath conductance of maize leaves differing in age and nitrogen content. Plant, cell & environment **34**, 2183–99.

Yoshimura Y, Kubota F, Ueno O. 2004. Structural and biochemical bases of photorespiration in C4 plants: quantification of organelles and glycine decarboxylase. Planta **220**, 307–317.

Zeppel MJB, Lewis JD, Chaszar B, Smith R a, Medlyn BE, Huxman TE, Tissue DT. 2012. Nocturnal stomatal conductance responses to rising [CO2], temperature and drought. The New phytologist **193**, 929–938.

Zheng Y, Xu M, Shen R, Qiu S. 2013. Effects of artificial warming on the structural, physiological, and biochemical changes of maize (Zea mays L.) leaves in northern China. Acta Physiologiae Plantarum **35**, 2891–2904.

Zhu X-G, Shan L, Wang Y, Quick WP. 2010. C4 rice - an ideal arena for systems biology research. Journal of integrative plant biology **52**, 762–70.

List of publications

Articles in internationally reviewed academic journals

Retta, M., Ho, Q., Yin, X., Verboven, P., Struik, PC., Nicolai, BM. 2016. A two-dimensional microscale model of gas exchange during photosynthesis in maize (Zea mays L.) leaves. Plant science, **246**, 37-51.

Retta, M., Yin, X., van der Putten, P., Cantre, D., Berghuijs, H., Ho, Q., Verboven, P., Struik, PC., Nicolai, BM. 2016. Impact of anatomical traits of maize (Zea mays L.) leaf as affected by nitrogen supply and leaf age on bundle sheath conductance. Plant science, **252**, 205-214.

Berghuijs HNC, Yin X, Ho QT, Driever SM, Retta MA, Nicolai BM, Struik PC. 2016. Mesophyll conductance and reaction-diffusion models for CO_2 transport in C_3 leaves; needs, opportunities and challenges. Plant science **252**, 62–75.

Ho, Q., Berghuijs, H., Watté, R., Verboven, P., Herremans, E., Yin, X., Retta, M., Aernouts, B., Saeys, W., Helfen, L., Farquhar, G., Struik, PC., Nicolai, BM. 2016. 3-D microscale modeling of CO2 transport and light propagation in tomato leaves enlightens photosynthesis. Plant, cell & environment, **39**, 50-61.

Berghuijs, H., Yin, X., Ho, Q., van der Putten, P., Verboven, P., Retta, M., Nicolai, BM., Struik, PC. 2015. Modeling the relationship between CO_2 assimilation and leaf anatomical properties in tomato leaves. Plant science, **238**, 297-311.

Ho, Q., Verboven, P., Fanta, S., Abera, M., Retta, M., Herremans, E., Defraeye, T., Nicolai, BM. 2014. A multiphase pore scale network model of gas exchange in apple fruit. *Food and bioprocess technology*, **7** (2), 482-495.

Papers at international scientific conferences and symposia, published in full in proceedings

Retta, M., Ho, Q., Yin, X., Verboven, P., Berghuijs, H., Struik, PC., Nicolai, BM. 2016. Exploring anatomical controls of C_4 leaf photosynthesis using a 3-D reaction-diffusion model. Model-IT. Wageningen, 11-14 October 2015.

Abera, M., Retta, M., Berghuijs, H., Struik, PC., Verboven, P., Nicolai, BM. 2014. Virtual Microstructural Leaf Tissue Generation Based on Cell Growth Modeling. 29th International Horticultural Congress. Brisbane, Australia, 17-24 August 2014.

Abera, M., Fanta, S., Retta, M., Herremans, E., Defraeye, T., Ho, Q., Verboven, P., Nicolai, BM. 2013. Application of virtual fruit tissue geometries to postharvest studies. Proceedings of InsideFood Symposium 2013. INSIDEFOOD Symposium. Leuven, Belgium, 9-12 April 2013 (art.nr. 070P).

Ho, Q., Verboven, P., Herremans, E., Retta, M., Defraeye, T., Nicolai, BM., Yin, X., Thapa, R., Struik, PC. 2012. A 3-D microscale model for CO2 gas transport in tomato leaves during photosynthesis. In Luo, W. (Ed.), Bertin, N. (Ed.), Heuvelink, E. (Ed.), IV International Symposium on Models for Plant Growth, Environmental Control and Farm Management in Protected Cultivation - HortiModel2012: Vol. 1. HortiModel2012: Models for Plant Growth, Environmental Control and Farm Management in Protected Cultivation. Nanjing, 4-8 November 2012 (pp. 215-222).

Meeting abstracts, presented at international scientific conferences and symposia, published or not published in proceedings or journals

Retta, M., Ho, Q., Yin, X., Verboven, P., Berghuijs, H., Nicolai, BM., Struik, PC. 2014. A two-dimensional micro-scale model of gas exchange during photosynthesis in maize (Zea mays L.) leaves. Plant Biology Europe FESPB/EPSO. Dublin, 22-26 June 2014, Abstract No. 0388.

Ho, Q., Verboven, P., Fanta, S., Abera, M., Retta, M., Herremans, E., Defraeye, T., Nicolai, BM. 2012. Pore cell network modeling of gas exchange in fruit. Soft matter approaches to structure foods: FD158. Hof Van Wageningen, Netherlands, 2-4 July 2012.

PE&RC Training and Education Statement

With the training and education activities listed below the PhD candidate has complied with the requirements set by the C.T. de Wit Graduate School for Production Ecology and Resource Conservation (PE&RC) which comprises of a minimum total of 32 ECTS (= 22 weeks of activities)

Review of literature (4.5 ECTS)

- Essentials of C_4 Photosynthesis and gas exchange modelling (Bio-fluidics group seminar series)

Writing of project proposal (4.5 ECTS)

- Multi-scale modelling of gas exchange in photosynthesis tissue

Post-graduate courses (6.5 ECTS)

- Inverse modelling in earth and environmental sciences; University of California and KU Leuven (2012)
- Life science technology watch; Arenberg doctoral school, KU Leuven (2012)

Deficiency, refresh, brush-up courses (6.5 ECTS)

- Theory and methods of applied research; UGhent and KU Leuven (2011)
- Multiscale transport phenomena of Biosystems; KU Leuven (2011)

Competence strengthening / skills courses (5.6 ECTS)

- Presentation skills for doctoral students; KU Leuven (2012)
- Ethics and philosophy in animal science (RI&EA); WGS (2012)
- Exploitation of research technology & knowledge transfer; Research and Development, KU Leuven (2012)
- Academic writing for doctoral students; KU Leuven (2012)

PE&RC Annual meetings, seminars and the PE&RC weekend (1.2 ECTS)

- PE&RC Weekend last year's edition (2015)
- PE&RC Day: one's waste...another's treasure? (2015)

Discussion groups / local seminars / other scientific meetings (6.1 ECTS)

- Bio-Fluidics group seminar series (2012-2014)
- Journal club and presentation of results (2012-2014)
- Scientific integrity for starting PhDs (2014)

International symposia, workshops and conferences (4.4 ECTS)

- Plant biology Europe FESPB/EPSO; poster presentation; Dublin, Ireland (2014)
- Model-IT; oral presentation; Wageningen, the Netherlands (2015)

Lecturing / supervision of practicals / tutorials (3 ECTS)

- Engineering properties of biomaterials: practical exercises-water activity measurement (2014, 2015)